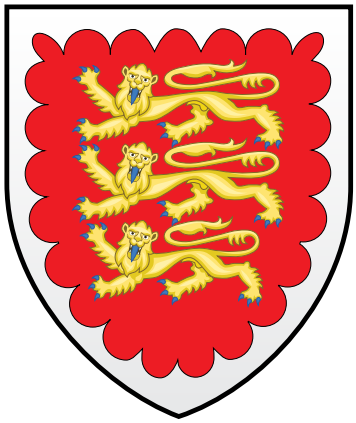
Thermoelectric Effects in Carbon Nanostructures

From Quantum to Mesoscopic Influences





Achim Harzheim
Oriel College
University of Oxford

Supervisors:
Prof. G. Andrew D. Briggs
Dr. Jan A. Mol
Dr. Pascal Gehring

A thesis presented for the degree of
Doctor of Philosophy
Trinity 2020

Acknowledgements

Completing my DPhil in Oxford has been an incredible experience and significantly expanded my scientific horizon to a point I couldn't have fathomed at the end of my Bachelor degree. At the same time, my DPhil enabled me to get to know British culture and experience the traditions, quirks and peculiarities of completing a degree at an institution that is almost a thousand years old. As is the case with most endeavours this thesis and the work contained in it would not have been possible without a variety of friends, supervisors and teammates. They helped me directly through scientific guidance or indirectly by giving general advice and encouragement as well as the sometimes sorely needed distraction from my research efforts. Here I want to thank all the people that have contributed to my thesis in various ways for their support.

First and foremost I wish to thank my supervisors Prof. Andrew Briggs, Dr. Jan Mol and Dr. Pascal Gehring. I was fortunate to have three supervisors that worked together well and were each able to provide valuable expertise, guidance and support in their own ways. Andrew, thank you for enabling me to do my DPhil in your group by first and foremost bringing me to Oxford but also for finding an appropriate scholarship for me. Throughout my DPhil you have provided me with the freedom to conduct my own research and venture into areas that might not have been exactly what you envisioned for me. In addition your understanding of my extracurricular interests (mainly rowing) at the same time as making sure I am still focused on my DPhil were greatly appreciated.
Most of the daily supervision was performed by my other two supervisors Jan and Pascal who had an outsized influence on the work presented here.

Jan, during my time in Oxford you have helped me countless times with answering scientific questions as well as getting the equipment (far too often the VISA communication between the equipment and the PC) to work. Throughout this I could always rely on you to prioritize helping me over other pressing work or even being home on time. You've always had an open ear for both my personal and academic problems and suggestions in how to tackle them. While maybe not as obviously important as the other points, you were also an incredibly helpful resource in how to navigate the myriads of policies and forms required by the university and the department. In addition, even after you had left Oxford you continued to check in and help which is by no means a given.
Most of the initial fabrication and measurement protocols I used to perform my first measurements were taught to me by my last but by no means least supervisor Pascal. Pascal, I will miss our constant brain storming sessions and bouncing ideas of each other on what to measure, how to do it and why it is interesting for the greater community. You've helped me whenever I was stuck in data analysis or in interpreting my results and were definitely the main driving force in most of the experiments described in this work. Be it in establishing a collaboration, coming up with an interesting project or helping me refine my own ideas for measurements and projects I could always rely on you. More than just being a supervisor you've become a friend during my PhD that I could rely on for advice on every aspect of academic and non-academic life. The additional knowledge about beer in the UK, both Ale from the pub or home-brewed and the appreciation of pub culture I learned from you are something I will fondly remember too.
While not my supervisors during my DPhil I also want to thank Prof. Philip Kim and Dr. Ke Wang for enabling me to engage in research during my undergraduate degree and their encouragement and support which laid the groundwork that made this thesis possible.

Apart from my supervisors, my collaborators played a major role in making my DPhil a success. In allowing me access to advanced measurement methods and offering their expertise they were able to provide me with opportunities I did not have at Oxford. The most important collaboration with Lancaster opened up a new scientific avenue for me, SThM measurements, and directly led to the realization of two published projects while also inspiring a third one. Here I want to thank Dr. Jean Spiece, Dr. Charalambos Evangeli and Prof. Oleg Kolosov for their tremendous help and expertise. In addition to the long nights in the lab attempting to get the

very handy SThM system to work I will remember the long nights in the city centre usually crowned or ruined by a last pint at the Apothecary.
The second major collaboration during my DPhil was with the van der Zant lab at the Delft University of Technology, Pascal's new group. While not all of the projects worked I always enjoyed my time there, felt incredibly welcome in the group and had access to the superior fabrication facilities in Delft. In addition, one of my favourite projects, the single material graphene thermocouple, was realized through this collaboration. I want to thank Prof. van der Zant and Pascal for making this collaboration possible and all members of the van der Zant group for welcoming me and helping me in my time there. I also want to thank Nikos Papadopoulos who was always there to help with fabrication and over the last few years put a lot of work into unfortunately mostly unsuccessful projects.
At this point I also want to thank the team at IBM research in Zurich, Bernd Gotsmann and Fabian Koenemann for their help in calibrating the single material graphene thermocouples. The temperature maps recorded using their SThM system will be remembered as one of the quickest and least troublesome measurements in the course of my DPhil.
Lastly, I want to thank Prof. Colin Lambert's group in Lancaster for their theoretical support and providing me with a never-ending flow of ideas for tweaking the thermoelectric properties in nanostructures.

If collaborations outside of Oxford enabled me to broaden my access to other scientific equipment and expertise my colleagues and friends at the department made it possible to fully take advantage of what Oxford offers and made the experience so much more enjoyable. Whether it was sharing an office, meeting for lunch or bumping into each other in the cleanroom these encounters usually brightened up my day and often lead to helpful scientific discussions.
I want to thank Jakub for helping me develop a theory to describe the thermal transport in the graphene quantum dots as well as being an excellent teacher in all theory matters.
I wish to thank Jake Swett who started his DPhil at the same time as me and who over time as we shared an office became a good friend at Oxford. Apart from his incredible work ethic he was always there to provide help with fabrication as well as supplying wafers of pre-patterned chips to fabricate into devices. In addition, we often shared the same frustration over having to fill out one of the thousands of forms required by the department or other bureaucratic hurdles and engaged in

a variety of discussions of both academic and general nature. I also want to thank Jasper Fried and John Cully for being such good office mates and tolerating my expansionist tendencies when it came to desks and screens and Xinya Bian for his help with my experiments and measurement setups as well as his iconic nicknames. Additionally I want to thank the other members of the wider Mol group from the chemistry department James Thomas and Bart Limburg.
Lastly, I want to thank the German gang, Matthias Mergenthaler, Felix Schupp, Armin Krupp and Tim Grob, the German Stammtisch lunch meetings, which were often overrunning the planned 60 minutes, were always something to look forward to.
I thank Paul Pattinson for managing the cleanroom and helping with everything related to the encompassing tools, for always taking time to try to figure out problems with me and for encouraging me to row for the blues team.
My time at the department would not have been as enjoyable without Sapna (Sapples), particularly after the initial antipathy was overcome. The at least weekly lunch meetings were consistently the highlight of my week and at this point I probably owe you thousands of pounds in lunch money. In addition, your terrible jokes did make me smile most of the time though not necessarily because of the punch line. While we did not manage to have our goodbye pub crawl as planned I'm sure we will manage a substitute event and I won't forget that you still owe me a night worth of pints. Thank you for being a great friend. I also want to thank Vik for the conversations about life and the academic world in general and for her friendship.
I also want to thank all my non-DPhil related friends in the UK and all over the world for checking in on me, supporting me and just for being in my life. Here I thank my OUBC teammates (especially the 2019 and 2020 squad), Rory and Tessa, Dusan and Ivana, Josh, Dr. Dr. Grace Clough MBE, Geraldine and Erin, Frankie and my housemates Christine, Carlo, Lukas and Lucy. I thank my friends in the U.S., Maddie (Maggie), Pat and Sam as well as James. I thank my friends back in Germany at my home base Andi and Susi, Rocko, Schlotti, Dommel, Justus and Koesch. Particularly Justus and Koesch in combination with my brother have played a substantial role in motivating me to pursue and finish my DPhil.
At this point I also wish to mention Heidi who endured the majority of my DPhil at my side; thank you for being a big part of my life.
I want to thank all friends from my college, Oriel, particularly the OCBC for two headships and the opportunity to race in the most absurd rowing race in the world, bumps racing. Here, I want to highlight the members of OCBC bowside, Jan and

Phil. I also want to say thank you to my college family, my college-sister Maren and my college-mum Gabby who both made the college and Oxford that much more of a fun and welcoming place for me.

As almost everyone who knows me is aware I have also engaged in a somewhat time costly non-academic activity at Oxford that occupied most of my free time and then some: rowing. While trialling for the Blues squad has sometimes left me with little time to pursue my DPhil I have learned invaluable facts about myself and teamwork in the process as well as met incredible people and friends for life. I want to thank the OUBC coaches, Sean, Brendan and Andi for their patience with me and the administrative team Barbara and Caroline as well as the boatman Austin for their support. I also want to thank all three squads I had the honour of being a part of but especially Dusan, Ben, Iain, Felix and my summer housemates Charlie and Bambi as well as the OUWBC squads and especially Tina.

I am also especially thankful for the patience and support shown by my girlfriend Svenja throughout the last few months when both my rowing and my academic career came to a more or less successful end.

One of the most important parts of my life has also been my family without whom I would not have finished my DPhil let alone started it. Foremost I want to thank my parents who did not try to convince me to stay in Germany when I wanted to go abroad and financed my whole education. I want to thank my grandparents who were always proud of my academic achievements and my siblings and their partners who unceasingly encouraged and supported me along the way. Most importantly, I want to thank my whole family for their patience with me and understanding of my time constraints due to the DPhil and rowing.

Lastly I want to thank my assessors who have taken the time and effort to read and analyse my thesis, enabled an interesting discussion during the viva and provided valuable feedback.

Abstract

Heat from electrical devices, car engines, industrial processes and even our own body heat are an abundant, albeit difficult to harvest, energy source in today's society. As the extent of the climate crisis becomes clearer, recovering such waste heat can be an important step to design improved devices and reduce greenhouse gas emissions as well as the use of fossil fuels. Thermoelectric materials and devices are uniquely positioned to recover this waste heat and transform it to electricity due to their conversion characteristics and potentially small size. In addition, ever-increasing demands on computing power as well as further downscaling in chip sizes necessitates on-chip spot cooling and temperature sensing, which can be provided by thermoelectric devices.

So far, whenever research in thermoelectrics seemed to be at a dead end, a new approach, such as for example most recently nanostructuring and reduced dimensionality, have reinvigorated the field. While this has lead to unprecedented advances in the figure of merit, now regularly reported above unity, thermoelectric devices are still lacking the required conversion efficiency to compete with conventional heat engines, leaving them an option mostly for niche applications. Particularly in low-dimensional devices and structures, theoretically predicted high and competitive efficiency values are hard to obtain due to environmental factors and inherent limits in device design. In this dissertation, influences on the thermoelectric properties of carbon nanostructures due to coupling configurations, defects, geometrical considerations and other local effects are studied. A first experiment investigates the power factor in C_{60} molecules, contacted via electroburned graphene nanoconstrictions. The results suggest a threefold way to increase the achievable power factor in zero-dimensional structures: positioning the molecular energy levels close to the Fermi

energy levels of the leads, ensuring the tunnel coupling is optimized for the desired operating temperature and, in order to achieve a maximum power factor, the tunnel couplings to the source and drain need to be equal. Building on these conclusions, a temperature dependent study of the power factor in graphene quantum dots was performed, suggesting that a quantum dot can work as a quantum heat valve especially when contacted by non-ideal heat conducting leads. Apart from highlighting the importance of leads that conduct heat well to achieve a high performance, the findings also again emphasize the potentially detrimental effect tunnel coupling has on the power factor.

In order to analyse more localised effects, a Scanning Thermal Microscopy (SThM) approach was used to record thermoelectric maps (of both the Seebeck and Peltier effect) of graphene bow ties, revealing a geometrically dependent change in the Seebeck coefficient due to the impact of electron scattering at the graphene edges. This effect is exploited later to fabricate single-material graphene thermocouples that achieve an order of magnitude higher sensitivity than previously reported single-material metal thin film thermocouples. Lastly, Scanning Thermal Gate Microscopy (STGM) is developed, improving on the previously used SThM technique to achieve high resolution in thermovoltage maps at a fast scanning rate. STGM is then applied to graphene single-layer/bilayer junctions, demonstrating the influence of metallic contacts, layer thickness changes and local strain on the spatially distributed Seebeck coefficient in graphene.

The effects studied in this dissertation are aimed at helping to further the understanding of local thermoelectric properties and opening the path to improve on current device design and performances as well as facilitating the elimination of parasitic noise caused by undesirable thermoelectric effects.

Content

I FUNDAMENTALS **1**

1 Introduction **3**
1.1 Heat to Electricity Conversion . . . 3
1.2 Bulk Thermoelectrics . . . 5
1.3 Thermoelectrics in Nanodevices . . . 6
1.4 Thesis Synopsis . . . 8

2 Theory of Heat and Charge Transport **11**
2.1 Introduction . . . 11
2.2 Charge Transport in Zero-dimensional Structures . . . 12
2.2.1 The Different Coupling Regimes . . . 14
2.2.2 Vibrational States . . . 18
2.3 Thermoelectrics in Zero-dimensional Structures . . . 18
2.3.1 Landauer Formalism . . . 19
2.3.2 Fermi-Dirac Distribution . . . 20
2.3.3 The Landauer Formalism in Thermoelectrics . . . 21
2.3.4 Thermopower and Peltier Coefficient . . . 25
2.3.5 Rate Equation Approach . . . 27

3 Materials Used and Previous Measurements **31**
3.1 Graphene and Graphene Nanostructures . . . 32
3.2 Buckminsterfullerene . . . 34
3.3 Previous Thermoelectric Measurements in 0D and 2D Systems . . . 35
3.3.1 Thermoelectric Measurements in Quantum Dot Structures . . . 36
3.3.2 Two-dimensional Systems . . . 38

II EXPERIMENTAL DETAILS **41**

4 Fabrication **43**

4.1 Standard Fabrication Procedure . . . 43
4.1.1 Chip Preparation . . . 43
4.1.2 Electron Beam Lithography . . . 45
4.1.3 Development . . . 46
4.1.4 Deposition and Lift-off . . . 47
4.1.5 Graphene Transfer . . . 47
4.1.6 Graphene Patterning . . . 48
4.2 Electroburning and Graphene Quantum Dots . . . 49
4.3 Chip Design . . . 51

5 Measurement Setups **53**
5.1 AC (2ω method) and DC Measurement . . . 54
5.2 SThM Setup . . . 54
5.3 On-chip Measurement . . . 57
5.3.1 Cryogenic Setups . . . 57
5.3.2 Accounting for Intrinsic Error Sources . . . 58

III EXPERIMENTAL RESULTS **61**

6 Thermoelectric Measurements of C_{60} Molecule Devices **63**
6.1 C_{60} Thermoelectric Nanodevices . . . 64
6.2 Results and Discussions . . . 68
6.2.1 Low Temperature Characterization . . . 68
6.2.2 Thermoelectric Measurements . . . 71
6.2.3 Power Factor . . . 74
6.3 Conclusions . . . 77

7 Thermoelectric Properties of Graphene Quantum Dots **79**
7.1 Devices and Measurement Setup . . . 80
7.2 Rate Equation Model . . . 84
7.3 Thermovoltage and Heat Flow Through the GQD . . . 86
7.4 Power Factor . . . 94
7.5 Conclusions . . . 98

8 Geometry Dependent Thermoelectric Effects in Graphene **101**
8.1 SThM Measurement Configurations . . . 102
8.2 Experimental Results . . . 105

8.3 Modelling of the Electron Mean Free Path . . . 107
8.4 Other Geometries . . . 112
8.5 Current Dependency . . . 115
8.6 Conclusion . . . 118

9 Local Mapping of Thermoelectric Properties of Graphene Nanostructures via Scanning Thermal Gate Microscopy 121
9.1 STGM Measurement Configurations . . . 122
9.2 Rectangular Graphene Device . . . 125
9.3 Single-layer/Bilayer Graphene Junction . . . 128
9.4 Seebeck Coefficient Calculation . . . 133
9.5 Conclusion . . . 137

10 Single Material Graphene Thermocouples 139
10.1 Thermocouple Devices . . . 140
10.2 Thermocouple Characterization . . . 142
10.3 Conclusion . . . 147

11 Conclusions and Outlook 149
11.1 Summary . . . 149
11.2 Additional Systems for Thermoelectric Measurements . . . 152
11.3 Hydrodynamics and Thermoelectrics . . . 154

References 155

Appendix A Band Structure of Graphene 179
A.1 Single-layer Graphene . . . 179
A.2 Bilayer Graphene . . . 183

Appendix B Standard Fabrication Details 187
B.1 Chip Preparation . . . 187
B.2 Photoresist Application (Figure B.1a-b). . . . 188
B.3 Electron Beam Lithography (Figure B.1c). . . . 189
B.4 Development (Figure B.1d) . . . 191
B.5 Deposition and Lift-off (Figure B.1e-f) . . . 191
B.6 Graphene Transfer . . . 192
B.7 Graphene Patterning (Figure B.2) . . . 194

Appendix C Further Experimental Details **195**
C.1 Thermoelectric Measurements of C_{60} Molecule Devices 195
C.1.1 Calibration of the Heater: Vacuum and Variable Temperature Scanning Thermal Microscopy 195
C.1.2 "Additive" Method for Absolute Heater Temperature Calibration. . 196
C.1.3 Calibration of the Heater: COMSOL Simulations 199
C.1.4 Supporting Thermoelectric Data: C_{60} Junctions 200
C.2 Local Mapping of Thermoelectric Properties of Two-dimensional Structures via Scanning Thermal Gate Microscopy 217
C.2.1 Temperature Tip Calibration 217
C.2.2 Pseudo 2D Deconvolution 217
C.2.3 Approximation of the Width of the Temperature Distribution . . . 220
C.2.4 Extraction of Average Thermovoltage and Seebeck Coefficient from 2D Maps via Gaussian Fitting 220

I

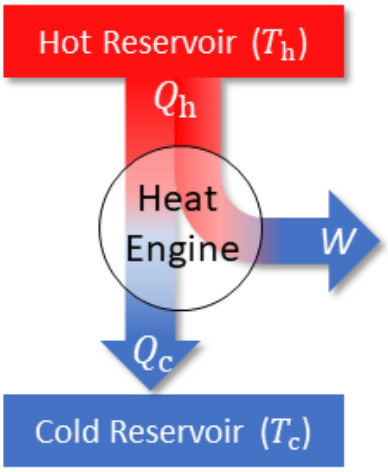
Fundamentals

1

Introduction

1.1 Heat to Electricity Conversion

The process of converting thermal energy into usable power has been a part of humanity's technological advancement since the industrial revolution, where chemical energy from fossil fuels was converted into heat and eventually mechanical power in steam engines. Similarly, today classical heat engines are used in large scale structures such as gas, coal or nuclear power plants to produce electricity. These classical heat engines usually rely on a heat source turning water (or another coolant) into vapour, which then drives through a turbine, thereby spinning the turbine and creating electricity. They can be found in most power plants and offer a cheap, reliable way of turning heat into electricity with a reasonable efficiency.
A different way of heat to energy conversion is to utilise thermoelectric effects. Here, thermoelectric devices are defined as relying on thermoelectric phenomena, that is the interplay between heat currents and electrical currents, to function. The two most prominent thermoelectric effects are the Seebeck effect, which converts a heat current into an electrical current and its counterpart, the Peltier effect, which converts an electrical current into a heat current and can be used for heating or refrigeration.
Thermoelectric devices have long been seen as a potential addition to renewable energy production due to their obvious potential for energy harvesting of waste heat, however, they have been plagued by high costs, low efficiency and the often toxic materials needed to produce them [1]. Currently, the most efficient thermoelectric devices at working temperatures of up to 450 K tend to comprise toxic or scarce materials such as bismuth, telluride, antimony or selenium [2–4].



Where
T_c, T_h denote Reservoirtemperatures (K)
Q_h, Q_c denote Heat flux (W)

$$W = \text{Work (W)}$$

$$\eta = \frac{W}{Q_h} = \frac{Q_h - Q_c}{Q_h}$$

$$\eta_{max} = \frac{T_h - T_c}{T_h}$$

Figure 1.1 Schematic of the functioning of a heat engine that uses the temperature gradient between two reservoirs to extract work.

While classic heat engines have steadily improved and today gas or coal power plants can reliably reach efficiencies of up to 40 %, the newest generation of bulk thermoelectric generators is predicted to only achieve 15 % in the best case scenario [3]. Here efficiency is defined as the ratio between extracted work and heat energy provided: $\eta = \frac{W}{Q_h} = 1 - \frac{Q_c}{Q_h}$, where Q_h and Q_c are the heat flow out of the hot reservoir and into the cold reservoir, respectively (see Figure 1.1). The maximum achievable efficiency of a heat engine depends only on the temperature difference between the hot and cold reservoir. One such attainable maximum efficiency is the Carnot efficiency $\eta_{max} = 1 - \frac{T_c}{T_h}$, where T_c is the temperature of the cold reservoir and T_h is the temperature of the hot reservoir.
Despite their comparably low efficiencies, thermoelectric generators, devices that turn heat into an electrical current using thermoelectric effects, also have numerous advantages over classical heat engines. Unlike for example a turbine that is turned by the water vapour created when a heat source boils water, they do not require any moving parts. As a result they are much less prone to material failure and require little to no maintenance. In addition, unlike classical heat engines, thermoelectric generators can convert an arbitrarily small heat gradient into electricity, providing a possible solution for small and everyday waste heat harvesting.
There are two main research routes currently explored in creating more efficient thermoelectric devices: finding better materials or composites for bulk thermoelectrics or using nanostructuring and reducing dimensionality. These two approaches will be introduced below.

1.2 Bulk Thermoelectrics

The field of thermoelectrics as we know it today emerged after the second World War, when developments in semiconductor physics brought thermoelectrics into the spotlight. One of the major first contributors was Abram Fëderoviĉ Ioffe who introduced the dimensionless figure of merit ZT [5]:

$$ZT = \frac{S^2 G}{\kappa} T \,, \tag{1.1}$$

where S is the Seebeck coefficient, G the electrical conductance, κ the thermal conductance and T the operating temperature. The Seebeck coefficient quantifies the thermovoltage V_{th} created as a result of a temperature divergence ΔT, i.e. $S = -\frac{V_{\text{th}}}{\Delta T}$. ZT is used as an equivalent for efficiency in thermoelectric generators or coolers as a maximum ZT leads to a maximisation of the energy conversion efficiency. Its relationship with the previously defined efficiency is $\eta = \frac{\Delta T}{T_{\text{h}}} \frac{\sqrt{1+ZT}-1}{\sqrt{1+ZT}+T_{\text{c}}/T_{\text{h}}}$, where the temperature to calculate the figure of merit ZT is the operating temperature plus $\Delta T/2$. In order to become competitive with existing heat conversion approaches, it is believed that a ZT of about 2 to 3 needs to be reached at high temperatures, and lower values of $ZT > 1$ at room temperature. To illustrate, a thermoelectric device with a ZT of 3 operating at a temperature difference between 773 K and 303 K will approach half of the Carnot efficiency [6].

Initial successes such as in 1947, when Telkes *et al.* were able to fabricate a thermoelectric generator exceeding 5 % efficiency at $\Delta T = 400\,\text{K}$ [7] or when Goldsmid *et al.* demonstrated cooling at 273 K [8] were not followed up by more results. While thermoelectric devices were able to fill some niche needs for rural areas cut off from electrification [9] and were even used to fabricate a commercially available but ultimately unsuccessful refrigerator, the continuously low efficiency and no clear pathway for improvement resulted in a slow down in development as funding and interest vanished.

Yet, while a widespread and commercial use of thermoelectric devices did not materialise, they nonetheless play an import role in applications that require low-maintenance and high reliability. The most prominent area in which thermoelectrics are regularly employed is probably space exploration, where Radioisotope Thermoelectric Generators (RTGs) are used to power unmanned probes and rovers, exploiting the heat radiated by radioactive decay. For example Voyager 1, which was launched in 1977, has been working for more than four decades and is the first

man-made object to cross into interstellar space, all powered by an RTG using a plutonium-238 source.
A resurgence of research into thermoelectrics has been caused by the seminal work of Dresselhaus and Hicks in 1993 when they theoretically showed that reducing the dimensionality of thermoelectric materials could significantly increase their efficiency [10, 11]. These theoretical predictions have since been tested by various research groups and the principle is by now well established. The techniques employed range from fabricating nanocomposites from nanocrystal blocks [12], nanostructuring quantum dot superlattices [13] to the exploitation of negative correlations between electrical and thermal conductivity [14] as well as band engineering [15]. While ZTs of up to 2 have been achieved using these methods, in order to be industrially viable, a further increase especially outside of laboratory conditions is required. In addition to nanofabrication, other pathways for an increase in ZT are investigated, such as using SnSe crystals or other materials with an unusual anisotropic and anharmonic bonding structure [16]. In general, nanoengineering of thermoelectric properties, including for bulk materials and devices to for example decrease their thermal conductivity remains a big focus of thermoelectric engineering [17].
In the next section, an introduction to and definition of nanoscale thermoelectrics is given.

1.3 Thermoelectrics in Nanodevices

The main difference between thermoelectrics on the nanoscale and a traditional bulk thermoelectric is the length scale of the device or structure compared to the thermalisation length scale of the charge carrier. In bulk thermoelectrics, the charge carriers thermalise on a much smaller scale than any device dimension while for nanodevices, the scale of thermalisation is on the order of, or much bigger than, the device geometries (see Figure 1.2). When working with nanoscale thermoelectrics, the Boltzman transport equations that capture all bulk thermoelectrics are not applicable anymore as the system can not be assumed to be in equilibrium [18]. Instead, the small length scales associated with nanoelectronics lead to quantization effects. For example in a quantum dot, a small island that can be occupied by electrons, discrete energy levels are formed (due to the similarity with atoms, quantum dots are often referred to as artificial atoms) and phenomena such as Coulomb blockade can be observed. More emphasis on quantum dots, their electronic and thermoelectric properties and how to fabricate them will be put later in this thesis.

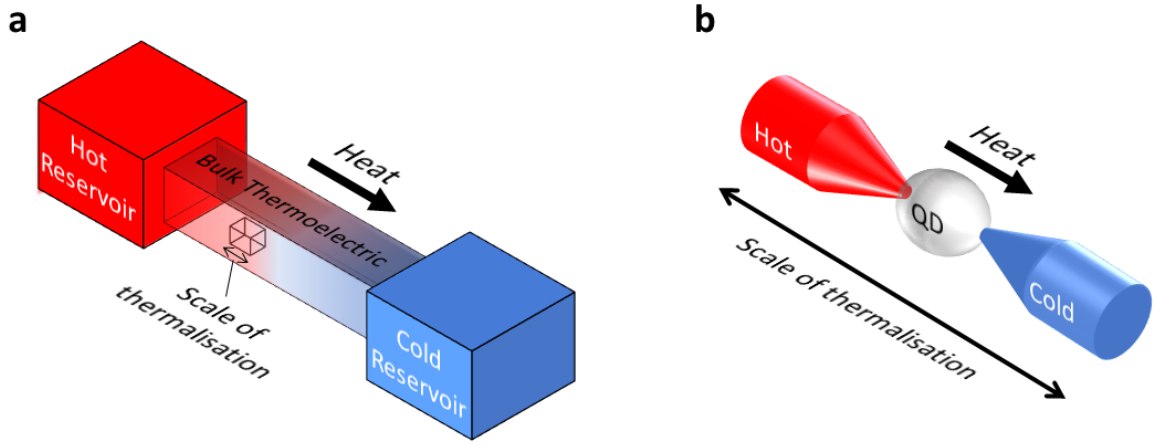


Figure 1.2 Schematic of a bulk thermoelectric vs. nanoscale thermoelectric. a) In bulk thermoelectrics, the length scale associated with electron thermalisation is shorter than any device structure length scale. b) In nanoscale thermoelectrics, the length scale of thermalisation is on the order of or larger than the device size, which here is a quantum dot contacted by a hot and cold reservoir.

Most nanostructures are still larger than the Fermi wavelength of an electron, meaning electrons behave as free particles within the structure that experience scattering at defects and can tunnel through boundaries, however usually the length scales involved are still below the coherence length of electrons, meaning phase information is preserved. This permits inherently non-equilibrium effects such as interference phenomena (Young's interference, Fabry-Perot, Aharonov-Bohm effect, etc.) to play a major role and profoundly influence the transport characteristics, illustrating the limits of the Boltzmann transport theory [19]. The Seebeck coefficient in nanostructures is theoretically directly correlated with the transmission probability through the device, and double digit ZT values have been predicted but not measured yet [20].

In order to use a nanoscale thermogenerator, we need to extract work in the form of electrical power generated by the thermoelectric effect. Similar to potential energy, where a mass is moved, the work in a thermoelectric device is done by moving an electron from a region of low chemical potential to a region of high chemical potential. If a device moves N electrons from a chemical potential μ_1 to a chemical potential μ_2 in a time Δt, the power generated is given by $P = \frac{(\mu_2 - \mu_1)N}{\Delta t}$. Here we can easily write the electrical current in terms of how many electrons we are moving in a certain time as $I = \frac{Ne}{\Delta t}$, where e is the elementary electron charge. Similarly, the voltage can be expressed through the difference in chemical potential $eV = \mu_1 - \mu_2$.

Then we arrive at the familiar expression for the electrical power $P_{\mathrm{el}} = -IV$, as expected.

To summarise, it is clear that thermoelectric devices, both on the nanoscale and in bulk, need to increase their efficiency substantially to challenge classical heat engines heavily used today. However, it is important to also recognise the potential of thermoelectrics to recover waste heat where regular heat engines can not be used, such as for small temperature gradients, under harsh conditions and isolation that do not permit regular maintenance and on very small length scales. These application niches become more important as an ever expanding amount of computing power is demanded, resulting in greater waste heat produced by electronic devices and the motorisation in developing countries is accelerating. Against the backdrop of a man-made climate crisis, the gains of efficiency promised by the use of thermoelectric generators in these applications become increasingly attractive.
In addition, hunting for high efficiencies and finding ways to generate larger power is not the only goal of studying nanoscale thermoelectrics but rather these systems can aid our understanding of the underlying physics. Thermoelectric measurements probe different phenomena than regular charge conductance measurements, for example providing information about the electron-hole symmetry with respect to the Fermi level in systems described by the Landauer-Büttiker scattering theory [21, 22] or offering additional insight into the entropy of a system [23].

1.4 Thesis Synopsis

The work in this thesis comprises the thermoelectric properties of carbon nanostructures, starting with quantum dots or zero-dimensional devices and extending to two-dimensional structures in graphene. Throughout, the attention is on how environmental influences and intrinsic device characteristics change the Seebeck coefficient, both locally and globally.
Chapter 2 covers the underlying theory of charge and energy transport in low dimensional structures, introducing both the Landauer-Büttiker Formalism and a rate equation model. In chapter 3 a brief description of the materials used, namely graphene and C_{60}, is given in addition to a review of existing literature on thermoelectric experiments in low dimensions. Then in the next part of the thesis, chapter 4 describes the standard fabrication procedures for most devices in this work and chapter 5 details the measurement setups and methods used. Finally, in the experi-

mental part, chapter 6 presents a detailed study of the thermoelectric properties of C_{60} molecules contacted by graphene electrodes. The results show a good agreement between a single-level Landauer-Büttiker, the Mott formula model and experimental results. In addition, a strong dependence of the thermoelectric properties on the coupling strength, asymmetry and operating temperature is found. These findings stimulated a study using graphene quantum dots in chapter 7, where the influence of a change in temperature and tunnel coupling are in detail studied employing a cryostat with temperature control. The results of the C_{60} study are confirmed and in addition the importance of high heat conduction in the leads for a high efficiency is highlighted. After documenting the considerable influence the device geometry and coupling strength has on the thermoelectric properties in quantum dot structures, the local thermoelectric response of a graphene bow tie (similar to the ones used to contact both the graphene quantum dots and the C_{60} molecules previously) and other graphene nanostructures is investigated. Using a Scanning Thermal Microscope based system in chapter 8 it is found that the device geometry directly impacts the Seebeck coefficient. In graphene constrictions or narrow channels, an increased influence of electron scattering from the edges leads to a lower electron mean free path which in turn causes a smaller Seebeck coefficient. The effect is observed both in a thermovoltage and Peltier measurement. The influence of defects, strain, as well as thickness changes in graphene are further illuminated in chapter 9 using a DC SThM thermovoltage measurement method (or Scanning Thermal Gate Microscopy). This guarantees the elimination of frequency induced effects and allows for a high scanning rate at a high resolution. These high resolution thermovoltage maps then enable a calculation of corresponding Seebeck coefficient maps via deconvolution. Lastly, in chapter 10, the effect discovered in chapter 8, namely the width dependence of the Seebeck coefficient in graphene, is used to fabricate single-material graphene thermocouples that have a higher sensitivity than previously developed single-material metal thermocouples. All of the results are summarised in chapter 11 in addition to an outlook on possible future work.
All experimental chapters (6-10) were previously published or submitted for publication as detailed at the beginning of each chapter and the respective content is based on said publication.

2

Theory of Heat and Charge Transport

2.1 Introduction

Electronic devices exhibit very different physical transport phenomena in the micro-, meso- and macroscopic world. The most interesting and well-studied effects can be seen on the microscopic scale when structures get as small as a few nanometres. At this length scale, classical descriptions tend to be invalid and it is necessary to employ quantum mechanics to describe the behaviour of nanodevices.
A conductor is considered low-dimensional if one or more of its dimensions becomes smaller than the Fermi wavelength λ_F, which is the wavelength of electrons at the Fermi energy and is typically on the order of tens of nanometres depending on the material. In order to create a two-dimensional (2D) structure, 2D Electron Gases (2DEG) such as GaAs [24] or natural 2D materials, such as graphene [25] or MoS_2 [26] can be employed such that $L_z < \lambda_F$ where L_z is the size of the reduced dimension.
Similarly, a one-dimensional structure can be created through a thin wire, such as silicon nanowires [27] or carbon nanotubes [28], where a size constraint in two dimensions is achieved ($L_Z, L_Y < \lambda_F$).
If $L_Z, L_Y, L_X < \lambda_F$ a zero-dimensional structure is formed. This can be achieved by creating a quantum dot (QD) in a 2D material or 2DEG via gating or etching or by using zero-dimensional objects, such as nanoparticles or single molecules like C_{60} molecules, as active components of an electronic device. In these devices, the size confinement leads to a quantization of the available energy levels if the level spacing, which is dependent on the QD size, between the levels is the largest energy gap associated with the system (compared to for example the charging energy, see next section). For an island with a small level spacing, there is still an energetic cost

related to adding an electron due to the Coulomb repulsion between electrons. Below, we will focus on QDs and their transport properties, followed by an overview over their thermoelectric characteristics.

2.2 Charge Transport in Zero-dimensional Structures

Lithographically defined QDs can be regarded as an island that can be filled with electrons and if desired coupled to one or multiple source, drain and gate electrodes (see Figure 7.1). The source and drain reservoirs are capacitatively (where an electric field induces displacement currents) and tunnel coupled (where electrons tunnel through barriers onto and off the dot) to the QD, while the gate (or multiple gates) is only capacitatively coupled. Following the constant interaction model, we can derive the characteristics of electronic transport through such a structure [29].

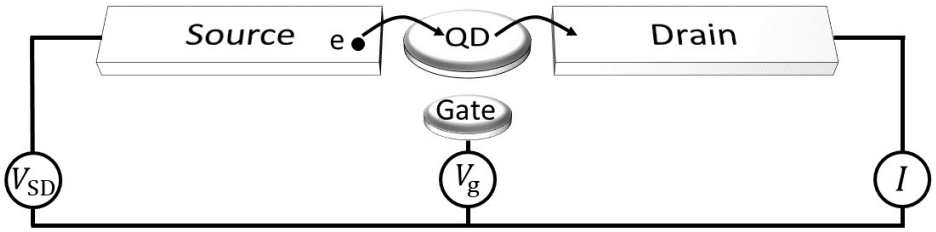


Figure 2.1 Schematic of a Quantum Dot.

In this model, the interaction between electrons that are driving the transport are determined by the total capacitance

$$C = C_s + C_d + C_g \,, \tag{2.1}$$

where C_s, C_d and C_g are the capacitances between the QD and the source, drain and gate, respectively.
The total ground state energy for N electrons on the dot, $U(N)$, is then determined by the applied source, drain and gate voltages (V_s, V_d and V_g, respectively) as well as the corresponding capacitances:

$$U(N) = \frac{[e(N - N_0) + C_s V_s + C_d V_d + C_g V_g]^2}{2C} + \sum_{n=1}^{N} E_n \,. \tag{2.2}$$

Here eN_0 is the charge present on the dot at zero bias and zero gate voltage due to positive background charges in the substrate and $\sum_{n=1}^{N} E_n$ is the sum over all occupied levels on the dot. Then the single-particle energy level spectrum is independent of the number of electrons N on the dot [29]. The chemical potential of the dot occupied by N electrons is defined as

$$\mu(N) = U(N) - U(N-1) = E_C(N - N_0 - \frac{1}{2}) - \frac{2E_C}{e}(C_s V_s + C_d V_d + C_g V_g) + E_N \,, \tag{2.3}$$

where $E_C = e^2/2C$ is the charging energy relating to the Coulomb interaction of electrons on the dot [30]. In order to add another electron to the dot, the addition energy E_{add} is needed

$$E_{add} = \mu(N+1) - \mu(N) = \Delta E + E_C \,. \tag{2.4}$$

ΔE is the level spacing caused by the QDs spatial confinement in all three dimensions, which creates a discrete energy spectrum. Yet, if two electrons with different spin are added to the same energy level, ΔE between the two can be zero. The charging energy E_C represents the repulsive interaction between electrons on the dot.
Adding another electron to the dot then exhibits an energetic cost E_{add} which leads to Coulomb blockade at sufficiently low temperatures ($k_B T < E_{add}$) where k_B is the Boltzmann constant and T is the temperature [29, 31]. In this regime and under the appropriate biasing conditions single electrons transfer through the QD occurs in a sequential fashion [32], and the device can be operated as a Single-Electron-Transistor [33].

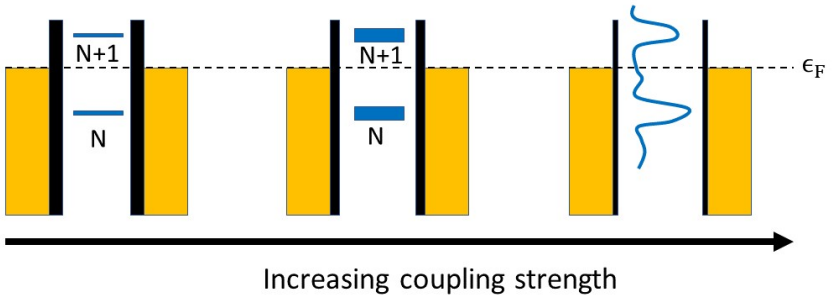


Figure 2.2 The three different coupling regimes as the tunnel barriers (black) between the electrodes and the QD change in strength. The $N+1$ and N charge state (blue) are well defined in the weak-coupling regime (left), become broader as coupling is increased (middle) and eventually give rise to a semi-continuous multi peaked transmission function for very strong coupling (right).

The coupling strength of the dot to the source and drain contacts is expressed by the tunnelling rates Γ_S and Γ_D, which depend on the overlap of the QD wave function with the lead states. This coupling can vary with the number of electrons on the dot as the wave function changes. The total coupling $\Gamma = \Gamma_S + \Gamma_D$ determines the level broadening of the respective QD orbitals.
Pronounced transport spectra can be seen towards cryogenic temperatures at which $E_C, \Delta E \gg k_B T$ and the thermal noise and smearing is drastically reduced [34]. Here three different transport limits can be distinguished, the weak coupling regime, the intermediate coupling regime and the strong coupling regime (see Figure 2.2).

2.2.1 The Different Coupling Regimes

The weak coupling regime is defined in the limit where $\Gamma \ll E_C, E_{\text{add}}(N), k_B T$ and is dominated by Coulomb blockade [35]. The effect shows most clearly in a charge stability diagram, which is obtained by measuring the gate and bias dependence of the current and then plotting it in a two-dimensional map (see Figure 2.3a). The Coulomb Blockade (CB) manifests as diamond shaped regions of very low current, so called Coulomb diamonds, in which transport is blocked. In these regions the energy cost to add an electron onto the QD exceeds the available energy and therefore no current can flow through the QD (Figure 2.3b).
The CB areas are separated by regions of high current, the Sequential Electron Tunnelling (SET) zones, where current flow through the QD is allowed via sequential electron tunnelling. Each Coulomb diamond corresponds to a certain number of electrons N occupying the QD where the number of electrons changes sequentially between neighbouring diamonds.
When looking closely at the SET regions, often lines running parallel to the edges of the Coulomb diamonds can be observed. These originate from orbital excited states [36], spin states [29] or vibrational states [37], which will be discussed later. These states are able to contribute to the current flow through the QD if their energy levels are reached by applying a higher bias voltage (Figure 2.4a). Such excited or vibrational states can yield information about the QD's energy spectrum and are especially helpful when attempting to identify specific molecules as each molecule has a distinctive vibrational fingerprint [38].
Furthermore, the height of the Coulomb diamond in the stability diagram is equal to the addition energy of the QD or molecule (see Figure 2.3a).
While it is possible to readily read out the addition energy and the energy of excited

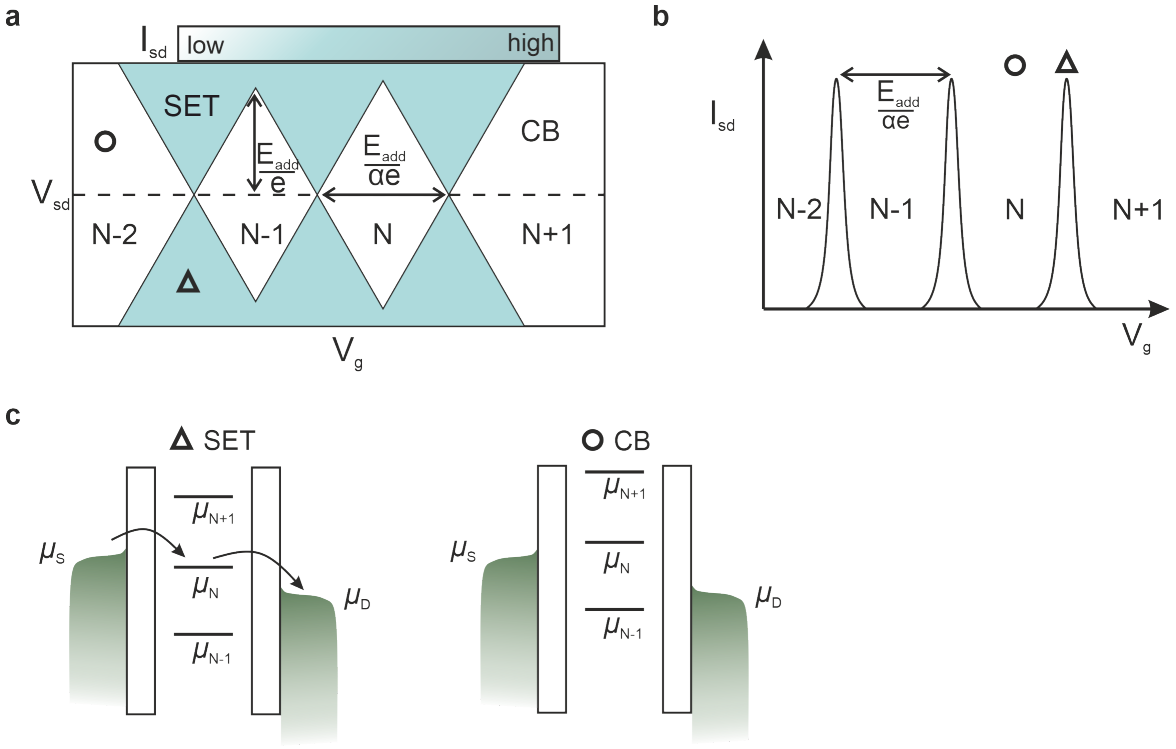


Figure 2.3 Electron transport through a QD in the weak coupling regime. a) Current map versus bias and gate voltage. The white areas correspond to regions where transport is blocked (CB, circle) while in the turquoise areas, the blockade is lifted by resonant tunnelling and SET occurs (triangle). Within the Coulomb blocked region, the number of electrons on the island is fixed while it oscillates between the left and right Coulomb diamond value in the SET region. α is the gate lever arm. b) Source-drain current as a function of gate voltage. When sweeping the gate, energy levels fall within the bias window and result in current spikes. Between the current spikes the electron level N on the island is fixed. c) Energy level alignment in a QD for SET (left, triangle in a and b) and CB (right, circle in a and b). The QD can be switched from CB where no electron transport through the dot is allowed to SET, where sequential electron transport is permitted by increasing the bias window or changing the gate voltage.

states, it is very challenging or almost impossible to infer the charge state of the QD, that is the number of electrons on the dot, from the stability diagram. Since the QD is part of the device and therefore a larger system, the neutral charge state can be deceiving when only considering the dot itself. Assuming the QD is at no applied bias and no gate voltage and therefore seemingly in the neutral charge state, it might still be partially charged due to interactions with the junction or background charges in the substrate (see also equation 2.2).

One can correlate the stability diagram or a gate sweep measuring the conductance or current through the QD to the different level alignments of the contacts and the dot orbitals (see Figure 2.3c). When the electrochemical potential of the source and drain is aligned with the dot's orbit, transport through the QD is allowed and results in a current peak in the gate trace. The corresponding transport mechanism is called resonant tunnelling. While the levels are aligned the number of electrons on the dot fluctuates between N or $N+1$ as electrons hop on and off the QD. In between the peaks the electrochemical potentials are not aligned, there is no resonant tunnelling through the QD due to Coulomb blockade and the number of electrons on the dot is fixed [29].
In addition, the various capacitances between the QD and the contacts as well as the gate lever arm (or gate coupling parameter) can be extracted from the slopes of the diamonds as the negative slope and positive slope are equal to $-|e|C_G/(C-C_S)$ and $|e|C_G/(C_S)$, respectively. Since the gate lever arm is given by

$$\alpha = \frac{C_G}{C}\,, \tag{2.5}$$

one can thereby quantify the strength of the gate coupling [29, 34].
In order to extract the source and drain coupling it is possible to fit a model for the transmission probability of the QD to the Coulomb peak in the zero bias conductance trace.

In the strong coupling limit $\Gamma \gg E_C, E_{add}(N), k_B T$. In this regime the QD and lead states hybridise and the Coulomb blockade is smeared out by higher order processes [39]. The transport is now dominated by elastic coherent tunnelling. In this limit, the conductance can be approximated as $G \simeq \frac{2e^2}{h}\mathcal{T}(E)$, where $\mathcal{T}$ is the transmission function through the QD. In the case of a single, well-isolated energy level a simple Breit-Wigner resonance can be used for the transmission function (see chapter 6). This enables the direct verification of experimental measurements of the conductance, particularly in experiments in which one can control the coupling to a certain extent [40, 41].

Lastly, the intermediate coupling regime has attributes of both limits, it still exhibits a noticeable CB but also shows transport within the "Coulomb blocked" region.
The two most noticeable new transport channels available in this regime are elastic

and inelastic cotunnelling. As can be seen in Figure 2.4 these higher-order transport mechanisms involve the simultaneous tunnelling of two electrons.

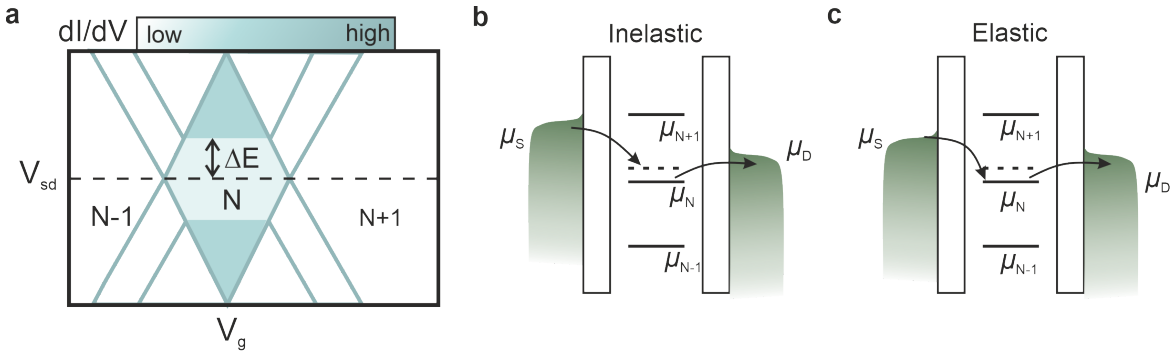


Figure 2.4 Higher Order Tunnelling in a QD. a) Differential conductance map of a QD stability diagram. The thick lines show the energy levels of the island and form the Coulomb diamond edges in a stability diagram. Additional lines resulting from resonant tunnelling through excited states are visible parallel to these lines and a background conductance due to both elastic and inelastic cotunnelling in the Coulomb blocked region can be seen. b-c) When an electron tunnels off the island to the drain electrode and is replaced by an electron from the source electrode the process is called cotunnelling. In inelastic cotunnelling the dot is left with a different energy than before the process (b), while for elastic cotunneling the dot is left in the same state as before the cotunnelling process (c). The distance between the excited state and μ_N is equal to ΔE.

As depicted in Figure 2.4b, initially the QD is in a state with an unoccupied excited state still below the electrochemical potential of the leads in contrast to resonant tunnelling where the excited state is between the source and drain electrochemical potential. When the electron tunnels out of the QD onto the drain, the QD is left in a virtual state and there are two possibilities for the orbit to be refilled. First, the new electron simultaneously tunnelling in from the source lead occupies the ground state again, therefore leaving the QD in exactly the same configuration as before. This is called elastic cotunnelling (Figure 2.4c). If the new electron, however, tunnels into the excited state, the QD has changed its energy and the process is called inelastic cotunnelling (this is depicted in Figure 2.4b). The electron can subsequently relax into the ground state, rendering the QD again in the initial configuration. Importantly, for inelastic cotunnelling to take place, a bias larger than the excitation energy of the dot has to be applied and since the QD excitation is created at the expense of the bias applied, electron energy is conserved. Both elastic and inelastic cotunnelling lead to conduction in the blocked Coulomb diamond region. When mapping the differential conductance of the QD, i.e. a $\frac{dI}{dV}$ as a function of V_S and

V_g plot, elastic cotunnelling results in a nonzero background conductance in the Coulomb blocked region, while inelastic cotunnelling manifests itself as an area of increased conductance. This region is bound by a line parallel to the x- or gate axis of the stability diagram, which intersects with the excited state lines within the SET region (see light turquoise area in Figure 2.4a) [42].

2.2.2 Vibrational States

Vibrational states are relatively rare in solid state QDs but rather ubiquitous in molecules, as they tend to have additional degrees of freedom depending on how they are coupled to the leads. We will discuss vibrational states of C_{60} molecules that were observed in transport measurements in chapter 6.
Vibrational states manifest as lines in the SET region that run parallel to the Coulomb diamond edge, just as expected from excited or higher states, and typically range from 1 to 100 mV [43, 44]. Whenever an electron tunnels on or off the molecule this leads to a reconfiguration of the molecule's equilibrium position, which is also a result of a changing molecular wave function. The vibrational spectra are unique for different molecules and are therefore an accepted albeit not always highly reliable fingerprint of a molecule [38]. One can differentiate between internal vibrational degrees of freedom that cause a deformation of a molecule when an electron is tunneling on or off, such as a change from a round sphere to an ellipsoid in a C_{60} molecule [44], and center-of-mass oscillations in which the whole molecule vibrates with molecule specific modes. However, the position of vibrational states and whether they are clearly visible in transport measurements is naturally highly dominated by the positioning and coupling of the molecule to the contacts and the substrate surface as well as the material used for each, respectively [45]. This can result in unusual or unsymmetrical spectra as well as differing intensities that can not be explained with known molecular vibrational modes [44].

2.3 Thermoelectrics in Zero-dimensional Structures

This section discusses the basics of thermoelectricity in zero-dimensional structures or QDs. We will approach thermoelectricity by considering the charge carriers responsible for the thermoeletric effect. It is also possible to use a purely thermo-

dynamical approach, which leads to the same result [46]. For all purposes in this section, a two-terminal structure is assumed, which is also exclusively used in the experiments. Therefore a Landauer formalism is employed, however it is possible to generalize the approach to multiple terminals by utilizing the Landauer-Büttiker formalism.

2.3.1 Landauer Formalism

In order to make predictions about the electronic and thermoelectric properties of QDs, a good model for electronic transport in mesoscopic to molecular-scale devices is necessary. In the limit of predominantly SET and assuming coherent transport, extending the Landauer formalism (originally a model for electrical conduction) towards thermoelectric effects has proven successful and is widely used [20, 47, 48].

The Landauer formalism is a concept formulated in 1947 by Rolf Landauer that models conduction as transmission. The basic assumption is that two electron reservoirs are connected by a scatterer (QD island for the transport measurements presented here) through which electron transport is possible. The transport is then determined by the probability of electrons moving from one reservoir to the other through the scatterer. This probability is always between 0 and 1, which means there is an upper limit on conductance.
Employing the Landauer approach, the current through such a structure can be written as:

$$I = \frac{2e}{h} \int f(T,\epsilon)\mathcal{T}(\epsilon)d\epsilon \,, \tag{2.6}$$

where $\mathcal{T}$ is the transmission probability of an electron at energy ϵ to move from one reservoir to the other across the connection [46]. $f(T,\epsilon)$ is the Fermi-Dirac distribution of the source reservoir at temperature T and energy ϵ with e and h denoting the elementary charge and the Planck constant, respectively.
What this formula essentially states is that in order to quantify the current through the connection, one needs to consider one reservoir, determine the probability that there is an electron at a certain energy ($f(T,\epsilon)$) and what the probability is that this electron travels to the other reservoir ($\mathcal{T}(\epsilon)$). Multiplying this probability with the elementary charge e gives the current for one energy level with a factor of 2 added due to spin degeneracy. After adding all of these possible transport channels together, which is done by taking the integral over all energies, and accounting for dimension normalization via the Planck constant one receives the current I [46, 49].

Then, the electrical conductance can be written as the derivative of the current given by

$$G = -2\frac{e^2}{h}\int \frac{\partial f(T,\epsilon)}{\partial \epsilon}\mathcal{T}(\epsilon)d\epsilon \,, \tag{2.7}$$

where $2\frac{e^2}{h} = G_0$ is the conductance quantum. There are multiple different approaches for defining the transmission function with varying degrees of complexity but usually it is a product of tunnel couplings and Green function terms [50].
More sophisticated theoretical approaches and refined Landauer formulas, which are out of the scope of this work and will not be discuss here, exist and can be found in the literature [47, 51].

2.3.2 Fermi-Dirac Distribution

As the approach towards thermoelectricity presented is based on the transmission of electrons between two reservoirs, it is vital to understand how electrons behave and distribute in these systems, especially with respect to temperature. The contacts to zero-dimensional junctions can usually be described by many-electron systems in which particles obey Pauli's exclusion principle, such as crystal-like bulk materials and semi-conductors. Here, the energy distribution of the particles can be described by the Fermi-Dirac (FD) distribution:

$$f^0(\epsilon) = \frac{1}{e^{[(\epsilon-\mu)/k_BT]}+1} \,, \tag{2.8}$$

where μ is the chemical potential, k_B the Boltzmann constant, T the temperature and ϵ the energy. The FD distribution is only valid for systems in which the number of electrons is big enough such that the addition of an electron has a negligible effect on μ.
For very high temperatures T, $e^{[(\epsilon-\mu)/k_BT]} \gg 1$ the FD distribution approaches the distribution of particle speeds in an ideal gas (a so called Maxwell-Boltzmann distribution). At very low temperatures, $f^0(\epsilon) = 1$ for $\epsilon \leq \mu$ and 0 above. Then the FD distribution essentially resembles a step function with all states below the chemical potential filled and all above empty.
One can calculate the number of electrons in a crystal by multiplying the density of states $N(\epsilon)$ with the FD distribution and summing up this product for all energies:

$$n = \int_0^\infty f^0(\epsilon)N(\epsilon)d\epsilon. \tag{2.9}$$

The density of states $N(\epsilon)$ denotes the number of electron states per unit of energy and volume and differs for distinctive materials.
In such a system the chemical potential is defined as the amount of energy needed to add an additional electron to the system and naturally this quantity has an inherent temperature dependence as the energy of the system changes with T. An approximation for the chemical potential as a function of temperature and energy has been developed using the Sommerfeld expansion, which is valid in the low temperature limit [52]:

$$\mu \approx \epsilon_F - \frac{\pi^2}{6}(k_B T)^2 \frac{1}{N(\epsilon_F)} \frac{\partial N(\epsilon)}{\partial \epsilon}|_{\epsilon=\epsilon_F}. \tag{2.10}$$

As is evident from this equation, the chemical potential decreases as the temperature rises, resulting in a potential gradient whenever a temperature gradient is applied. Any difference in T will therefore lead to a flow of electrons as the cost of adding another electron to the hot side would be lower than adding it to the cold side. This results in the build-up of a thermoelectric voltage in an open circuit .

2.3.3 The Landauer Formalism in Thermoelectrics

There exist two common models that generally explain the way electrons distribute heat and charge in a solid: the Boltzmann equation and again the Landauer formalism. The Boltzmann approach has been commonly used in the past and was originally derived for diluted gases but treats particles semi-classically, that is following Newtons' laws. In the case where quantum effects play a role in transport, that is if the potential of the structure varies sharply with respect to the particle average thermal wavelength, the Boltzmann approach is no longer valid. In this case, the Landauer formalism, which is used for low temperature thermoelectric calculations in mesoscopic structures, is more applicable [53, 52]. The Landauer formalism has the advantage of assuming a constant mean-free path, rather than a constant relaxation time of the electrons as the Boltzmann approach does, which is more useful in experiments. In addition, the Landauer approach is valid in the ballistic and quasi-ballistic regime as well as for quantum engineered structures [47]. The Landauer formalism was developed for the theoretical treatment of charge conductivity in one-dimensional conductors [54] and mesoscopic devices [55] before being extended to thermoelectric transport [56, 57]. In addition, the Landauer formalism has also recently been extended to describe bulk materials [47]. There are more

complex and further developed theoretical approaches that e.g. include many-body interactions such as the Keldysh approach [58, 59], to describe the thermoelectric properties of QDs and single-molecule devices, though the Landauer formalism is usually the basis for these more intricate approaches [60].

We have already seen how to calculate the current using the Landauer formalism in equation (2.6):

$$I = \frac{2e}{h} \int f(T,\epsilon)\mathcal{T}(\epsilon)d\epsilon.$$

It is possible to formulate a similar expression for the flow of heat $\dot{Q}$ from one reservoir to the other by multiplying the particle transmission with the particle energy $(\epsilon - \mu)$ rather than the charge e:

$$\dot{Q} = \frac{2}{h} \int (\epsilon - \mu) f(T,\epsilon)\mathcal{T}(\epsilon)d\epsilon. \tag{2.11}$$

Assuming that applying a voltage or a temperature gradient will only lead to a local perturbation, i.e.

$$T = T_0 - \Delta T$$

$$\mu = \mu_0 - e\Delta V \ ,$$

the FD distribution can be written as

$$f(T,\epsilon) = f^0 - \frac{\partial f}{\partial \epsilon}\left[e\Delta V - \frac{\epsilon - \mu}{k_B T}\Delta T\right], \tag{2.12}$$

where f^0 is the familiar equilibrium FD distribution.
To arrive at an expression for the current through a device, it is necessary to consider the contribution from the thermoelectric part, that is the electron flow caused by a thermal gradient ΔT and the electrical contribution due to an applied source-drain bias ΔV:

$$I = G\Delta V - L\Delta T \tag{2.13}$$

and similarly for the heat flux:

$$\dot{Q} = LT\Delta V - K\Delta T. \tag{2.14}$$

Here G is the electric, L the thermoelectric and K the thermal conductance. One can derive an analytic expression for I and $\dot{Q}$ by using equation (2.12) and plugging it

into equation (2.6) and (2.11). Only the perturbative part of the FD distribution is used in the following as the equilibrium condition naturally assumes no thermal or bias gradient

$$I = -\frac{2}{h}\int e\frac{\partial f}{\partial \epsilon}\left[e\Delta V - \frac{\epsilon-\mu}{k_B T}\Delta T\right]\mathcal{T}(\epsilon)d\epsilon \tag{2.15}$$

$$\dot{Q} = -\frac{2}{h}\int (\epsilon-\mu)\frac{\partial f}{\partial \epsilon}\left[e\Delta V - \frac{\epsilon-\mu}{k_B T}\Delta T\right]\mathcal{T}(\epsilon)d\epsilon. \tag{2.16}$$

By combining the temperature and chemical potential perturbation with equation (2.13)/(2.15) and equation (2.14)/(2.16) all three transport coefficients G, L and K can be calculated.

$$G = 2\frac{e^2}{h}\int -\frac{\partial f}{\partial \epsilon}\mathcal{T}(\epsilon)d\epsilon \tag{2.17}$$

$$L = 2\frac{e^2}{h}\frac{k_B}{e}\int -\frac{(\epsilon-\mu)}{k_B T}\frac{\partial f}{\partial \epsilon}\mathcal{T}(\epsilon)d\epsilon \tag{2.18}$$

$$\frac{K}{T} = 2\frac{e^2}{h}\left(\frac{k_B}{e}\right)^2\int \left[\frac{(\epsilon-\mu)}{k_B T}\right]^2\frac{\partial f}{\partial \epsilon}\mathcal{T}(\epsilon)d\epsilon. \tag{2.19}$$

These expressions are derived from the Landauer formalism and are therefore valid for the 1D case, where $\mathcal{T}$ has a value between 1 and 0 depending on transmission probability. One can extend this formula to three dimensions by introducing the transport distribution function Ξ [61, 62]. Assuming a smooth energy distribution with respect to the wave-vector k this function can be written as

$$\Xi(\epsilon) = \frac{h}{2}N(\epsilon)\tau(k)v_k \cdot v_k\,, \tag{2.20}$$

where τ is the time between scattering events, v_k is the wave-vector velocity and $N(\epsilon)$ is the density of states. Plugging this into the transport coefficient equations (2.17), (2.18) and (2.19) yields the same formulas just with a different transport function [46]:

$$\sigma = -2\frac{e^2}{h}\int \frac{\partial f^0}{\partial \epsilon_k}\Xi(\epsilon)d\epsilon \tag{2.21}$$

$$\alpha = -2\frac{e^2}{h}\frac{k_B}{e}\int -\frac{(\epsilon-\mu)}{k_B T}\frac{\partial f^0}{\partial \epsilon_k}\Xi(\epsilon)d\epsilon \tag{2.22}$$

$$\frac{\kappa}{T} = 2\frac{e^2}{h}\left(\frac{k_B}{e}\right)^2\int \left[\frac{(\epsilon-\mu)}{k_B T}\right]^2\frac{\partial f^0}{\partial \epsilon_k}\Xi(\epsilon)d\epsilon. \tag{2.23}$$

The previous equations are precise analytic expressions, however if $\Xi(\epsilon)$ varies slowly with respect to the energy range $k_\mathrm{B}T$ around $\mu = \epsilon$ and $k_\mathrm{B}T \ll \mu$, a Sommerfeld expansion with respect to $\frac{k_\mathrm{B}T}{\epsilon_F}$ can be applied [53]

$$\sigma \approx \frac{2e^2}{h}\Xi(\epsilon_F) \tag{2.24}$$

$$\alpha \approx 2\frac{\pi^2}{3}\frac{k_B e}{h}k_B T\frac{\partial\Xi(\epsilon_F)}{\partial\epsilon}\bigg|_{\epsilon=\epsilon_F} \tag{2.25}$$

$$\kappa \approx 2\frac{\pi^2}{3}\frac{k_B^2}{h}T\Xi(\epsilon_F)\,, \tag{2.26}$$

where only the first term in the expansion was retained as the following terms are on the order of $O(k_\mathrm{B}T/\mu)^2$ [53].
It is then possible to derive links between the transport coefficients such as

$$\kappa \approx \frac{\pi^2}{3}\frac{k_B^2}{e^2}T\sigma. \tag{2.27}$$

From this expression, it is clear that the quotient of the thermal conductance and charge conductance is a constant

$$L_0 = \frac{\kappa}{\sigma T} = \frac{\pi^2}{3}\frac{k_B^2}{e^2}\,,$$

which is called the Lorenz number. This relation is known as the Wiedemann-Franz law and stems from the fact that both thermal and electrical conductance rely on the free electrons in a material to carry heat and charge, respectively [63].
The more interesting relation for this work however is the one between the electrical and the thermoelectric conductance. It turns out that after employing a Sommerfeld expansion, the thermoelectric conductance is proportional to the derivative of the charge conductance with respect to energy.

$$\alpha \approx \frac{\pi^2}{3}\frac{k_B}{e}T\frac{\partial\sigma}{\partial\epsilon}|_{\epsilon=\epsilon_F}. \tag{2.28}$$

2.3.4 Thermopower and Peltier Coefficient

The basis of thermoelectric measurements is the Seebeck effect, that we have mentioned previously, which was discovered in 1821 and later published on by Thomas Johann Seebeck [64]. It is the working principle of any thermocouple, and manifests itself through a voltage drop across a junction of two dissimilar materials (with two different Seebeck coefficients) when heating one side of the junction. The Seebeck coefficient is defined as the negative voltage difference ΔV induced per unit temperature change ΔT and is measured in V/K:

$$S = -\frac{\Delta V}{\Delta T}. \tag{2.29}$$

Similarly, as discovered by Jean-Charles Peltier in 1834, it is possible to heat or cool such a junction by inducing an electric current via the Peltier effect. In the 1850s Lord Kelvin realized the close connection between the two effects and formulated the Peltier coefficient as:

$$\Pi = ST. \tag{2.30}$$

Using the Landauer approach, the Seebeck coefficient can be calculated from the thermoelectric conductivity, by setting the current in equation (2.13) to zero (open circuit condition). Then

$$\begin{aligned} 0 &= G\Delta V - L\Delta T \qquad &\Leftrightarrow \\ \sigma\Delta V &= \alpha\Delta T \qquad &\Leftrightarrow \\ \frac{\Delta V}{\Delta T} &= \frac{\alpha}{\sigma}\,. \end{aligned}$$

Here the substitution to move from the one-dimensional to the generalised case was used in going from line one to two (see previous section), and therefore:

$$S = -\frac{\Delta V}{\Delta T} = -\frac{\alpha}{\sigma}. \tag{2.31}$$

But from the previous section, equation (2.28), there exists a relation between the thermoelectric and the charge conductance. Plugging in this expression for α gives

$$S = -\frac{\pi^2}{3}\frac{k_B}{e}T\frac{\partial \ln(\sigma)}{\partial \epsilon}|_{\epsilon=\epsilon_F}. \tag{2.32}$$

This equation is called the Mott formula and is the most commonly used equation in thermoelectrics [65–67]. It's main message is that the Seebeck coefficient changes with the carrier transmission above and below the Fermi level. As one shifts the orbitals, an asymmetry of transmission around the Fermi energy (in the energy-window $k_B T$) leads to electrons migrating to the cold (warm) side, leading to a negative (positive) Seebeck coefficient [68]. It is important that while the Mott formula is widely used, it remains a simplification and does not assume charge carrier interaction or electron-phonon interactions, making it obsolete in conditions where these interactions are strong [69]. There are prominent examples for which the Mott formula breaks down such as low-disorder graphene [70] and quantum dots in the Coulomb blocked region [71]. The formulas above are, as discussed, only valid in the linear regime, leaving out sharply varying density of states [72] and more exotic potentials [73].
In order to quantify the efficiency of a thermoelectric device the three conductances can be combined in the dimensionless figure of merit

$$ZT = \frac{S^2 T \sigma}{\kappa}. \tag{2.33}$$

To achieve a high figure of merit, it is essential to maximize both, the Seebeck coefficient and the charge conductance while minimizing the thermal conductance. However, classically the transport coefficients are all inherently connected and particularly σ and S are mutually contra-indicated, meaning that it is impossible to boost one without decreasing the other. In nanostructures one can, to a certain extent, address these two factors independently and can disconjugate them [74]. In this way, figure of merits over one [13, 75] and greater than two have been observed in $PbTe_{0.7}S_{0.3}$ (> 2) and SnSe (2.6) [76, 16].
The figure of merit is also informative for the heat flow across a device in an open circuit configuration. Since no current is flowing, there is a heat flow equal to $-\kappa \Delta T$, which consists of a purely thermal contribution and an electrical contribution due to electrons moving under the influence of the finite electric field created by the thermal gradient ($E \propto T$). The figure of merit ZT sets the relative strength between the heat flow caused by the electric field and the purely thermal conductivity, meaning that if $ZT = 1$ these components are equal in strength [46].
Another figure often used to quantify the usefulness of a thermoelectric material as

a heater or cooler is the power factor given by

$$\mathcal{P} = S^2\sigma.$$

The power factor is proportional to the maximum achievable output power density of a thermoelectric device in the linear regime and can therefore be seen as more meaningful than the figure of merit for unlimited or cost-free heat sources (such as geothermal heat and waste heat from car engines). In addition, it tends to be much easier to probe than the figure of merit, which necessitates a thermal conductance measurement.

2.3.5 Rate Equation Approach

A different approach to modelling electronic and thermoelectric transport through a low-dimensional structure in the weak coupling limit is to employ a Rate Equation (RE) model. Here, charge transport through for example a QD is modelled as a sequence of electron hopping events, where a hopping rate is assigned for hopping on or off the QD from each reservoir, respectively. The Rate Equation model is explored in more detail including the treatment of vibrational states in the literature [77].
We will limit the RE model to no excited states in the QD energy spectrum, that is we are only considering electron transport through the N and $N+1$ charge states. In addition, we assume that only one added transport electron is present on the QD at any time, the RE model can however be extended to include more sophisticated situations if necessary.
Within these limitations, the QD can be described by the Hamiltonian

$$H_S = \sum_{\sigma=\uparrow,\downarrow} \epsilon_0 \, a_\sigma^\dagger a_\sigma + U n_\uparrow n_\downarrow \,, \tag{2.34}$$

where ϵ_0 is the position of the QD energy level with the creation (annihilation) operator $a_\sigma^\dagger$ (a_σ) and σ denoting the electron spin. The second term describes the on-site electron-electron repulsion with strength U. Again, as mentioned above, we assume that a double population of the QD is not possible and set $U \to \infty$. Using a quantum master equation approach, we can then write the occupation probability of the QD in terms of hopping on/off rates (where we ignore the repulsive $U n_\uparrow n_\downarrow$ term

in the equations of motion) [78]:

$$P_N = \frac{n_{N+1}(\bar{\gamma}_L + \bar{\gamma}_R)}{n_{N+1}(\gamma_\mathrm{L} + \gamma_\mathrm{R}) + n_N(\bar{\gamma}_\mathrm{L} + \bar{\gamma}_\mathrm{R})} \; ; \tag{2.35}$$

$$P_{N+1} = \frac{n_N(\gamma_L + \gamma_R)}{n_{N+1}(\gamma_\mathrm{L} + \gamma_\mathrm{R}) + n_N(\bar{\gamma}_\mathrm{L} + \bar{\gamma}_\mathrm{R})} \; . \tag{2.36}$$

Here, P_N (P_{N+1}) is the probability of the QD being in the N ($N+1$) charge state and n_N (n_{N+1}) is the respective electron degeneracy. The hopping rates on (γ_l) or off ($\bar{\gamma}_l$) the QD from the left ($l = L$) or right ($l = R$) reservoir are given by

$$\overset{(-)}{\gamma}_l = 2\,\Gamma_l \int \frac{\mathrm{d}\epsilon}{2\pi} f_{\pm l}(\epsilon) K(\epsilon) \; . \tag{2.37}$$

Lifetime broadening is introduced via the density of states of the QD $K(\epsilon_0)$, which can often be assumed to have a simple Lorentzian line shape. The Fermi-Dirac distributions are denoted as $f_{+l}(\epsilon) \equiv f_l(\epsilon)$ and $f_{-l}(\epsilon) \equiv 1 - f_l(\epsilon)$ for hopping on and off the QD, respectively.
Then, the current I can be found at, for instance, the left interface by multiplying the probability for electron occupation of the dot with the respective hopping rate:

$$I = \frac{e}{\hbar}[P_N \gamma_L - P_{N+1}\bar{\gamma}_L]. \tag{2.38}$$

Simplifying equation 2.38 gives:

$$\begin{aligned} I &= \frac{e}{\hbar} n_N n_{N+1} \frac{\gamma_L(\bar{\gamma}_L + \bar{\gamma}_R) - \bar{\gamma}_L(\gamma_L + \gamma_R)}{n_{N+1}(\gamma_\mathrm{L} + \gamma_\mathrm{R}) + n_N(\bar{\gamma}_\mathrm{L} + \bar{\gamma}_\mathrm{R})} \\ &= \frac{e}{\hbar} n_N n_{N+1} \frac{\gamma_\mathrm{L}\bar{\gamma}_\mathrm{R} - \gamma_\mathrm{R}\bar{\gamma}_\mathrm{L}}{n_{N+1}(\gamma_\mathrm{L} + \gamma_\mathrm{R}) + n_N(\bar{\gamma}_\mathrm{L} + \bar{\gamma}_\mathrm{R})}. \end{aligned} \tag{2.39}$$

We can perform a similar operation for the heat current $\dot{Q}$, which can be written in terms of occupation probabilities as

$$\dot{Q} = \frac{1}{\hbar}[P_N \zeta_L - P_{N+1}\bar{\zeta}_L] \; , \tag{2.40}$$

where the energy transfer rates are given by:

$$\overset{(-)}{\zeta}_l = 2\,\Gamma_l \int \frac{\mathrm{d}\epsilon}{2\pi} f_{\pm l}\,(\epsilon)\epsilon\, K(\epsilon) \; . \tag{2.41}$$

Then,

$$\dot{Q} = \frac{1}{\hbar}\left(n_{N+1}\zeta_L P_N - n_N\bar{\zeta}_L P_{N+1}\right) \; ; \tag{2.42}$$

$$\dot{Q} = \frac{1}{\hbar}\frac{n_{N+1}n_N\zeta_L(\bar{\gamma}_L+\bar{\gamma}_R) - n_{N+1}n_N\bar{\zeta}_L(\gamma_L+\gamma_R)}{n_{N+1}\gamma_L + n_{N+1}\gamma_R + n_N\bar{\gamma}_L + n_N\bar{\gamma}_R} \; . \tag{2.43}$$

In order to ensure convergence of the above expressions, we take the limit of small lifetime broadening, i.e. $\Gamma \to 0$. Then, the term proportional to $(\zeta_L\bar{\gamma}_L - \bar{\zeta}_L\gamma_L)$ vanishes and we can write $\dot{Q}$ as:

$$\dot{Q} = \frac{n_N n_{N+1}}{\hbar}\frac{\zeta_{\mathrm{L}}\bar{\gamma}_{\mathrm{R}} - \gamma_{\mathrm{R}}\bar{\zeta}_{\mathrm{L}}}{n_{N+1}(\gamma_{\mathrm{L}}+\gamma_{\mathrm{R}}) + n_N(\bar{\gamma}_{\mathrm{L}}+\bar{\gamma}_{\mathrm{R}})} \; . \tag{2.44}$$

Both the Landauer formalism and the RE approach have advantages and depending on the system modelled either or both are appropriate to use. The Landauer formalism does not account for degeneracy but includes lifetime broadening for both the electrical current and the heat flux. The RE approach naturally includes degeneracy in its hopping rates but in order to ensure convergence of the heat current $\dot{Q}$ we need to assume little to no lifetime broadening ($\Gamma \to 0$).
In order to better understand the interplay between heat and charge flows in nanoscale devices, we will quickly introduce the Onsager reciprocal relations, which were derived by Lars Onsager on the basis that microscopic dynamics of thermodynamic forces are time reversible [79]. The prime example in thermoelectrics is the relation between the Peltier and the Seebeck coefficient of a thermoelectric material with the equality between an electrical current causing a heat flow and a heat flow causing an electrical current, respectively, being a manifestation of the Onsager reciprocal relations. For our purposes when studying a low-dimensional thermoelectric system, we can write the relation between heat and current flow using the Onsager matrix:

$$\begin{bmatrix} I \\ \dot{Q} \end{bmatrix} = \begin{bmatrix} L_{11} & L_{12} \\ L_{21} & L_{22} \end{bmatrix} \cdot \begin{bmatrix} \Delta V \\ \Delta T \end{bmatrix} \; , \tag{2.45}$$

where L_{ij} are the Onsager modes. One method to obtain L_{ij} is to expand I and $\dot{Q}$ to the first order with respect to ΔT and ΔV, which will be used in chapter 7 to model experimental results.

3

Materials Used and Previous Measurements

Carbon based low-dimensional structures have attracted interest since the early 1980s when Curl, Smalley and Kroto discovered the Buckminsterfullerene (named after the architect Richard Buckminster Fuller), a carbon atom cage resembling a football with an atom at each vertex [80]. Shortly after, carbon nanotubes were brought to the attention of the scientific community by Sumio Iijima, a Japanese physicist, who discovered the cylindrical arrangement of carbon atoms in a hexagonal "chicken wire"-like structure [81]. Both of these discoveries led to increased research in carbon nanostructures and a multitude of proposed applications such as drug delivery, electrodes for superconductors and molecular sensing [82–84]. However, one important member of the family of low-dimensional carbon structures was missing: graphene, a two-dimensional structure, adding to the Buckminsterfullerene zero-dimensional and the carbon nanotubes one-dimensional structure. Essentially a sheet of carbon atoms oriented in a hexagonal pattern, graphene was theoretically known since 1950 but was hypothesised to not be stable at room temperature and atmospheric pressure [85]. All attempts to synthesise it via shearing of graphite flakes or chemical exfoliation resulted in either thin graphite or a solution of graphite fragments, until in 2004 Novosolev and Geim started an unprecedented research surge when they were able to exfoliate pristine graphene on a Si/SiO_2 substrate from a graphite flake using only scotch tape [86].

In this chapter we will introduce the materials and structures used throughout the experimental work in this thesis as well as give an overview over the literature concerning previous thermoelectric measurements in low-dimensional systems. Starting with graphene, its basic physical properties and the different types of graphene are listed. We then briefly discuss graphene quantum dots before moving

to Buckminsterfullerene or C_{60} molecules. Lastly, previous thermoelectric studies on low-dimensional devices are reviewed.

3.1 Graphene and Graphene Nanostructures

Here we will give a quick overview over the most important material properties of graphene with a more detailed description of single-layer and bilayer graphene as well as their band structure available in Appendix A.
Graphene has multiple properties that make it attractive for use in nanoscale experiments. Due to its hexagonal structure (see Figure 3.1), each carbon atom has three direct neighbours. Between these neighbouring atoms, in-plane σ-bonds are formed from a combination of one s-orbital with only two p-orbitals, namely p_x, p_y and s. This enables strong bonding and a high structural integrity but also renders the electrons too tightly bound to contribute to electronic transport. However, the fourth orbital, p_z, forms a π-bond between carbon atoms through covalent bonding. This π-bond determines the band structure at low energies in single-layer graphene, which can be approximated as a so-called Dirac cone, with a linear energy dispersion, no band gap and relativistic electron dynamics [87]. In addition, the charge carrier density in graphene can be controlled via an electric field and the majority carrier switched between electrons and holes [86, 88]. Practically, it is then possible to manipulate graphene via a back or local gate [89]. Graphene has a high room-temperature electron mobility of about $2.5 \times 10^5\,\mathrm{cm^{-2}\,V^{-1}\,s^{-1}}$ and therefore a high electrical conductivity as well as a large electron mean free path [90, 91]. In addition to its electrical properties, graphene exhibits a very high thermal conductivity of above $3000\,\mathrm{W\,mK^{-1}}$ at room temperature [92].
Importantly, high quality graphene samples are relatively easy and inexpensive to fabricate and can be patterned into any desired shape with standard cleanroom fabrication techniques (see chapter 4). While bilayer graphene has slightly different properties to single-layer graphene, such as a quadratic dispersion relation, its fundamental characteristics namely a high electrical and thermal conductivity remain the same. This is also true for few layer graphene, with the boundary between few layer graphene and graphite typically set at ten layers [93, 94].
Regarding the thermoelectric properties of graphene, studies have shown that the sign and amplitude of the Seebeck coefficient depends on the type and density of the majority charge carrier [95, 96]. In addition, metallic contacts form vertical junctions that exhibit both Peltier [97] as well as Seebeck signals [98]. Single-layer and bilayer

graphene have also been shown to possess slightly different Seebeck coefficients due to the difference in band structure [99], a characteristic that will be studied further in chapter 9.

While there are many different ways to synthesize graphene such as for example

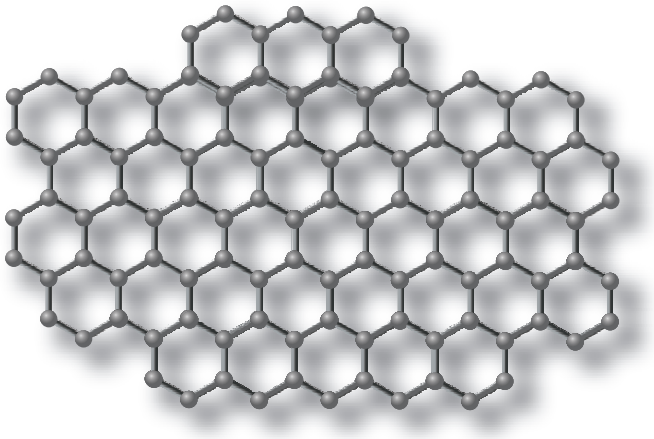


Figure 3.1 Schematic of the hexagonal structure of graphene.

liquid exfoliation and growth on SiC, the two most common ways are Chemical Vapour Deposition (CVD) growth and mechanical exfoliation [91]. The latter yields high quality samples with few defects and good control over the charge carrier density. However, mechanical exfoliation tends to be a strenuous and time extensive process that usually yields flake that are at most tens of micrometres wide and long [100]. Here, a piece of graphite, such as highly oriented pyrolytic graphite, is applied to a piece of tape, with some of the graphite sticking to the tape. Then in order to thin the layer of graphite, the tape is applied to another tape and this process is continued further until the tape is sufficiently covered and the graphite residue is considered thin enough. Lastly, the graphite tape is brought down on a Si/SiO_2 wafer after which pieces of graphene can be found among the graphite debris left by the tape. These flakes of graphene can then be patterned and contacted using the methods described in chapter 4.

CVD graphene on the other hand tends to have a higher amount of defects and exhibits grain boundaries as well as multilayer platelets. At the same time it tends to yield large areas covered with graphene and a roll-to-roll production process for almost square metre sized graphene films has been reported [101]. In the CVD growth process, a thin metal foil, typically copper, is placed into a furnace under a methane/hydrogen atmosphere and heated to around 1000 °C [102]. Through this,

the naturally present oxide layer on top of the Cu is reduced, leading to the nucleation of carbon atoms [103]. From these numerous growth centres on the copper foil, graphene domains start to grow and eventually merge to cover the whole substrate. In a next step, the copper foil can be etched away and the graphene placed on a substrate, with the details of this process discussed in chapter 4. The CVD graphene used in this thesis was either grown by the Warner group (Department of Materials, University of Oxford) as indicated at the beginning of chapter 6 and 8 or purchased from Graphenea.
Both exfoliated and CVD grown graphene can be relatively easily oxygen plasma etched and therefore shaped in the desirable device structure (see chapter 4). By nature graphene is already a two-dimensional material but by patterning it into narrow ribbons or small islands it is possible to create a one-dimensional or zero-dimensional device due to confinement (more on how confinement changes the energy landscape to create low-dimensional energy spectra in graphene is discussed in chapter 2). While graphene nanoconstrictions will be used in chapter 6 to contact C_{60} molecules, graphene quantum dots comprising a small island tunnel coupled to graphene reservoirs are employed in 7. In addition, graphene and its local thermoelectric properties are studied in chapter 8 and 9 and a thermoelectric device made out of graphene is characterized in chapter 10.

3.2 Buckminsterfullerene

Later in this work we will present thermoelectric measurements of Buckminsterfullerene or C_{60} molecules, which we will quickly introduce here.
As the name C_{60} already suggests, Buckminsterfullerenes are made up of 60 carbon atoms that are each connected to three neighbours via two single and double covalent bonds. As a result the structure of the C_{60} molecule is made up of hexagon and pentagon rings of carbon atoms (see Fig. 3.2) that resemble a football, hence the popular nickname buckyballs. Due to the π-electron conjugation, C_{60} molecules are semiconducting with electrons being the charge carriers [104].

C_{60} can be relatively easy synthesised by arc discharge [105], are readily functionalised with anchor groups [106] and can be used to trap atoms inside of its cage, changing its electrical properties [107]. All of this makes C_{60} a rewarding and interesting molecule to research in a preliminary study of molecular systems but most importantly it is a relatively well known molecule due to the early discovery in



Figure 3.2 Schematic C_{60} molecule structure.

1985 [80]. There have also been various studies of the thermoelectric properties of C_{60} molecules, where multiple buckyballs were stacked on top of each other [108], anchored to different materials [109] or measured as a C_{60} layer [110].
In order to produce the C_{60} molecules used in this work, an arc discharge method was employed, though different fabrication methods relying on similar principles exist [111]. In arc discharge, a voltage is applied between two graphite rods serving as electrodes and placed in a buffer gas atmosphere (such as helium) at high temperatures [112, 113]. The voltage applied ignites an arc discharge between the rods, resulting in the formation of a plasma which consumes part of the graphite electrodes. The soot resulting from this reaction contains C_{60} molecules which can then be extracted and purified (for example through high-performance liquid chromatography). As detailed at the beginning of chapter 6, the C_{60} molecules measured here were produced by the Porfyrakis group (Department of Materials, University of Oxford) and were, prior to measurement, functionalised with pyrene anchor groups [114].

3.3 Previous Thermoelectric Measurements in Zero- and Two-dimensional Systems

The thermoelectric properties of low-dimensional, especially zero-dimensional, systems have attracted interest as early as the 1990s when a series of experiments were spearheaded by Beenakker and Mohlenkamp on GaAs/AlGaAs gate defined QDs and Dresselhaus and Hicks developed their theory of thermoelectrics in low-dimensional systems. An increased thermoelectric efficiency compared to bulk thermoelectrics can here be achieved by manipulating and increasing the density of states available in the system. This in addition enables the decoupling of the thermal and electrical conductance that are usually firmly connected through the

Lorenz number. In this chapter early experiments on and recent developments in thermoelectric properties of low-dimensional structures are summarized.

3.3.1 Thermoelectric Measurements in Quantum Dot Structures

In the first thermoelectric experiments on QDs, sawtooth shaped oscillations in the thermopower could be seen with respect to back gate voltage, where each oscillation responded to an additional electron added to the dot [115]. This agreed well with a single electron tunneling approximation (SETA) theory introduced previously [71]. The big advantage of probing the thermopower over previously employed measurement methods, such as a conductance measurements, was that it is possible to measure the excitation spectrum, and therefore the linear response regime, close to the equilibrium rather than the addition spectrum. This enables the observation of the fine structure in the thermopower, which is difficult to observe in conductance measurements as it is suppressed for $e^2/c \gg \Delta E$. This allows the probing of the level spacing in QDs [71].
However, depending on the occupation of the QD, deviations in the line shape of the thermovoltage have been reported. For few or many electron QDs, a conductance-derivative or a sawtooth shaped thermovoltage can be observed, respectively [116]. This is attributed to a change from SET to inelastic co-tunnelling dominated transport in the Coulomb blocked region, here caused by lowering the temperature from 1.5 K to 40 mK.
The thermoelectric temperature response in a QD was additionally studied in QDs defined in single-walled carbon nanotubes [117]. Here it was found that the Seebeck coefficient decreases approximately proportional to the inverse of the temperature.

In gate defined QDs, such as in GaAs/AlGaAs structures, it is possible to readily change the coupling of the dot to the leads by increasing or decreasing the respective gate voltage. This, in addition to an applied magnetic field, makes it possible to use the QD as a thermal rectifier, as the SET through non-zero orbital momenta is subdued for high asymmetry and magnetic fields [118]. An imbalance in the transport is also observed for a Kondo correlated QD, where an asymmetry between hole and electron transport in the strongly Kondo correlated regime manifests itself as a suppression of the negative thermovoltage [119]. For a strong Kondo correlation, a reversal in the sign of the thermocurrent I_{th} has been observed for a QD epitaxially grown in nanowires [120]. This sign reversal was eliminated by applying a large

magnetic field or manipulating the temperature.
In the non-linear regime where high heating power was used such that $\Delta T \gg T, \Delta E/k_B$ additional effects are found. Here, a reversal of the thermovoltage sign can be observed, suggesting that a change in the dominant transport mode has occurred [121]. In further experiments studying the non-linear regime, the thermocurrent was probed and found to be saturating and even decreasing for higher heater currents [122, 123]. This can be explained by the Fermi-Dirac distribution in the reservoirs being broadened sufficiently to allow transport through multiple energy levels in the QD. Then the behaviour of the thermocurrent is determined by the distribution of thermally excited electrons in the leads relative to the energy levels of the QD.
For most of the measurements described here, either a Laundauer approach or a single electron tunnelling approximation is used to model the experimental results. While some, at least quantitative, agreement is achieved, often the experimental data cannot be reproduced or explained satisfactory within these theoretical approaches [124]. One possible reason for this discrepancy is the need to account for the input impedance and damping constant in the measurement setup when studying QDs [125]. These effects as well as additional influences such as asymmetries in the tunnel coupling or the nature and thermal conductance of the leads is further explored in this thesis and a new theoretical approach including these factors is introduced.
In more recent experiments on QD solid-state thermal generators, Thierschmann *et al.* have fabricated a three-terminal device that decouples charge and heat flow, enabling the harvesting of thermal fluctuations through current rectification [126]. The device consists of two capacitatively coupled QDs, one being the cold and the other the hot reservoir, and is theoretically able to operate at Carnot efficiency [127]. This was however not shown in this experiment as limits on the achievable asymmetry reduced the efficiency. Using a QD embedded in a nanowire Joseffson *et al.* were able to approach the Carnot efficiency in a QD heat engine [128]. Here, the power produced by the QD heat engine was directly measured through an external load.

A different way to localize a QD is to contact a molecule and create a molecular device. Molecular electronic and thermoelectric measurements are an area that has seen a fair amount of experimental activity in the last decade and we will summarize some of the most important and relevant findings below.
Thermoelectric measurements on molecules were effectively established by Reddy

et al. in a study researching the length dependence of the Seebeck coefficient, which simultaneously highlighted how crucial a good control over the molecular energy levels of the molecule is to achieve a high Seebeck coefficient [129]. A good control over the energy of the molecular junction was shown by Kim *et al.* [130]. Their study shows a good control over the energy spectrum of the molecule in question through back gating as well as the ability to create an unusually high temperature gradient through the molecule, which lead to some of the highest Seebeck coefficient values reported in molecules to date.
In general, the sign of the Seebeck coefficient in molecules is found to be an indicator for HOMO or LUMO dominated transport [131]. While the usage of the thermopower measurement in order to infer information about the transport mode has been reported previously [132] there is some concern as environmental factors can have a considerable influence as well. It has been shown that depending on the contact material, the same molecule exhibits a different sign in the thermopower not induced by a change in the HOMO/LUMO transport [109].
Other influences on the Seebeck coefficient are the length of the molecules, where it has been shown that S increases or decreases approximately linearly with chain length depending on the molecule [129, 133]. Another factor are the end groups of molecular junctions which can change the dominant transport channel [134].
In this work, C_{60} molecules are chosen to study the impact of tunnel coupling since their fundamental thermoelectric properties have been characterised previously [135, 108, 130]. In addition, the electronic characteristics of C_{60} molecules have been extensively investigated, using a wide variety of techniques such as the first molecular three terminal configuration [136], electromigrated junctions (both Au and graphene) [137, 138], scanning tunneling microscopy [139, 140] and mechanical break junctions [141].

3.3.2 Two-dimensional Systems

A combination of zero- and two-dimensional systems, quantum dot superlattice (QDSL) structures have emerged as a possible approach to high efficiency in thermoelectrics, with results indicating very high figure of merit values of around 2.0 at 300 K for PbSeTe based devices [13]. This is attributed to a delta-function distribution of the density of states and discrete energy levels as well as low lattice thermal conductivity and favourable carrier scattering mechanisms compared to classic solid-state thermoelectric devices. Such QDSLs take advantage of an ordered lattice structure and are closer related to two-dimensional materials than QDs. In

the following we will shortly discuss the thermoelectric properties of a fully two-dimensional material, graphene.
First experiments on the Seebeck coefficient in graphene revealed that it is possible to tune its sign and magnitude considerably by changing the majority carrier and the charge carrier density to a maximum value of $S \approx 80$ to $100\,\mu V\,K^{-1}$ [95, 96]. In these measurements the Mott formula agreed quantitatively with experimental data but showed some deviations for higher temperature measurements. In addition, a quantization of the Seebeck coefficient with respect to energy and a Nernst signal were observed. A variety of proposals and studies aiming to increase the Seebeck coefficient in graphene have been published, including defect or band engineering [142, 143] and nano structuring [144]. Other two-dimensional materials, which exhibit similar electronic properties to graphene, mainly transition metal dichalcogenides (TMDCs) such as MoS2, MoSe2, WS2, and WSe2, have also come into focus for thermoelectric measurements and applications [145]. However, rather than for individual TMDCs or graphene, the highest ZT values have been proposed for hybrid devices that are combining multiple materials, with the calculated efficiency reaching a ZT of up to 3 [146, 147]. While the global thermoelectric properties of two-dimensional materials are relatively well known, the local effects are not as well studied. While a variety of local imaging techniques have been developed, such as employing conducting SThM tips [148, 149], photocurrent measurements [150, 151] and scanning near-field microscopy [152], these either require an electrical contact between the measurement tip and the sample or inherently measure a mix of photovoltaic and thermoelectric phenomena. In this thesis, both the Peltier and Seebeck coefficient in graphene nanostructures is probed and a method for high resolution, localized thermovoltage measurements is presented.

II

Experimental Details

4

Fabrication

While not usually the sole focus of a DPhil or PhD, developing good fabrication skills and ensuring a failure-free fabrication procedure is a crucial part of successful experimental research, especially in the field of nanoelectronics. In order to produce devices that behave as expected and guarantee the reproducibility of observed effects and behaviour in these devices, it is crucial to follow a set protocol for fabrication. In addition, fabrication details and methods are important as they can determine crucial device characteristics (see chapter 8). This chapter will introduce the standard device fabrication procedures followed in this work.

4.1 Standard Fabrication Procedure

In this section the baseline fabrication procedure for contacted and patterned graphene devices is explained, for more detailed and device-specific recipes we refer to Appendix B and the respective publication each experimental chapter is based on. Unless otherwise specified, all of the described fabrication steps were carried out in the physics department ground floor cleanroom facilities in the Dennis Wilkinson Building at the University of Oxford.

4.1.1 Chip Preparation

The substrate used for all devices is Si/SiO_2, with a 300 nm thick oxide layer. The silicon can be separately contacted and used as a global back gate. The substrate is purchased as a 3 inch wafer and subsequently divided in $\approx$1 cm^2 pieces. The small chip size is necessary since multiple machines needed in the fabrication process, for example the electron beam lithography machine and the oxygen plasma, are

not designed for 3" wafers. Furthermore, the measuring setups are devised to take 1x1 cm chips.
For fabrication on the scale of a few nanometres to succeed it is essential to both work in a clean environment (ensured by the cleanroom facilities) as well as to properly prepare and clean the samples one works with. Dust or dirt grains are often on the order of or bigger than the structures written and therefore can substantially disturb the fabrication process. After having diced the Si/SiO_2 wafer in 1x1 cm big pieces, the chips are sonicated in a beaker filled with Acetone and subsequently transferred to a beaker with Isopropanol (IPA) and again sonicated, with each sonication step being 5 min long. Depending on the perceived contamination of the wafer and on the eventual measurement planned (such as molecular measurements) the chips are afterwards immersed in a piranha solution (sulfuric acid (H_2SO_4) and hydrogen peroxide (H_2O_2) in a 3:1 ratio) to remove any organic residues for 10 min [153].
Now that the chips are thoroughly cleaned, they can be prepared for the next step in the fabrication, Electron Beam Lithography (EBL) patterning, which requires a photosensitive resist (Figure 4.1a,b).
To ensure a uniformly coated chip with a constant-height resist layer free of foreign particles or air bubbles spin coating is used, where the chip is mounted on a spinning disk via a vacuum chuck. The thickness of the film is determined by the resist composition and evaporation rate as well as the spinning speed chosen. Typically, the thickness is proportional to the inverse square root of the spin speed.
After pipetting the resist onto the chip, it is first spun slowly (at 1000 revolutions per minute) for ten seconds during the ramping stage to flow the resist all over the chip and get rid of excess solvent and afterwards it is spun at 3000 revolutions per minute for 60 s to achieve the desired thickness of the resist.
The last step to prepare the chips for lithography is to bake the resist after spinning it. This is done at a temperature above the glass transition point of the resist, here we use 180 °C, so that the resist starts to flow again, ensuring a uniform thickness covering the whole chip. In addition, this baking step will evaporate any remaining solvent in the resist.
Now the chip can be further processed using EBL or if another layer of resist is required, the process of photoresist application is repeated.
Depending on the application and desired patterning procedure, different photoresists are chosen with two main groups of resist used in EBL: positive and negative resist. When aiming to deposit a metal layer, we use PMMA which is a positive resist. In a positive resist, the area exposed by the EBL will get washed away in

development and therefore this is where a subsequent etching process/metal deposition takes place (see Figure 4.1). The other sort of resist used is negative resist, where the exposed area remains and can function for example as an etch mask (see Figure 4.2, we will use this resist later on to define the graphene pattern).

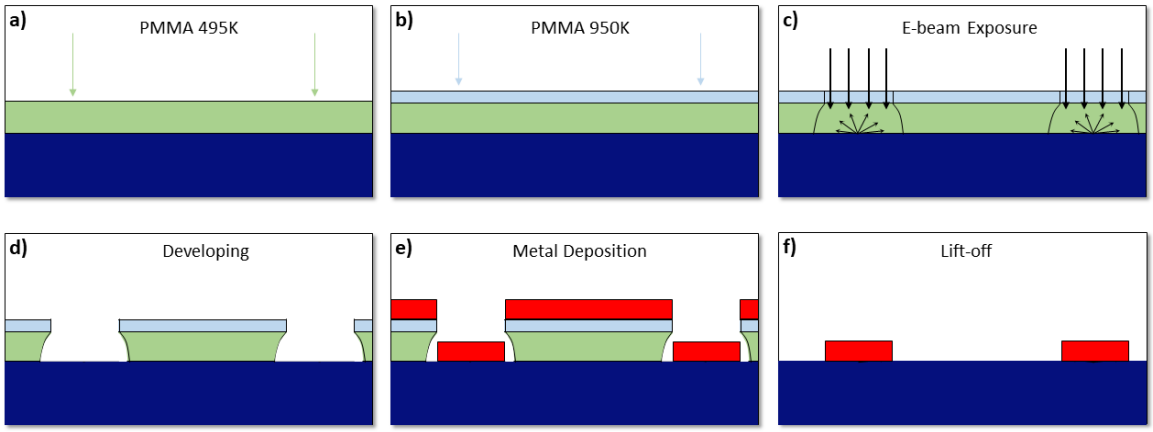


Figure 4.1 Metal Deposition Schematic. a) Application of the first photoresist. b) Addition of the second layer of photoresist. c) E-beam exposure, with secondary electron scattering from the substrate. d) Developing of the resist, leaving an undercut. e) Deposition of metal using a thermal or e-beam evaporator. f) Lift-off aided by the undercut leaving the final metal structure on the substrate.

4.1.2 Electron Beam Lithography

In a simplified way, the EBL machine works by shooting a beam of electrons in a user-predefined pattern on the photoresist, thereby exposing certain parts and causing molecular chain scission (positive resist) or cross-linking (negative resist). The crucial metric here is the exposure dose, which is measured in $\mu C\,cm^{-2}$ and which needs to be carefully adjusted in order to write small features with the required sharpness. If the dose is too low, the resist will not be completely exposed and the feature will look spotty with holes in it. Then any metal deposition will be evaporated on resist residues, resulting in a rough rather than smooth surface. If the dose is too high on the other hand, sharp features such as a corner will be bloated and closely spaced features will melt into each other, possibly short-cutting different leads. The right dose can be found by performing a dose test, where the desired feature is written in different doses ranging from clearly underexposing to clearly overexposing doses and subsequently inspected by, for example, an SEM.

For the fabrication in this work, a JEOL EBX 5500F S EBL system is used. In order to expose an area with a certain dose, the machine fills the pattern to be written with dots of the size of the electron beam width, about 0.5 nm. Then, depending on the dose, the ebeam exposes every other dot or in greater intervals to achieve the desired area dose, with the spacing calculated from the beam current and the minimum beam speed. For the PMMA resists utilized here, we use an area dose of $600\,\mu C\,cm^{-2}$.
As can be seen in Figure 4.1c, the effect of the electron beam on a double layer resist is twofold. First, the electrons hitting the first layer of PMMA 950K A3 expose the resist mostly in the area of direct impact, defining the pattern to be written. The second layer on the other hand is also affected by the proximity effect and secondary scattered electrons backscattered from the SiO_2 substrate. These second hand backscattered electrons which are still energetic enough to break the polymer chains are creating an undercut (Figure 4.1d). The undercut is desirable for metal depositions since it greatly facilitates a clean lift-off process, as discussed later.
In a negative resist on the other hand, the E-beam exposure cross-links rather than breaks the polymer resist, meaning the exposed area remains after development (see Figure 4.2).

4.1.3 Development

After the resist has been exposed, the chip needs to be developed in order to wash away the resist that is not contributing to the pattern. Either the area where the polymer chains have been cut (positive resist) or where the resist is not cross-linked (negative resist) is washed away by the developer (Figure 4.1d). For PMMA, we typically use an IPA:MIBK (Isopropyl Alcohol: Methyl Isobutyl Ketone in a 3:1 ratio) mixture, developing the chip in the mixture for 60 s and afterwards immersing it in IPA to stop the developing process. It is important to have the correct time for the developing process, as over- or underdeveloping has similar effects to over- or underexposing the sample. In order to improve the resolution of the writing or to prevent cracking of the resist due to strain (such as for resist on top of a hexagonal Boron-Nitride flake) cold development can be used, which slows down the development process. Here, the resist is developed at or below 0 °C, increasing the required developing times by at least a factor of two [154].

4.1.4 Deposition and Lift-off

After the pattern has been developed and inspected under an optical microscope, the desired metal layer can be deposited. For this work, this is done by a thermal evaporator, where the desired evaporation metal is placed in a metal boat, that is heated through Joule heating, causing the metal to evaporate (Figure 4.1e-f). The sample is mounted upside down above the evaporation source and the thickness of the metal evaporated is measured via a quartz crystal sensor [155]. For the Au contacts, a few nanometres of chrome are deposited first to act as an adhesion layer for the gold [156]. Subsequently, a layer of Au about 100 nm thick is deposited. It is important to deposit a sufficient layer of Au so that the wire bonding performed later to contact the sample does not punch through the Au and oxide and thereby shorts the backgate. However, when transferring graphene on the device after the contacts are written, a higher Au layer means that the graphene has to bridge a bigger horizontal distance, making it more prone to breaking at this point. In order to satisfy both requirements, one can perform two evaporations, one for the contacts up to about 45 nm in height and a second one on the contact pads which can be up to 150 nm high.
The limiting factor for deposition thickness is the thickness of the resist. In order to facilitate the lift-off, the process where the remaining photoresist is dissolved by Acetone, the metal deposition thickness should be smaller than one third of the undercut photoresist thickness. This ensures that the solvent can flow under the deposited metal deposition layer via the undercut defined earlier and dissolve the resist from multiple sides (see Figure 4.1e).

4.1.5 Graphene Transfer

After the Au contacts and heater have been patterned by the procedure above, we are now ready to transfer graphene on top of the chip. We use mostly Chemical Vapor Deposited (CVD) graphene due to the ease of use and the ability to fabricate a multitude of devices simultaneously. For further information on CVD graphene synthesis see chapter 3. CVD graphene is grown on a copper substrate and will usually have PMMA spun on top of it to ease transferring.
The first preparation step is to remove the backside graphene via a Reactive Ion Etcher (RIE) to selectively etch the graphene on the backside of the copper foil (an RIE is preferred to an oxygen plasma etcher since it offers greater directionality). Subsequently, the graphene on the copper foil is placed in an Ammonium Persulfate

(APS) solution to etch away the copper.
After the copper is etched away, graphene with a PMMA layer on top is floating in the APS solution. The PMMA is important to support the graphene, preventing it from rolling up, tearing or developing creases. In order to wash away the APS residues from the graphene, the graphene sheet is subsequently transferred to a new beaker with fresh de-ionized water at least four times. After the APS residue has been washed away, we can now pick up the graphene with the pre-patterned Si/SiO_2 chip. Subsequently, the chip is left to dry and then, in order to release tension in the graphene and make sure it conforms to the underlying profile, the chip is placed on a hot plate at 180 °C for at least two hours. This temperature is above the glass transition temperature of most commercially available PMMA.
After this step, the chip is immersed in Acetone for a few hours to remove the PMMA resist on top of it and subsequently a patterned chip with graphene on top is retrieved.

4.1.6 Graphene Patterning

In order to pattern the graphene structures, such as a graphene bow tie, a negative resist is used (typically MAN 2403 here). Similar to the previous procedure, we start by applying the resist via a spin coater on a chip with a layer of graphene transferred to it and then bake the chip before loading it into the EBL. Here, as discussed previously, the area exposed represents the desired structure as exposure cross-links the resist. We use a dose of $120\,\mu C\,cm^{-2}$. Afterwards, the chip is developed and then washed in deionized water to stop the developing process. At this point, the graphene on the chip is covered with a pattern of cross-linked resist that is now used as an etching mask (Figure 4.2c, d). The chip is loaded into an oxygen plasma etcher and etched, with the exact etching rate depending on the instrument used. The cross-linked resist can then be removed, leaving only the graphene pattern on the chip.
The graphene patterned in this way is highly p-doped due to exposure to the negative resist as well as interaction with SiO_2 surface charges [157]. This intrinsic doping can be reduced greatly through annealing of the sample, which can lower the charge neutrality voltage substantially down to approximately 40 to 80 V from over 100 V.
The fabrication process of exfoliated graphene devices is similar to the one for CVD graphene devices outlined above. After exfoliation onto the substrate, contacts can be written to the graphene flake using the process laid out at the beginning of this chapter and the flake can be etched into the desired form via the same procedure as

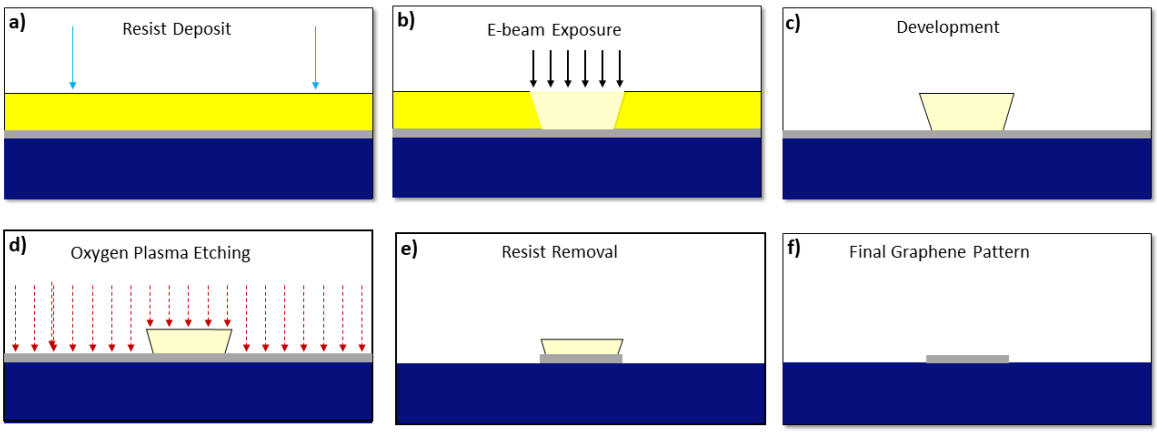


Figure 4.2 Graphene Patterning Schematic. a) Deposit of negative resist on top of the graphene. b) Exposure with the e-beam, crosslinking the resist. c) Development, leaving the patterned resist structure on top of the graphene. d) Oxygen plasma etching, the resist serves as an etching mask. e) Removal of the resist layer on top of the graphene structure. f) Final graphene structure at the end of the fabrication run.

used for CVD graphene.

A last word on the fabrication process described here briefly and in more detail in Appendix B. It might seem like this process involves a lot of waste due to using excessive amounts of solvent for the chip cleaning, as well as dropping photoresist next to the chip, but following the recipe closely can actually help reduce waste. While it might be possible to cut corners and shorten procedures as well as use up less resources in the short run this often leads to faulty device fabrication or unwanted contamination. Then, in addition to wasting time, a whole new fabrication run will have to be initiated, wasting far more material then if the original recipe would have been followed.

4.2 Electroburning and Graphene Quantum Dots

To open up a nanogap in the graphene bow ties, making it possible to contact the C_{60} molecules or produce graphene quantum dots, we employ feedback controlled electroburning. Here a voltage is applied across the device and stepwise increased while the resulting current is measured. As soon as a reduction in the current is observed, the voltage is quickly ramped to zero and the process is repeated (see Figure 4.3a). Depending on the desired outcome, that is a nanogap in the graphene

bow tie or a graphene quantum dot, this is done until a device resistance of $\geq$1 GΩ or $\geq$500 MΩ, respectively, is reached. In order to ensure the necessary speed for continuous probing of the current and ramping down the voltage quickly enough an Adwin-Gold system with 1 MHz clocking speed is used to monitor and supply power.

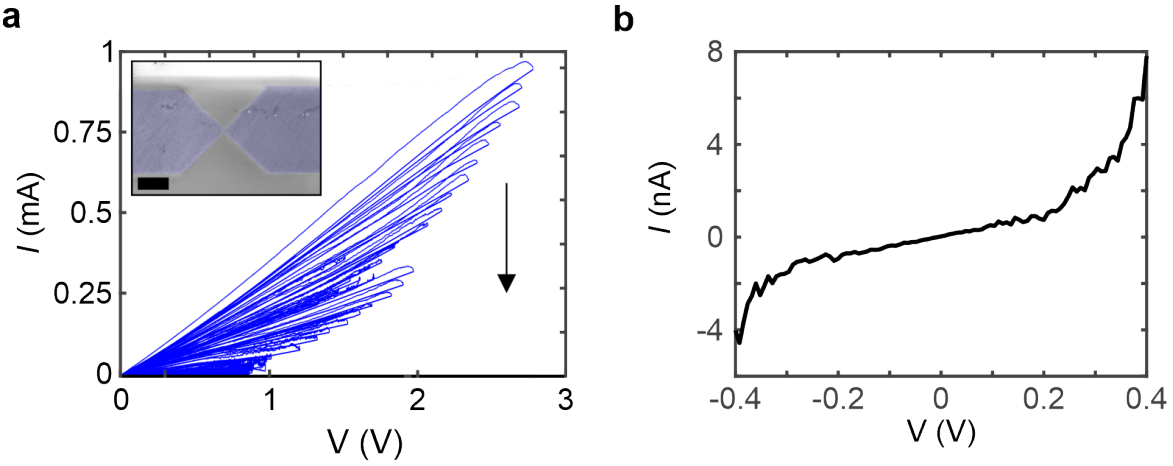


Figure 4.3 a) IV traces during feedback controlled electroburning, a decrease in the current triggers the ramping down of the applied voltage. Inset: false colour SEM image of a graphene bow tie, the scale bar indicates 1 µm. b) Typical IV trace for a nanogap device.

Electroburning of graphene is believed to be caused by a combination of sublimation and a chemical reaction of the carbon atoms with oxygen in air, both of which are thermally activated [158]. Reports of graphene electroburned under vacuum indicate that the sublimation process itself is enough to cause the electroburning process [159]. In general, the electroburning seems to start from the edges of the sample, developing into a crack spanning the graphene sheet [160] and it is possible to confine the gap formation geometrically to a predefined area through for example a bow tie geometry (Figure 4.3a inset) [161].
In order to probe the size of the gap, an electrical characterization method is used. After measuring the tunnel current through the gap (Figure 4.3b), the curve can be fitted to a Simmons model [162], from which a typical gap-size of several nanometres can be inferred [161, 160, 159].

4.3 Chip Design

While the chip design used in this work is not exceedingly complicated, there are still multiple important considerations when designing the chip.
A typical bow tie device structure is shown in Figure 4.4. The two sides of the bow tie are contacted via gold leads, with the leads splitting into four branches to enable a four-point resistance measurement. In order to have a well defined temperature gradient along the sample that can be probed via the resistance measurement, it is crucial to fabricate a heater that extends over the whole sample width and encompasses the splitting points. Otherwise geometric factors have to be taken into consideration when calibrating the temperature difference as was done in chapter 6.
A second consideration for the temperature gradient is the location of the heater as well as the length of the graphene channel. The heater wire should be placed as close

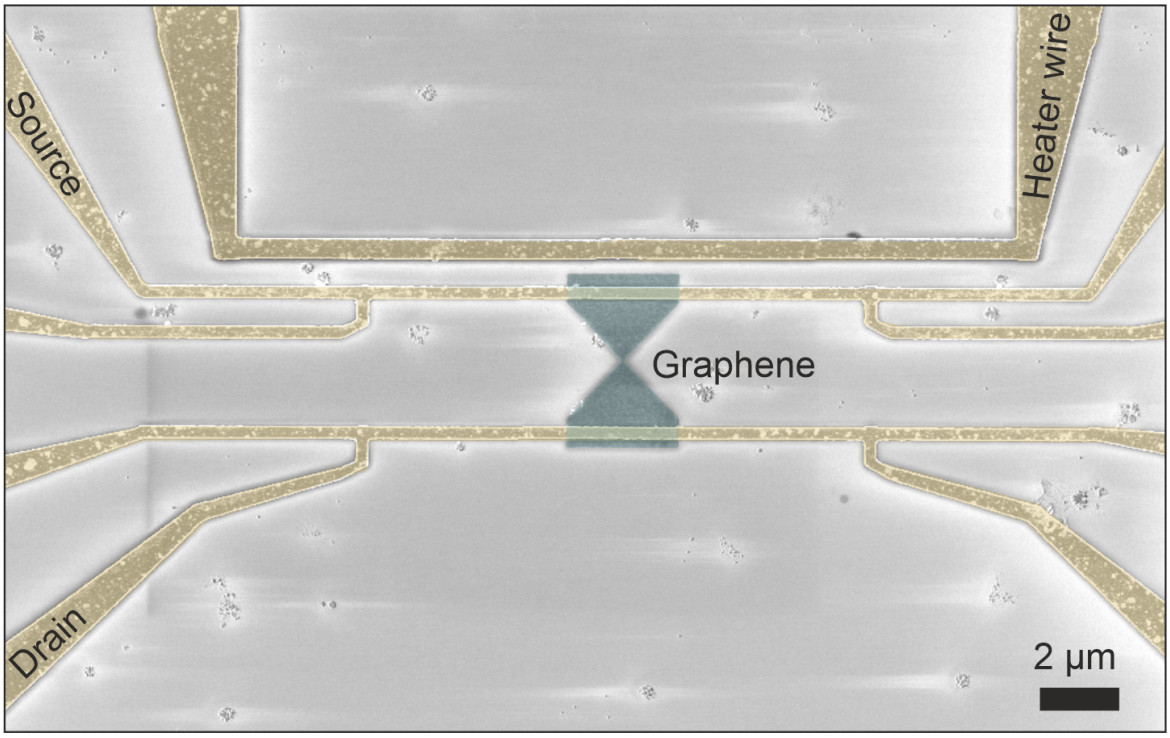


Figure 4.4 False colour SEM image of a typical device with two contacts (source/drain, gold coloured) to a graphene bow tie (graphene, turquoise coloured) next to a heating wire (heater wire, gold coloured). Each of the contacts has 4 leads to enable a four-point resistance calibration.

to the contact as possible since heat generated by Joule heating quickly dissipates in the Si/SiO_2 substrate (see chapter 10 for temperature maps of a heating wire on a

Si/SiO_2 substrate) yet it needs to be far enough away to allow for a certain amount of misalignment during the fabrication. Here, the heater is placed $\sim$300 nm away from the source contact. The length of the graphene channel similarly should be long enough to facilitate a temperature gradient along the device and make the fabrication of a bow tie possible. However, for the C_{60} molecule and the graphene quantum dot measurements a sufficient temperature gradient has to be established at the constriction across the dot or C_{60} molecule. Since graphene has a long thermalisation length, heat from the contacts is transported to the junction through the electron leads, however we found an excessively long channel length ($\geq$ 10 µm) can lead to an effective temperature difference of zero. A channel length of 2 to 4 µm seems to present a good compromise considering the above mentioned considerations.
Regarding the width of the graphene bow tie, two main concerns have to be weighed against each other. The larger the constriction the more stable the sample and therefore the higher the chance that the device is fully functioning after fabrication but on the other hand, a wide constriction is difficult or impossible to electroburn. Here 100 nm is used to address both concerns.
Graphene also enables the fabrication of side gates with relative ease either during the patterning step or via electroburning [163]. While this was successfully demonstrated in etch defined graphene quantum dot devices, for the work in this thesis only global back gates are used. These are achieved by contacting the Si substrate.
Lastly, for SThM based measurements, there are further requirements on the chip design. First of all, since the position on the chip during thermal measurements is inferred by the simultaneous AFM height topography images recorded, an abundance of small markers to indicate the location on the chip should be used. In addition, so as avoid interference of the wire bonds with the SThM tip, the chip is ideally fabricated with long leads from the wire bonding pads to the active device area being scanned.

5

Measurement Setups

There are two main measurement setups which are used in this work. One is an on-chip measurement, which probes the global thermoelectric properties across the device and which is used in chapter 6, 7 and 10. The other one is an SThM based method, where we scan over the sample with an SThM to study the thermoelectric properties on a local level. This method is used in the experiments presented in chapter 8 and 9. The two methods are schematically displayed in Figure 5.1, showing

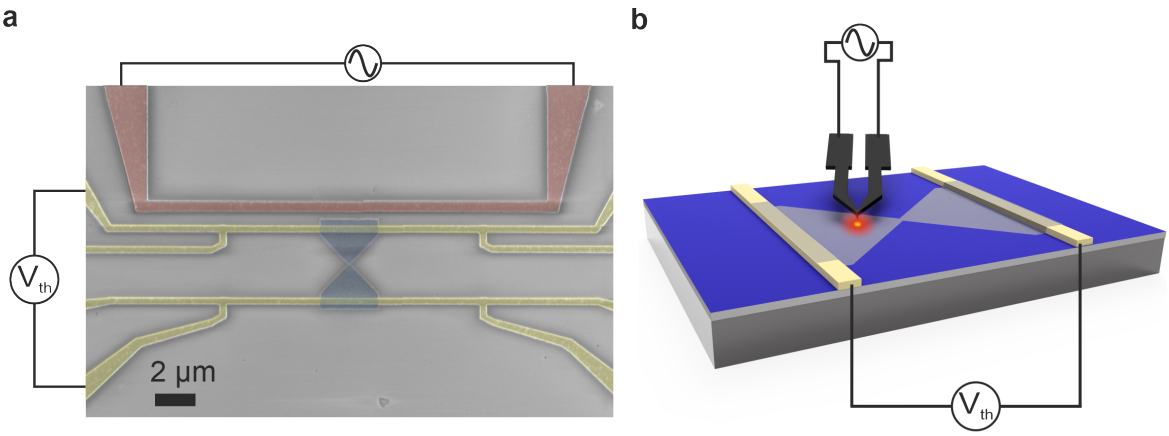


Figure 5.1 a) False colour SEM of a typical on-chip thermometry setup. The heater (red) is excited via an AC voltage bias while the thermovoltage across the device (here a graphene bow tie in blue) is measured between the contacts (yellow). b) Schematic of a typical SThM measurement setup, here depicted scanning a graphene bow tie. The SThM tip is heated up via an AC voltage bias applied between the two legs while the thermovoltage is measured across the contacts of the sample.

the typical electrical configuration for an AC thermovoltage measurement using an on-chip heater (left) and the SThM setup (right). Both measurement approaches can

be run in an AC or DC configuration. We will first discuss the two configurations and afterwards the two measurement setups.

5.1 AC (2ω method) and DC Measurement

For most measurements presented in this work, the thermovoltage is probed using an AC measurement method. In the AC or 2ω method, the heater is driven at a frequency f_{heater}, producing a thermal gradient along the substrate at a frequency $2f_{\text{heater}}$. The voltage drop caused by this temperature difference, the thermovoltage, is then measured at the second harmonic $2f_{\text{heater}}$ utilizing a lock-in amplifier to ensure a high signal-to-noise ratio. In order to achieve full thermalisation of the sample with the heater when using the 2ω method it is important to choose a sufficiently low frequency. In this work $f \leq 17\,\text{Hz}$ was employed for all measurements.
In the AC measurement, it is important to contrast the root-mean-square (RMS) versus the peak-to-peak (PP) sinusoidal signal. Since we assume a well thermalised sample, $1/2$ of the PP voltage is used to inform the heater calibration. In addition, as the lock-in amplifier displays the RMS of the detected signal, a factor of $\sqrt{2}$ has to be multiplied to extract the true PP signal. Similarly, as we are measuring the second harmonic, with the signal oscillating between zero and V_{th} around $1/2\ V_{th}$, the lock-in amplifier uses $1/2\ V_{th}$ as the zero point and displays only half the full amplitude. The final signal thus has to be multiplied by $2\sqrt{2}$.
A DC measurement, on the other hand probes the thermovoltage signal as a DC current is run through the heater, causing a constant temperature gradient. This technique is employed in chapter 9.

5.2 SThM Setup

In order to study the local thermal properties of the samples researched in this work a Scanning Thermal Microscope (SThM) is used. This is effectively an Atomic Force Microscope (AFM) with a microfabricated resistor incorporated close to the tip. The SThM tip employed here is a two-legged Si cantilever purchased from Anasys Instruments with a low doped, and therefore high electrical resistance, Si heater area above a conical tip (see Figure 5.2a). Since doped silicon rather than a thin metal film is used as the resistance heater it is possible to heat the Si probes to high temperatures and, in addition, the etching process makes it possible to fabricate probes with a small tip end radius comparable to regular AFM probes. In order to

maintain a constant force between the sample and the probe the microscope employs a standard AFM feedback loop [164]. This enables us to simultaneously measure the topography of the sample as well as the thermoelectric properties.
To probe a sample, it is placed in a chip socket located on a platform suspended from springs to minimize vibrations (Figure 5.2b). The chip socket has a Peltier element installed underneath it to measure the sample temperature and heat up or cool down the sample if desired. A camera installed on the SThM head enables us to localise the sample optically and the complete SThM is placed in a high vacuum environment to prevent parasitic heat transfer between the tip and the sample and therefore achieve a better thermal resolution (Figure 5.2c,d) [165, 166].

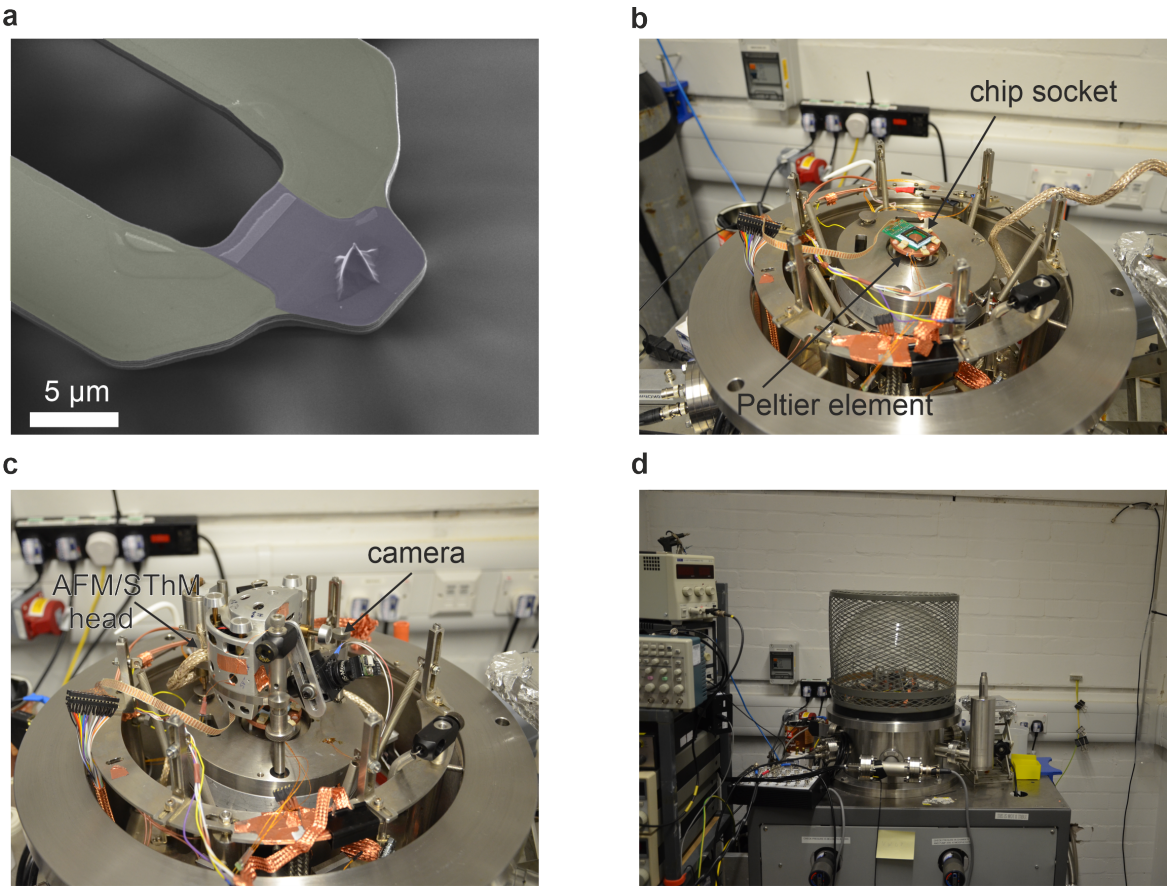


Figure 5.2 a) False colour SEM image of a typical SThM tip showing the high doped/low resistance (yellow) and low doped/high resistance (blue) Si region. b) Chip carrier on top of the suspended platform with an integrated Peltier element inside the vacuum chamber. c) Assembled SThM, with the AFM/SThM head including the camera mounted on the measuring platform. d) Ready to measure SThM inside the vacuum bell jar.

The SThM probe can act as both a heater and a sensor. To calibrate the probe, its electrical resistance as a function of the temperature is mapped and the probe excess temperature caused by self-heating of the heater as a function of electrical power is quantified [167]. This makes it possible to assess the thermal resistance of the cantilever R_p which was between 6×10^4 and $1.2 \times 10^5\,\mathrm{K\,W^{-1}}$ for the probes in the studies presented here. During measurements, we monitor the probe resistance changes through a modified Wheatstone bridge with the resulting signal amplified and fed into a Stanford Research Systems (SRS) 830 lock-in amplifier.
Two combined bias voltages are applied to the bridge, a high frequency AC component which provides high sensitivity through lock-in detection and a DC component. The DC part results in Joule heating of the probe and therefore, when brought into contact with the sample surface, the probe cools down (heats up) depending whether there is an increase (decrease) of the heat flux to the sample. This in turn is related to the sample local heat transport characteristics. These changes in the probe temperature cause variations in the probe electrical resistance which are then detected via the AC readout. Depending on the measurement performed, a higher or lower AC or DC component is applied.
Measuring precise temperature maps of operating devices is challenging due to probe-sample contact variations during the scanning process, which can cause artefacts. One way to correct for this effect is to take into account the heat flux from the heated tip to the sample, which requires an oscillating temperature field in the sample, created through an applied AC bias [165].
AC temperature variations in the sample can then be detected by the SThM sensor and a corrected temperature map is obtained using

$$\Delta T_{\mathrm{sample}} = \Delta T_{\mathrm{sensor0}} \frac{\Delta V_{\mathrm{AC}}}{\Delta V_{\mathrm{AC}} - \Delta V_{\mathrm{DC}}} \,. \tag{5.1}$$

Here, $\Delta T_{\mathrm{sample}}$ is the temperature increase in the sample, $\Delta T_{\mathrm{sensor0}}$ the temperature of the SThM tip before contacting the substrate, ΔV_{AC} the SThM resistance change at the AC driving frequency applied to the device and ΔV_{DC} the SThM signal due to the tip-sample heat flux. Then, for Peltier or Joule heating measurements (such as the ones described in chapter 8), ΔV_{AC} is measured at the driving frequency or first harmonic (for Peltier heating/cooling) and the second harmonic (for Joule heating), respectively.

5.3 On-chip Measurement

The other setup used in this thesis is an on-chip measuring system. Here all measurement and heating electronics are located on the substrate plane and typically global thermovoltage measurements are performed. Depending on the devices measured, the environment needed is either just a vacuum chamber (chapter 10) or for the zero-dimensional devices a cryogenic system (chapter 6 and 7). In the following we will quickly introduce the cryogenic systems used and the necessary corrections when measuring zero-dimensional devices.

5.3.1 Cryogenic Setups

All experiments studying the transport and thermoelectric properties of zero-dimensional devices, such as quantum dots and molecules (Chapter 6 and 7) were performed in cryogenic measurement setups with temperatures at or below 77 K. This low temperature is necessary to limit temperature broadening, which can smear out the fine structure in these device for temperatures where $k_B T > E_C, \Delta E$. To measure Coulomb blockade and the gate dependent thermoelectric signal in quantum dots and molecules, 77 K is usually sufficient due to the high addition energy in the devices studied here. As introduced in chapter 2, in order to be able to probe Coulomb blockade $k_\mathrm{B} T < E_\mathrm{add}$ is required. However, to detect the C_{60} molecule vibrational finger print in the sequential tunnelling regime in chapter 6 we require temperatures $\leq$4 K. We use both a self-built dipstick system and a cryogen-free measurement system with a base temperature of 3 to 4 K purchased from Oxford Instruments.
The dip-stick setup consists of a sealed metallic tube that can be placed in a dewar with either liquid nitrogen or liquid helium and after thermalisation reaches 77 K or 4 K, respectively. The dip-stick is outfitted with 44 measurement lines leading to the bottom of the stick where the sample is installed. For a thermoelectric device chip where each device requires 4 connections (2 for the heater, and 1 each for source and drain) and when a global back gate is used this means we can contact a maximum of 10 devices per cooldown. An additionally installed thermocouple gives information about the temperature of the sample space. In order to perform a measurement, the dip-stick is pumped down to $< 1 \times 10^{-4}$ mbar, slowly placed in the dewar and secured with an external frame. After about an hour, depending on the cryogenic liquid used, it will reach the temperature of the cooling liquid. Crucially, liquid nitrogen and helium boil off over time and have to be topped up to avoid the dip-stick

warming up.
In order to perform longer lasting experiments at low temperatures and for measurements requiring temperature control, the Oxford Instruments cryogen-free system was used. In the Oxford Instruments system, a pulse-tube cooler to cool a cold head to which the measured sample is thermally anchored allows for measurement temperatures between 3 K and 40 K with high temperature stability. While higher temperatures can be reached as well they provide less temperature stability. This system was mainly used for the study of graphene quantum dots described in chapter 7.

5.3.2 Accounting for Intrinsic Error Sources

An intrinsic source of error in low dimensional thermovoltage measurements using the described cryogenic setups is the load resistance of the preamplifier or lock-in amplifier, R_Ω, and the inherent system capacitance C. When the gate dependent device resistance $R_D(V_g)$ is comparable to R_Ω, the measured thermovoltage is reduced by a factor of $R_\Omega/(R_D(V_g)+R_\Omega)$. This correction is used in the study presented in chapter 6 and since the A-B function of the amplifier was utilized $2xR_\Omega$ was applied for the correction. The device dependent resistance is calculated by taking the inverse of the conductance $R_D(V_g) = G_D(V_g)^{-1}$.
The second error source is the inherent system capacitance, whose contribution in combination with the load resistance R_Ω can be inferred from analysing the schematic measurement circuit in Figure 5.3.

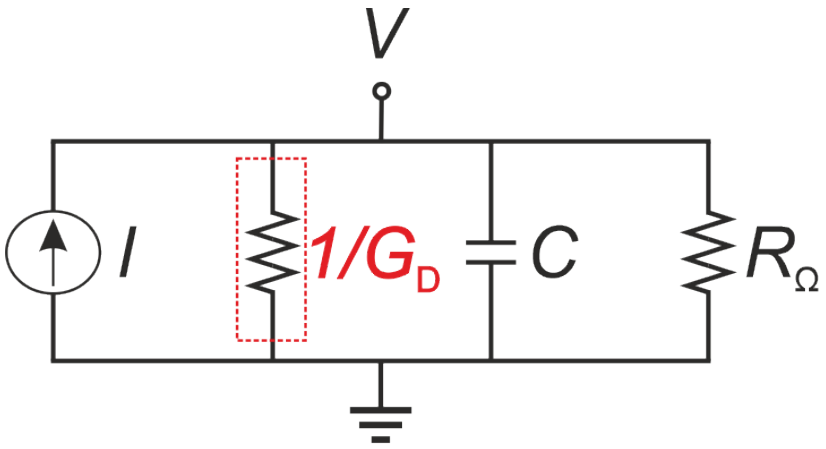


Figure 5.3 Schematic of a measurement circuit when probing the voltage V through a device with the effective device resistance $1/G_D$ due to a current I, taking into account the capacitance C of the system and the load resistance R_Ω.

From $V = Q/C$, it follows that

$$\frac{dV}{dt} = \frac{dQ}{dt}\frac{1}{C} = \frac{I}{C}\,. \tag{5.2}$$

Then, an expression for the current can be written using the circuit in Figure 5.3:

$$I = V(G_\mathrm{D} + 1/R_\Omega) + C\frac{dV}{dt}\,, \tag{5.3}$$

with both the current $I = I_\mathrm{th}e^{2iwt}$ and the voltage $V = V_\mathrm{th}e^{2iwt}$ being time dependent. Rewriting Equation (5.3) gives

$$I_\mathrm{th}e^{2iwt} = V_\mathrm{th}(G_\mathrm{D} + 1/R_\Omega)e^{2iwt} + 2V_\mathrm{th}Ci\omega e^{2iwt}\,, \tag{5.4}$$

which can be used to determine V_th by taking the absolute value. Since $\omega = 2\pi f$, the thermovoltage can then be written as

$$V_\mathrm{th} = \frac{I_\mathrm{th}R_\Omega}{\sqrt{(1 + G_\mathrm{D}R_\Omega)^2 + (4\pi f R_\Omega C)^2}}\,, \tag{5.5}$$

where I_th is the thermocurrent. This correction is used for the analysis of the measurement results in chapter 7.

We note that the load resistance plays a role if $R_\mathrm{D} \geq R_\Omega$. For the measurement presented in this thesis, three different amplifiers and therefore three different load resistances are used. In chapter 6, either the Stanford Research Systems (SRS) SR830 lock-in amplifier is directly used, meaning $R_\Omega = 10\,\mathrm{M}\Omega$ or in combination with an SRS SR560 voltage pre-amplifier, meaning $R_\Omega = 100\,\mathrm{M}\Omega$. Since it was realized that the load resistance plays a role in determining the measured thermovoltage, subsequently an SRS SR551 high impedance preamplifier was used for all other measurements, resulting in $R_\Omega > 1\,\mathrm{T}\Omega$.

III

Experimental Results

6

Thermoelectric Measurements of C_{60} Molecule Devices

The results in this chapter were previously published as "Field-Effect Control of Graphene-Fullerene Thermoelectric Nanodevices" by Pascal Gehring, Achim Harzheim, Jean Spièce, Yuewen Sheng, Gregory Rogers, Charalambos Evangeli, Aadarsh Mishra, Benjamin J. Robinson, Kyriakos Porfyrakis, Jamie H. Warner, Oleg V. Kolosov, G. Andrew D. Briggs and Jan A. Mol in *Nano Lett.* **2017**, 17, 11, 7055-7061 [138]. The author contributions are as follows: PG and JAM conceived the study, YS and JHW provided the CVD grown graphene, GR and KP provided the C_{60} molecules, PG and AH fabricated the devices, PG, JS, CE and OVK performed the SThM calibration, PG and AH performed the measurements, PG, AH, and JAM discussed the results, PG wrote the manuscript and all authors commented on the manuscript.

C_{60} molecules or buckyballs are a natural starting point for molecular measurements since they are well studied and have relatively simple and symmetric features [37, 168, 169]. Due to a long standing interest, production of buckyballs as well as methods for integration into device structures are well advanced [170–172].
Recently, C_{60} and other molecules have become a natural focus of research efforts in the thermoelectric community as the search for a high power factor and figure of merit in devices has expanded into the nanoscale regime, following Dresselhaus and Hicks seminal papers on reducing dimensionality [11, 10]. The key reason for this is that, rather than being mutually contraindicated as they are in conventional or bulk thermoelectric materials [173], the thermal conductance κ, the thermopower S and electrical conductance G can be controlled independently in nanodevices [174]. As a result, a variety of nanostructures such as carbon nanotubes [117], quantum

dots [121, 125, 123] and molecular devices [130, 108, 175, 134, 133, 135, 131, 140] have been investigated with respect to their thermoelectric properties. Molecules are a particularly promising system as the thermopower S is determined by their chemical composition [134], the position of intra-molecular energy levels relative to the work function of metallic electrodes [135], the molecule lengths within a family of molecules [175, 133], and the interaction between two neighbouring molecules [108] at the molecular scale. However, despite these many possible avenues for manipulating the Seebeck coefficient, only disappointing maximum values of S in the $\mu V K^{-1}$ range have been achieved up to date [130, 68]. One of the most important tools to maximise the thermopower is the ability to control the energetic position and influence the "steepness" of the transport resonances [176].

6.1 C_{60} Thermoelectric Nanodevices

C_{60} molecules are studied since they are stable in most atmospheres and have been shown to couple to graphene electrodes [37]. In addition, as their thermoelectric properties have been investigated extensively using various techniques such as STM based break junctions [135, 108] and electromigrated gold break junctions [130] they serve as an ideal testbed for developing molecular measurement methods.
To contact the buckyballs, graphene electrodes are used as they make it possible to avoid screening of the gate electric field caused by metal electrodes. Then, using a global back-gate, the orbital energy levels of the molecule can be shifted with respect to the electrochemical potential of the leads [177]. The C_{60} molecules are functionalised with pyrene anchor groups to facilitate bonding to the graphene electrodes (see Figure 6.3a for a schematic of the C_{60} molecular structure with pyrene anchor groups) [147, 114].
The devices are made by patterning CVD graphene into bow ties on top of pre-deposited gold contacts (see chapter 4), where each contact has four leads to allow for four-terminal resistance measurements (see Figure 6.1a). These resistance measurements can then be used to quantify the temperature difference across the device. Next to one contact, 1 µm away from the junction, a gold microheater is fabricated, enabling us to create a temperature gradient across the junction by passing a current through the microheater (see Figure 6.1b-d) [117, 95, 15].
In order to contact the C_{60} molecules, nano-gaps are opened in the graphene bow ties via feedback-controlled electroburning (see chapter 4). Since electroburning can lead to the formation of quantum dots due to graphene islands or ribbons being formed

[178] the gaps are characterized at 77 K in a vacuum by measuring a stability diagram (measuring the source-drain current I_{sd} as a function of gate, V_g, and bias voltage V_{sd}). Empty gaps exhibit non-linear $I_{sd} - V_{sd}$ curves and little to no gate modulation (see Figure 6.3b) and pre-characterized devices that show any form of Coulomb blockade are excluded from the study. Subsequently, the C_{60} molecules are deposited by immersing the sample in a 10 µmol C_{60} chloroform solution for 1 min followed by blow drying with nitrogen gas. Afterwards, the devices are cooled down and again characterized with respect to molecular signatures by measuring a stability diagram. 1080 two-terminal devices were fabricated and feedback-controlled electroburned, however due to limitations of the setup (namely a total of only 44 connections into the dipstick) only 100 of these devices were studied at low temperatures. Overall, 16 devices showed signatures of a molecule in the junction, which is defined as: 1) a clear change from no gate modulation to Coulomb blockade after molecule deposition and 2) vibrational fingerprints in the excited state spectrum measured in the sequential tunnelling regime.

To quantify $S = -V_{th}/\Delta T$, the temperature drop across the junction ΔT is estimated via the four-point resistance measurement, a COMSOL simulation and an SThM measurement.
In the rest of the chapter, the gradient obtained from the four-point resistance measurement is used to analyse the experimental results since it constitutes a calibration performed for each device and for the actual measurement conditions (at 77 K and in a vacuum). To extract the temperature difference, the device resistance as a function of temperature and heater power are measured (see Figure 6.2). From linear fits to the four-point measurements, the increase in ΔT across the junction as a function of the heater power P_{heat} can be written as

$$\frac{\partial \Delta T}{\partial P_{heat}} = \frac{A}{C} - \frac{B}{D}\,, \tag{6.1}$$

where A (B) are the change of resistance with respect to heater power of the right (left) contact and C (D) are the change of resistance with respect to temperature of the right (left) contact, respectively.
Here, it is crucial to discuss possible error sources to the determined temperature difference ΔT across the junction as they significantly influence the calculated thermopower and powerfactor. The first error source is due to the device geometry, with the heater being smaller than the contacts, resulting in the temperature distribution

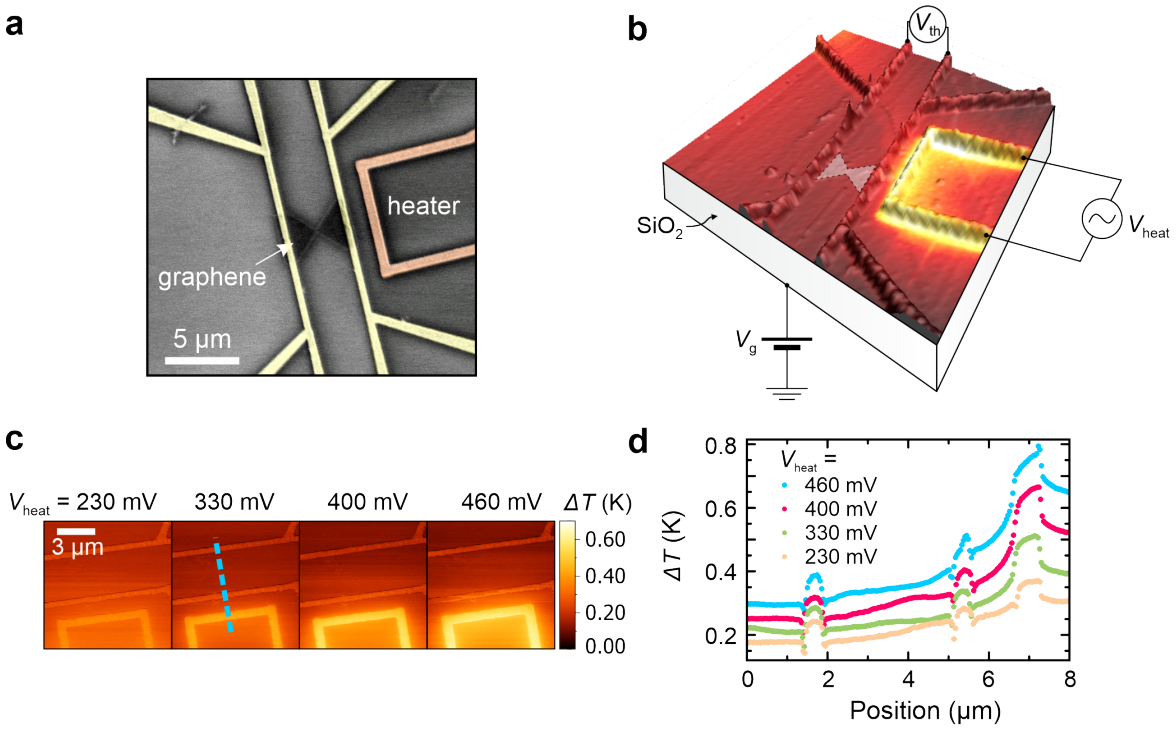


Figure 6.1 a) False-colour scanning electron microscopy image showing the device. b) SThM map overlaid with an AFM height profile showing the setup for a typical thermovoltage measurement. c) SThM images for different voltages applied to the micro-heater. d) Temperature profiles along the device extracted from the maps shown in c (see blue dashed line).

along the electrical contacts not being uniform. To correct for this error, a temperature profile $T(y)$ between the contact points used for the resistance measurement, y_1 and y_2, is calculated via COMSOL (see Appendix). Then the average temperature of the contact segment $y_2 - y_1 = 11\,\mu\text{m}$ is given by

$$T_{\text{average}} = \frac{1}{y_2 - y_1} \int_{y_1}^{y_2} T(y) dy \,. \tag{6.2}$$

This results in a geometrical correction factor of $(T_{\max} - T_0)/(T_{\text{average}} - T_0) = 1.2$ that has to be taken into account for the resistance temperature difference calibration. Another error source is the calibration measurement itself, where the temperature coefficient of resistance is extracted. The inherent uncertainty of $\frac{\partial \Delta T}{\partial P_{\text{heat}}}$ can be estimated using a standard propagation of error:

$$\Delta\left(\frac{\partial \Delta T}{\partial P_{\text{heat}}}\right) = \sqrt{\left(\frac{1}{C}\Delta A\right)^2 + \left(-\frac{A}{C^2}\Delta C\right)^2 + \left(-\frac{1}{D}\Delta B\right)^2 + \left(\frac{B}{D^2}\Delta D\right)^2}\,, \tag{6.3}$$

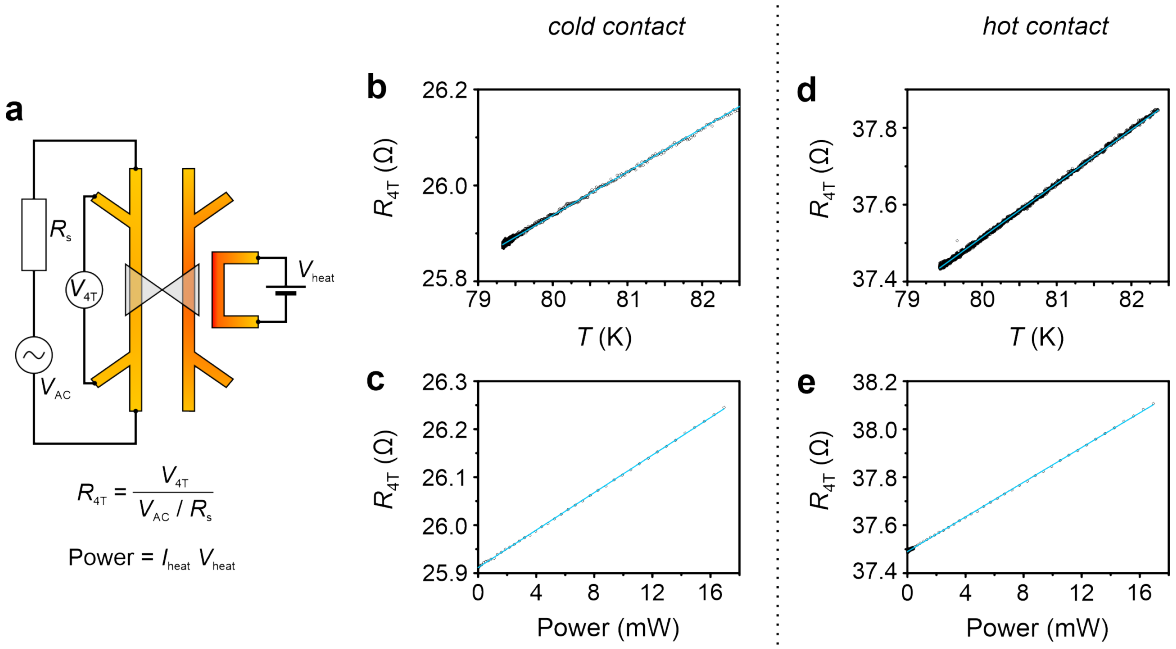


Figure 6.2 a) Four-terminal resistance measurement setup. The series resistor is $R_S = 110\,\mathrm{k\Omega}$ and a voltage of $V_{AC} = 150\,\mathrm{mV}$ is applied to the heater at a frequency of $f = 1013\,\mathrm{Hz}$ resulting in an AC current of $I_{AC} = 1.4\,\mu\mathrm{A}$. b-e) Four-terminal resistance as a function of temperature and power for the cold (b and c, respectively) and hot (d and e, respectively) contact. A linear fit is displayed in blue.

where ΔA, ΔB, ΔC and ΔD are the standard deviations of the fitting parameters A, B, C and D respectively extracted from Figure 6.2. Then the error in the temperature calibration is $\Delta\left(\frac{\partial \Delta T}{\partial P_{\mathrm{heat}}}\right) = 9\,\mathrm{KW}^{-1}$ for a temperature of $\frac{\partial \Delta T}{\partial P_{\mathrm{heat}}} = 48\,\mathrm{KW}^{-1}$. This is equal to an uncertainty in the temperature drop across the device of 18.75 % or approximately 20 %, which is used in the remainder of the chapter as the uncertainty for all calculations.

Incorporating the error analysis into the resistance measurements we find a temperature difference between the hot (next to the micro-heater) and cold contact as a function of heater power of $\Delta T / P_{\mathrm{heater}} = 58 \pm 11\,\mathrm{KW}^{-1}$ at $T_0 = 77\,\mathrm{K}$. This value is corroborated by the other two calibration methods, the COMSOL finite-element simulations which gives $\Delta T / P_{\mathrm{heater}} = 50\,\mathrm{KW}^{-1}$ and the SThM method giving $\Delta T / P_{\mathrm{heater}} = 63 \pm 10\,\mathrm{KW}^{-1}$ under ambient conditions. The SThM approach is shown in Figure 6.1b which displays a simultaneously recorded temperature and height map overlaid on top of each other. Using different heater powers, a power-dependent temperature gradient can be extracted and used to inform the temperature difference estimations (see Appendix C for more details on the COMSOL and SThM calibration approaches).

6.2 Results and Discussions

6.2.1 Low Temperature Characterization

The nanogaps created via electroburning are characterized at 77 K before molecule deposition in order to ensure that they are empty and do not exhibit any gate dependent features. In Figure 6.3b such stability diagrams indicating an empty gap are shown for three typical devices, exhibiting little to no gate dependence. After molecule deposition, Coulomb blockade can be observed, featuring separate Coulomb diamonds with high addition energy (see Figure 6.3c).

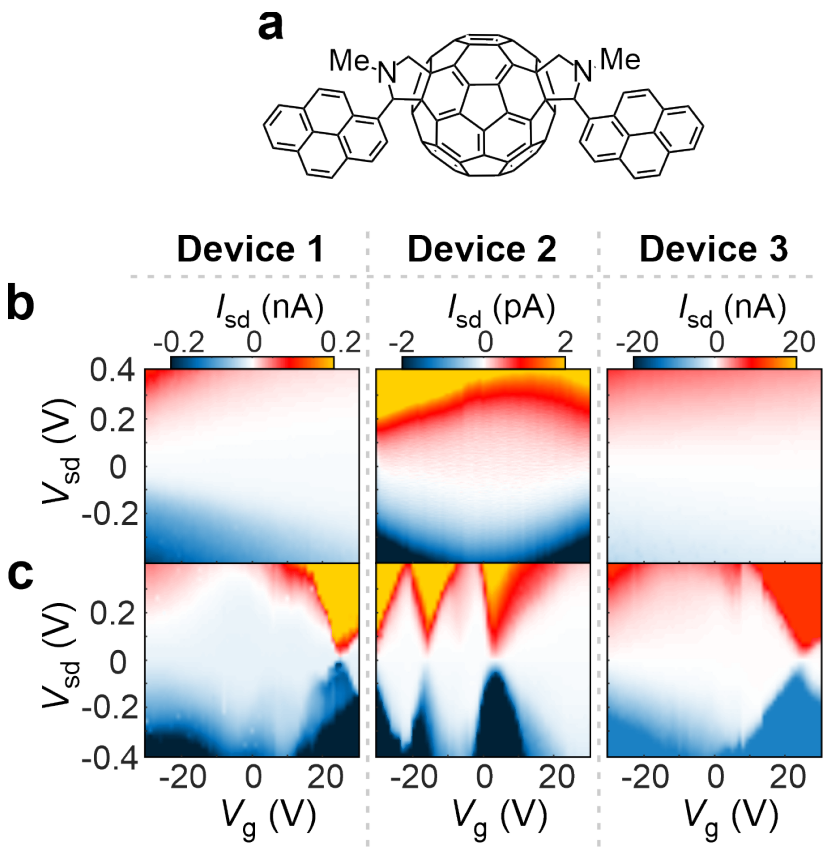


Figure 6.3 a) Schematic of the C_{60} molecular structure with pyrene anchor groups. b-c) Pre (b) and post (c) molecular deposition stability diagram of three typical devices. All measurements are performed in a vacuum at 77 K.

In this chapter, we concentrate on devices exhibiting closing and non-overlapping diamonds as this suggests that a single molecule dominates the transport. In addition, well-isolated energy levels tend to exhibit a large Seebeck coefficient and are more straight forward to interpret and analyse. Additional data for all other measured

devices is shown in Appendix C and [138]. All devices were studied in the accessible gate and bias voltage range of -30 to 30 V and -400 to 400 mV, respectively.
While the sequential electron tunnelling behaviour in Figure 6.3c suggests the formation of a molecular junction [179, 158, 37], we additionally cooled down multiple devices to lower temperatures of $T < 5$ K to further study their transport characteristics. Specifically, we investigated the sequential tunneling regime for vibrational modes. The C_{60} buckyball, as every molecule, has a distinct vibrational finger print, consisting of the energetic position of all vibrational modes such as Raman active vibrational modes and centre-of-mass motion of the molecule with respect to the electrodes [37]. These positions depend strongly on temperature, the tunnel coupling to the leads [180] as well as Franck-Condon factors [136, 181], which can vary substantially between different molecular junctions. In addition, accurate molecule vibrational spectroscopy is complicated by density of state fluctuations in the graphene lead, which can result in features inside the SET regime that do not run parallel to the edges of the Coulomb diamond [182].

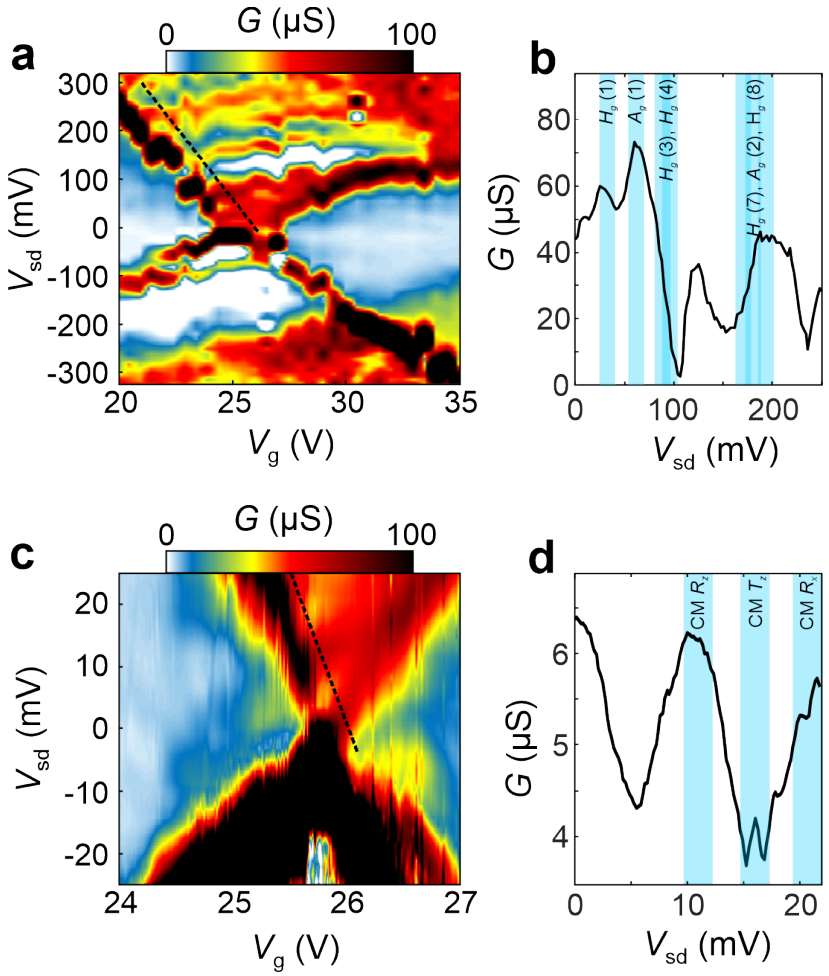


Figure 6.4 a-b) Differential conductance map of device 1 (a) with the corresponding energy spectrum extracted along the black dotted line (b) c-d) Differential conductance map of an additional device (c) with the corresponding energy spectrum extracted along the black dotted line (d). All measurements are taken in a vacuum at 3.2 K.

An example of a low-temperature characterization is shown in Figure 6.4 for Device 1. After extracting the energy position of the vibrational modes from the stability diagram (black dotted lines), they are mapped on the vibrational fingerprint of the C_{60} molecule (blue shaded area). Additional vibrational spectroscopy for other devices can be found in Appendix C. Overall, 7 out of 16 measured single molecule junctions showed evidence of vibrational excited states and 4 out of 16 devices broke during the attempt to cool them down from 77 K to $<$5 K.

6.2.2 Thermoelectric Measurements

Next, the thermoelectric properties of the single-molecule junctions are studied. In order to do this, the 2ω method is used where an AC voltage at a frequency f_{exc} is applied to the micro-heater and the thermovoltage drop over the sample is recorded at the second harmonic $2f_{exc}$ between the two contacts using an SRS 830 lock-in amplifier (see also chapter 5). The frequency used is 17 Hz to ensure a full thermalisation of the sample with the heater and the measurements are concentrated around the Coulomb peaks of the molecular junctions as the thermvoltage signal elsewhere is on the order of the measurement setup noise level. We also measure a conductance trace of the junction over the same gate range to connect the thermoelectric and transport properties of the molecule at their respective energy (see Figure 6.5a). The conductance traces for all devices show a single peak as expected from an isolated single energy level [183].
In contrast, the thermovoltage can be observed to first increase from the noise level around zero, then switch signs at the charge neutrality point to subsequently decrease and finally rise towards the zero level again (see Figure 6.5).

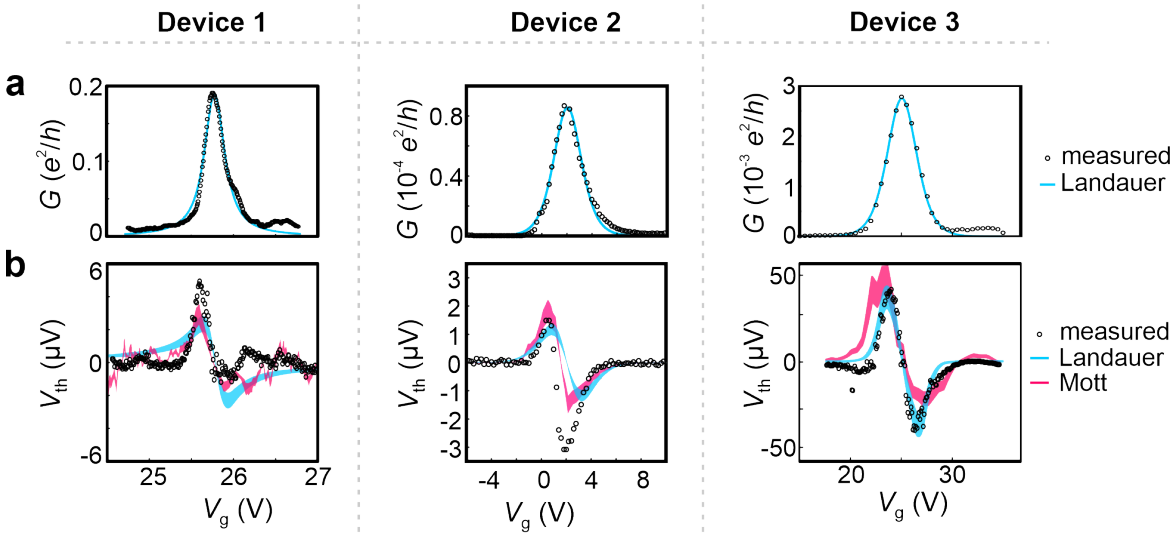


Figure 6.5 a) Measured electrical conductance (black dots) and theoretical calculations using a Landauer approach (blue line) as a function of back gate voltage. b) Measured thermovoltage (black dots) and theoretical calculations using a Landauer (blue line) and Mott formula approach (pink line) as a function of back gate voltage. The error introduced in the fits via the uncertainty of the temperature calibration is indicated by the width of the lines.

The temperature drop across the device is extracted through the four-terminal resistance measurements as $\Delta T = 45 \pm 9\,\mu K$, $\Delta T = 100 \pm 20\,\mu K$ and $\Delta T = 180 \pm 36\,\mu K$ for Device 1, 2 and 3 respectively. This enables us to determine the Seebeck coefficient $S = \Delta V / \Delta T$, which ranges from 1.5 to $460\,\mu V\,K^{-1}$, about an order of magnitude larger than the Seebeck coefficients found in STM break junction experiments with metallic electrodes.

In the following, we will treat the molecule as a single non-degenerate energy level and use the Landauer formalism to describe the transport. As was introduced in chapter 2, the conductance in such a system is given by

$$G(V_g, T_0) = \frac{2e^2}{h} \int \frac{\partial f(T,E)}{\partial \epsilon} \mathcal{T}(E) d\epsilon \,, \tag{6.4}$$

where $f(T,E)$ is the Fermi Dirac distribution and $\mathcal{T}(E)$ the transmission probability across the device. In the linear bias and temperature regime, we can also write the conductance G in terms of the moments of the transmission coefficient L_i [20]:

$$L_i = \int_{-\infty}^{\infty} (E - E_F)^i P(E) dE \,, \tag{6.5}$$

with the non-normalised probability distribution given by $P(E) = -\mathcal{T}(E)\partial f(T,E)/\partial E$ [176]. Then the electrical conductance can be written as $G = 2e^2/hL_0$. For a single, well-isolated molecular level in the strong coupling regime a Breit-Wigner resonance is a good approximation for the transmission probability [29]. $\mathcal{T}(E)$ is then given by

$$\mathcal{T} = \frac{\Gamma_L \Gamma_R}{(\Gamma_L/2 + \Gamma_R/2)^2 + [(e\alpha V_g - E_0) - E]^2} \,. \tag{6.6}$$

Here E_0 is the energy of the transport resonance, α the gate coupling, which can be extracted from the stability diagrams (see chapter 2), and Γ_L and Γ_R the tunnel coupling to the left and right lead, respectively. The derivative of the Fermi-Dirac distribution is given by $\frac{\partial f(E)}{\partial E} = \frac{1}{4k_B T_0} \cosh^{-2}\left(\frac{E}{2k_B T_0}\right)$. In the strong coupling limit, where $\Gamma = (\Gamma_L + \Gamma_R)/2 \gg k_B T_0$, equation (6.4) simplifies to $G \approx \frac{2e^2}{h}\mathcal{T}$, making it possible to infer the tunnel couplings to the leads from the height and width of the Coulomb peak. Similarly, in the weak coupling limit, $\Gamma \ll k_B T_0$, the height of the conductance peak is proportional to $\frac{\Gamma_L \Gamma_R}{\Gamma_L + \Gamma_R}$ and the width of the peak is determined by $k_B T_0$.

Just like the conductance, the Seebeck coefficient can be written in the Landauer

formulation using the transmission coefficient modes as

$$S = -\frac{1}{eT_0}\frac{L_1}{L_0}\,. \tag{6.7}$$

As we have see in chapter 2, for a smooth transmission function $\mathcal{T}(E)$, that is $\mathcal{T}(E)$ varying slowly as a function of energy E on the scale of $k_\mathrm{B}T_0$ and therefore $\Gamma \gg k_B T_0$, S can be simplified to the Mott approximation

$$S = -\frac{\pi^2 k_B^2 T_0}{3e\alpha}\frac{1}{G}\frac{dG}{dV_\mathrm{g}}\,. \tag{6.8}$$

Using the Landauer formalism in equation (6.7) and the Mott approximation in equation (6.8) we can compare the experimental results to theoretical calculations. Here, the tunnel couplings necessary to calculate the transmission $\mathcal{T}(E)$ are extracted by fitting the gate-dependent conductance traces with equation (6.4) for $\Gamma \gg k_\mathrm{B}T_0$. For thermally broadened conductance peaks, that is $\Gamma \ll k_\mathrm{B}T_0$, the tunnel couplings are found by fitting the conductance traces with $G = G_\mathrm{max}\cosh^{-2}([\alpha V_\mathrm{g} - E_0)/2k_\mathrm{B}T_0)])$, where $G_\mathrm{max} = e^2/(\hbar 4k_\mathrm{B}T_0)\Gamma_\mathrm{L}\Gamma_\mathrm{R}/(\Gamma_\mathrm{L}+\Gamma_\mathrm{R})$ [184], $T_0 = 77\,\mathrm{K}$ is fixed and symmetric coupling ($\Gamma_\mathrm{L} = \Gamma_\mathrm{R}$) is assumed to facilitate the fitting. While not making it possible to uniquely determine Γ in the weak coupling regime, a good agreement with the data can still be obtained since S is relatively insensitive to the coupling for $\Gamma \ll k_\mathrm{B}T_0$.
The temperature difference across the device is obtained via the four-terminal resistance calibration as discussed above with the resulting error indicated by the width of the calculated curve in Figure 6.5. Here we assume that the temperature of the contacts is identical to the temperature next to the junction since graphene has a cooling length of up to 7 µm [185], exceeding the approximately 1.7 µm between the junction and the gold contacts in the devices. Since a smaller temperature gradient leads to a larger Seebeck coefficient, the values here can then be regarded as lower bounds for S. Furthermore, the thermovoltage calculations were corrected for the input impedance of the voltage amplifier via a damping factor (see chapter 5).
Another error source is the thermovoltage created in the graphene leads, but since the graphene used is strongly p-doped and therfore far away from the charge neutrality point, we do not expect a noticeable gate dependency of the graphene Seebeck coefficient [95]. As we do not observe a constant offset of the thermovoltage, we assume that the influence of the graphene leads on the thermopower is negligible.

Table 6.1 Transport and thermoelectric characteristics for single-level C_{60} devices.

Device	Γ (μeV)	χ	α (meV/V)	E_0 (meV)	S_{max} (μV/K)	G_{max} **(e^2/h)**	$(S^2G)_{max}$ (k_B^2/h)	T_0 (K)
1	1350	15	13	335	27	0.2	0.14	3.2
2	1	–	9	12	30	10^{-4}	0.04	77
3	44	–	9	221	220	0.003	0.01	77
4	650	–	10	188	140	0.08	0.08	77
5	8	–	6	53	238	0.006	0.02	11
6	85	–	11	84	460	0.01	0.11	77
7	$1.2 \cdot 10^4$	$1.2 \cdot 10^4$	62	564	1.5	$2 \cdot 10^{-4}$	$7 \cdot 10^{-4}$	77

The experimental results are in good agreement with the calculated thermovoltage curves reproducing the line shape and the amplitude well despite the uncertainties in ΔT and Γ. While this confirms the single molecular level assumption, discrepancies are clearly visible in the fitting to the Landauer theory and Mott formula. For instance, asymmetries in the thermovoltage as well as the amplitude are not always well represented. There are a number of explanations for the divergence. First, the Landauer approach used here assumes that the conductance peak reaches a maximum at the same point as the thermovoltage zero crossing. However, as we will see in the next chapter, charge degeneracy, which is not included in the Landauer approach, can play a crucial role when determining the right position of conductance peak. Furthermore, the Mott formula was originally developed for a non-interacting electron gas with a weak energy dependent conductance and is therefore not necessarily applicable in the Coulomb blocked regions of the QD. Other error sources include gate hysteresis effects caused by measuring the thermovoltage and the conductance separately as well as non-ideal and non-linear heat transport throughout the device. Clearly, while the measured trends are well represented, multiple effects are not accounted for which will be studied and discussed further in chapter 7.

6.2.3 Power Factor

Since we are measuring both the thermopower S and the electrical conductance G in the C_{60} devices we are also able to study the power factor given by $\mathcal{P} = S^2G$. While

the Seebeck coefficient quantifies the extent of the heat to energy conversion and gives important information about the thermoelectric properties of the device, it alone does not necessarily correlate with the heat to energy conversion performance. Instead, in the linear response regime (i.e. where the operating temperature is much bigger than the temperature difference $T_0 \gg \Delta T$) the power factor is a better quantity to consider as it is proportional to the maximum power density of the thermoelectric generator and gives a measure of achievable output power [186].
The power factor as a function of gate voltage for device 1-3 is depicted in Figure 6.6 and the maximum $\mathcal{P}_{\text{max}}$ of additional devices in table 6.1.

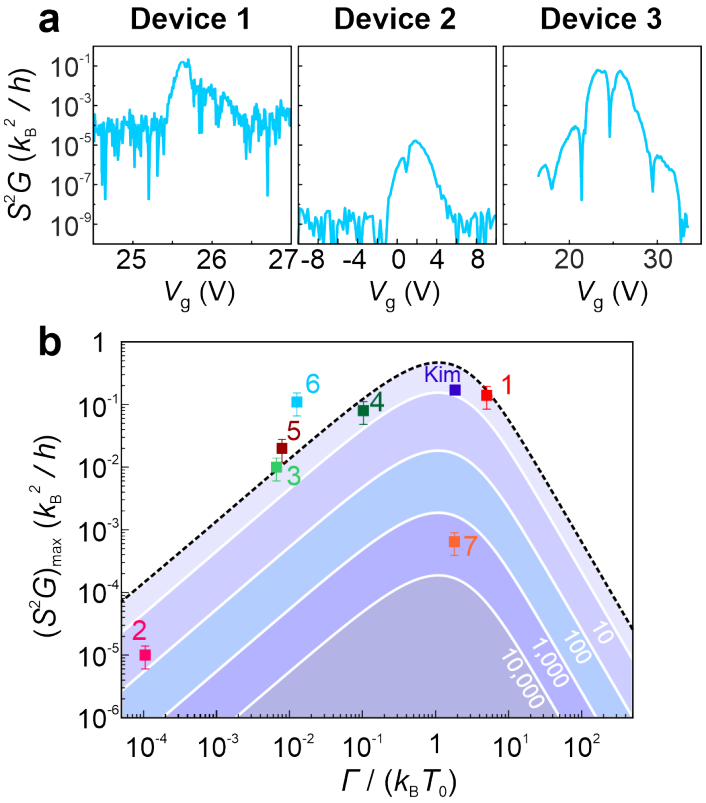


Figure 6.6 a) Back gate dependent power factor for devices 1-3 b) Maximum $\mathcal{P}$ as a function of the temperature normalized tunnel coupling $\Gamma/k_B T_0$ in a log-log plot. The devices measured in this study and Kim *et al.* [130] are indicated as squares with error bars stemming from the error propagation in ΔT discussed previously. The dashed black line and the white lines indicate theoretical powerfactors calculated using equation (6.9) and different ratios between the fast and slow tunnelling rates $\chi = \Gamma_{\text{fast}}/\Gamma_{\text{slow}}$, with the black line denoting $\chi = 1$.

Crucially, we find that $\mathcal{P}$ can be tuned over several orders of magnitude by the back gate to a maximum value of 0.01-0.14k_B^2/h (see Figure 6.6a and table 6.1). This

again highlights the importance of having full electrostatic control over the discrete molecular energy levels in order to optimize the device performance. The same is seen in the literature, where the maximum power factor in C_{60} molecules reported is orders of magnitude smaller for devices without electrostatic control [140, 135, 108] and comparable to the values found here for those with gate control [130].
To gain further insight into the experimental results, the maximum power factor of the devices studied here is plotted as a function of the temperature normalized with the tunnel coupling (Γ/k_BT_0) in a log-log plot (Figure 6.6). These values can then be compared to a theoretical maximum $\mathcal{P}$ calculated from

$$\mathcal{P} = S^2G = \frac{2}{hT_0^2}\frac{L_1^2}{L_0}\,. \tag{6.9}$$

In addition to the theoretical maximum for symmetrical coupling (black dashed line), we calculate the maximum for asymmetric coupling between the two leads (white lines). Since the couplings can be interchanged without changing the resulting transmission probability (see equation (6.6)) we define the asymmetry ratio between the tunneling rates χ in terms of a fast, $\Gamma_{\text{fast}} = \max(\Gamma_L,\Gamma_R)$, and slow, $\Gamma_{\text{slow}} = \min(\Gamma_L,\Gamma_R)$, tunnel coupling as $\chi = \Gamma_{\text{fast}}/\Gamma_{\text{slow}}$. The theoretical maximum power factors for different coupling ratios χ ranging from 10 to 10000 are plotted in Figure 6.6b as white lines. The maximum power factor with respect to the tunnel coupling is an insightful quantity since S and G are contra-indicated with respect to tunnel coupling, meaning a stronger coupling is expected to decrease the Seebeck coefficient and increase the conductance and vice versa for weaker coupling. We find that $\mathcal{P}_{\max}$ has a maximum as Γ approaches k_BT_0 of $\mathcal{P}_{\max} \approx \frac{1}{2.2}k_B^2/h$ at $\Gamma \approx 1.1\,k_BT_0$ and decreases exponentially on either side of this maximum. Three of the shown devices, that is device 1 and 7 as well as the device from Kim *et al.* [130], were measured close to this ideal temperature normalized gate coupling of $\Gamma \approx 1.1\,k_BT_0$. Device 1 and Kim *et al.* are consequently close to the theoretical maximum with relatively symmetric coupling to the leads of $\chi = 15$ at least for device 1. In contrast, device 7 is several orders of magnitude below the maximum value due to the highly asymmetric coupling of $\chi \approx 10^4$.
For the devices measured in the weak coupling regime, $\Gamma \ll k_BT_0$, a lower bound for the tunnel coupling can be written as $\Gamma_{\text{lower}} = 4k_BT_0\frac{2h}{\pi e^2}G_{\max}$ as can be deduced from the discussion above. For these devices, that is devices 2-6, we observe an increasing $\mathcal{P}_{\max}$ with increasing Γ_{lower} as would be expected since $\Gamma_{\text{lower}} \propto G_{\max}$.
No devices were measured in the strong coupling regime, where $\Gamma \gg k_BT_0$, but

as is shown in Figure 6.6b we would expect a decreasing maximum power factor with increasing tunnel coupling due to the reduction of the Seebeck coefficient with lifetime broadening.

Clearly asymmetry is affecting the power factor adversely. This happens due to the twofold impact of asymmetry on both the conductance and the energy dependent Seebeck coefficient, as is shown in Figure 6.7. In the weak coupling regime, $\Gamma \ll k_B T_0$, both the calculated energy dependent Seebeck coefficient and the factor $\frac{\Gamma_L \Gamma_R}{\Gamma_L + \Gamma_R}$, which is proportional to the conductance peak height, decrease substantially with increasing asymmetry. Apart from considerably reducing the power factor as we have seen previously, coupling asymmetry affects the basic electric and thermoelectric properties of the molecular junction and can reduce them by an order of magnitude.

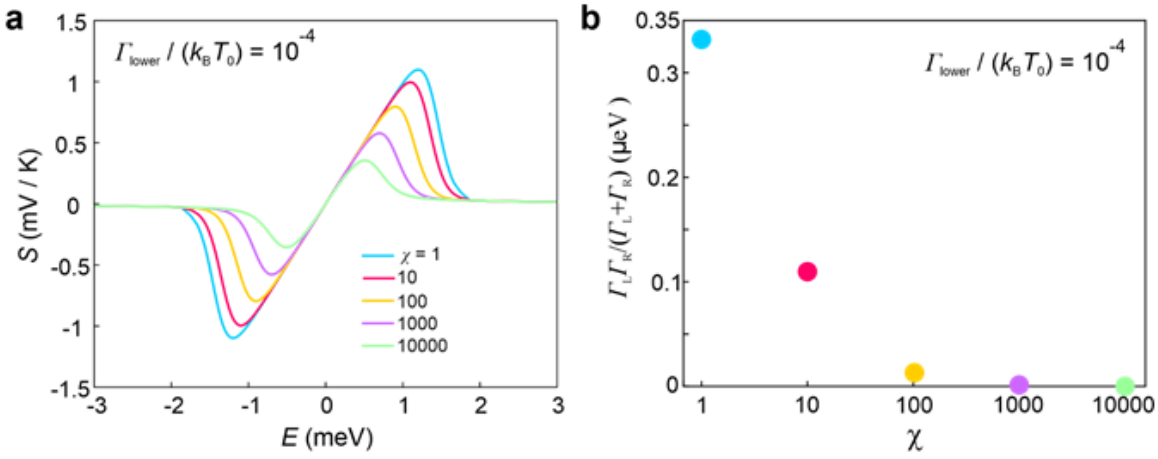


Figure 6.7 (a) Energy dependent Seebeck coefficient calculated for different coupling asymmetries χ (b) Influence of coupling asymmetry on the conductance peak height $G_{max} \propto \frac{\Gamma_L \Gamma_R}{\Gamma_L + \Gamma_R}$ for the same coupling asymmetries.

6.3 Conclusions

In this chapter, the thermoelectric properties of C_{60} fullerene molecules anchored between graphene contacts were studied. It was shown that the device structure lends itself well to studying molecular junctions as we were able to establish a temperature gradient across the junction and measure the gate dependent thermovoltage. The good control over the transmission of the molecule via a back gate enabled the focus on sharp, isolated resonance features and made it possible to achieve a power factor

that approaches the limit of a thermally and lifetime broadened Coulomb peak. In addition, from the findings described here, it is possible to make some recommendations to maximize thermoelectric performance in molecular nanodevices.
First, energetic control over the molecular energy levels needs to be achieved in order to align these with the Fermi levels of the electrodes as having the energy level of the electrodes close to the center of the transmission resonance maximizes the Seebeck coefficient. Secondly, the tunnel coupling strength Γ and the operating temperature T_0 should be such that thermal broadening is comparable to lifetime broadening $\Gamma \approx 1.1\, k_B T_0$. And lastly, the tunnel coupling to the left (Γ_L) and right (Γ_R) lead should be as symmetric as possible to maximise the power factor.
From the results, it is clear that a crucial factor in determining the thermoelectric properties in nanodevices is the tunnel coupling. Asymmetric coupling as well as a non-ideal operating temperature with respect to lifetime broadening can lead to order of magnitude changes in the Seebeck coefficient, the electrical conductance and as a result in the power factor. It is therefore clear that a more carefully designed study of the influence of coupling and other environmental factors on the power factor needs to be conducted. In the next chapter, graphene quantum dots are used to study the temperature dependence of the power factor and further understand the influence of the geometry and coupling on the thermoelectric properties of zero-dimensional nanodevices.

7

Thermoelectric Properties of Graphene Quantum Dots

This chapter is based on "Role of metallic leads and electronic degeneracies in thermoelectric power generation in quantum dots" by Achim Harzheim, Jakub K. Sowa, Jacob L. Swett, G. Andrew D. Briggs, Jan A. Mol, and Pascal Gehring published in *Phys. Rev. Research* **2020**, 2, 013140 [187]. The author contributions are as follows: PG and JAM conceived the study, AH and JLS fabricated the devices, JKS provided the theoretical framework, AH performed the measurements and analysed the results, AH, JKS, JAM and PG discussed the results, AH wrote the manuscript and all authors commented on the manuscript.

As we have seen in the previous chapter, various factors that can influence the thermoelectric properties of nanoelectronic devices are not yet well documented and understood. Characteristics such as the tunnel coupling asymmetry and strength can change the achievable power factor by orders of magnitude making it imperative to further study these effects. In the previous study on C_{60} molecules we were limited by being able to only measure at set temperatures as well as having to measure the electronic transport and thermoelectric properties separately and sequentially.
For the measurement of the GQDs, a parallel measuring scheme based on [188] is employed and the sample is loaded in a temperature controllable cryostat to investigate the temperature dependence of its thermoelectric characteristics. In addition, to simplify the measured system compared to the previous chapter (chapter 6), we now employ electroburned graphene quantum dots (GQD). These are fabricated by electroburning a graphene constriction until only a filament or island is left (see chapter 5), leading to Coulomb blockade and sequential transport at low tempera-

tures [178]. Rather than having to consider vibrational modes and HOMO/LUMO levels the GQDs are fully characterized by the size of the island and the resulting transport behaviour.
This allows us to now study the role of intrinsic properties of QDs such as the electron degeneracy and specific device characteristics such as the influence of the leads.
We find that the spin degeneracy of the QD states significantly impacts the zero-bias conductance and therefore the power factor and leads to an increase in the latter. Contrarily, non-ideal heat exchange through the leads can result in a suppression of the power factor around the charge degeneracy point and have a substantial influence on the temperature dependence.

7.1 Devices and Measurement Setup

As mentioned previously, QDs have been of interest to the thermoelectric community since Dresselhaus and Hicks predicted an unprecedented increase in efficiency with decreasing dimensionality [11, 10]. Recently, novel ways of exploiting the characteristics of QDs have resulted in high thermoelectric efficiencies, even almost reaching the Carnot limit [126, 128]. As seen in the last chapter, device characteristics such as tunnelling asymmetry can have profound influences on the Seebeck coefficient or the electrical conductance or both, in turn changing the power factor drastically. So far, only limited research has been conducted on intrinsic device features such as the heat exchange within the leads or the energy-level degeneracy. Similar to the previous chapter, the focus in characterising the thermoelectric properties of the device will be on the power factor since it gives a good indication of device performance while not requiring complex thermal conductance measurements. The devices used here are electroburned GQDs, which are explored in more detail in chapter 5. Electroburning regularly produces QDs with relatively high addition energies, making it possible to study well isolated energy levels (see Figure 7.1). The GQD graphene leads are connected to gold contacts and in order to create a temperature gradient an electric current is applied to a microheater near the source contact, thereby inducing Joule heating.
Both the thermovoltage V_{th} as a result of this temperature gradient and the electrical conductance G are measured simultaneously. This is crucial to avoid artificial offsets between the two measurement cycles that can be introduced by hysteresis effects, energy shifts in the device or temperature fluctuations in the cryostat. In order to

precisely determine the energy dependent power factor, which consists of G and V_{th}, any mismatch with regards to energy needs to be avoided as it can lead to wrong estimates of $\mathcal{P}$.
The two quantities are measured at different frequencies to avoid crosstalk. The conductance through the QD is determined by applying an AC voltage through a series resistor to the source contact at $\omega_1 = 91\,\text{Hz}$ and measuring the resulting voltage drop V_{co} with a Zurich Instrument MFLI lock-in amplifier. The heater current is applied at $\omega_2 = 17\,\text{Hz}$ to ensure sufficient thermalisation of the device and the thermovoltage drop between the two contacts is then probed at the second harmonic $2\omega_2$ using an SRS SR830 lock-in amplifier as discussed in chapter 5. The device measurement schematic is also depicted in Figure 7.1a. To avoid the error correction made necessary in chapter 6 due to a short heater, the heater is here designed to be substantially longer than the contacts, ensuring a homogenous temperature gradient.
For the device conductance, the device resistance R_{D} is the quantity of interest since the conductance is simply given by: $G = 1/R_{\text{D}}$. Then for the measurement setup shown in Figure 7.1a R_{D} is given by:

$$R_{\text{D}} = \frac{V_{\text{co}}}{I_{\text{co}}} = \frac{V_{\text{co}}}{V_{\text{exc}}/(R_0 + R_D)} = (R_0 + R_D)\frac{V_{\text{co}}}{V_{\text{exc}}} = \frac{R_0 V_{\text{co}}}{V_{\text{exc}} - V_{\text{co}}}\,,$$

where R_0 is the load resistor to source a current I_{co} by applying a known excitation voltage V_{exc} and V_{co} is the measured voltage across the GQD. From here, it is relatively straightforward to obtain the conductance $G = 1/R_{\text{D}}$ from the measured quantity V_{co} (if the applied voltage V_{exc} and the external resistance R_0 are known):

$$G = \frac{V_{\text{exc}} - V_{\text{co}}}{R_0 V_{\text{co}}} = \frac{V_{\text{exc}}}{R_0 V_{\text{co}}} - \frac{1}{R_0} = \frac{V_{\text{exc}}}{R_0 V_{\text{co}}} - G_{\text{c}}\,. \tag{7.1}$$

We note that the measured conductance is independent of the magnitude of the external resistor R_0 except for a known constant offset $G_{\text{c}} = 1/R_0$ that can be subtracted. It is therefore not necessary to use a resistor such that $R_0 \gg R_D$ to get an accurate relative measurement of the sample conductance. Here, a series resistance of $R_0 = 1\,\text{M}\Omega$ is used.

The second metric is the Seebeck coefficient, which, as introduced previously, is indirectly inferred from the thermovoltage measurement and the temperature difference across the device. While the thermovoltage is directly measured as described above and in chapter 5, the temperature difference between the gold contacts is obtained by a four-point resistance calibration [182]. To this end, an AC current is applied

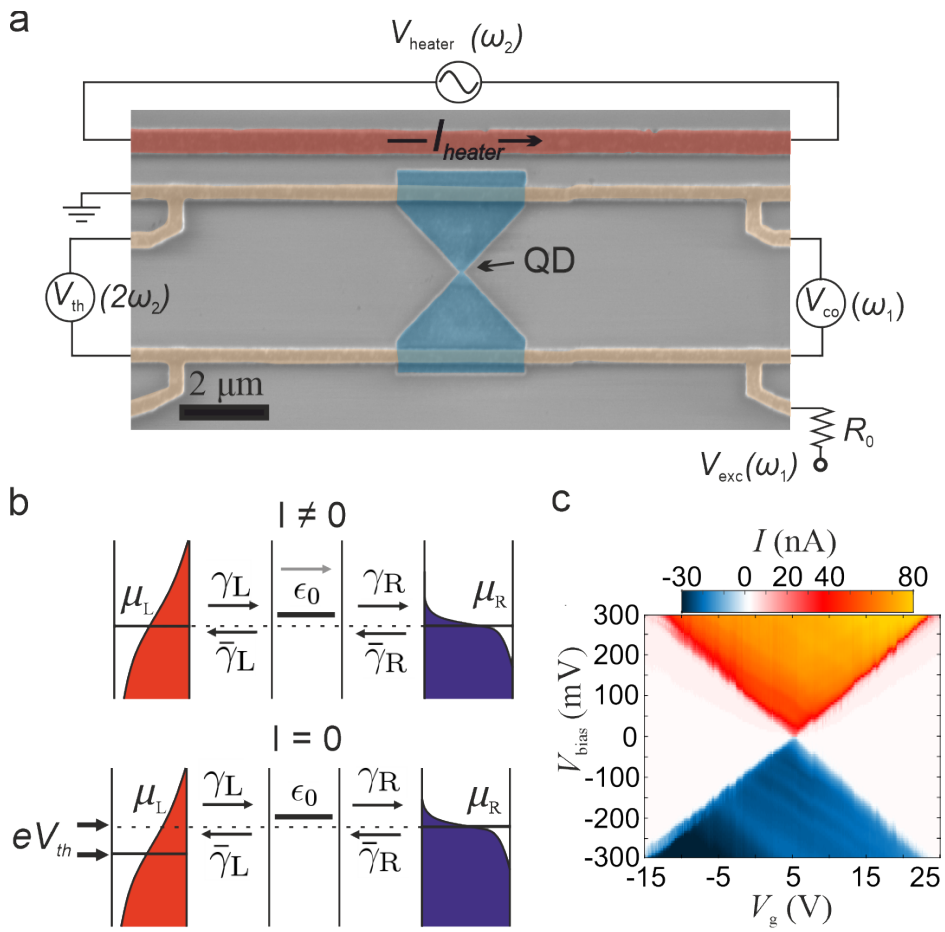


Figure 7.1 a) False-color SEM image of the quantum dot located within the graphene bow tie (blue) and connected via two gold contacts (yellow). The microheater placed next to the device is depicted in red and the measurement setup is schematically depicted. b) Energy diagram schematics of our device for a thermal bias causing a thermal current (top) and under open circuit conditions causing the build up of a thermovoltage (bottom). c) Stability diagram of a typical Device.

to each contact separately (sourced by the voltages V_{exc1} and V_{exc2} respectively) at frequencies ω_1 and ω_2, which are typically 17 Hz and 91 Hz (see Figure 7.2a). At the same time, the voltage response at those frequencies is probed with two separate lock-in amplifiers, enabling us to extract small resistance changes on the order of 0.3 Ω in each contact.

The resistance is monitored constantly as the temperature in the cryostat and the heating power through the micro heater are changed. As the heating power is changed from 0 to 2.3 mW, a considerable shift in the device resistance curve can be used to give an indication of how much each contact side heats up (see Figure 7.2b

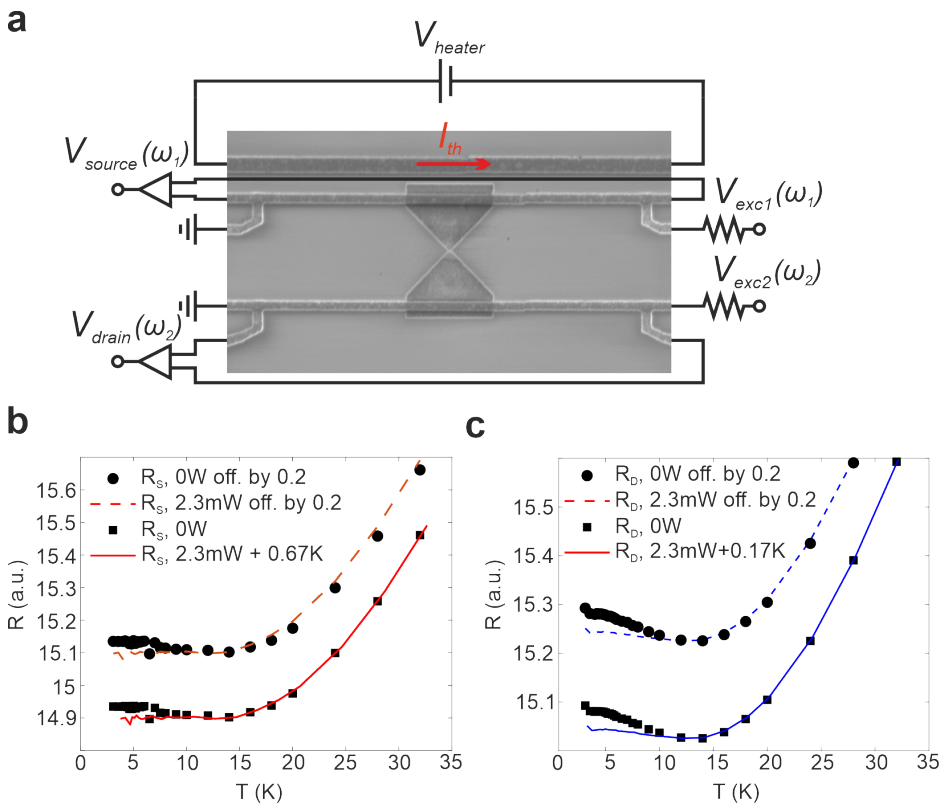


Figure 7.2 a) SEM image of the quantum dot device showing the contact calibration measurement schematics. b-c) Contact calibration for the source (b) and drain (c) contact. The measured resistance as a function of temperature at 0 mW heating power is shown by the dashed line while the resistance at 2.3 mW heating power is symbolized by the dots. Both curves are offset by 0.2 Ω for clarity. We then plot the 0 mW heating power curve (squares) overlaid with a shifted 2.3 mW curve, giving us the temperature increase due to Joule heating of the microheater.

and c). Due to the non-linear behaviour of gold at low temperature (<10 K), and its local resistance minimum at low temperature, the contact resistance calibration can be unreliable in this regime [189]. However, since the heating power stays constant at 2.3 mW we assume a constant temperature difference for all measurements, which is equal to the higher-temperature calibration value. At higher temperatures we obtain $(T_H - T_C) \approx 0.5 \pm 0.1\,\mathrm{K}$ which is also supported by the temperature difference $(T_H - T_C) = 0.52\,\mathrm{K}$ extracted from the thermovoltage measurements using a rate equation model outlined later in this chapter. In addition to the error introduced by Au's low temperature behaviour, local fluctuations in the cryostat temperature can add a random error source. Clearly, the temperature calibration is the biggest error source in the measurements with $\approx 20\,\%$ meaning we can neglect the measurement errors for G and V_{th} as they have a much smaller uncertainty [138]. Propagating the

error for the power factor $\Delta\mathcal{P}$ then gives

$$\Delta\mathcal{P} = \sqrt{\left(\frac{\partial\mathcal{P}}{\partial S}\Delta S\right)^2} = 2SG\Delta S = 2S^2G\frac{\Delta S}{S}\,, \tag{7.2}$$

where ΔS is the error in S.

7.2 Rate Equation Model

When a current is applied to the microheater, a temperature gradient along the device is established, broadening the Fermi distribution in the hot GQD lead (closer to the heater) compared to the cold GQD lead (further away from the heater). This induces a thermocurrent between the two contacts which in the open circuit measurement configuration used here results in a thermovoltage drop to nullify the thermocurrent (see Figure 7.1b). In order to model the weakly coupled GQD a RE approach is used as introduced in chapter 2 and previously in literature [78, 190]. Compared to the Landauer approach used in chapter 6, the RE model can account for electron degeneracy, which as we shall see later is crucial in modelling the temperature dependence of the conductance and power factor.
From equation 2.39 we can then write the current through the QD, I, as a combination of hopping on/off ($\gamma/\bar{\gamma}$) events from the left/right lead to and from the QD ($\gamma_\mathrm{L}/\gamma_\mathrm{R}$):

$$I = \frac{e}{\hbar}n_N n_{N+1}\frac{\gamma_\mathrm{L}\bar{\gamma}_\mathrm{R} - \gamma_\mathrm{R}\bar{\gamma}_\mathrm{L}}{n_{N+1}(\gamma_\mathrm{L}+\gamma_\mathrm{R}) + n_N(\bar{\gamma}_\mathrm{L}+\bar{\gamma}_\mathrm{R})}. \tag{7.3}$$

Here again, e is the electron charge, $\hbar$ is the reduced Planck constant and n_N and n_{N+1} are the degeneracies of the electronic ground states of the N and $N+1$ charge states, respectively. In addition, the hopping rates are given in equation 2.37 as $\overset{(-)}{\gamma}_l = 2\,\Gamma_l \int \frac{\mathrm{d}\epsilon}{2\pi} f_{\pm l}(\epsilon)K(\epsilon)$. For the measurements taken here only spin degeneracy needs to be taken into account, resulting in $n_\mathrm{N} = 1$ and $n_{\mathrm{N}+1} = 2$ as extracted from the temperature dependence of the conductance [184].
Similarly, we can derive an expression for heat transport through the dot, $\dot{Q}$, in the limit of small lifetime broadening ($\Gamma \to 0$) as done in equation 2.44 and arrive at

$$\dot{Q} = \frac{n_N n_{N+1}}{\hbar}\frac{\zeta_\mathrm{L}\bar{\gamma}_\mathrm{R} - \gamma_\mathrm{R}\bar{\zeta}_\mathrm{L}}{n_{N+1}(\gamma_\mathrm{L}+\gamma_\mathrm{R}) + n_N(\bar{\gamma}_\mathrm{L}+\bar{\gamma}_\mathrm{R})}\,.$$

The energy transfer rates $\overset{(-)}{\zeta}_l = 2\Gamma_l \int \frac{d\epsilon}{2\pi} f_{\pm l}(\epsilon)\epsilon K(\epsilon)$ are defined in the same manner as the charge transfer or hopping rates with respect to notation. Lifetime broadening is introduced in this model via the density of states

$$K(\epsilon) = \Gamma / [\Gamma^2 + (\epsilon - \epsilon_0)^2] \,, \tag{7.4}$$

with $\Gamma = (\Gamma_L + \Gamma_R)/2$.

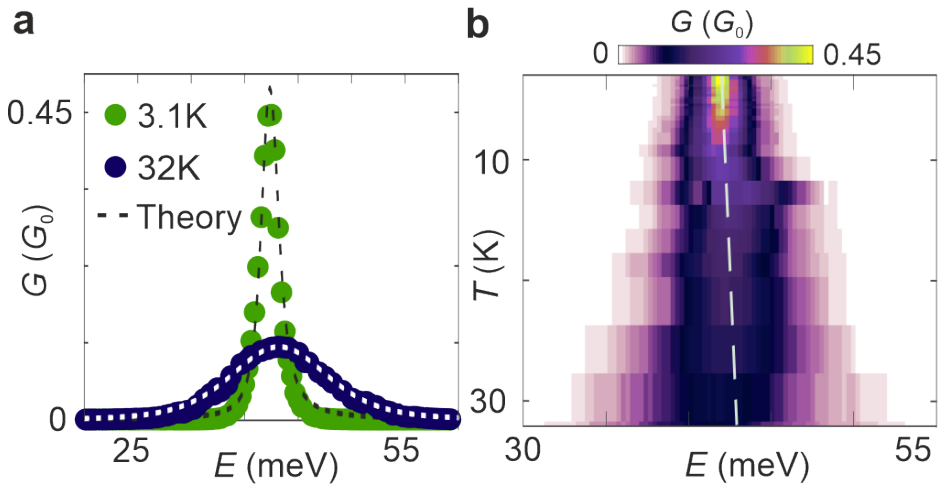


Figure 7.3 a) Conductance trace as a function of energy at 3.1 (green dots) and 32 K (purple dots) including RE fits (black and white dashed lines). b) Conductance peak as a function of temperature and energy including a RE fit (white dashed line).

Using the RE approach we can model the electrical conductance through the GQD. First, a lever arm of $\alpha = \frac{dE}{deV_g} = 7.9\,\mathrm{meV\,V^{-1}}$ is extracted from the stability diagram in Figure 7.1 and subsequently the zero-bias differential conductance $G = \frac{dI}{dV}\big|_{V=0}$ as a function of V_g at $T = 3.1$ K is fitted to obtain the tunnel couplings (see Figure 7.3a black dashed line).

As can be seen in Figure 7.3a, the conductance trace has a Lorentzian line shape, which is in accordance with the choice of the density of states and what is generally expected for a single-electron transistor [191]. The tunnel couplings obtained from the fit are $\Gamma_L \approx 0.2\,\mathrm{meV}$ and $\Gamma_R \approx 1.1\,\mathrm{meV}$.

Using these values it is possible to study the temperature dependence of the conductance, which is shown in Figure 7.3a and b. With increasing temperature the conductance peak amplitude decreases and the peak itself becomes broader. In addition, the whole conductance peak shifts to the right with higher tempera-

ture. This behaviour has been predicted theoretically by Beenakker [184] and is caused by entropy changes in the system [192]. Specifically, the shift is equal to $\Delta E_{\text{shift}}(G_{\text{max}}) \approx \frac{1}{2}\ln(2)k_{\text{B}}T$, where $\ln(2)k_{\text{B}}$ can be viewed as the entropy associated with populating a doubly degenerate electronic level. The experimental value of $\Delta E_{\text{shift}}(G_{\text{max}})$ is equivalent to both the theoretical prediction using the RE model and the value expected from Beenakker [184].
The shift with temperature is shown in Figure 7.3a and b, with the fit from the RE model indicated by the black/white dashed lines. The RE model is able to capture the temperature dependence of the conductance well, with the tunnel and gate coupling extracted from the low temperature measurement of the GQD. The good agreement between experimental and theoretical results confirms the validity of using a RE approach to model transport through the GQD.

7.3 Thermovoltage and Heat Flow Through the GQD

In a second step, the thermovoltage response of the GQD is considered as the micro-heater is excited at a frequency f_{exc}. V_{th} is measured in the usual 2ω configuration at the second harmonic $2f_{\text{exc}}$ as detailed in chapter 5. The thermovoltage response as a function of energy is shown in Figure 7.4. As the GQD energy level moves from below to above the charge neutrality point the sign of the thermovoltage changes from negative to positive in accordance with the Mott formula, indicating a change in transport carriers from holes to electrons [67, 73]. However, deviating from the Mott relation (which is essentially stating that $V_{\text{th}} \propto dG/dV_{\text{g}}$), the thermovoltage exhibits a wide suppressed region around the charge neutrality point where V_{th} is essentially zero. A second characteristic of the thermovoltage is the decrease of the amplitude by over an order of magnitude when moving from 3.1 K to 32 K which is the opposite effect of what would be expected from a single level model [182].

Both the suppression and the temperature response are attributed to non-ideal heat exchange within the leads. In this case the contact regions directly coupled to the GQD are at temperatures T_{L} and T_{R} respectively while the rest of the contact, the "hot" and "cold" reservoirs, are at temperatures T_{H} and T_{C}. The immediate contact regions and the reservoirs are not perfectly thermalised but rather are coupled (T_{L} to T_{H} and T_{R} to T_{C}) via a thermal conductance $\kappa(T)$ that includes both electrical and phononic heat transport. In addition, the left and right immediate contact regions

are not only electrically but also thermally coupled through the quantum dot by a temperature and gate dependent contribution $\kappa_{el}(\epsilon, T)$ and a phononic/substrate contribution $\kappa_{loss}(T)$. Here κ_{loss} accounts for both the phononic transport through the GQD and the substrate (SiO_2 on Si) and is only temperature dependent. This is summarized in the thermal circuit shown in Figure 7.4c. Since a perfectly thermalised contact is almost impossible we believe that such non-ideal heat exchange is prevalent in most thermoelectric zero-dimensional measurements even when the effects are not as extensive as in this study.

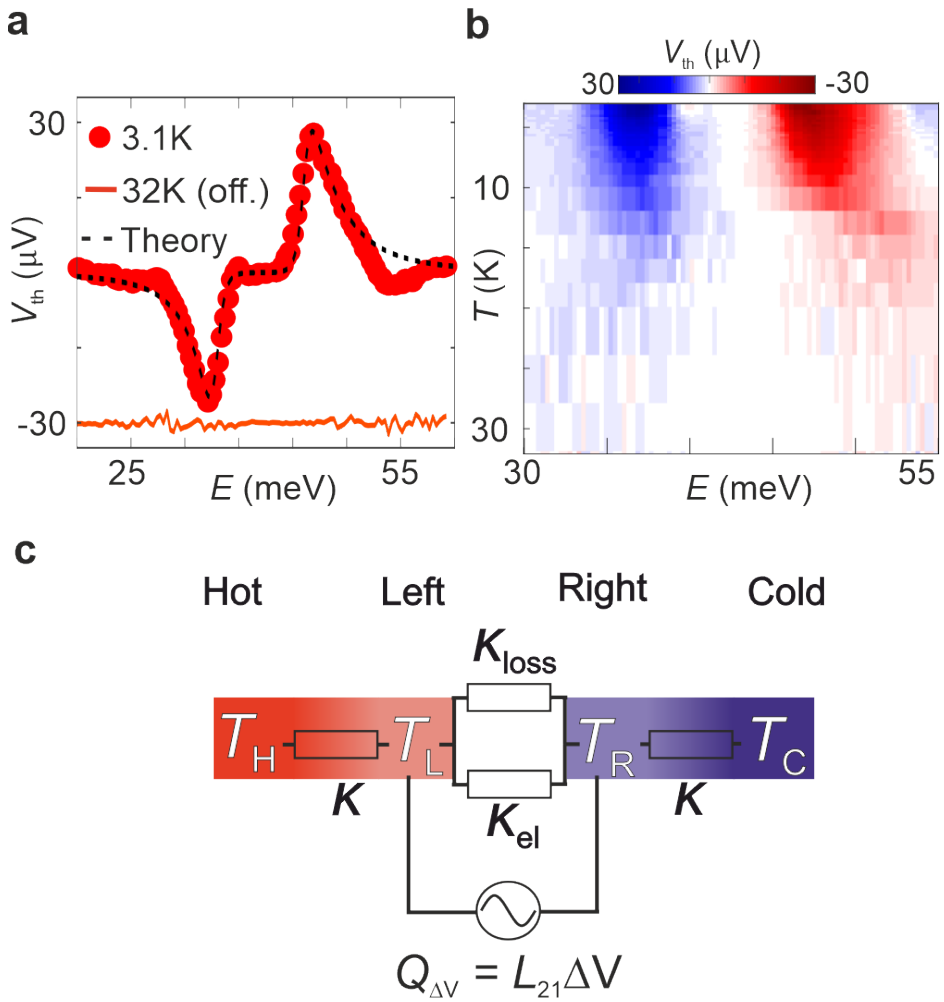


Figure 7.4 a) Thermovoltage trace as a function of energy at 3.1 (red dots) and 32 K (red line) including the RE fit at low temperature (black dashed line). The 32 K trace is offset by $-30\,\mu V$ for clarity. b) Thermovoltage as a function of temperature and energy. c) Thermal circuit diagram.

In the following we will develop a model for the thermovoltage through a QD with non-ideal heat exchanging contacts as well as accounting for the load resistance (R_Ω) and the inherent capacitance (C) of the system. This is done by first arriving at an expression for $\Delta T_{\text{effec}} = T_{\text{L}} - T_{\text{R}}$ to calculate the thermocurrent from equation (7.3) or (2.39). Finally, the open circuit thermovoltage is calculated using the approach in chapter 5, equation 5.5, which is the quantity measured.

In order to quantify κ_{el} and κ_{loss} and thereby ΔT, the heat and current flow through the GQD have to be considered. This is done by examining the Onsager matrix given in equation (2.45) as

$$\begin{bmatrix} I \\ \dot{Q} \end{bmatrix} = \begin{bmatrix} L_{11} & L_{12} \\ L_{21} & L_{22} \end{bmatrix} \cdot \begin{bmatrix} \Delta V \\ \Delta T \end{bmatrix} .$$

The thermal and electrical transport through the GQD is given by the Onsager modes L_{ij} can be calculated by expanding I and $\dot{Q}$ to the first order with respect to ΔT and ΔV:
First, we note that neglecting lifetime broadening enables us to write the charge transfer rates as

$$\gamma_{L/R} = \Gamma_{L/R} f_{L/R}(\epsilon_0) , \tag{7.5}$$

and

$$\bar{\gamma}_{L/R} = \Gamma_{L/R}[1 - f_{L/R}(\epsilon_0)] . \tag{7.6}$$

Now, assuming a bias voltage is applied only to the left lead and setting $n_N = 1$, $n_{N+1} = 2$, the expression for current can be simplified to:

$$I = \frac{e}{\hbar} \frac{2\Gamma_L \Gamma_R [f_L(\epsilon_0) - f_R(\epsilon_0)]}{\Gamma_L f_L(\epsilon_0) + \Gamma_R f_R(\epsilon_0) + \Gamma_L + \Gamma_R} . \tag{7.7}$$

To extract the mode L_{11} in Equation (7.3), we can expand I linearly as a function of ΔV which yields:

$$L_{11} = \frac{e^2 \Gamma_L \Gamma_R}{\Gamma_L + \Gamma_R} \frac{1}{k_{\text{B}} T (3 + 3\cosh(\epsilon_0 / k_{\text{B}} T) - \sinh(\epsilon_0 / k_{\text{B}} T))} . \tag{7.8}$$

To obtain L_{12}, we expand I to the first order with respect to ΔT. Since

$$\overset{(-)}{\gamma}_L(T + \Delta T) \approx \overset{(-)}{\gamma}_L(T) + 2\Gamma_L \frac{1}{2\pi} f'(\epsilon_0) \left[\mp \frac{\epsilon_0}{T} \right] \Delta T , \tag{7.9}$$

we obtain

$$L_{12} = \frac{e\Gamma_L\Gamma_R}{\Gamma_L+\Gamma_R}\frac{\epsilon_0}{(k_\mathrm{B}T)^2(3+3\cosh(\epsilon_0/k_\mathrm{B}T)-\sinh(\epsilon_0/k_\mathrm{B}T))}\,. \tag{7.10}$$

We can now again expand the heat flow (to the first order in ΔV and ΔT) analogously to what we have done for the electric current I. We set $\gamma_L \approx \gamma_L^0 + \gamma_L^V\Delta V$ and $\zeta_L \approx \zeta_L^0 + \zeta_L^V\Delta V$ yielding

$$\dot{Q} \approx \frac{n_{N+1}n_N}{\hbar}\frac{(\zeta_L^0+\zeta_L^V\Delta V)\bar{\gamma}_R-(\bar{\zeta}_L^0+\bar{\zeta}^V\Delta V)\gamma_R}{n_{N+1}\gamma_L^0+n_{N+1}\gamma_L^V\Delta V+n_{N+1}\gamma_R+n_N\bar{\gamma}_L^0+n_N\bar{\gamma}_L^V\Delta V+n_N\bar{\gamma}_R} \tag{7.11}$$

Then,

$$L_{21} = \frac{n_{N+1}n_N}{\hbar}\frac{\zeta_L^V\bar{\gamma}_R-\bar{\zeta}_L^V\gamma_R}{n_{N+1}\gamma_L^0+n_{N+1}\gamma_R+n_N\bar{\gamma}_L^0+n_N\bar{\gamma}_R} - \frac{n_{N+1}n_N(\zeta_L^0\bar{\gamma}_R-\bar{\zeta}_L^0\gamma_R)(n_{N+1}\gamma_L^V+n_N\bar{\gamma}_L^V)}{\hbar(n_{N+1}\gamma_L^0+n_{N+1}\gamma_R+n_N\bar{\gamma}_L^0+n_N\bar{\gamma}_R)^2}\,. \tag{7.12}$$

The second term on the right-hand side of Equation (7.12) vanishes in the limit of $\Delta V \to 0$, yielding the L_{21} mode as:

$$L_{21} = \frac{1}{\hbar}\frac{n_{N+1}n_N(\zeta_L^V\bar{\gamma}_R-\bar{\zeta}_L^V\gamma_R)}{n_{N+1}\gamma_L^0+n_{N+1}\gamma_R+n_N\bar{\gamma}_L^0+n_N\bar{\gamma}_R}\,. \tag{7.13}$$

Using the expressions for the energy transfer rates

$$\overset{(-)^V}{\zeta}_L = 2\Gamma_L\frac{1}{2\pi}f'(\epsilon_0)[\mp\epsilon_0]\,, \tag{7.14}$$

and taking $n_N = 1$ and $n_{N+1} = 2$, we can simplify L_{21} to:

$$L_{21} = \frac{e\Gamma_L\Gamma_R}{\Gamma_L+\Gamma_R}\frac{\epsilon_0}{(k_\mathrm{B}T)(3+3\cosh(\epsilon_0/k_\mathrm{B}T)-\sinh(\epsilon_0/k_\mathrm{B}T))}\,. \tag{7.15}$$

Finally, an analogous expansion can be performed to the first order in ΔT, where

$$\overset{(-)^{\Delta T}}{\zeta}_L = 2\Gamma_L\frac{1}{2\pi}f'(\epsilon_0)[\mp\frac{\epsilon_0}{T}]\epsilon_0\,. \tag{7.16}$$

Proceeding analogously to what we have done above, we obtain:

$$L_{22} = \frac{e\Gamma_L\Gamma_R}{\Gamma_L+\Gamma_R}\frac{\epsilon_0^2}{(k_\mathrm{B}T)^2(3+3\cosh(\epsilon_0/k_\mathrm{B}T)-\sinh(\epsilon_0/k_\mathrm{B}T))}\,. \tag{7.17}$$

We leave this operation understood. From the Onsager matrix we can see that the electrical contribution to the heat flow through the GQD is given by L_{22} since the term involving L_{21} can be neglected. This gives $\kappa_\mathrm{el} = L_{22}$.
Thermal transport through the GQD is energy dependent due to k_el and therefore off resonance k_loss is dominating ($\kappa_\mathrm{el} \ll \kappa_\mathrm{loss}$) for $|\epsilon_0| \gg \Gamma, k_\mathrm{B}T$. We can then derive the effective temperature gradient across the GQD from the thermal circuit in Figure 7.4c. The cumulative heat flow between the hot and cold reservoir is given by adding up all thermal conductances:

$$\dot{Q}_{HC} = \frac{1}{\frac{1}{\kappa}+\frac{1}{\kappa}+\frac{1}{\kappa_{loss}}}(T_H - T_C)\,. \tag{7.18}$$

The overall heat flow given above must be equal to the heat flow through the GQD between the right and the left lead, which far away from resonance is given by

$$\dot{Q}_{QD} = \kappa_{loss}(T_\mathrm{L} - T_\mathrm{R})\,. \tag{7.19}$$

Setting these heat flows equal $\dot{Q}_{HC} = \dot{Q}_{QD}$ gives

$$T_\mathrm{L} - T_\mathrm{R} = \frac{\kappa}{2\kappa_{loss}+\kappa}(T_H - T_C) = r_\kappa(T_H - T_C)\,. \tag{7.20}$$

For perfect heat exchanging contacts, where $\kappa_{loss} \ll \kappa$ the temperature difference between the two GQD leads is equal to the reservoir temperature difference $(T_\mathrm{L} - T_\mathrm{R}) \to (T_H - T_C)$ as there is no parasitic heat flow through the GQD. However, for $\kappa_{loss} \gg \kappa$, no temperature difference across the GQD can build up due to an efficient heat flow through the substrate.
Closer to the resonance we have to consider the energy dependent electrical contribution to the thermal flow as well. Using Kirchhoff's law for the thermal circuit shown in Figure 7.4d we can arrive at an expression for the heat currents in and out of the immediate contact region at temperatures T_L and T_R:

$$L_{21}\Delta V + \kappa(T_H - T_\mathrm{L}) + (\kappa_{el}+\kappa_{loss})(T_\mathrm{R} - T_\mathrm{L}) = 0\,; \tag{7.21}$$

and

$$-L_{21}\Delta V + \kappa(T_C - T_\mathrm{R}) + (\kappa_{el} + \kappa_{loss})(T_\mathrm{L} - T_\mathrm{R}) = 0. \tag{7.22}$$

Adding equation (7.21) to equation (7.22) gives

$$\kappa[T_H + T_C - (T_\mathrm{L} + T_\mathrm{R})] = 0,$$

which just implies $T_\mathrm{L} + T_\mathrm{R} = T_H + T_C$. When subtracting equation (7.22) from equation (7.21) we arrive at an expression for the temperature difference

$$2L_{21}\Delta V + \kappa[(T_H - T_C) - (T_\mathrm{L} - T_\mathrm{R})] - 2(\kappa_e + \kappa_{ph})(T_\mathrm{L} - T_\mathrm{R}) = 0. \tag{7.23}$$

As noted previously, $\kappa_\mathrm{e} = L_{22}$ for open circuit conditions. While we do apply a small AC current through the GQD to measure the conductance of the dot, this is applied at a considerably higher frequency than the thermoelectric measurements (91 Hz compared to 17 Hz). As a result, the current averages out to zero on the timescale of the thermovoltage measurements and $\kappa_\mathrm{e} \approx L_{22}$ is still valid. From equation 5.5 in chapter 5 the thermovoltage and thermocurrent in a realistic measurement circuit including a load resistance R_Ω and an inherent system capacitance C is given by

$$V_\mathrm{th} = \frac{I_\mathrm{th} R_\Omega}{\sqrt{(1 + GR_\Omega)^2 + (4\pi f R_\Omega C)^2}} = \beta I_\mathrm{th}\,. \tag{7.24}$$

Here G is the system's electrical conductance and f the measurement frequency. Plugging in V_th for ΔV in equation 7.23 with $I_\mathrm{th} \approx L_{12}$ and solving for $(T_\mathrm{L} - T_\mathrm{R})$ gives us the final expression for the temperature difference across the GQD

$$(T_\mathrm{L} - T_\mathrm{R}) = \frac{\kappa(T_H - T_C)}{\kappa + 2(L_{22} + \kappa_{ph}) + 2L_{21}L_{12}\beta}\,. \tag{7.25}$$

Here the electrical conductance G in β can be written as $G \approx L_{11}$ or calculated via complex step derivation from the measured signal. In addition, L_{12} and L_{21} are known from equation (7.10) and (7.13).
Using the energy dependent temperature difference we can then calculate a thermocurrent via the RE model given in equation (7.7). Since we measure a thermovoltage under open circuit conditions, we then find the voltage that nullifies the thermocurrent, which is the final modelled thermovoltage. Using this model we can fit the thermovoltage trace at 3.1 K shown in Figure 7.4a using the system capacitance C and the temperature difference between the reservoirs $T_\mathrm{H} - T_\mathrm{C}$ as fitting

parameters and holding $r_\kappa = 1$. The fit, which reproduces the experimental data well, gives $C \approx 3\,\mathrm{nF}$ and $T_\mathrm{H} - T_\mathrm{C} = 0.52\,\mathrm{K}$ which is in good agreement with the contact calibration giving $T_\mathrm{H} - T_\mathrm{C} = 0.5 \pm 0.1\,\mathrm{K}$.

The second effect in the thermovoltage is the relatively quick decrease of the amplitude with temperature. Even though this can not be explained with a single-level model using either a Landauer or RE approach, we note that a decreasing thermovoltage with increasing temperature is reported for nearly every measurement of zero-dimensional systems in the literature [121, 193, 117, 116]. While inverse relations between temperature and thermovoltage have been measured in metallic islands this is due to a continuum of energy levels which is not applicable here [194]. As can be seen in Figure 7.5a, the thermovoltage measured across the source and drain contact decreases starkly as we increase the temperature. We can model this behaviour well by fitting the thermovoltage at each temperature and extracting an r_κ, which essentially determines the effective temperature drop over the GQD, $T_\mathrm{L} - T_\mathrm{R}$ (see Figure 7.5b). Deviations between the experimental measurements and the theoretical fit, most noticeably around the charge degeneracy point, are attributed to the lack of lifetime broadening in the RE model as well as the high noise levels for higher temperature measurements. The resulting r_κ drops sharply with temperature which explains the similar behaviour of the thermovoltage as the two are connected through the effective temperature drop via equation (7.20). The connection is also illustrated in Figure 7.5c.

We attribute this effect to changes in the thermal conductances between the reservoirs and the GQD and across the GQD away from resonance, which is expressed in $r_\kappa = \kappa/(2\kappa_\mathrm{loss} + \kappa)$.

While the thermal conductances can not be studied directly here, this trend can be explained by a combination of the temperature dependent thermal conductances of the substrates and in graphene, which has non-linear characteristics [195] and exhibits size-dependent effects that are influenced by the geometry of the device [196, 197].

The thermal transport across the GQD away from resonance (where we can neglect any electrical contribution) is given by κ_loss, which is composed of the phononic transport through the dot and the thermal conductance through the Si/SiO_2 substrate. Here, the substrate, in particular the 300 µm of doped Si, is most likely dominating κ_loss. On the other hand, κ is given by the thermal conductance across the graphene-gold interface at the contacts and through the triangular graphene lead. While we can not probe the immediate vicinity of the GQD and its thermal con-

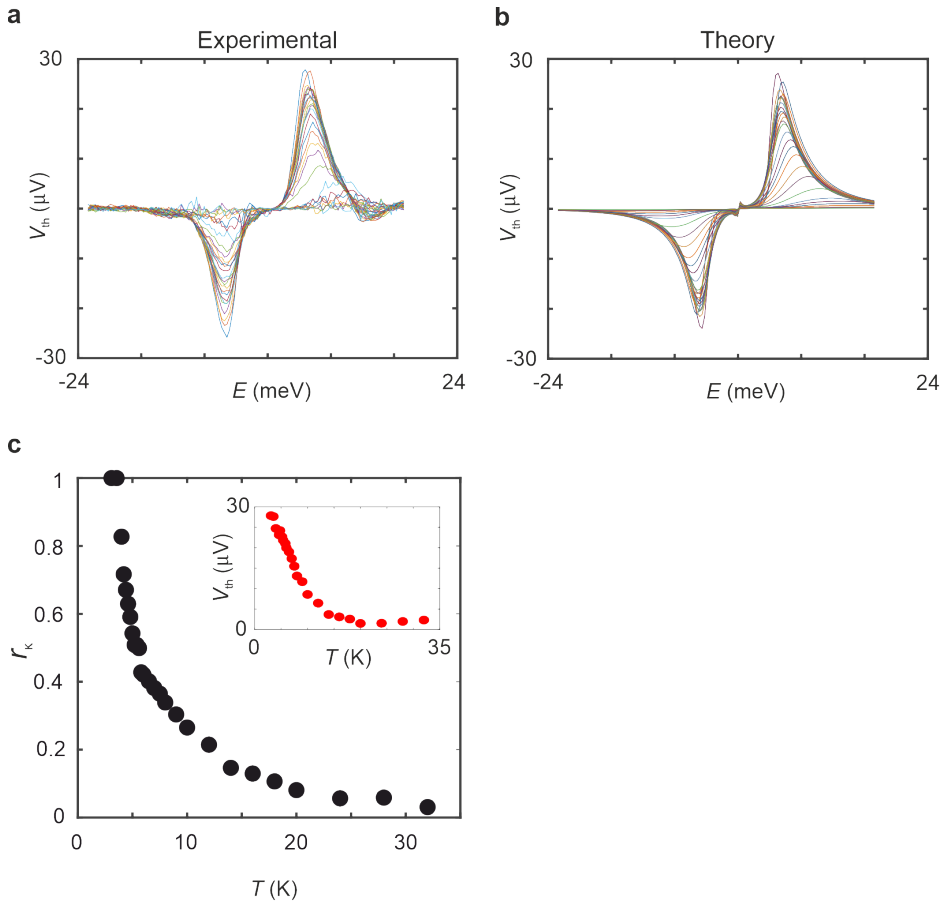


Figure 7.5 a) Energy dependent thermovoltage measurements at different T (3.1 - 32 K). b) Modelled energy dependent thermovoltages at different T (3.1 - 32 K). c) Ratio r_κ as a function of T. The inset shows the thermovoltage maximum amplitude as a function of temperature.

ductance and therefore cannot quantify the reasons for the temperature dependence of r_κ, it is crucial to note that the thermal conductance of the graphene electrodes can not be assumed to be equal to bulk graphene. As extensive research on graphene nanoribbons and other nanostructures has shown, the magnitude and temperature dependence of the thermal conductance in such structures depends on the exact geometry and other factors such as edge disorder [198–201, 92]. Since the leads most likely resemble graphene nanoribbons with edge defects introduced by electroburning and oxygen plasma patterning it is highly complex to quantify the thermal conductance of the graphene electrode. Yet, we note that a decreasing thermal conductance has been predicted for graphene nanoribbons with edge disorder [202]. More importantly though, as mentioned above, it is quite likely that the heat transport is dominated by substrate effects such that $\kappa_{\text{loss}} > \kappa$ leading to $r_\kappa \approx \kappa/2\kappa_{\text{loss}}$.

Over the studied temperature range the thermal conductance of Si increases by over an order of magnitude [203] and that of SiO_2 increases with temperature as well [204] though at a smaller rate than Si. Since $r_\kappa \approx \kappa/2\kappa_{\mathrm{loss}}$ this would result in a decrease of r_κ by over an order of magnitude as observed experimentally.
From this, we conclude that the overall temperature-dependence of r_κ is determined by the Si/SiO_2 substrate effects.
Independent of the effects discussed above, another factor influencing the line shape of the thermovoltage is the degeneracy of the relevant charge ground states. As has recently been reported, degeneracy can cause an asymmetry between the positive and negative peak of the thermovoltage [23].

7.4 Power Factor

After discussing the thermovoltage and conductance in detail and understanding the influence charge degeneracy as well as non-ideal heat conducting leads have on these quantities we now finally turn to the power factor. The power factor $\mathcal{P}$ can be extracted from the electrical conductance and thermovoltage measurements as $\mathcal{P} = S^2G = [V_{\mathrm{th}}/(T_{\mathrm{H}} - T_{\mathrm{C}})]^2 G$.
Figure 7.6a shows the power factor for G and V_{th} measured at 3.1 K, with $\Delta T \approx 0.52\,\mathrm{K}$. First, we observe a clear asymmetry of $\mathcal{P}$ with respect to the charge degeneracy point, which is caused by the shift of the conductance peak (V_{th} is always zero on resonance, independent of T). In addition, a strong reduction of the power factor around resonance can be seen, which is attributed to the corresponding suppression in V_{th} due to the influence of non-ideal heat exchanging contacts as discussed above. In order to show the impact of a degenerate compared to a non-degenerate GQD energy level on the power factor we calculate $\mathcal{P}$ with $n_N = 2$, $n_{N+1} = 1$ (degenerate GQD energy level) or $n_N = n_{N+1} = 1$ (non-degenerate GQD energy level), respectively, while holding all other parameters constant. The result is shown in Figure 7.6b and exhibits a good qualitative agreement with the experimental data for the degenerate case. The calculation makes it clear that the asymmetry observed in the measurements is most likely due to the electron degeneracy of the GQD and crucially shows that the power factor can be increased substantially by exploiting this effect.

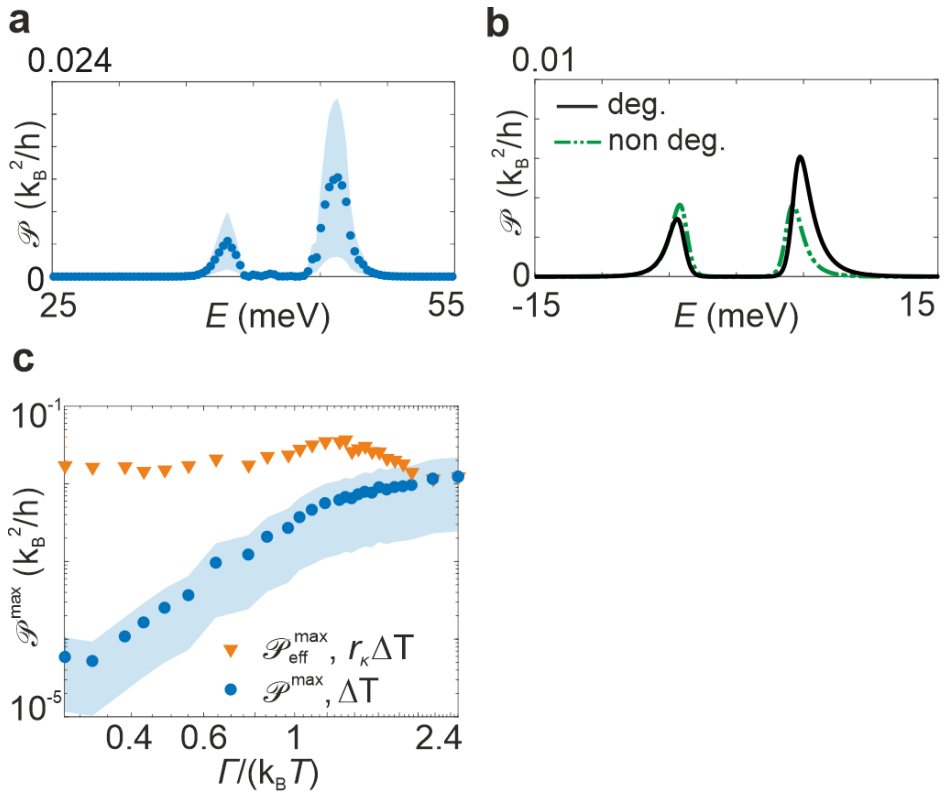


Figure 7.6 a) Experimental power factor as a function of energy at 3.1 K. b) Calculated power factor for a degenerate (black line) and non-degenerate (dot-dashed green line) energy level, holding all other parameters constant. c) Maximum power factor $\mathcal{P}^{\max}$ as a function of temperature and tunnel coupling. The blue dots show $\mathcal{P}^{\max}$ calculated with the temperature drop between the contacts (ΔT) and the orange triangles $\mathcal{P}^{\max}$ calculated with the effective temperature drop ($r_\kappa \Delta T$). In all plots $\Delta T \approx 0.52\,\mathrm{K}$ and the blue shading indicates the error bars due to the temperature uncertainty.

In the following we will study the temperature dependence of the power factor, which was one of the main motivations for this set of measurements as we aimed to establish the existence of a local power factor maximum with respect to T and Γ. Previously in chapter 6, we were able to calculate the position of this local maximum as $\Gamma \approx 1.1\, k_\mathrm{B} T$, however the experimental evidence for its exact shape was unsatisfactory. This proposed local maximum should exist as a result of the interplay between S and G which increase and decrease with higher $k_\mathrm{B}T/\Gamma$, respectively. While a small deviation from the calculated theoretical maximum is expected due to the degenerate nature of the GQD and the influence of the non-ideal contacts, the overall shape of the curve should be visible. Yet, we do not find that trend in the experimental data (see Figure 7.6c blue dots) due to the decrease of the

thermovoltage with increasing temperature (Figure 7.5c inset). Instead, the power factor just decreases with increasing temperature.

However, if we replace the calibrated (and assumed to be operating temperature

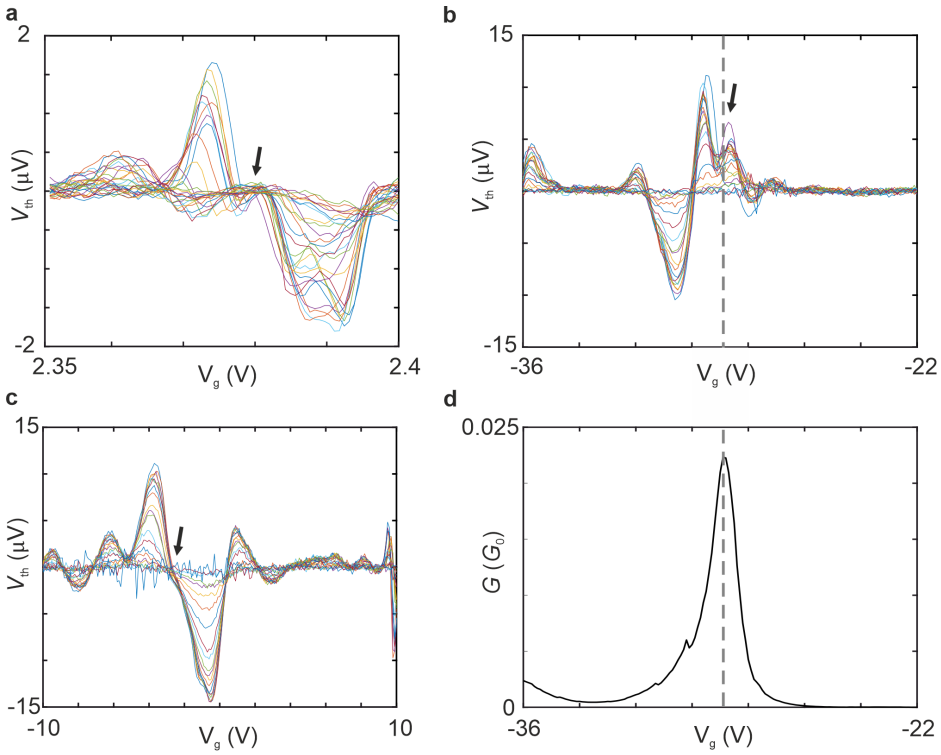


Figure 7.7 a-c) Additional measurements of the gate-dependent thermovoltage for three additional devices at operating temperatures ranging from 30 mK to 1800 mK (a) and 4.5 K to 32 K (b+c). d) Conductance trace measured at 4.5 K and simultaneously to the thermovoltage in b. The black arrows indicate the position of the simultaneously measured conductance peak and therefore the suppression in the thermovoltage traces. The temperature difference is $T_H - T_C \approx 0.52$ K for all measurements.

independent) temperature difference $T_H - T_C$ with the effective one extracted from the thermovoltage fits $T_L - T_R$ (see section 7.3) the expected curve is recovered. As can be seen in Figure 7.6c (orange triangles), $\mathcal{P}_{\text{eff}}^{\text{max}}$ reaches a maximum at $\Gamma \approx 1.3 k_B T$ in relatively good agreement with the theoretical predictions. In addition, the predicted shape of the curve is retrieved with the effective maximum power factor decreasing for a higher/lower $\Gamma/k_B T$ compared to the local maximum. The effect is slightly blurred out at high T due to the high level of noise with respect to the signal in the thermovoltage measurement at these temperatures.

The suppression of the thermovoltage around resonance as well as the decreasing

thermovoltage with increasing temperature is found for multiple other devices, as shown in Figure 7.7.

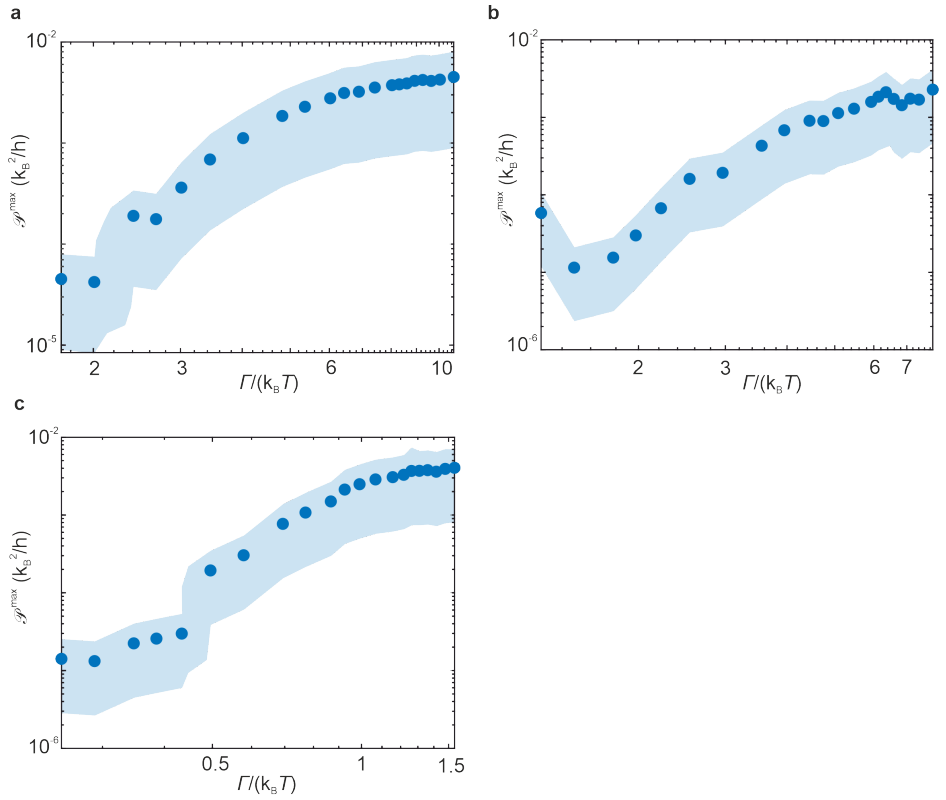


Figure 7.8 a-c)Additional experimental measurements of the maximum power factor for three different devices between 4.5 to 32 K with respective coupling strengths of $\Gamma \approx 4.1\,\mathrm{meV}$ (a), $\Gamma \approx 3\,\mathrm{meV}$ (b) and $\Gamma \approx 0.6\,\mathrm{meV}$ (c). The temperature difference is $T_\mathrm{H} - T_\mathrm{C} \approx 0.52$ K for all measurements.

While the suppression ranges from quite pronounced (Figure 7.7a) to an only light suppression resulting in a slightly flatter lineshape (Figure 7.7c) some degree of reduction or modification from a smooth shape (as expected from a simple Mott formula approach) is visible for all devices included in this study. Interestingly, for the device in Figure 7.7b no suppression on resonance is visible. However, to the right of the zero-crossing a dip in the thermovoltage is observed, which coincides with the peak maximum of the simultaneously measured conductance. This indicates that it is the energy dependent heat drop through the QD due to κ_el that causes this dip in the thermovoltage.
Crucially, for all the shown devices and thermovoltage traces, a decreasing power factor with increasing temperature is observed, even for a less pronounced suppression of the thermovoltage (see Figure 7.8). In addition, the behaviour is observed for

a variety of tunnel couplings (0.6 to 4.1 meV) and is well reproducible. As discussed previously, the high temperature values of the maximum power factor are not very reliable as the thermovoltage at this point approaches the noise level and therefore the power factor is prone to errors.
All of the above suggests that the decreasing power factor with increasing temperature, which we attribute to non-ideal heat-exchanging, is a persistent effect that has to be taken into consideration when optimizing or quantifying the efficiency of a QD thermoelectric generator.

7.5 Conclusions

In this chapter, the influence of non-ideal contacts and electronic degeneracy on the thermoelectric properties of electroburned GQDs was investigated by a temperature and energy dependent simultaneous measurement of the electrical conductance and thermovoltage. All results were observed in multiple devices and are supported by a RE model that successfully captures all phenomena.
We have shown that a degenerate GQD energy level causes a temperature dependent shift of the conductance peak compared to a non-degenerate level. This in turn gives rise to an asymmetric and enhanced power factor, a result that can potentially be used to engineer and optimize the power factor in zero-dimensional structures. On the contrary, non-ideal heat exchanging contacts and heat flow through the GQD were observed to have a detrimental impact on the measured thermovoltage. Specifically, an efficient electronic heat transport across the GQD leads to a suppression of V_{th} around resonance. In addition, the impact of the temperature dependent thermal conductance of the substrate results in a decreasing effective temperature gradient over the GQD and therefore a decreasing thermovoltage with increasing temperature. The suppression of the thermovoltage in turn leads to a suppressed power factor in the vicinity of the charge degeneracy point and causes the local optimum of the power factor that naturally arises due to the nature of S and G to disappear. While the described effects might not always be as noticeable as they are in this study (most probably due to the device structure including triangular graphene leads) they are likely ubiquitous in low dimensional thermoelectric devices.
The results therefore present an important step in understanding phenomena governing heat-to-energy conversion in zero-dimensional devices and open a pathway to improved engineering of efficient devices with a high thermoelectric power factor.

While the main goal of this study was reached, that is mapping out the power factor with respect to Γ/k_BT, the results present further evidence that measurements of zero-dimensional thermoelectric properties are strongly influenced by environmental as well as device intrinsic characteristics. In chapter 6 we have seen evidence that the tunnel coupling with respect to the temperature but also its symmetry are crucial in determining the size of the power factor and can lead to order of magnitude differences. This result is experimentally confirmed here but in addition we have seen how non-ideal heat exchanging contacts can also have an outsized influence on the power factor, again drastically changing the amplitude in addition to the line shape. Furthermore, the electron degeneracy of the energy levels has to be taken into account when analysing thermoelectric measurements in zero-dimensional structures.

Though these results are somewhat discouraging with regards to achieving reproducible measurement conditions for molecular thermoelectric generators they are simultaneously exciting as they show that a whole world of effects has not been considered yet. These can be used to engineer the power factor and improve on previous results for the efficiency of zero-dimensional and molecular thermogenerators. In addition, it is clear that thermal transport on the nanometre scale, which is crucial for future electronic developments, has not been fully grasped yet.

As we have seen, the structure of the leads in the device has a pronounced effect on its thermoelectric characteristics. Yet it is difficult to understand and quantify these and possibly other influences in a global measurement setup. In order to extract information about local thermoelectric characteristics an SThM technique will be used in the next two chapters. In the remainder of the thesis we will study the thermoelectric properties of geometrically engineered graphene nanostructures (such as the triangular graphene leads used here).

8

Geometry Dependent Thermoelectric Effects in Graphene

This chapter is based on "Geometrically Enhanced Thermoelectric Effects in Graphene Nanoconstrictions" by Achim Harzheim, Jean Spiece, Charalambos Evangeli, Edward McCann, Vladimir Falko, Yuewen Sheng, Jamie H. Warner, G. Andrew D. Briggs, Jan A. Mol, Pascal Gehring and Oleg V. Kolosov published in *Nano Lett.* **2018**, 18, 12, 7719-7725 [205]. The author contributions are as follows: PG and OVK conceived the study, YS and JHW provided the CVD grown graphene, AH fabricated the devices, PG, AH, JS and CE performed the measurements, AH, JS, CE, EM, VF, JAM, PG and OVK discussed the results, EM derived the theoretical framework, JS performed the COMSOL calculations, AH wrote the manuscript and all authors commented on the manuscript.

As we have seen in chapters 6 and 7, reducing dimensionality has a profound effect on the thermoelectric properties of nanodevices. Crucially, not only the intrinsic device characteristics but also the device environment plays a role in determining the Seebeck coefficient and the power factor. From the previous chapters it is clear that the bow tie device geometry has an effect on device performance due to its non-ideal heat conduction, however the constriction by itself can also have a more direct influence. Recently interest into such classical confinement has developed [206, 207], revealing that local defects and constrictions can cause a variety of thermoelectric effects. Yet, in order to fully characterize the graphene bow ties it is necessary to study the local rather than global thermoelectric properties. While it is possible to use scanning laser setups for this, they can introduce undesirable optical effects, only enable Seebeck measurements and tend to have a large spot size on the order of

µm. Instead, a Scanning Thermal Microscopy (SThM) setup is used, which enables the local probing of both the Seebeck and Peltier effect with a resolution of tens of nanometres. Compared to the Seebeck effect its Onsager reciprocal, the Peltier effect, has not received much experimental attention despite its obvious appeal for thermal management applications. The main reason for the lacklustre interest in the Peltier effect in general is due to the complexity of measuring small temperature gradients locally. In this chapter, the local thermoelectric properties of graphene bow ties and other nanostructures are studied. The aim of this chapter is to both better understand the geometrical implications of the current device structure used in the previous chapters as well as generally study the thermoelectric behaviour of patterned graphene locally in the presence of a heat source or when applying a current.

8.1 SThM Measurement Configurations

The measurements are performed using an SThM as introduced in chapter 5. All measurements are performed in a high vacuum environment to eliminate parasitic heat transfer between the tip and the sample caused by conduction and convection. The resolution of the measurements is limited by the extent of the tip-sample contact which is on the order of tens of nanometres. Importantly, we use two different measurement modes, making it possible to map the Seebeck effect with one approach and Joule heating and the Peltier effect simultaneously using the other (see Figure 8.1). Before the measurements, the SThM probe's electrical resistance as a function of temperature and the probe temperature due to self-heating are calibrated [167]. In this way we can quantify the thermal resistance of the cantilever R_p which is between 6×10^4 and $1.2 \times 10^5\,\mathrm{K\,W^{-1}}$ for all probes used. In the following we will introduce the two measurement methods.

First, to probe the Seebeck effect, an AC voltage of $V_\mathrm{heater} \approx 2.24\,\mathrm{V_{pp}}$ is applied to the SThM tip at a frequency $f = \omega_\mathrm{th} = 57\,\mathrm{Hz}$, which ensures full equilibrium within the probe and sample for each AC cycle. This causes a Joule heating modulation in the SThM resistor resulting in an excess temperature of about 60 K. However, we are interested in the tip-sample contact temperature increase, which can be deduced by considering the thermal resistance of the probe and the spreading resistance of

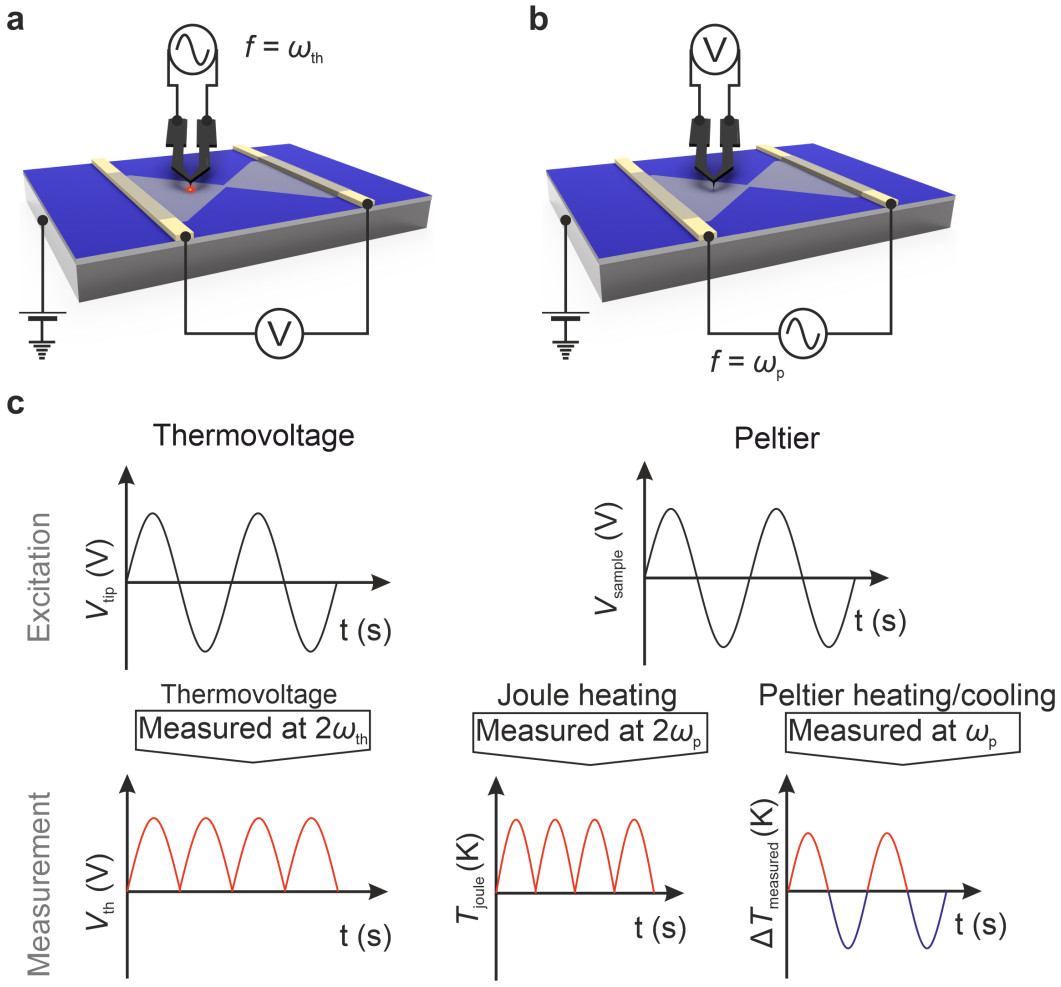


Figure 8.1 a) Schematic of the setup for the thermovoltage measurement where a hot tip is scanned over the sample and the global voltage drop is recorded. b) Schematic of the setup for the Peltier measurement where the sample is excited with a current and the SThM is scanned over the sample recording the temperature. c) Voltage excitation and signal response for the two respective measurement configurations. Left, the tip is excited with an AC voltage and the thermovoltage is measured at the second harmonic. Right, the sample is excited with an AC voltage and then the Peltier response is measured at the same frequency simultaneously to the Joule heating response measured at the second harmonic.

the sample (estimated theoretically in [208, 209]), giving

$$\Delta T \approx 18 \pm 2\,\mathrm{K}\,. \tag{8.1}$$

This heated tip is then scanned over the sample as the global thermovoltage drop over the device is recorded with an SRS 560 voltage preamplifier and demodulated

at the second harmonic ($2\omega_{\text{th}}$) using an SRS SR830 lock-in amplifier, resulting in a thermovoltage map of the device (see Figure 8.1a). This measurement does not require electrical contact between the tip and the sample, compared to previously reported methods [210], and therefore eliminates uncertainties associated with the electrical tip-sample contact strength.
For the Peltier measurement, the SThM is used in a more conventional way, that is to probe the local temperature. To this end, we apply an AC voltage at a frequency $f = \omega_{\text{p}} = 17\,\text{Hz}$ to the device through the global contacts as shown in Figure 8.1b and Figure 8.2. At the same time, an AC voltage at a high frequency with a DC offset is applied to the SThM tip. Here, the DC offset heats up the probe, which when brought into contact with the sample then heats up/cools down depending on the change of heat flux to the sample [211]. This method developed by Menges *et al.* allows the simultaneous measurement of the Peltier effect and Joule heating while making it possible to eliminate probe-sample contact variations that can lead to artefacts [165]. A corrected temperature map is calculated by taking into account both the AC (ΔV_{AC}) and DC (ΔV_{DC}) component of the SThM signal measured which is the variation with respect to the AC driven sample excitation and the time averaged sensor signal respectively. Then the temperature change of the sample is given by

$$\Delta T_{\text{sample}} = \Delta T_{\text{sensor0}} \frac{\Delta V_{\text{AC}}}{\Delta V_{\text{AC}} - \Delta V_{\text{DC}}}\,, \tag{8.2}$$

where $\Delta T_{\text{sensor0}}$ is the temperature of the probe before contacting the sample. The variation in probe heater temperature is detected via the AC component ΔV_{AC} as the SThM tip is scanned over the sample (see Figure 8.2). This signal is simultaneously demodulated using two SRS SR830 lock-in amplifiers at the second harmonic ($2\omega_{\text{p}}$) to capture the Joule heating and at the first harmonic ω_{p} to probe the Peltier heating (cooling).
In addition, for both measurements, the force between the sample and the probe is kept constant by using a standard AFM feedback loop, which enables us to always obtain a height profile of the sample for both the Peltier and thermovoltage scan [164].

The samples are made by transferring single layer or multilayer CVD graphene onto a Si/SiO_2 chip with pre-patterned Cr/Au contacts which was subsequently patterned and etched into the different geometries via EBL and oxygen plasma etching, respectively (see chapter 4).

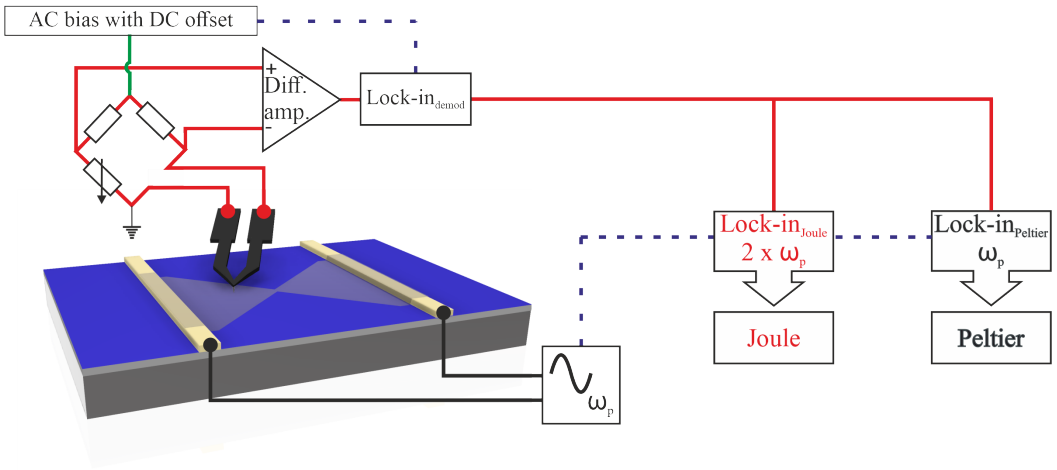


Figure 8.2 Nanoscale mapping of the Peltier effect in graphene nanoconstrictions. An AC voltage bias Vbias at ω_p induces an AC I_{bias} through the constriction (black lines). In addition, a low AC bias with a DC offset is applied to the SThM tip through a Wheatstone bridge (magenta line). During scanning, the resulting signal in the tip (red lines) is demodulated at the respective frequency. The resulting thermal signal is then again demodulated at the first (ω_p) and second ($2\omega_p$) harmonic, probing the Peltier heating (cooling) and Joule heating, respectively. The blue dashed lines symbolize the reference signal lines.

8.2 Experimental Results

A Peltier heating (cooling), Joule heating and topography map for a typical bow tie device are shown in Figure 8.3. It is important to note here, that the Peltier signal is the measured amplitude multiplied by the sign of the phase signal. Therefore it represents the temperature at a certain phase at the maximum applied modulation voltage. Crucially, no Peltier heating (cooling) is taking place for a time average over multiple cycles of the AC current [165].

Both the Peltier and the Joule map show a high spatial signal dependence, with a strong response from the graphene around the constriction. The Joule heating is highest inside the constriction, leading to a temperature increase around the narrowest bit of the bow tie by about 5 K, which gets less strong the further away from the constriction we move. This is expected as the local current density increases for a thinning graphene strip [212].

The butterfly like Peltier signal, which is positive on one side of the constriction and negative on the other side, indicating a heating (cooling) effect, in contrast is not as easily explained. Since the bow tie is made from graphene, a single material,

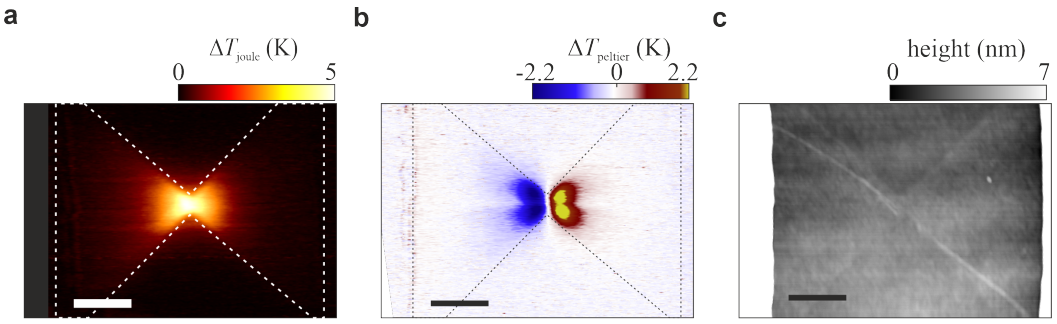


Figure 8.3 Simultaneous measurement of the Peltier effect, Joule heating and topography. a) Joule heating map, showing the hot spot in the middle of the constriction. b) Peltier effect map showing the main heating (cooling) effects around the constriction. c) Simultaneously recorded height map used to outline the position of the constriction in the Peltier heating (cooling) and Joule heating images. In panels b and c, the dashed-dotted lines indicate the contact position and the dashed line the outline of the graphene constriction. All scale bars are 1 µm.

no Peltier junction is created and we would predict only a Peltier signal at the Au contacts as the material and therefore the Seebeck and Peltier coefficient change [97]. While there is some signal around the contacts, which can be explained by a Peltier junction formed between gold and graphene [213], the Peltier signal is at least an order of magnitude stronger and much more prominent in the graphene bow tie. As can be seen in Figure 8.3b, the Peltier signal outlines the bow tie constriction, exhibiting cooling (heating) on the left (right) side of the constriction and a node in the middle of it. The signal is broadened out around the edges due to heat spreading into the substrate. This can be assumed to be the main heat sink as heat dissipation into the device in areas with and without graphene differs by less than 5 % in accordance with previous findings [167]. For the measurement shown in Figure 8.3b, a current of $I_{\text{bias}} = 90\,\text{mA}$ was applied which leads to heating (cooling) by about 2.2 K on either side of the constriction.

A similar signal to the Peltier measurement was found for the thermovoltage measurement of the bow tie shown in Figure 8.4a, with a positive thermovoltage on the left side of the constriction and a negative on the right side, separated by a node in the middle of the bow tie. This open-circuit condition measurement suggests that the signal stems from a changed local Seebeck coefficient around the constriction rather than a current induced effect. In addition, we perform a "DC Peltier measurement" to rule out phase effects or accidental phase errors by measuring the bow tie with a positive and a negative square wave applied and subsequently subtracting the two resulting temperature maps (see Figure 8.4b). The DC Peltier map shows the

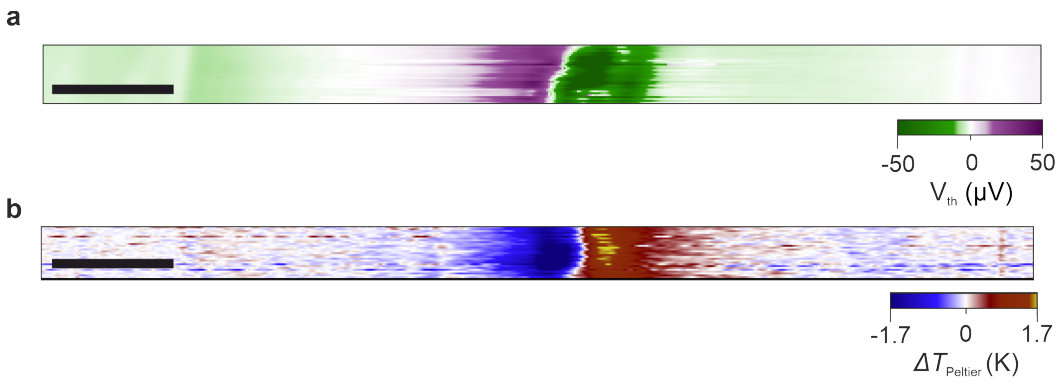


Figure 8.4 Mapping of the thermovoltage and DC Peltier effect in a graphene nanoconstriction. a) Thermovoltage measurement of a bow tie junction. b) DC Peltier measurement of a bow tie junction. The image is created by subtracting two maps measured with opposite sign square waves applied. The scale bars denote 500 nm.

same heating (cooling) distribution as the AC measurements, again suggesting that an intrinsic effect is causing the Peltier signal. While we studied both few-layer and single layer graphene bow ties, no discernable difference could be extracted in their behaviour with both showing the characteristic bipolar Peltier/thermovoltage signal, respectively. A certain spread in the amplitude of the heating (cooling) or thermovoltage and the strength of the asymmetry between the left and the right side of the bow tie was observed independently of the graphene thickness.

8.3 Modelling of the Electron Mean Free Path

A geometric dependency of the Seebeck coefficient similar to what we observe has been reported previously for metallic thin-film strips and Au nanowires, where the signal was explained by a reduced electron mean free path (EMFP) due to defects and grain boundaries in the metal. In graphene the EMFP at room temperature is much larger than in metals and typically on the order of hundreds of nanometres [90]. Here we believe that it is substantially reduced by defect potentials stemming from the edges of the device as observed previously [214], which were created by the patterning of the sample via oxygen plasma etching. The reduction in the EMFP can be as high as 80 % for edge defects [142].
In order to support this hypothesis and model the drop of the Seebeck coefficient caused by the decrease of the EMFP, we develop a theory for a geometry dependent S. We start by defining the electrical current density (j) in the linear response regime

due to an electric field (E) and a temperature gradient (ΔT):

$$j = \sigma E - \sigma S \Delta T \,, \tag{8.3}$$

where σ is the electrical conductivity. Considering only the current along the x-axis where $E = -dV/dx$ gives

$$j_x = -\sigma \frac{dV}{dx} - \sigma S \frac{dT}{dx} \,. \tag{8.4}$$

We can then calculate the spatial dependence of S by considering how the resistance of a graphene strip changes with varying width. From the diffusive conductance of a rectangular graphene strip $G_d = \frac{2e^2}{h} k_F l \frac{W}{L} = 1/R$ we can calculate the respective resistance, where k_F is the Fermi wave number, l the mean free path, L device length and W the device width. In a bow tie configuration, the graphene strip width varies along the length of the device and the maximum width is given by $Y = 2t + W$, where W is the minimum width (see Figure 8.5).

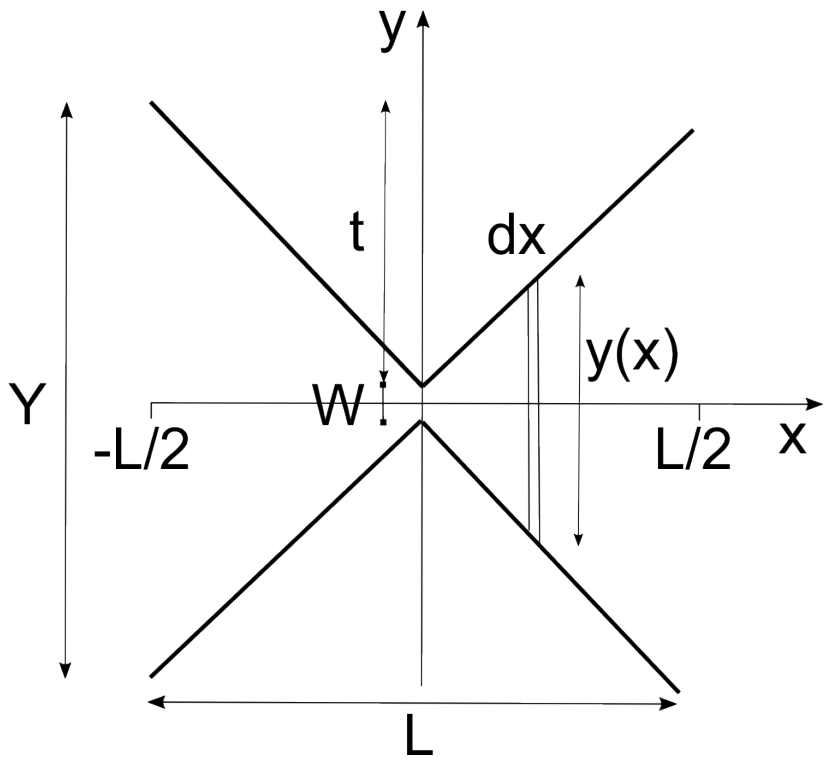


Figure 8.5 Schematic of a bow tie junction of length L, maximum width Y, minimum width W and constriction width $y(x)$.

We can use this to write the position dependent conductance and the contribution to the overall resistance by a graphene strip as

$$G(x) = \frac{2e^2}{h} k_F l(x) \frac{y(x)}{dx} = 1/R(x)\,, \tag{8.5}$$

where

$$l(x) = l_0 \left[1 + c_n \left(\frac{l_0}{y(x)} \right)^n \right]^{-1} \tag{8.6}$$

is the position dependent mean free path. Here l_0 is the bulk mean free path, and n and c_n are real numbers.
In order to determine the overall resistance of the bow tie, we integrate the graphene strip resistances in equation (8.5) with respect to x, assuming that the EMFP is only affected by scattering in the transverse direction. This is reflected in the EMFP dependence of $y(x)$ however, since $y(x)$ is a function of x we change variables to x in order to integrate. This gives

$$R = \frac{h}{2e^2} \int_0^{L/2} \frac{1}{k_F l(x)} \frac{dx}{y(x)} \approx \frac{h}{2e^2} \frac{1}{k_F l_0} \left(\frac{L}{Y} \right) \left[\ln\left(\frac{Y}{W} \right) + \frac{c_0}{n} \left(\frac{l_0}{W} \right)^n \right], \tag{8.7}$$

where we used $Y \gg W$. The first term is very similar to the diffusive (Drude) resistance introduced earlier, leaving us with a total resistance that is approximately equal to a diffusive (first term) and a boundary scattering contribution (second term) [215]. The boundary scattering for $n = c_n = 1$ is then $R \approx \frac{h}{2e^2} \frac{1}{k_F W} \left(\frac{L}{Y} \right)$.
We can write the Seebeck coefficient as a function of resistance using the Mott formula as

$$S = \frac{\pi^2 k_B^2 T}{3e} \frac{1}{R(\epsilon)} \frac{dR(\epsilon)}{d\epsilon} \Big|_{\epsilon = \epsilon_F}\,. \tag{8.8}$$

Plugging in equation (8.7), where we use $\epsilon = hvk$ (v is the charge carrier velocity), and considering the resistance of a graphene strip from equation (8.5) we arrive at an expression for the local width dependent thermopower $S(x)$:

$$S(x) = -\frac{\pi^2 k_B^2 T}{3\epsilon_F e} \left[1 + nU \frac{l(x)}{l_0} - (n-1)U \right], \tag{8.9}$$

where $U = \mathrm{d}\ln(l_0)/\mathrm{d}\ln(\epsilon)\big|_{(\epsilon=\epsilon_F)}$ is the exponent of any power law dependence of the EMFP on energy. U is expected to be between the short-range disorder or electron-phonon interaction value, $U = -1$, and the long-range Coulomb interaction value, $U = 1$ [216, 217]. Equation (8.9) predicts a spatial constriction width depen-

dence of the Seebeck coefficient through the EMFP $l(x)$. Specifically, it predicts a decrease of the Seebeck coefficient for a reduced channel width, meaning we will have areas in the graphene bow tie with different Seebeck coefficients even though the material has not changed.
We can then model $V_{\text{th}}(x) = \int_R^L S\nabla T$ using the temperature distribution and equation (8.9) and compare it to a 1D thermovoltage line-cut through the experimental result shown in Figure 8.4. To this end, $V_{\text{th}}(x)$ is calculated by integrating $S\nabla T$ at every point of the line trace over the whole device length. This is essentially a convolution, in which the Seebeck coefficient S maintains its spatial distribution while the temperature gradient ∇T is moved along the length of the device, i.e. from L to R (see Figure 8.6a). This is in accordance with the measurements, where the temperature gradient caused by the tip is scanned over the sample and therefore changes with respect to the position x while the global thermovoltage is recorded at each point. Since $S(x)$ is only dependent on the constriction width its line shape does not change as the tip is moved.

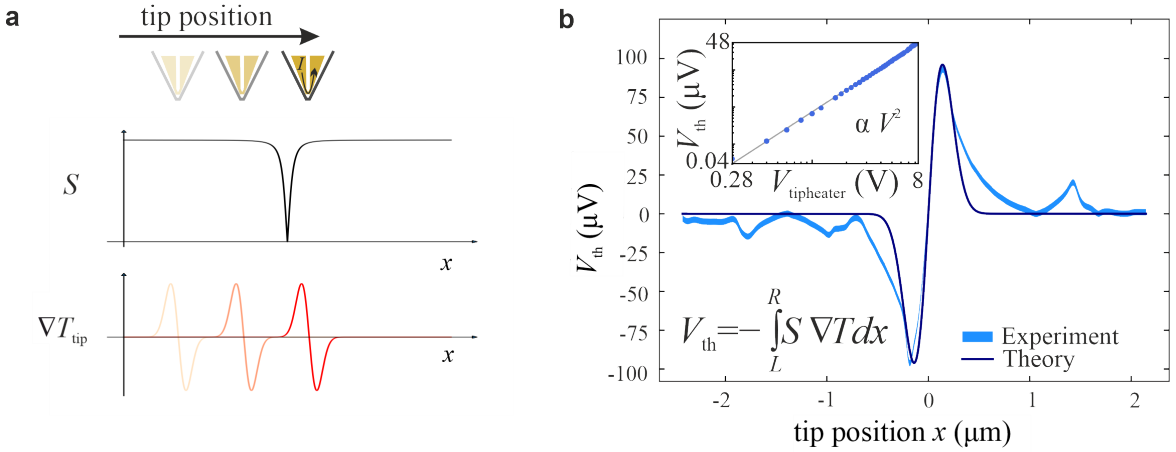


Figure 8.6 a) From the top: schematic of the tip movement along the sample; 1D section cut through the middle of the constriction of the calculated Seebeck coefficient S; the tip-defined moving thermal gradient corresponding to the tip position indicated at the top. b) 1D linecut through the measured thermovoltage (blue) and the theoretical fit (purple), respectively. The inset displays the quadratic tip voltage dependence of the thermovoltage signal in a log-log plot.

The heater temperature is deduced from a calibration and theoretical considerations as discussed previously and is given by $\Delta T \approx 18 \pm 2\,\text{K}$ (see equation (8.1)), where we assume a standard Gaussian distribution of heat spreading in the sample due to its point source nature. While the tip temperature calibration carries an error of 20 % that is propagated through the calculations and the line shape of the temperature

distribution created by the heated tip is only approximated, we note that this will only lead to an over/underestimation of the effect. The conclusions and main results of this chapter remain valid.

Fitting the thermovoltage in Figure 8.6b with $\Delta T \approx 18 \pm 2\,\mathrm{K}$ gives the dimensionless parameters $c_n \approx 0.56$, $n \approx 2.6$ and $U \approx 0.88$. While the fit agrees very well with the measured thermovoltage with regards to amplitude and line shape in the immediate vicinity of the junction, more than 500 nm away we observe a deviation. This is likely due to the model not taking into account geometrical influences on the heat distribution of the tip away from the junction. Nonetheless, the overall characteristics and trends are well captured, again confirming the hypothesis that the main heat spreading takes place in the substrate. The extracted parameters can then be used to calculate S from equation (8.9), giving a bulk value of $S \approx 118\,\mu\mathrm{V\,K^{-1}}$ in accordance with previous measurements on graphene at high temperature [95]. However, as can be seen in Figure 8.2a, the value of the Seebeck coefficient reduces to $S_{\mathrm{min}} \approx 0.34\,\mu\mathrm{V\,K^{-1}}$ in the middle of the bow tie constriction, a change by three orders of magnitude.

This large reduction is attributed to the difference of terms in equation (8.9), which leads to substantial variations in the Seebeck coefficient, even for relatively small changes in the EMFP (such as here the decrease in the EMFP by one order of magnitude).

In order to reproduce the measured Peltier effect we turn to Finite Element Analysis (FEA) using COMSOL Multiphysics. Since the current through the device was recorded and all device geometries are known from the AFM measurements, the only two unknown parameters are the electrical and thermal conductivity of the graphene geometry. These are extracted by fitting the Joule heating at $1\,\mathrm{V_{pp}}$ in the constriction to the COMSOL model (see yellow dots Figure 8.7b) and yield $\sigma = 5 \times 10^5\,\mathrm{S\,m^{-1}}$ and $\kappa = 120\,\mathrm{W\,m^{-1}\,K^{-1}}$, respectively. Since we can reproduce the Joule heating at higher currents well using these parameters, they are then used to calculate the Peltier effect. In order to simulate the Peltier effect, the extracted position dependent Seebeck coefficient was used as a given in the COMSOL model and the resulting heating (cooling) when a current was run through the geometry was computed. Figure 8.7c shows the experimental Peltier heating (cooling) compared to the computed signal, displaying a good agreement between the experimental results and the theoretical prediction from the COMSOL model. Slight deviations in amplitude and line shape are attributed to the nonconformity of the defects in the graphene edges as well as to the effect discussed in section 8.5.

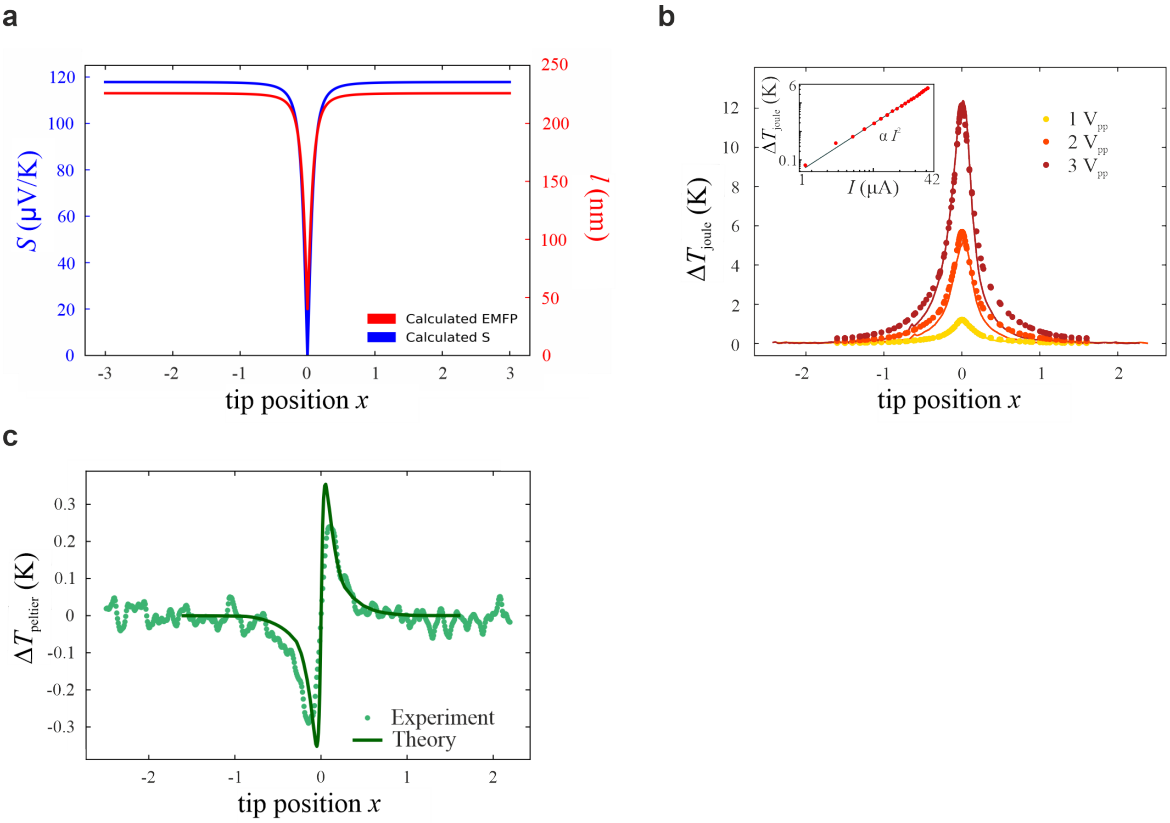


Figure 8.7 a) Calculated EMFP and S using the fitting parameters obtained from Figure 8.6. b) Line-cuts of the Joule heating in the constriction at three different excitation voltages (dots) and corresponding COMSOL model (lines). Inset: Current dependency of the Joule heating signal. c) Line cut through the bow tie Peltier signal at 1 V_{pp} excitation bias experimentally (green dots) and a COMSOL simulation using the calculated Seebeck coefficient in (a) (green line). The zero of the tip position is centered at the middle of the constriction for all figures.

8.4 Other Geometries

In order to study the influence of geometrical confinement on the Seebeck coefficient in graphene further, we have patterned other structures that do not represent a bow tie. The first structure is an island geometry, where wide parts of graphene are connected to each other and the leads via 100 nm constrictions, giving us a better control over the change from bulk to edge-scattering dominated regions and low to high current density. This makes it possible to test the hypothesis of a reduction in the EMFP being responsible for the observed signal and allows us to rule out hot (cold) carriers from the Au/graphene junctions as the cause for the measured effect.

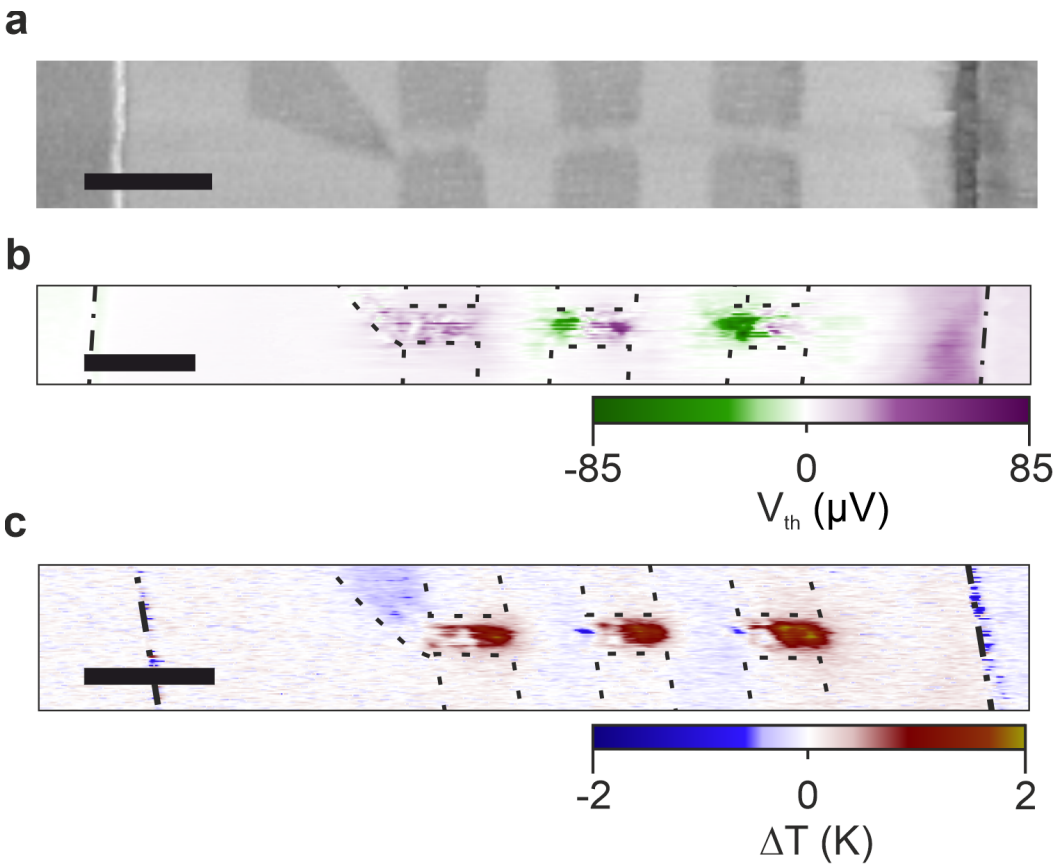


Figure 8.8 a) Lateral Friction image of the island structure. A tear in the graphene on the left side creates an additional constriction in this device. b) Thermovoltage map of the island geometry. c) Peltier map of the island geometry. The dashed lines indicate the border of the graphene structure and the dashed-dotted lines the border of the Au contacts. The scale bar is 500 nm in all figures.

As can be seen in Figure 8.8, the island geometry exhibits heating (cooling) in the Peltier measurement as well as a corresponding positive (negative) thermovoltage pattern in the thermovoltage measurement at the constrictions. This behaviour of a signal around and within the ribbons of reduced width is in accordance with the proposed spatially dependent Seebeck coefficient. Crucially, the signal is of comparable strength in each of the three constrictions including the middle one, ruling out a hot/cold carrier effect. While the thermovoltage signal is somewhat symmetric in the constrictions, the Peltier heating exceeds the cooling significantly. This asymmetry in the Peltier signal that deviates from the thermovoltage signal is discussed further in the next section. In addition, small variations and a fine structure of the signal within the ribbons is visible, which we attribute to the high susceptibility of the EMFP and therefore the Seebeck coefficient to defects, charge

puddles and variations in the width introduced by the oxygen plasma patterning or substrate effects. Such nanoscale variations have been observed previously when studying graphene using photocurrent nanoscopy [218] and are further investigated below for a graphene wire structure.

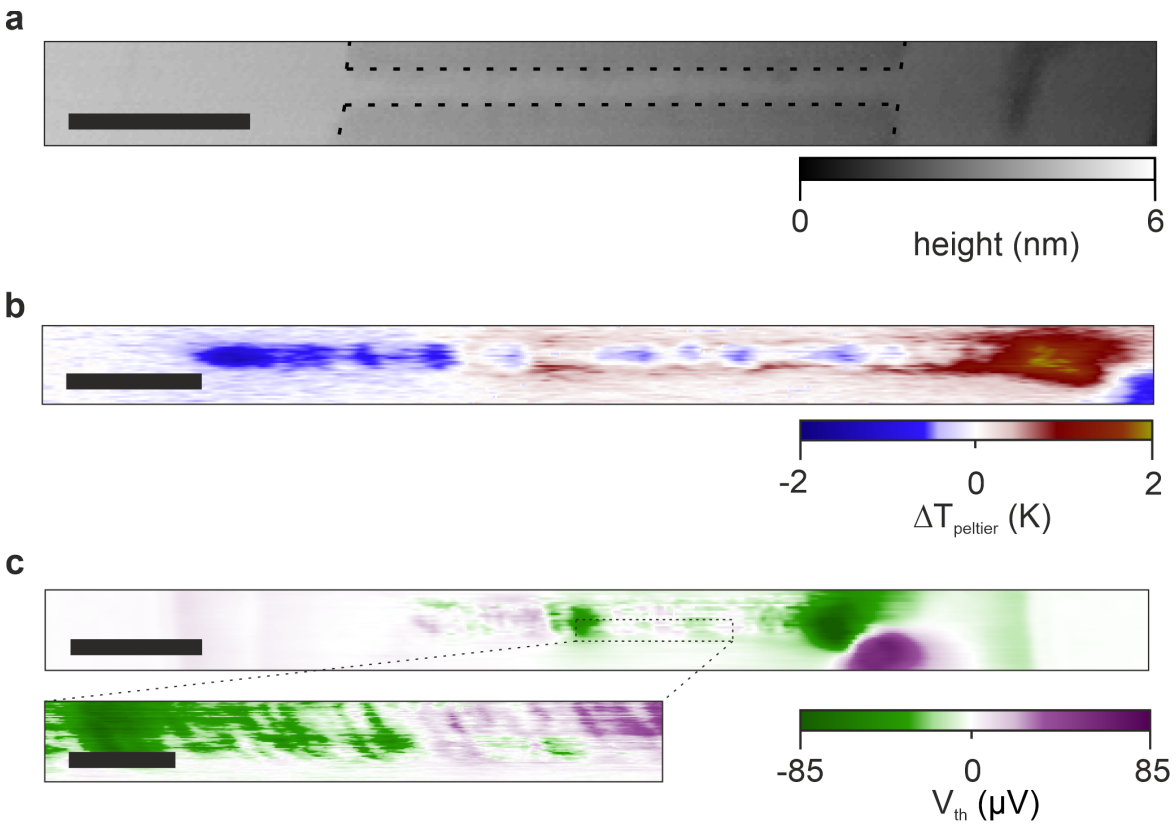


Figure 8.9 a) Lateral Friction image of the graphene wire. b) Peltier map of the graphene wire. c) Thermovoltage map of the graphene wire. The dashed lines indicate the border of the graphene structure and the dashed-dotted lines the border of the Au contacts. The scale bars are 500 nm in a and c for the main measurement, 250 nm for b and 100 nm for the close up in c.

The second structure studied is a long graphene wire connecting two graphene reservoirs. As can be seen in Figure 8.9, a strong signal is exhibited within the wire. In addition to the observed heating (cooling) signals and thermovoltage in the narrow graphene channel, there is a signal on the right side of the graphene wire, most likely stemming from a defect in the graphene. Both the thermovoltage and Peltier map of the wire show sign changes on the scale of hundreds of nanometers and a fine structure which is especially visible in the thermovoltage measurement. This can be attributed to the small scale defects introduced in the graphene or the

contamination of the edges and therefore a small scale change in the potential around the edges. The close up of said fine structure in Figure 8.9c highlights the resolution of the used measurement technique. We note that in all devices tested in this study (bow ties, graphene island, graphene wire), the geometry induced thermoelectric effect is prevalent and of comparable strength. In addition, all devices show a signal within and in the direct vicinity of the constriction but none in the bulk graphene and a comparably small signal at the Au graphene junction.

8.5 Current Dependency

In addition to recording Peltier and thermovoltage maps, we have studied the current dependency of the observed effects by placing the tip in a place with a prominent signal in the bow tie devices as the current through the device I_{bias} (for the Peltier/Joule measurement) or through the SThM tip I_{heater} (for the thermovoltage measurement) is increased. For the thermovoltage and Joule heating signal, we observe a square dependence on the applied current as displayed in the insets in Figure 8.6b and 8.7b respectively. This is to be expected and in accordance with the Joule-Lenz law, which states that the power in a conductor is proportional to the applied current squared times the resistance $P \propto I^2 R$. However, for the Peltier measurements, we observe a deviation from an initially linear current dependency to a higher order for larger currents. As can be seen in Figure 8.10a we can fit the current dependency reasonably well using a combination of a linear and cubic term with the changeover point at about 33 µA. This is in contrast to the expected linear dependence predicted by $\dot{Q} = \Pi I_{\mathrm{bias}} = STI_{\mathrm{bias}}$.
The unusual current dependency is attributed to an electron wind like effect as illustrated in Figure 8.10b. For low currents at which the drift velocity of electrons in the sample is much smaller than the Fermi velocity $v_{\mathrm{d}} \ll v_{\mathrm{F}}$, hot carriers originating from the middle of the constriction due to Joule heating disperse in an approximately radial pattern around the heat spot (displayed on the left). Here, the average electron can be assumed to travel the EMFP distance τv_{F} (where τ is the relaxation time) before depositing its thermal energy within the graphene lattice, creating a circle of higher temperature around the Joule heating temperature spot. However, in the experiments, higher currents were used, which in combination with a narrow junction can result in high drift velocities

$$v_{\mathrm{d}} = \frac{I}{neW}\,, \tag{8.10}$$

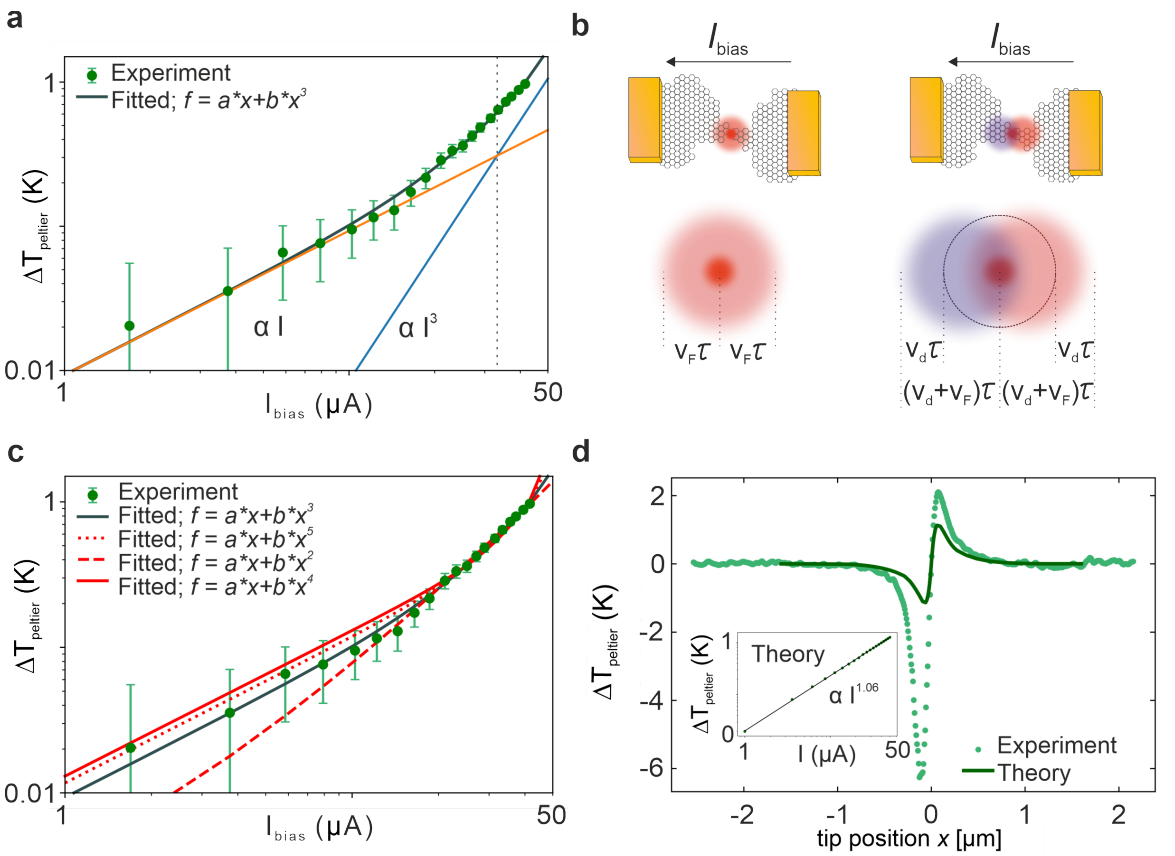


Figure 8.10 a) Current dependency of the Peltier signal (green dots) and fit using a linear and cubic term (green line). The orange line (linear with respect to the current) and the blue line (cubic with respect to the current) serve as a guide to the eye with the black dashed line indicating the switchover point from linear to cubic dependency. b) Schematic explaining the electron wind effect, which is not visible at lower currents (left) but becomes appreciable as $v_\mathrm{d} \approx v_\mathrm{F}$ (right). c) Current dependency of the Peltier signal (green dots) and different order fits. d) Experimental (green dots) and COMSOL calculation of the Peltier heating/cooling (green line) at $3\,\mathrm{V_{pp}}$. The inset shows the current dependency of the COMSOL simulated Peltier heating, which is linear, save for a small correction ($\propto 1.06$) due to the Joule heating.

where I is the current, $n = 10^{16}\,\mathrm{cm}^{-2}$ is the assumed carrier density [219] and $W = 100\,\mathrm{nm}$ is the width of the constriction. Plugging in the maximum current used in the experiment $I = 85\,\mu\mathrm{A}$ gives a drift velocity of $v_\mathrm{d} \approx 0.49 \times 10^6\,\mathrm{m\,s}^{-1}$, which is comparable to the Fermi velocity. As a result, the area in which energetic electrons are depositing their thermal energy within the graphene lattice is shifted by $v_\mathrm{d}\tau$ as shown on the right in Figure 8.10b, creating a cooling (heating) section by sweeping electrons in the direction of the current. A similar effect has been observed in graphene devices for varying gate voltages [220]. For this effect we would not

expect a linear current dependence of the heating (cooling) spots due to the Peltier effect but rather a mixture of an increasing drift velocity (linearly increasing with current) and the temperature dependence of the hot carriers due to Joule heating (quadratic current dependency). These two combine to an additional cubic term in the current dependency for $v_d \approx v_F$. We note, that for a graphene channel with a much longer width than $v_d\tau$, we would expect only the start and end of the reduced width channel to exhibit this response linked to the drift velocity as was confirmed by measurements of the graphene wire.

While the explanation of the non-linearity of the Peltier effect with a heat drift in the construction due to high drift currents fits the data, it is important to note that other explanations need to be considered as well. One other reason for the non-linearity could be the temperature dependence of the Seebeck effect in graphene [95]. As Joule heating increases the local temperature, the Seebeck coefficient changes, giving rise to a fifth order current dependency $\dot{Q} \propto STI \propto T^2 I \propto T^5$, which as can be seen in Figure 8.10c would fit the data reasonably well, if worse than a cubic dependence. However, as the measurements are performed at room temperature ($\approx 300\,\mathrm{K}$), the impact of the few degrees increase in the sample temperature on the Seebeck coefficient (see Figure 8.3a) can be neglected. Even for Joule heating as high as 10 K, the resulting change of the temperature is less than 7%, which is too weak to explain the observed drastic non-linear effect. In addition, any temperature dependent effects are taken into account in the FEA of the Peltier heating (cooling) as it solves for the full thermoelectric equation. As can be seen in Figure 8.10d, the COMSOL model does not predict the non-linear increase in the Peltier effect and suggests a deviation from linear Peltier heating by only 6 %, two orders of magnitude lower than the experimentally observed change to a higher order exponent.

Crucially, we observe the non-linear current dependency in every device investigated in this study, that is not only for the bow tie geometries but also the island and wire structure. The additional current dependencies are shown in Figure 8.11 and show a good agreement with the cubic contribution fit.

Interestingly, the value of the switchover current is different for all structures, suggesting that the geometry has a profound influence on the drift velocity in the devices.

While the model of a heat drift is deemed the most likely explanation at this point, unfortunately the quality of the data does not rule out other causes. Clearly, it is necessary to further investigate the effect in order to strengthen this theory and explain the observed behaviour in detail.

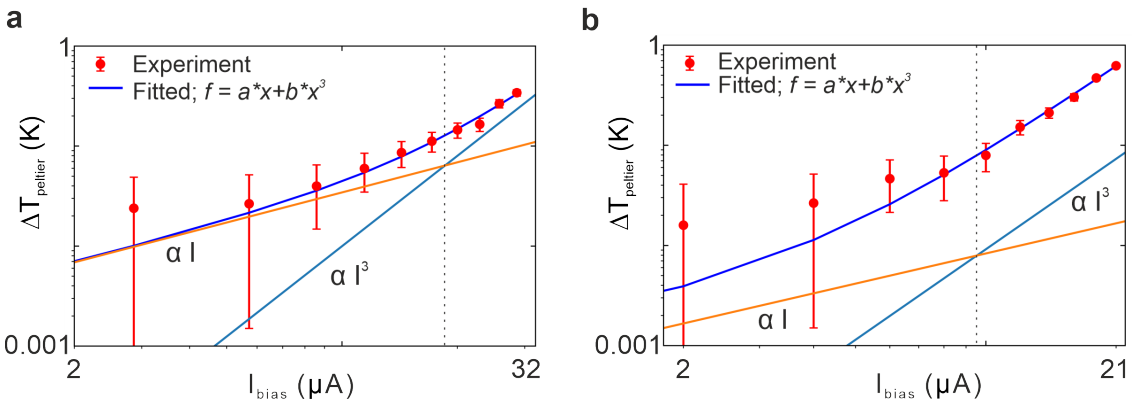


Figure 8.11 a-b) Current dependency of the Peltier signal (red dots) and fit using a linear and cubic term (blue line) for the island (a) and wire geometry (b). The orange line is linear with respect to the current and the purple line is cubic and they serve as a guide to the eye with the black dashed line indicating the switchover point from linear to cubic dependency.

8.6 Conclusion

In this chapter, the local thermoelectric properties of graphene nanostructures were studied using an SThM based method. Rather than measuring the global thermovoltage, this technique enables the imaging of localized effects due to defects, geometrical considerations or the influence of metallic contacts. In the measurements we observe a geometry dependent signal for both the Peltier effect and the Seebeck effect, which is dominating over the expected signal at the graphene-Au junction at the contacts. We attribute this to a spatially sensitive EMFP, which is reduced for narrow constrictions due to an increased influence from scattering at the edge defects. This reduced EMFP in turn results in a local variation and decrease of the Seebeck coefficient, explaining the observed signal. While a similar effect has previously been detected in Au nanowires, graphene has a comparatively larger EMFP at room temperature which is well defined due to graphene's two-dimensional nature. We are able to measure this geometrical manipulation of the Seebeck coefficient in different structures (island, bow tie and wire geometry) and, by using a theory for a width dependent EMFP, can extract a position dependent S from the data. In addition, we also observe an unexpected non-linearity in the current dependency of the Peltier effect which is attributed to a heat drift current due to the high charge carrier drift velocities in the nanoconstrictions.
We believe such geometrical effects are prevalent in two-dimensional nanostructures or van der Waals heterostructures and can lead to undesired heating (cooling) effects.

In addition, a temperature gradient over such a device can result in a parasitic thermovoltage drop, making the findings important for future thermal and electrical as well as photothermoelectric measurements in two-dimensional nanoscale electronic devices.
Apart from being important in informing future experimental designs, the presented results open the way to efficient thermal management in integrated circuits made out of two-dimensional materials. By changing the width of graphene channels using electron beam lithography, it should be possible to create precision fabricated two-dimensional thermocouples or Peltier elements. In chapter 10 we will act on this idea and study single material thermocouples made out of graphene. In addition, while the presented techniques are informative on and make possible a complete study of the local thermoelectric properties in two-dimensional structures, they tend to be rather complicated and require the use of multiple lock-in amplifiers to analyse the data. The AC technique has the added disadvantage that it tends to either require a long time to scan a sample or blur out effects due to the simultaneous movement of the tip and application of a sinusoidal heating current. In chapter 9 we will develop a more direct way of mapping the thermovoltage in graphene devices using a DC method, offering a higher resolution for the thermovoltage maps. Furthermore, rather than using CVD grown graphene (which allows for scalability), we will use exfoliated graphene as it exhibits less defects and provides better control over the charge carrier concentration.

9

Local Mapping of Thermoelectric Properties of Graphene Nanostructures via Scanning Thermal Gate Microscopy

This chapter is based on "Direct Mapping of Local Seebeck Coefficient in 2D Material Nanostructures via Scanning Thermal Gate Microscopy" by Achim Harzheim, Charalambos Evangeli, Oleg V. Kolosov and Pascal Gehring, in *2D Materials* **2020**, 7, 4, 041004 [221]. The author contributions are as follows: OVK and PG conceived the study, PG fabricated the devices, AH performed pre- and post-characterization of the devices, AH, CE and PG performed the measurements, AH, CE, OVK and PG discussed the results, AH wrote the manuscript and all authors commented on the manuscript.

In this chapter we will introduce a novel, non-invasive SThM based termovoltage measurement method called Scanning Thermal Gate Microscopy (STGM). Rather than using an AC current to heat the SThM tip as in the last chapter, a DC current is employed. The main advantage of this is that limitations on the scanning speed due to the timescale of the AC excitations are no longer present, therefore reducing blurring effects in the thermovoltage maps and enabling higher scanning speeds. Since a DC current is used to excite the tip, we can only measure thermovoltage maps in this study and not the Peltier effect or Joule heating. Employing a deconvolution method it is then also possible to use the high resolution thermovoltage maps to calculate corresponding Seebeck maps.
Such investigations into the thermoelectric properties of two-dimensional devices are crucial to investigate the influence of defects, metallic contacts and changes in carrier concentration, which can have a drastic impact on local thermoelectric char-

acteristics [222–224]. More knowledge of the fundamental thermoelectric properties of materials and devices is needed to enable the design of efficient devices such as photovoltaic and thermoelectric hybrid structures and help eliminate parasitic thermoelectric noise in nanoscale devices [225].
While thermovoltage measurements are possible using a scanning photocurrent setup, there are multiple drawbacks to this method such as the laser spot size, which is typically on the order of micrometers, the difficulty in estimating the temperature increase due to the laser and the inherent mixing of photo thermoelectric and photovoltaic effects in the measurement [150, 151]. Other SThM based measuring methods that have been developed require an electrical contact between a conducting SThM tip and the sample, adding an additional uncertainty to the measurements [149, 148].
In this chapter STGM is used to measure exfoliated graphene devices, including a single-layer graphene (SLG) bilayer graphene (BLG) junction. Due to the nature of STGM, which can only probe the surface of materials, it is mostly suitable to measure two-dimensional or thin film samples. Here graphene is used since it is the most-studied material of the two-dimensional family, shows promise for wafer scale integration [226, 227] and its thermoelectric properties can be manipulated by a variety of methods [95, 96, 228]. Yet, the thermoelectric characteristics of graphene have mostly been studied on a global scale or in combination with photocurrent measurements. This chapter aims to introduce a method to record high resolution thermovoltage maps, further illuminate what influences the local thermoelectric properties in two-dimensional materials and in addition investigate the connection between thermovoltage and Seebeck coefficient.

9.1 STGM Measurement Configurations

The measurements are performed using the same SThM setup as in chapter 8 and 5, again placed in a high vacuum environment to prevent heat transfer through convection and the formation of a water meniscus between the tip and the sample, which would lower the achievable resolution. The SThM tip is heated up for the measurements by applying an AC voltage component of $V_{\text{heater}} = 4\,\text{V}_{\text{pp}}$ at a frequency of 91 kHz with a 4 V DC offset. The AC voltage applied makes it possible to simultaneously measure the thermal conductance of the sample while not interfering with the DC measurements due to the high frequency. This applied voltage results in a temperature increase in the SThM tip due to Joule heating, which can be quantified by the calibration procedure laid out in chapter 5. In short, the tip resistance as a

function of temperature is recorded on a heated stage inside a high-vacuum chamber, which can then be used to quantify the tip heating with respect to a voltage applied. Importantly, the temperature increase at the tip-sample contact is a fraction of the temperature rise inside the resistive heater and depends on the thermal conductivity of the sample surface [167, 229]. For the voltages applied here, the tip heats up by $T_{\mathrm{tip}} \approx 53\,\mathrm{K}$, where the excess temperature is defined with respect to the microscope stage and for a tip in contact with the SiO_2 substrate or graphene. The SThM tip then presents a local heat source, which is scanned over the sample while the global thermovoltage drop is recorded (see Figure 9.1 for a measurement schematic). The thermovoltage is amplified using an SRS SR650 low-noise preamplifier and an SRS SR560 high-impedance voltage preamplifier, and crucially no electrical contact between the tip and the sample is required, eliminating any uncertainty related to the strength and consistency of such a contact [210]. Offsets introduced by the amplifiers are accounted for by subtracting the background signal far away from the sample from the thermovoltage map.

The samples are fabricated by exfoliating highly oriented pyrolytic graphite on a Si chip later used as a global back gate with a 300 nm thick isolating layer of SiO_2. Subsequently, the devices are patterned and etched if required and 1 nm Ti/50 nm Au contacts are deposited on top of the graphene. In a final step the devices are annealed at 350 °C in a forming gas atmosphere for 30 minutes.

As explored in chapter 8, the tip position dependent thermovoltage build up due to a temperature increase caused by the hot tip $T(x)$ and for a given Seebeck coefficient distribution $S(x)$ can be written as

$$V_{\mathrm{th}}(x_{\mathrm{T}}) = -\int_{x_{\mathrm{L}}}^{x_{\mathrm{R}}} S(x)\frac{\partial T(x-x_{\mathrm{T}})}{\partial x}dx\,. \tag{9.1}$$

Here, x_{T} denotes the position of the SThM tip, x_{L} and x_{R} the position of the left and right contact, respectively, and $\frac{\partial T(x-x_{\mathrm{T}})}{\partial x}$ the position dependent derivative of the temperature increase profile caused by the tip. For a symmetric temperature distribution $T(x)$, V_{th} in equation (9.1) reflects the local variations in $S(x)$ with respect to x_{T} on a length scale given by the thermal resistances of the sample. In addition, equation (9.1) specifies that the thermovoltage is given by a convolution of $S(x)$ with the derivative of the temperature profile $\mathrm{d}T/\mathrm{d}x$. For a single-layer/bilayer graphene (SLG/BLG) junction for example, where the symmetry in $S(x)$ is broken at the transition from SLG to BLG, we observe a positive thermovoltage signal at the junction (Figure 9.1b). The measurement configuration, where the source contact (S)

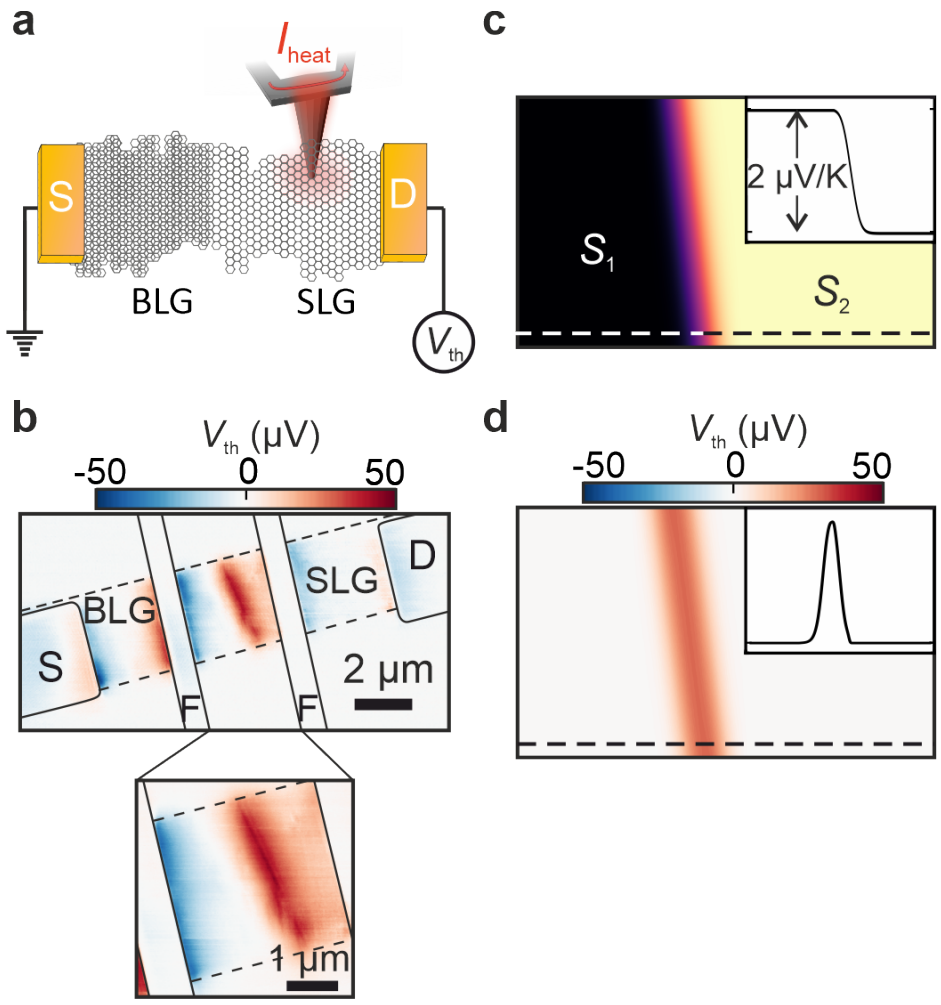


Figure 9.1 a) STGM measurement setup schematic. b) Recorded thermovoltage map of a SLG/BLG junction device. The thermovoltage is measured between the source (S) and drain (D) contact with the other two contacts left floating (F). The dashed black lines indicate the position of the graphene flake and the black drawn through line the gold contacts. c) Simulated Seebeck signal used for the deconvolution going from S_1 to S_2, resulting in $\Delta S = 2\,\mu\mathrm{V\,K}^{-1}$. The inset shows a line trace through the Seebeck map with the position of the cut indicated by the dashed line. d) Calculated thermovoltage map obtained by convoluting the Seebeck map in (c) with the temperature distribution $dT(x)$ (see Appendix C). The inset shows a line trace through the thermovoltage map with the position of the cut indicated by the dashed line.

is grounded and the thermovoltage is measured at the drain contact (D) is depicted in Figure 9.1a. In addition to the thermovoltage at the junction, further signals at the floating (F) and measuring contacts are visible which will be discussed later on in this chapter. The positive thermovoltage at the junction can be explained by different Seebeck coefficients for BLG and SLG due to the respective dispersion relations and has previously been reported [99].
We can model this behaviour by assuming a device which comprises two connected materials with different Seebeck coefficients S_1 and S_2, as depicted in Figure 9.1c. Then we can calculate the expected thermovoltage signal due to $S(x)$ by convolving the Seebeck coefficient distribution with the derivative of the temperature distribution $\mathrm{d}T/\mathrm{d}x$ (see equation 9.1). For the calculation here we assume a difference in Seebeck coefficient between the materials of $\Delta S = S_2 - S_1 = 2\,\mu\mathrm{V\,K^{-1}}$ [99] and a Gaussian shaped temperature distribution [230]. Convolving each line of the Seebeck distribution in Figure 9.1c with the temperature distribution gives a thermovoltage map as shown in Figure 9.1d. The result of the convolution is a positive thermovoltage along the change in Seebeck coefficient, reproducing the experimental results for the SLG/BLG junction well. It is important to note that the width of the thermovoltage signal is determined by the length scale of the Seebeck coefficient transition from S_1 to S_2 and the width of the temperature distribution. Later in this chapter we will use this characteristic to quantify the transition length scale, extracting information about the band bending due to a thickness change in graphene.

9.2 Rectangular Graphene Device

We will first apply STGM to a rectangular single-layer graphene device (Figure 9.2). The device is p-doped at $V_\mathrm{g} = 0$ due to the interaction of graphene with SiO_2 surface charges and exhibits its charge neutrality point (CNP) at $V_\mathrm{g} \approx 28\,\mathrm{V}$ (see gate dependent resistance trace in Figure 9.2c) [157, 231]. We record a thermovoltage map at three different gate voltages: for a strongly p-doped sample at $V_\mathrm{g} = -15\,\mathrm{V}$, close to the CNP at $V_\mathrm{g} = 28\,\mathrm{V}$ and for a strongly n-doped sample at $V_\mathrm{g} = 45\,\mathrm{V}$ (Figure 9.2a). At $V_\mathrm{g} = -15\,\mathrm{V}$, a signal of approximately $30\,\mu\mathrm{V}$ can be seen when the hot STGM tip is on or close to the source contact and a signal with similar strength but opposite sign is observed for the STGM tip on the drain contact. There is little to no signal when the tip is scanned over the graphene channel. Around the CNP a strong chaotic signal with changing polarity appears in the channel. For an n-doped sample the signal on the graphene is again reduced though in comparison to the

p-doped case some variation is visible. At the contacts the signal has changed signs with respect to the p-doped sample, with the drain contact now exhibiting a negative thermovoltage and the source contact a positive thermovoltage.

In the following, the origin of the observed thermovoltage signals will be explored. Thermovoltage signals can be explained by the preference of charge carriers to diffuse towards a higher density of states (DOS) to maximize their entropy. This results in charge carriers moving from hot regions in a material or device towards colder regions, with the driving force being the amount of entropy gained and the size of the temperature difference ΔT. Then, depending on the measurement configuration as well as the majority carrier in the system, a positive or negative thermovoltage build-up is observed. In the device, the graphene underneath the Au contacts is shielded from the back gate voltage and therefore constantly p-doped. For an n-doped channel ($V_g = 45\,\mathrm{V}$) the DOS at the Fermi energy is larger in the graphene channel than it is underneath the contacts, causing electrons to diffuse from the contacts into the channel (Figure 9.2a right). This leads to the build-up of a positive (negative) thermvoltage at the drain (source) contact. While the DOS at the Fermi energy for a p-doped sample is again larger in the channel than it is underneath the contacts, the majority carriers are now holes rather than electrons (Figure 9.2a left). Therefore, a negative (positive) thermovoltage at the drain (source) contact is observed.

The chaotic signal in the graphene channel around the CNP is attributed to charge puddles that locally change the carrier concentration and are commonly observed for graphene on SiO_2 [218, 232]. This in turn leads to local variations of the Seebeck coefficient, which is extremely sensitive to changes in the charge carrier concentration close to the CNP with respect to sign and magnitude [218, 95]. Such large fluctuations and therefore differences in the Seebeck coefficient on the small length scale associated with charge puddles explain why the signal in the channel is much larger than around the contacts at the CNP.

It is important to note here that the thermal spreading resistance of the scanned surface and the tip-sample thermal interface resistance have a large impact on the tip-apex temperature. As the thermal spreading resistance is mainly determined by the thermal conductivity this is particularly relevant when scanning the Au contacts as they have a thermal conductivity two orders larger than SiO_2/graphene on SiO_2. This results in a reduction of the tip temperature from $T_{tip} \approx 53\,\mathrm{K}$ for the tip on SiO_2/graphene to $T_{tip} \approx 1.5\,\mathrm{K}$ when the tip is on the Au contacts and can distort the

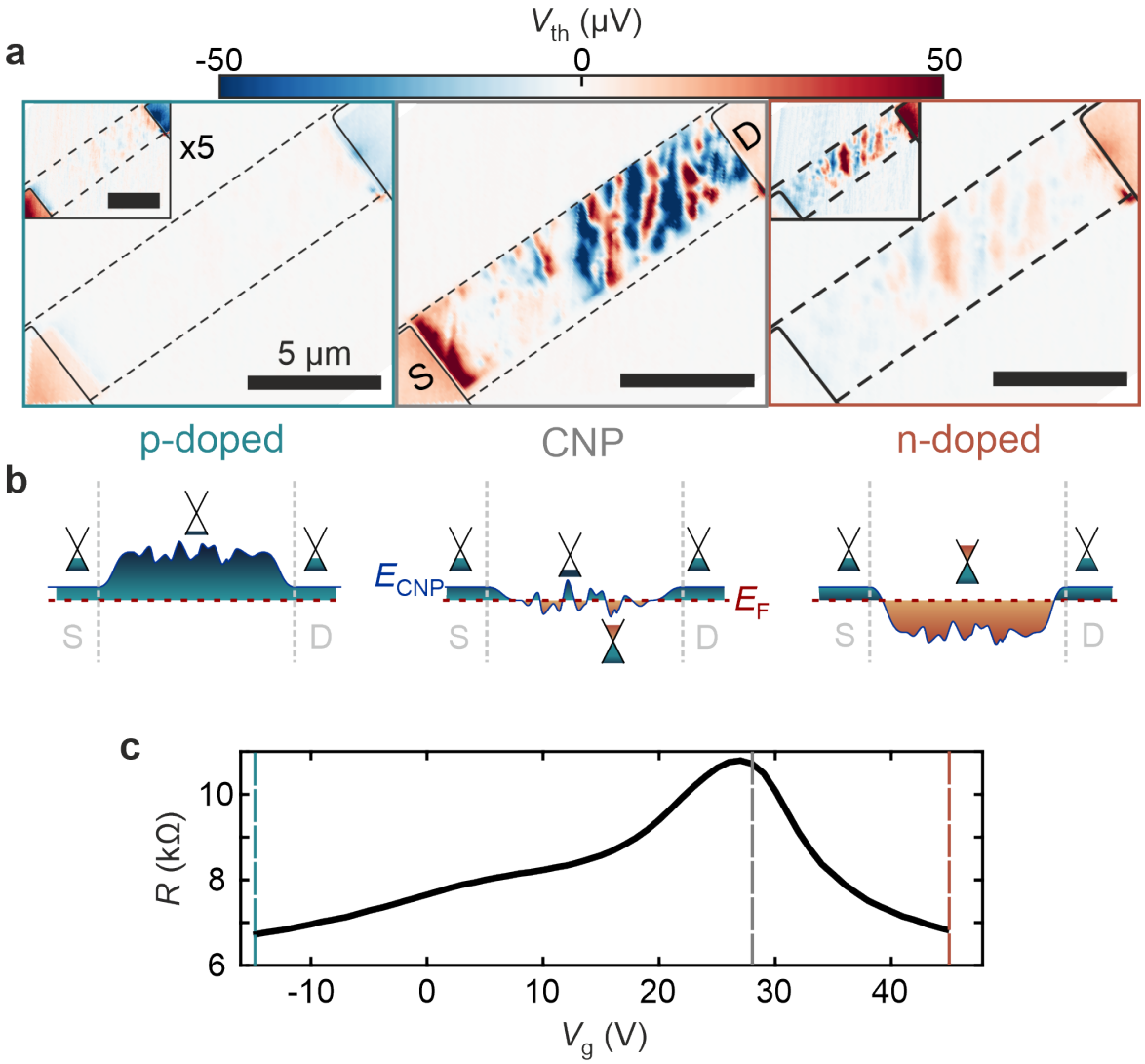


Figure 9.2 a) Thermovoltage maps recorded at three different back gate voltages. The insets show the same map at a five times higher sensitivity (V_{th} = -10 to 10 µV). All scale bars denote 5 µm. The dashed black lines indicate the position of the graphene flake and the black drawn through lines the gold contacts. b) Schematic showing the energy distribution in the graphene channel and under the contacts relative to the Fermi energy for a p-doped (left) and n-doped (right) graphene channel and at the charge neutrality point or CNP (middle). c) Gatetrace of the device with the CNP around 28 V. The dashed lines indicate the three gate voltages at which the above maps were recorded.

thermovoltage amplitudes observed [167].

9.3 Single-layer/Bilayer Graphene Junction

Next, we will apply STGM to a graphene device with changing thickness, that is with a SLG/BLG junction. The device has four contacts, with the two opposite ones being used as source (S) and drain (D) for the measurement and two left floating (F) as shown in Figure 9.3. While a detailed gate trace is not available due to measurement complications, the sign change in the thermovoltage signal on the contacts as well as measurements on other samples suggest that our gate range is sufficient to change the majority carrier in this sample. We therefore assume that the sample is p-doped for low V_g and n-doped for high V_g with the CNP located around $V_g = 10$ to 12.5 V. Similar to the previous device, a strong thermovoltage around the measurement contacts can be seen that changes sign as we move from a p-doped to an n-doped sample. In addition, the floating contacts exhibit a bipolar signal which switches polarity as the majority carriers are changed in accordance with previous observations in photocurrent scanning microscopy measurements [98]. This is due to the floating contacts locally doping the graphene underneath and pinning the carrier density. In general, the Fermi level pinning by the contacts leads to a strongly inhomogeneous change in the carrier density distribution in the sample with varying back gate voltage. Rather than occurring simultaneously over the whole sample, the change sets out at the SLG/BLG junction and moves towards the edges (right-hand column Figure 9.3a).

STGM also allows us to directly image the gate screening due to a layer of graphene. While the characteristic chaotic and bipolar thermovoltage signal caused by charge puddles can be seen in the SLG area of the device around the CNP (similar to the rectangular device), little to no such signal is observed on the BLG side (see Figure 9.3a, $V_g = 10/12.5$ V). This is attributed to the electric field exhibited by the surface dipoles in the SiO_2 substrate being screened by the bottom layer of graphene and therefore not affecting the top layer in the BLG region [233, 234]. The same observation also provides evidence that the two graphene layers are thermally mostly decoupled as suggested previously [235]. Assuming the presence of charge puddles in the bottom layer of the BLG (as in the SLG area), heat induced in the top layer by the STGM tip and transmitted to the bottom layer should cause a thermovoltage

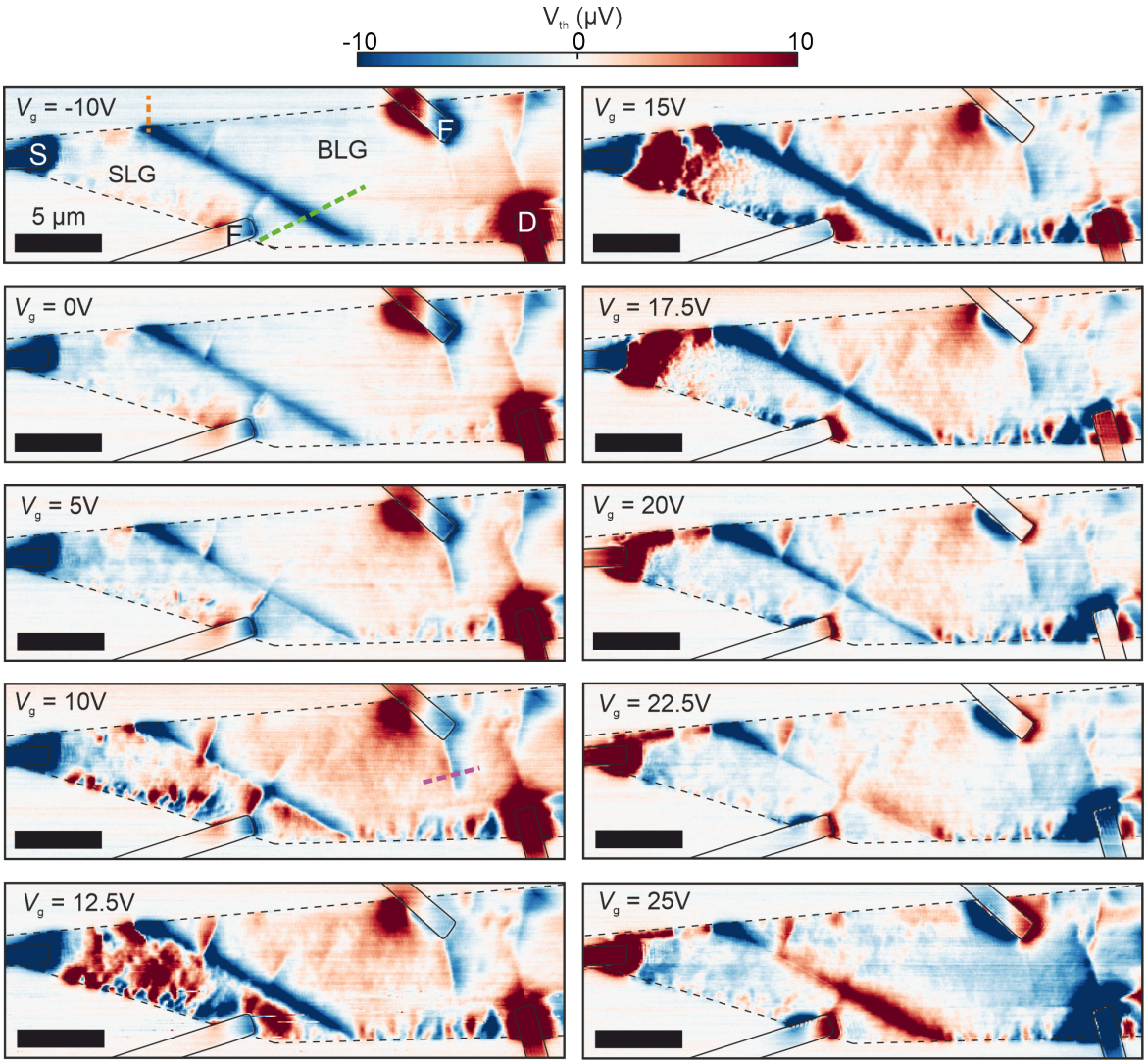


Figure 9.3 Thermovoltage maps at ten different gate voltages for a SLG/BLG junction device. The source and drain contacts are indicated by S and D respectively and the coloured dashed lines are the position of the line traces shown in Figure 9.5a-e. The dashed black lines indicate the position of the graphene flake and the black drawn through lines the gold contacts. All scale bars denote 5 μm.

signal, which we do not detect.
Furthermore, we observe thermovoltage signals along straight lines (see pink line at $V_g = 10\,\mathrm{V}$ in Figure 9.3a), which do not correspond to anything observable in the AFM height topography. We attribute this signal to strain or wrinkles in the graphene possibly induced by the contact deposition or the annealing step. Strain or wrinkles have previously been shown to cause changes in the Seebeck coefficient [236] and to exhibit a Peltier effect [237]. Lastly, a gate dependent strong signal is recorded when the STGM tip is scanned over the SLG/BLG junction in the middle of the sample (green dashed line top left Figure 9.3a). Such a signal, that changes from negative to positive as the back gate voltage is swept over the CNP, has been reported in scanning photocurrent measurements [238, 99]. Both the wrinkle and the SLG/BLG junction exhibit a signal with a non-linear gate dependence.
The reversal of the thermovoltage sign at the SLG/BLG interface when sweeping over the CNP indicates that there is a change in the Seebeck coefficient difference $\Delta S = S_{\mathrm{SLG}} - S_{\mathrm{BLG}}$. As introduced previously, carriers diffuse from regions with low DOS into those with high DOS with the main driving force being the resulting gain in entropy. Due to the quadratic dispersion relation in BLG around the CNP compared to the linear one for SLG, the DOS in BLG is larger than in SLG [239, 217]. For the measurement configuration used here, with the thermovoltage measured at the BLG area and the SLG area grounded, this results in a positive (negative) thermovoltage build up for electron (hole) dominated transport [99]. This is highlighted in Figure 9.5 where gate dependent thermovoltage line traces through the SLG/BLG junction are shown (the position of the line traces is indicated by the green dashed line in Figure 9.3, top left panel). The signal starts negative for a p-doped sample at $V_g = -10\,\mathrm{V}$ and changes to a positive signal for an n-doped sample at $V_g = 25\,\mathrm{V}$ (see Figure 9.5b, top). This peak (dip) visible in the line trace when the hot STGM tip crosses the SLG/BLG interface can be attributed to a stepwise change in the Seebeck coefficient between SLG and BLG as discussed in Figure 9.1. However, close to the CNP, a bipolar signal is visible that is not consistent with a change from S_{SLG} to S_{BLG} (Figure 9.5b, bottom). A similar signal is found for the wrinkles as shown for example in Figure 9.5c and suggests a dip or peak in the Seebeck coefficient rather than a transition. This is confirmed by a simulation similar to the one performed for a transition in Figure 9.1. As Figure 9.4 shows, a bipolar signal is a result of a dip (peak) in the Seebeck coefficient. Here, further simulations showed that having a differing Seebeck coefficient on either side of the drop (peak) does not change the bipolar nature of the resulting thermovoltage signal though it does impact the line

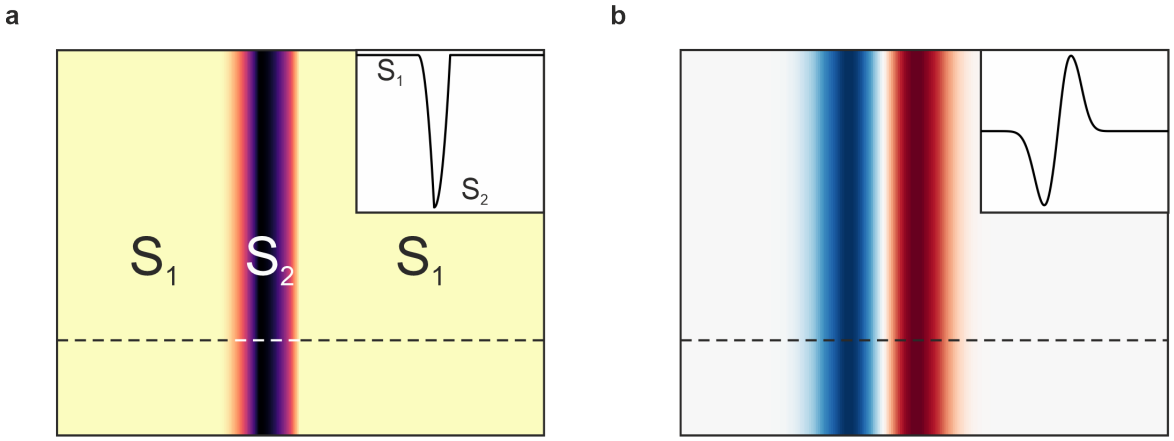


Figure 9.4 a) Simulated Seebeck signal dropping from S_1 to S_2 and rising back to S_1. The inset shows a line trace through the Seebeck map with the positon of the cut indicated by the dashed line. b) Calculated thermovoltage map. The thermovoltage map was obtained by convolving a) with the temperate distribution $dT(x)$. The inset shows a line cut through the thermovoltage map with the positon of the cut indicated by the dashed line.

shape. Since the bipolar thermovoltage signal observed is relatively symmetric we assume an approximately equal Seebeck coefficient on either side of the dip (peak) with respect to the height of the dip (peak). For the wrinkles such a sharp dip (peak) in the Seebeck coefficient can be explained by the local strain that caused the wrinkle to originate. Such local strain in graphene has been predicted to change the Seebeck coefficient in graphene, with the magnitude of this change being highest around the CNP [240]. Consequently, the wrinkles in the SLG/BLG sample exhibit a strong bipolar signal for V_g around the CNP. As the charge carrier density is increased, the change in the Seebeck coefficient due to strain is comparably smaller, leading to a decrease in ΔS and in the observable thermovoltage. While this accurately describes and explains the signal due to wrinkles in graphene, the SLG/BLG junction signal is more puzzling. We attribute this signal to the influence of nearby charge puddles that impact the line shape or to local symmetry breaking and disorder at the edges of the BLG which locally dope the graphene and change the Seebeck coefficient.

As mentioned previously, it is possible to extract a length scale for the Seebeck coefficient transition from the STGM measurements associated with different signals. We know that the thermovoltage signal's magnitude and shape is given by a convolution of the temperature difference dT/dx and the spatial Seebeck coefficient distribution $S(x)$. Therefore, knowledge about the shape and height of T as well as the thermovoltage measurements allows us to draw conclusions about $S(x)$. In

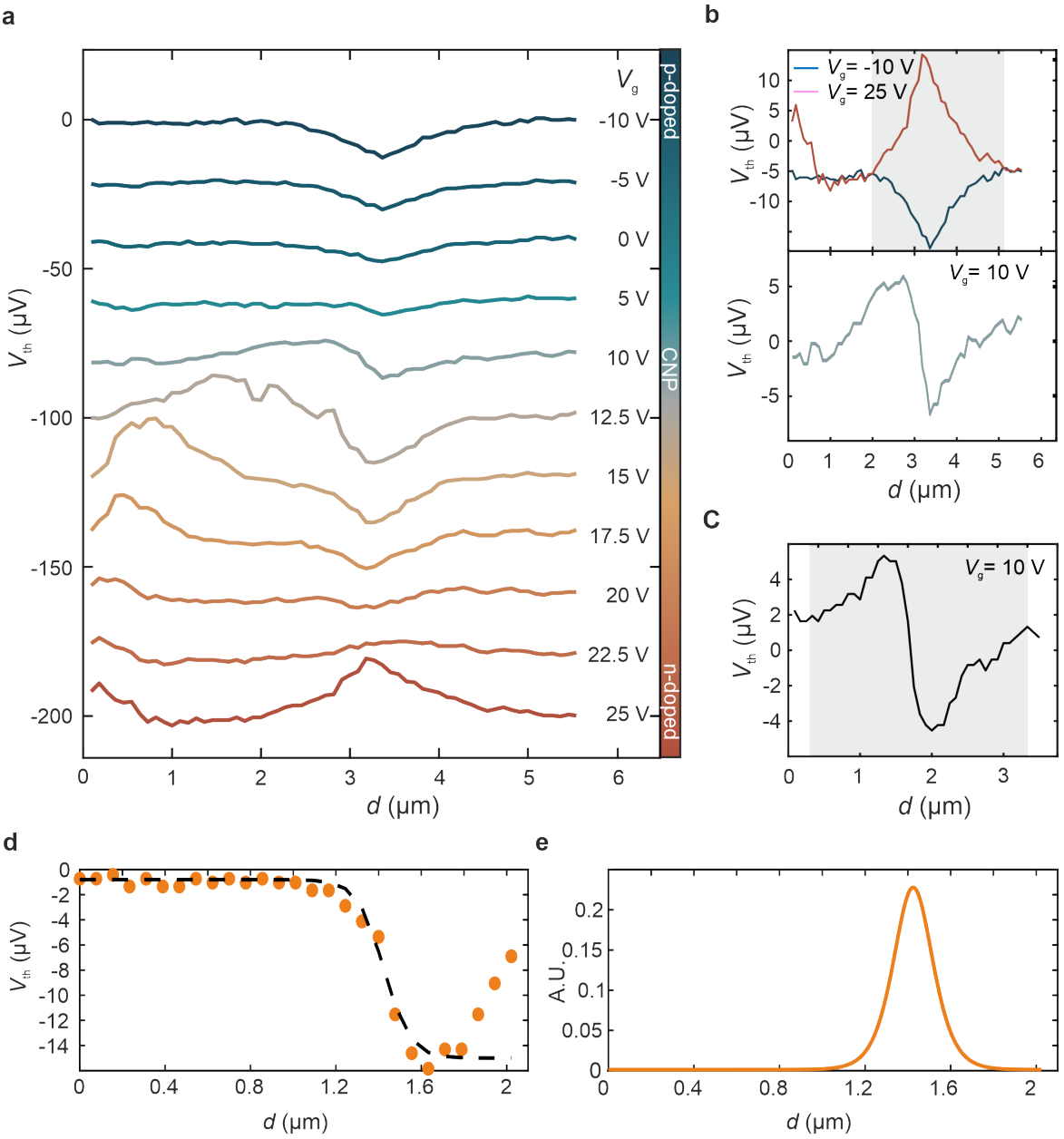


Figure 9.5 a) Linetraces through the SLG/BLG junction shown in Figure 9.3a (dashed green line) for different gate voltages. The line traces are offset by -20 µV each for clarity. b) Linetrace through the SLG/BLG junction at $V_g = -10\,V$ and $V_g = 25\,V$ showing a dip/peak (top) and at $V_g = 10\,V$ showing a bipolar signal (bottom). c) Line cut through the thermovoltage signal of a wrinkle in the SLG/BLG sample. The grey shaded area indicates the width of the signal. d) Line cut indicated in the top left panel in Figure 9.3 by the orange dotted line (orange dots) and a sigmoidal Boltzman curve fit (black dotted line). e) Derivative of the fit in b.

order to quantify the width of the temperature distribution we consider a direct line cut from an area with no thermovoltage signal on the SiO_2 substrate to the SLG/BLG junction with a strong signal (see Figure 9.3 at $V_g = -10\,\mathrm{V}$, orange dashed line). Here the width of the thermovoltage signal should be dominated by the width of the temperature distribution created by the STGM tip. We can fit the thermovoltage signal using a sigmoidal Boltzmann curve $f(x) = y_1 + (y_1 - y_2)/(1 + e^{\frac{x-x_0}{\Delta x}})$ and extract $\Delta x \approx 60$ nm (Figure 9.5d) [241]. This suggests a lateral resolution of $2\Delta x \approx 120$ nm for the measurement and by taking the derivative and fitting the result with a Gaussian curve we arrive at a width of the temperature distribution of $l_{\mathrm{dT}} \approx 1\,\mu\mathrm{m}$ (see Appendix C). Comparing l_{dT} to the length scales observed for the thermovoltages in the experiment, $l_{\mathrm{V}} \geq 3\,\mu\mathrm{m}$ (see Figure 9.5b and c), it is clear that the width of the measured signal can not be explained by limited spatial resolution. Since the thermovoltage is a convolution of $S(x)$ and dT/dx, its width l_{V} is approximately given by the sum of l_{dT} and the length scale associated with a change in the Seebeck coefficient, l_{S}. Knowing l_{dT} and l_{V} then makes it possible to calculate l_{S}, yielding information about band bending due to a transition in the Seebeck coefficient such as at the SLG/BLG junction (similar to the depletion region width in a semiconductor p-n junction, which is determined by the applied voltage and the doping level). Applying this to the STGM line traces across the SLG/BLG junction (shown in Figure 9.5b top) with $l_{\mathrm{V}} \approx 3\,\mu\mathrm{m}$ then gives $l_{\mathrm{S}} \approx 2\,\mu\mathrm{m}$. In addition, the measurement suggests that the transition length of the Seebeck coefficient is doping dependent and decreases for lower charge carrier concentration. While the wrinkle analysed in Figure 9.5c has a similar $l_{\mathrm{S}} \approx 2\,\mu\mathrm{m}$ to the SLG/BLG junction the underlying mechanism is different. For the wrinkle, l_{S} is expected to depend on the elastic properties of graphene whereas l_{S} at the junction is determined by charge carrier density. Importantly, the above analysis suggests that the transition of the Seebeck coefficient, even for an atomically sharp step between two two-dimensional materials, such as a SLG/BLG junction, takes place gradually on a length scale of micrometres.

9.4 Seebeck Coefficient Calculation

Going a step further than just extracting the length scale of the Seebeck coefficient change, we can attempt to recover complete Seebeck coefficient maps from the measured thermovoltage maps. As discussed previously and expressed by equation (9.1), the measured thermovoltage V_{th} is a convolution of the Seebeck coefficient

$S(x)$ and the tip position dependent temperature distribution $T(x)$. With enough knowledge about the temperature distribution it should then be possible to calculate the Seebeck coefficient from the thermovoltage signal using a deconvolution operation. However, in order to perform the deconvolution we have to make three main assumptions: 1) We assume that the heat distribution caused by the STGM tip is given by the Gaussian fit to the derivative of the sigmoidal curve in Figure 9.5e (see also Apendix C). 2) We assume a constant thermal spreading resistance for the scanned surfaces and therefore a constant tip-apex temperature $T_{\text{tip}} \approx 53\,\text{K}$. While this is clearly not justified for the whole sample the error introduced is relatively low when only considering the graphene channel. 3) The thermovoltage is measured along the x-axis in between two sample contacts. Therefore we deconvolute in the x-direction only and neglect any contribution along the y-axis. Here we rotate the thermovoltage maps before deconvolution to satisfy this assumption.
We use a regularized filter in combination with a constraint least-square restoration algorithm to carry out a 1D line deconvolution. To create the 2D Seebeck coefficient map, the quasi two-dimensional temperature distribution is line-by-line deconvoluted with the thermovoltage map (see Appendix C for more details). As the tip is moved over the sample, the centre of the two-dimensional temperature distribution naturally moves as well. At every point in the thermovoltage map we then perform a complete line-by-line deconvolution with the temperature distribution, the result of which is one point in the Seebeck coefficient map.
Such a deconvolution is shown in Figure 9.6a for the rectangular graphene device for the three different gate voltages analysed previously. Importantly, the deconvoluted signal on the contacts is not accurate since we assumed a constant tip-sample interface temperature of $T_{\text{tip}} \approx 53\,\text{K}$, which is not valid on the Au contacts as discussed. However, the graphene channel in between the contacts satisfies assumption 2). The trends of the Seebeck coefficient S in graphene expected from previous reports are observed, with the Seebeck coefficient changing from positive to negative as we sweep the back gate voltage across the CNP [95]. In addition, around the CNP, the Seebeck coefficient displays large local variations and sign changes, giving rise to the chaotic signal observed in the thermovoltage measurements (Figure 9.6a). To compare and evaluate the deconvolution method, we attempt to find the doping dependent Seebeck coefficient of the graphene channel with two additional methods: 1) by evaluating the gate dependent resistance trace of the device using the Mott Formula and 2) by using the temperature difference across the device induced by the STGM tip on top of one of the Au contacts and the corresponding thermovoltage

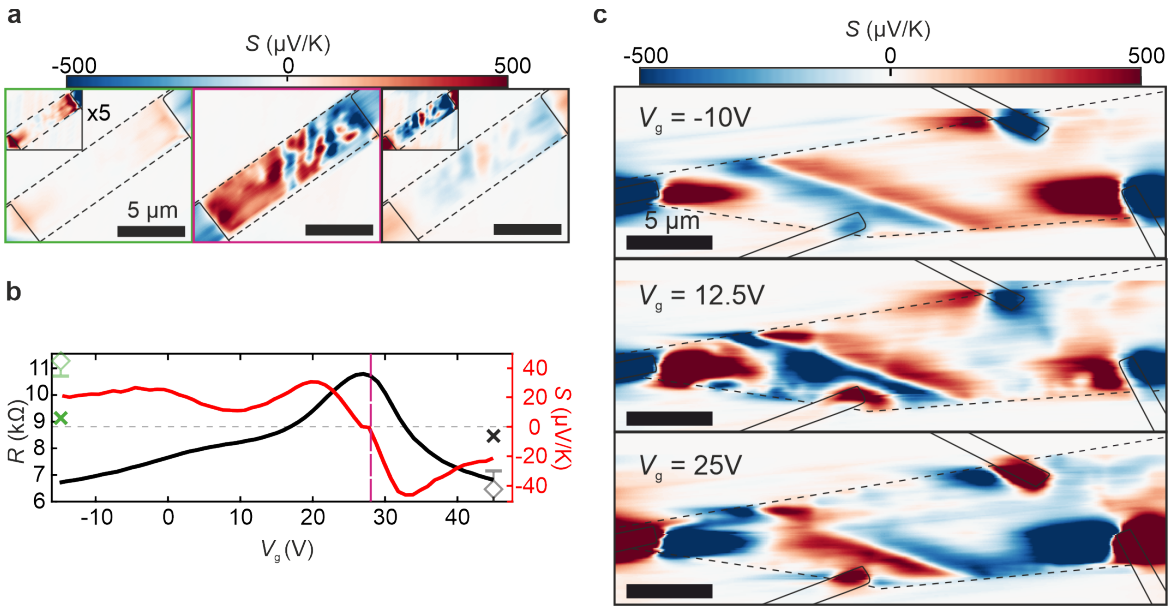


Figure 9.6 a) Deconvolution of the thermovoltage maps shown in Figure 9.2a. The insets show the same map at a sensitivity of $S = -100$ to $100\,\mu V\,K^{-1}$. b) Gatetrace of the rectangular device (black line), Seebeck coefficient calculated from Equation (9.2) (red line), Seebeck coefficient estimated from the thermovoltage maps (semitransparent diamonds) and the Seebeck coefficient extracted out of the deconvolution in a (crosses) as a function of back gate voltage. c) Deconvolution of the thermovoltage maps shown in Figure 9.3. All scale bars denote 5 µm. The dashed black lines show the position of the graphene flake and the black drawn through lines the positions of the gold contacts.

drop to calculate the Seebeck coefficient via $S = -V_{\text{th}}/\Delta T$.
For method 1), the Mott formula as introduced previously in chapter 2 is given by

$$S = -\frac{\pi^2 k_B^2 T}{3|e|}\frac{1}{G}\frac{dG}{dV_g}\frac{dV_g}{dE}\Big|_{E=E_F},$$

where the last part of the formula can be written as $\frac{dV_g}{dE_F}(V_g) = \sqrt{\frac{|e|}{C_g\pi}}\frac{2}{\hbar v_F}\sqrt{|V_g - V_D|}$ [95]. Then the full expression is

$$S = -\frac{\pi^2 k_B^2 T}{3|e|}\frac{1}{G}\frac{dG}{dV_g}\sqrt{\frac{|e|}{C_g\pi}}\frac{2}{\hbar v_F}\sqrt{|V_g - V_D|}\,. \tag{9.2}$$

Equation (9.2) can be evaluated numerically using only the resistance trace of the device shown in Figure 9.2c and the CNP gate voltage $V_{\text{D}} = 28\,\text{V}$, with the Fermi velocity in graphene $v_{\text{F}} = 10^6\,\text{m}\,\text{s}^{-1}$ [219] and the gate capacitance of $C_g = 115\,\text{aF}\,\mu\text{m}^{-2}$ [87]. The gate dependent Seebeck coefficient calculated is shown in Figure 9.6b. The Seebeck coefficient first increases towards the CNP to a maximum of $S \approx 30$ to $40\,\mu\text{V}\,\text{K}^{-1}$, switches signs at the CNP, further decreases to a minimum of $S \approx -45\,\mu\text{V}\,\text{K}^{-1}$ and then increases back to zero.
To calculate S using method 2), the average thermovoltage value on the contacts for a p-doped and n-doped sample are divided by the temperature difference induced by the STGM tip (we assume $\Delta T \approx 1.5\,\text{K}$). Here the thermovoltage values are extracted by plotting their distribution in a bar graph and fitting it with a fourpeaked Gaussian. Then the most likely event is picked, with the error given by the width of the respective Gaussian peak (see Appendix C Figure C.22). This gives S = 5.92 $\pm$3.2 $\mu\text{V}\,\text{K}^{-1}$ and S = $-$4.19 $\pm$1.49 $\mu\text{V}\,\text{K}^{-1}$ for the Seebeck coefficient in a p- and n-doped sample, respectively.
Lastly, the Seebeck coefficient in the graphene channel given by the deconvolution method presented here is extracted from the Seebeck coefficient maps in Figure 9.6a. Again, the S value distribution is plotted in a bar graph and fitted with a four peaked Gaussian, giving S = 44.94 $\pm$5.43 $\mu\text{V}\,\text{K}^{-1}$ and S = $-$42.91 $\pm$9.4 $\mu\text{V}\,\text{K}^{-1}$ for a p- and n-doped sample, respectively.
All three methods to obtain the Seebeck coefficient show quantitative agreement considering the assumptions necessary. Importantly, all methods find the same trend of a change in sign when crossing the CNP, as expected for graphene [95]. While method 2), that is using the thermovoltage measurements, differs here, this is most likely due to the difficulty and error in determining the temperature difference

across the device, ΔT.
This deconvolution method can also be applied to the more complex SLG/BLG sample. As can be seen in Figure 9.6c, there are clearly artefacts around the contacts due to the STGM tip temperature dropping. However, the general behaviour of the Seebeck coefficient predicted by theory and the thermovoltage measurements such as the change in the Seebeck coefficient difference across the SLG/BLG junction, that is $S_{\mathrm{SLG}} < S_{\mathrm{BLG}}$ at $V_{\mathrm{g}} = -10\,\mathrm{V}$ and $S_{\mathrm{SLG}} > S_{\mathrm{BLG}}$ at $V_{\mathrm{g}} = 25\,\mathrm{V}$, are visible [99]. Furthermore, the high fluctuations and sign changes associated with charge puddles can be seen around the CNP in the SLG area.
While the Seebeck coefficient values of up to $500\,\mu\mathrm{V\,K^{-1}}$ extracted in this chapter seem to be too high for a graphene channel, it is important to note that these do not correspond to a global S but rather to local variations in the Seebeck coefficient.

9.5 Conclusion

In this chapter, we have developed a method to record high resolution thermovoltage maps using STGM. By applying STGM to exfoliated graphene devices, we are able to image the effect of Fermi level pinning by metallic contacts on the gate dependent charge carrier distribution, resolve the thermoelectric fingerprint of charge puddles and quantify the length scale of the change in the Seebeck coefficient due to a thickness variation in graphene. Furthermore, STGM makes the strong local impact of strain on the Seebeck coefficient in both SLG and BLG visible. Using the thermovoltage maps recorded we are also able to calculate corresponding Seebeck coefficient maps using a deconvolution and find a good agreement with previously reported methods to extract the Seebeck coefficient.
Compared to the AC thermovoltage measurement in the previous chapter, here we are able to achieve a higher resolution at a high scan rate. This increased resolution enables us to perform a deconvolution to calculate corresponding Seebeck coefficient maps. In addition, the DC approach explored in this chapter ensures that no frequency induced effects are responsible for any phenomena observed in the thermovoltage measurements. Clearly, a combination of an AC approach to measure the Peltier effect and Joule heating with a DC approach to measure the thermovoltage should be used in the future, ensuring a full thermoelectric characterisation of the measured sample.
Yet, STGM on its own presents a valuable and accessible tool to study the local thermoelectric properties of two-dimensional and thin film materials and devices.

Studying planar junctions, local defects and the impact of metal contacts with STGM could open up possible avenues to increase device efficiency in thermoelectric devices and conversely help to inform strategies to eliminate parasitic thermoelectric noise in electronic devices. In addition, STGM could be used in a variety of exotic systems to provide additional and unique sample analysis and control capabilities as discussed in chapter 11.
In the following and last chapter the knowledge acquired about the influence of environmental factors on the local thermoelectric properties in graphene are put to use to design and test a single-material thermocouple.

10

Single Material Graphene Thermocouples

This chapter is based on "Single-Material Graphene Thermocouples" by Achim Harzheim, Fabian Könemann, Bernd Gotsmann, Herre van der Zant and Pascal Gehring published in *Advanced Functional Materials*, 2020, 2000574 [242]. In addition, the results in this chapter have been used to file a patent for a Single-Material Graphene Thermocouple under application number NL 2025000. The author contributions are as follows: AH and PG conceived the study, AH and PG fabricated the devices, AH performed the measurements, AH, PG and HvdZ discussed the results, FK and BG performed the heater calibration, AH wrote the manuscript and all authors commented on the manuscript.

From chapter 8 and 9 we have learned that local influences and material characteristics in two-dimensional materials can have an outsized influence on thermoelectric properties. Most pronounced and previously unexplored is the large change in the Seebeck coefficient due to the size confinement in graphene bow ties (see [205] and chapter 8). This led to the observation of substantial Peltier heating/cooling and bipolar thermovoltage signals. Naturally, this effect can be exploited to produce a device that relies on a change in the Seebeck coefficient, which usually requires joining two different materials with their respective Seebeck coefficients. The simplest such device is a thermocouple, which can be used to sense the temperature difference between its "sensing" (T_{sense}, where the two different materials are joined) and "measuring" end (T_{meas}) expressed as a thermovoltage build up due to the Seebeck coefficient difference [243]. The thermovoltage measured in such a device is given by

$$V_{\text{th}} = -[(S_1 - S_2)(T_{\text{sense}} - T_{\text{meas}})] \,, \tag{10.1}$$

where S_1 and S_2 are the Seebeck coefficients of the two materials used. From equation (10.1) we can see that V_{th} is proportional to the temperature difference $\Delta T = T_{\text{sense}} - T_{\text{meas}}$, making it possible to quantify ΔT via probing the thermovoltage drop.

Thermocouples are one option for on-chip temperature sensing, where accurate temperature information is becoming increasingly important as device downscaling continues [244, 245]. In order to avoid detrimental hot spot generation and inform thermal management, temperature sensors can be distributed along complex electronic circuits or devices to provide feedback to the control system and trigger the redistribution of the thermal load [246, 247]. Thermocouples are an ideal candidate for such temperature sensing as they are relatively cheap, self-powered and their signal stems from an intrinsic material property so they tend to have minimal variations in sensitivity [248].

In this chapter we produce and test thermocouples made out of a single layer of graphene by patterning a U-shaped graphene strip with a wide and a narrow leg. While single-material thermocouples have previously been reported for metals, they tend to have a large footprint and a relatively low sensitivity on the order of $1\,\mu\text{V}\,\text{K}^{-1}$ [249–252]. In addition, their thickness is on the order of hundreds of nm, complicating their integration into devices. Graphene on the other hand is a two-dimensional material and multiple efforts are already underway for its integration in two-dimensional van der Waals structures employing wafer-scale fabrication methods [253, 227]. Graphene is also an ideal candidate for a single material thermocouple due to its high bulk Seebeck coefficient [95] and long electron mean free path (EMFP) even at high temperatures [90].

10.1 Thermocouple Devices

The devices are fabricated from CVD grown graphene that is transferred on top of a Si chip with a 300 nm thick layer of SiO_2. After evaporating Ti/Au contacts on top of the graphene, the device structure (a U-shaped graphene strip contacted at the two ends) is defined via electron beam lithography and subsequent oxygen plasma etching. We fabricate long (4.3 µm) and short (2.5 µm) thermocouples with the bottom of the U-shape next to a meandering heater used to increase the temperature at the thermocouples sensing end to quantify the device performance. The sensing point of the thermocouples is located 700 nm away from the heater and the device orientation is orthogonal to the heater to ensure an equal vertical temperature gradient along

the device length (see Figure 10.1a). The thermocouples consist of a wide and a narrow leg, with the wide leg width kept constant at $w_0 = 1.5\,\mu m$ and the narrow leg width w being varied between 0.2 and 1 µm. Prior to any thermovoltage measurement, the device is probed by recording an IV trace. All devices showed linear IV characteristics and the traces are subsequently used to extract the device resistance R.

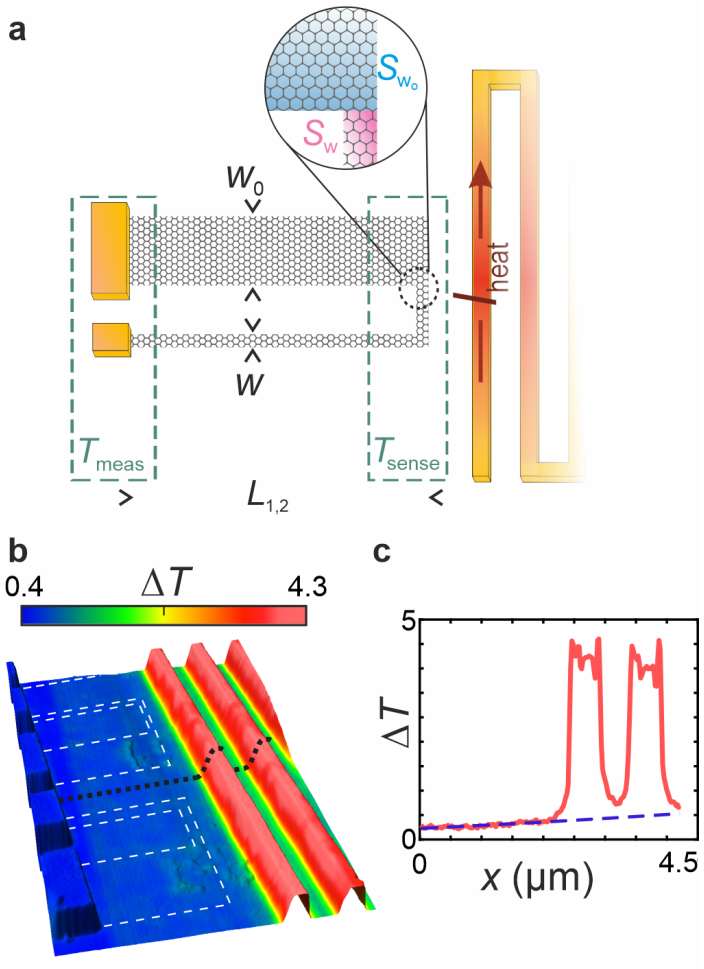


Figure 10.1 a) Schematic depiction of the device structure with the sensing point highlighted with the black dashed circle. b) Temperature distribution of a typical operating device measured using SThM at a heater power of 6.4 mW. The white dashed lines indicate the position of the graphene thermocouples and the black dashed line indicates the line cut shown in c. c) Temperature profile line extracted from (b) (pink line) and fit along the substrate (blue dashed line).

To calibrate the heater and more importantly evaluate the temperature distribution along the thermocouple we perform an SThM measurement of the device at different

heater currents, obtaining multiple temperature profile maps (see Figure 10.1b). Here the SThM is used in active mode, that is a voltage is applied to the cantilever resulting in a temperature rise for an out of contact tip [211]. As reported by Menges *et al.* [165] and introduced in chapter 5, a combined AC and DC method is used that excludes the influence of fluctuations in the tip-sample thermal contact resistance, which can lead to substantial artefacts. The temperature drop can then be quantified by fitting an exponential model, $dT = aI^2e^{bx}$, to a line cut extracted perpendicular to the heater. Here a and b are fitting parameters, I is the heater current and x is the distance along the line cut. The results are shown in Figure 10.1c with the line cut shown in pink and the fit as a dashed blue line. In order to only capture substrate effects, the fitting is started at least 500 nm away from the heater. Using this model, the position of the device relative to the heater and the power dissipated in the heater we can then calculate the temperature drop between the sensing and measuring points for both the long and short devices from a power and distance dependent temperature gradient along the substrate in the units of $\mathrm{K\,m^{-1}\,W^{-1}}$. For a heater power of $P = 1.3\,\mathrm{mW}$, which was used for the majority of the measurements, the temperature difference is then $\Delta T_{\mathrm{long}} = 22.35 \pm 2.97\,\mathrm{mK}$ and $\Delta T_{\mathrm{short}} = 14.3 \pm 2.17\,\mathrm{mK}$ for the long and short devices, respectively. Multiple devices were calibrated and all results were within the uncertainty range of each other. As we will see the error due to device variability is much larger than the standard deviation in the temperature and hence the error in ΔT is neglected for the following analysis.

10.2 Thermocouple Characterization

We start by studying the response of the thermocouple to a current applied to the heater. As is shown in Figure 10.2a, we measure the thermovoltage between the two thermocouple legs at the second harmonic of the applied heater current with an SRS 830 lock-in amplifier using the 2ω method (see chapter 5). A thermovoltage build up in the thermocouple that is proportional to the heater power is observed (see Figure 10.2b). The data shown here is for a short device with length $L_2 = 2.5\,\mu\mathrm{m}$ and a narrow leg width of $w = 0.2\,\mu\mathrm{m}$ since this device configuration is found to perform best as discussed later in this chapter. The temperature difference measured by the thermocouple is caused by Joule heating of the heater via the applied current. Then, in accordance with the Joule-Lenz law, we expect a quadratic relation between the power dissipated in the heater P and the current I applied, $\Delta T = T_{\mathrm{sense}} - T_{\mathrm{meas}} \propto P = I^2R$. From equation 10.1 we can see that a larger temperature difference ΔT caused

by a higher heater power leads to a higher thermovoltage, which is clearly visible in Figure 10.2b. Using the SThM calibration described in the previous section we can convert the heater power into a temperature difference, shown as the top x-axis in Figure 10.2b. In order to increase the sensitivity of the thermocouple, which is on the order of mK, the integration time of the measurement is increased from 1 s to 10 s with the results shown in Figure 10.1b and c respectively. The higher integration time lowers the response threshold of the graphene thermocouples further to $\approx 400\,\mu K$, highlighting their excellent sensing abilities.

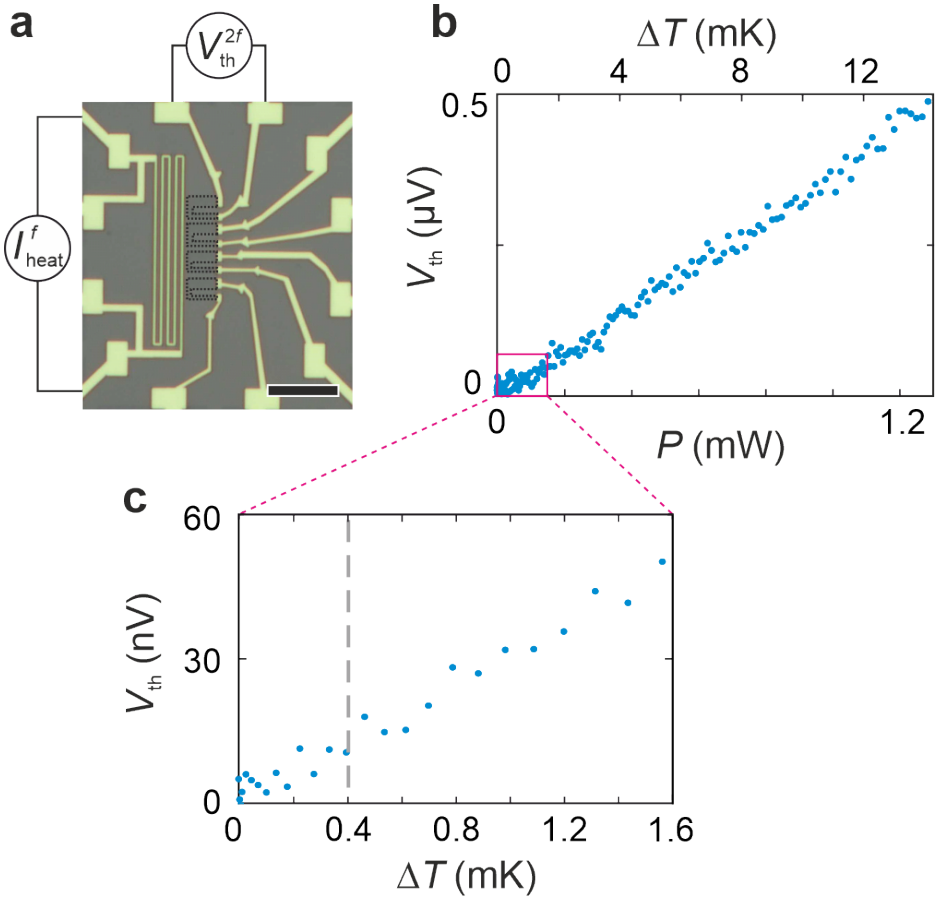


Figure 10.2 a) Optical microscopy image of the device layout including the measuring configuration. The graphene thermocouples are highlighted by the black dotted lines and the scale bar is 10 µm long. b) Thermovoltage response of a short junction $L_2 = 2.5\,\mu m$ with a narrow leg width of $w = 0.2\,\mu m$ as a function of heater power (temperature difference). c) The same measurement as in b with a higher integration time, the grey dashed line indicates the minimum temperature sensitivity.

The reason for the build up of a thermovoltage in the device is a change in the Seebeck coefficient between the wide ($w_0 = 1.5\,\mu m$) and the narrow leg ($w \leq 1\,\mu m$):

from S_{w_0} to S_w. As previously explored in chapter 8, this change in the Seebeck coefficient is caused by the increased influence of electron scattering from the edges of the graphene channel on the EMFP. As previously, the defects and irregularities at the edges of the graphene channel responsible for the scattering are introduced by the oxygen plasma patterning of the devices during fabrication as well as atmospheric contamination. Following the theory developed in chapter 8, we have an expression for the width dependence of the EMFP $l(w) = l_0\left[1 + c_n\left(\frac{l_0}{w}\right)^n\right]^{-1}$ (equation (8.6)), which we can combine with the Mott formula $S = \frac{\pi^2 k_B^2 T}{3e}\frac{1}{R(\epsilon)}\frac{dR(\epsilon)}{d\epsilon}\big|_{\epsilon=\epsilon_F}$ to arrive at a width dependent expression for the Seebeck coefficient in graphene (see chapter 8 for a detailed derivation). As before, l_0 is the bulk mean free path, c_n and n are numerical coefficients specifying the transport mode and the influence of scattering on the mean free path, respectively, and $R(\epsilon)$ is the energy dependent resistance in graphene. Even though the Mott formula can be inaccurate at high temperatures for graphene, it represents a good starting point and has been shown to reproduce trends in experimental data correctly [95]. The width dependent Seebeck coefficient $S(w)$ is then given by equation (8.9) as

$$S(w) = -\frac{\pi^2 k_B^2 T}{3\epsilon_F e}\left[1 + nU\frac{l(w)}{l_0} - (n-1)U\right],$$

where U is again the exponent of any power law dependence of the EMFP on energy, the Fermi energy is $\epsilon_F = \hbar v_F\sqrt{4\pi n/g_s g_v}$ and we use a Fermi velocity of $v_F = 10^6\,\mathrm{m\,s^{-1}}$, a spin and valley degeneracy $g_s = g_v = 2$ and a carrier density $n = 10^{16}\,\mathrm{m^{-2}}$ [254]. Since S decreases for a decreasing width of the graphene channel we expect the Seebeck coefficient difference between S_{w_0} and S_w, to be largest for the smallest w.

We can write the difference in Seebeck coefficients ΔS as

$$\Delta S = S_{w_0} - S_w = \frac{\pi^2 k_B^2 T n U}{3\epsilon_F e}\left[\frac{l(w_o) - l(w)}{l_0}\right]. \tag{10.2}$$

While the Seebeck coefficient in graphene is temperature dependent, due to the small temperature differences on the order of milli Kelvin created by the heater in this experiment we can assume that $S_w(T_{\mathrm{sense}}) \approx S_w(T_{\mathrm{meas}})$ and equally for S_{w_0}.

We then study the width dependence of 110 devices where the narrow channel width is varied from $w = 1\,\mu\mathrm{m}$ to $w = 0.2\,\mu\mathrm{m}$, recording both the thermovoltage and device resistance as shown in Figure 10.3. Here the thermovoltage was recorded at room temperature with a heater power of $P = 1.3$ mW or a temperature difference

of $\Delta T_{\text{long}} = 22.35 \pm 2.97\,\text{mK}$ and $\Delta T_{\text{short}} = 14.3 \pm 2.17\,\text{mK}$. Subsequently, ΔS was calculated from the thermovoltage signal and the temperature difference using equation (10.1). As predicted, a narrower leg width w leads to a higher difference ΔS (Figure 10.3a) and in addition to a higher device resistance (Figure 10.3b) for both long and short devices.

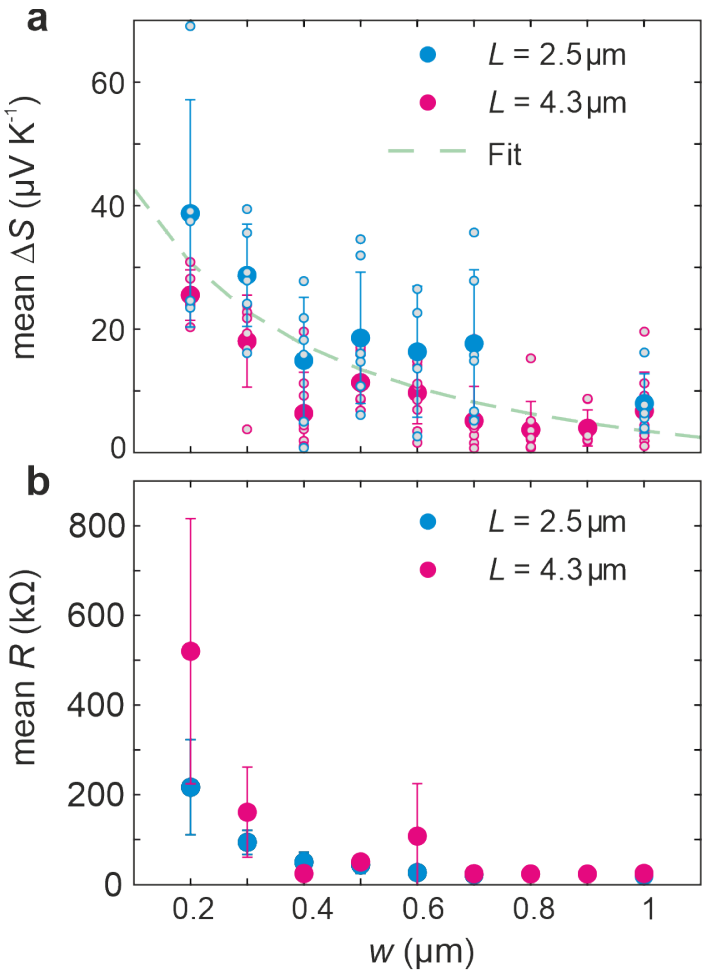


Figure 10.3 a) Mean Seebeck coefficient difference ΔS as a function of narrow leg width w for long ($L_1 = 4.3\,\mu\text{m}$, pink dots) and short devices ($L_2 = 2.5\,\mu\text{m}$, blue dots). The blue and red dot represent the mean value with the grey filled dots indicating single device measurements (with a pink or blue outline respectively) and the error bars the standard deviation with respect to the single device measurements. A fit of the data using equation (10.2) is shown as a green dashed line. b) Device resistance R as a function of narrow leg width w for long ($L_1 = 4.3\,\mu\text{m}$, pink dots) and short devices ($L_2 = 2.5\,\mu\text{m}$, blue dots). The blue and red dot represent the mean value and the error bars the standard deviation with respect to single device measurements.

The device resistance increase can be attributed to the same effect causing the increase in ΔS. Treating CVD graphene on SiO_2 as a diffusive conductor, the conductance is proportional to the EMFP in the diffusive transport regime, $\sigma \propto l_e$ [255]. As the conductance is inversely proportional to the device resistance R, we expect a decreasing EMFP to lead to an increase in resistance $l_e \propto 1/R$. Since a narrower leg width is associated with a smaller EMFP due to the higher influence of scattering at the edges, the device resistance should inversely scale with the narrow leg width. This relationship can be seen in Figure 10.3b.
Due to the EMFP being the determining factor for changes in both the device resistance and ΔS, changes in one quantity due to a variation in the leg width should be mirrored in the other. This can be seen in Figure 10.3 for the long devices (blue dots) where a small dip in the device resistance when changing w from 0.5 to 0.4 µm is reflected in the ΔS signal.
ΔS increases for both long $L_1 = 4.3\,\mu m$ and short $L_2 = 2.5\,\mu m$ devices as the channel width is reduced (Figure 10.3a). This trend in ΔS can be fitted with equation (10.2), using the same fitting parameters for the two lengths while accounting for the different ΔT. The fit gives $c_n = 0.96$, $l_0 = 248\,nm$, $n = 1.08$ and $U = 0.99$ in accordance with the previously extracted parameters in chapter 8 for CVD graphene. The small deviations can be attributed to the different geometry. Again, the U value of almost 1 suggests that mainly Coulomb interaction determines the amplitude of the mean free path, in accordance with scattering centres located along the graphene edges [217, 216]. Due to the uncontrollable nature of the defects introduced by oxygen plasma etching, which ultimately determine the effective EMFP and therefore ΔS, a high variability between individual as well as between long and short devices can be seen. While this leads to a relatively large standard deviation for the ΔS signals a clear trend can be established and, in addition, the Seebeck signal of the short and long devices are within one standard deviation of each other. Overall, a maximum mean sensitivity of $\Delta S \approx 39\,\mu KV$ is measured for a short device $L_2 = 2.5\,\mu m$ with a narrow leg width $w = 0.2\,\mu m$. This sensitivity is over an order of magnitude larger than previously reported values for single-material metal thermocouples [249–251].
In order to further improve the sensitivity of the graphene thermocouples, the two critical dimensions w_0 and w can be further adjusted. w_0 needs to be on the order of the electron free mean path in graphene, ideally multiple µm, to avoid any detrimental influence on the EMFP from electron scattering at the edges. Conversely w should be as small as possible to maximize the influence from electron scattering at the edges. Another avenue to improve the sensing abilities of the graphene thermocou-

ples is to increase the bulk value of the Seebeck coefficient. This can be achieved by oxygen plasma treatment of graphene [256], operating in the hydrodynamic regime [257], encapsulating graphene in hBN [258, 90] or gating graphene to change the carrier concentration and band structure [95, 143]. In addition, it is possible to use exfoliated rather than CVD grown graphene as it has a higher Seebeck coefficient due to its higher EMFP [91]. Exfoliated graphene also possesses less defects, making it better controllable. Yet it should be noted that most of the above mentioned methods have the disadvantage that they limit scalability due to complicating the fabrication process. On the other hand, a better control over the edge configuration of graphene and therefore the electron scattering behaviour is necessary to fabricate reproducible and well-defined thermocouples. While ongoing research in the manipulation of the edge configuration in graphene is encouraging, more sophisticated fabrication processes are needed [259, 260].

10.3 Conclusion

In this chapter a single-material graphene thermocouple made by patterning a U-shaped graphene strip with a wide and narrow leg was studied. Exploiting the width dependence of the Seebeck coefficient in graphene discovered in chapter 8, we are able to fabricate a two-dimensional thermocouple with a sensitivity over an order of magnitude higher than previously reported single-material thermocouples made out of metals. It is found that decreasing the width of the narrow leg increases the device sensitivity, a behaviour that is well captured by the established theoretical framework on the geometric dependence of the thermoelectric properties of graphene. The results presented here could be used to facilitate relatively cheap and simple on-chip thermometry that can be integrated into future graphene circuits, van der Waals heterostructures or even current MOS-FETs. In addition, graphene thermocouples have the potential to be used for the increasingly important task of temperature probing in cells and other living systems [261, 262] due to their relatively small footprint, high sensitivity and graphene's bio inert nature [263].
This chapter can be seen as a representation of the often sought after but seldom achieved full path from fundamental research to a practical application. Starting with the relatively abstract physical concept in chapter 8, that a narrow graphene channel has a lower Seebeck coefficient than bulk graphene due to the increased influence from electron scattering at the edges, we were able to develop a working

single-material graphene thermocouple that displays a substantial improvement over previously developed devices.

11

Conclusions and Outlook

The aim of this thesis was to study the thermoelectric properties in carbon nanostructures. Such thermoelectric studies can open pathways to increase the efficiency in thermoelectric devices and thereby help to make the jump from experimental studies to competitive application. Furthermore, understanding the thermoelectric properties in carbon nanostructures facilitates the elimination of thermoelectric noise in sensitive measurements or devices and can lead to the development of novel sensing applications. Crucially, the concepts developed here are general enough that they can be applied to other low-dimensional systems or bulk thermoelectrics. Below we will give a summary of the experimental results and afterwards an outlook on future developments and possible follow-up studies.

11.1 Summary

The first experiments presented in chapter 6 studying the Seebeck coefficient and power factor of C_{60} molecules highlight the important role of tunnel coupling on the thermoelectric device characteristics. After probing the thermovoltage and electrical conductance separately and modelling the experimental results with a Landauer type and Mott formula model the focus is shifted to the power factor due to its pivotal role in predicting device performance [186]. It was found that both asymmetry in the tunnel coupling to the left and right lead as well as the overall coupling strength with respect to the operating temperature T_0 can decrease the achievable power factor by orders of magnitude. In order to achieve a maximum power factor, the tunnel coupling should be symmetric and equal to $\Gamma \approx 1.1 k_B T_0$. In addition, energetic control over the molecular energy levels is important to maximize the

electrical conductance and thermovoltage and thereby the power factor.
In chapter 7, this relationship between coupling and operating temperature is further explored by measuring the power factor of graphene quantum dots as a function of temperature. While the results of chapter 6 are confirmed, an additional environmental impact on the thermoelectric properties in zero-dimensional structures is found. For non-ideal heat exchanging contacts, which are not a perfect heat conductor, there is strong evidence that the quantum dot serves as a quantum heat valve, effectively suppressing the thermovoltage and power factor around the resonance. Conversely, the electron degeneracy in a quantum dot leads to a shift in energy of the electrical conductance with respect to the thermovoltage, which can be used to increase the achievable power factor. Since contacts being non-ideal heat conductors will almost universally be relevant for any material albeit with different strengths, these results should be used to inform future device designs.
After observing the large impact environmental factors including the leads can have on the thermoelectric properties of the measured devices, a more localized measurement method using an SThM is employed in chapter 8. It is found that a graphene bow tie exhibits a thermoelectric and Peltier effect around a 100 nm constriction, with substantial Peltier heating and cooling of a few degrees on each side of the constriction. This behaviour is replicated in other structures and attributed to an increased influence of electron edge scattering for a narrow graphene channel. As electron edge scattering becomes more dominant with decreasing width, the electron mean free path in graphene and with it the Seebeck coefficient decreases. This knowledge about a change in the Seebeck coefficient due to geometrical considerations can be used to inform the design of devices relying on a difference in the Seebeck coefficient ΔS such as the thermocouple explored in chapter 10. On the other hand, this observation can help to eliminate electric noise due to undesirable thermoelectric effects in precision measurements on nanoscale devices.
A similar local scanning method is further developed in chapter 9 where a DC instead of an AC approach is used. This enables fast high resolution measurements of the thermovoltage in multiple graphene devices, revealing the influence of metallic contacts and thickness changes on the local thermoelectric properties in graphene. We are, in addition, able to extract the length scale on which the Seebeck coefficient changes, which even for an atomically sharp junction is on the order of µm, and can reconstruct Seebeck coefficient maps from the measured thermovoltage maps.
Lastly, the change in Seebeck coefficient for a narrow graphene channel observed in chapter 8 is used to fabricate a single-material graphene thermocouple in chapter 10.

The device is designed as a U-shaped graphene strip, consisting of one wide leg and one narrow leg with the temperature sensing taking place at the meeting point of the wide and narrow leg. Testing different device structures, a maximum sensitivity of $\Delta S \approx 39\,\mu V K^{-1}$ is found, which is over an order of magnitude higher than that of previously reported single-material metal thermocouples. Such thermometry that can be integrated into van der Waals heterostructures and future graphene circuits enables localized on-chip temperature probing. In order to improve on the current device, a better control over the edge structure and overcoming of fabrication limitations should enable a more reproducible thermocouple with an even higher sensitivity. In addition, the same principle used here can potentially be applied to fabricate a Peltier element, enabling targeted spot cooling and heating.

Moving forward, as this thesis has shown, device specific influences in zero-dimensional thermoelectric devices such as tunnel coupling or energy level degeneracy can increase or decrease the achievable power factor by orders of magnitude. More likely than not, additional factors impacting the thermoelectric performance in such devices can be found through further studies. New research into environmental influences on the power factor can play an important role in improving the efficiency of thermoelectric devices and enable their competitiveness with regular thermogenerators. Furthermore, the already achieved results presented here should inform future device designs. It is clearly advisable to ensure control over the tunnel coupling to the leads through for example local side gates and ideally be able to adjust the temperature in forthcoming experimental setups. Moreover, a structure with a high electron degeneracy should be explored as a possible path to increasing the power factor via a shift in the electrical conductance. Ideally the studies presented here should be complemented by measuring the thermoelectric properties of a QD as a function of tunnel coupling only. In addition, the interplay between the different thermal conductivities in QD devices should be further studied not only to boost efficiency but also as it can help control the heat flow through the structure similar to what was recently demonstrated by fabricating a nanoscale heat valve [264].

Fundamentally, thermoelectric measurements can not only highlight strategies to boost device efficiency but also reveal elementary physical effects. Especially on a local scale such effects can inform the design of novel devices and impact future research directions and measurement decisions. While one successful example is the single-material thermocouple characterized in chapter 10, in general applications

for temperature sensing or spot cooling that can be integrated into current circuit structures or future two-dimensional circuits will play an important role. Lastly, an in-depth understanding of the causes of local and global thermoelectric effects will help design nanoscale devices without thermoelectric noise components.

In the following, additional projects and research directions that were discussed and attempted during this work, but could unfortunately not be fully realized due to time constraints, and possible follow-up studies are presented.

11.2 Additional Systems for Thermoelectric Measurements

While the focus of this thesis is on carbon nanostructures and there mostly on graphene, a host of other two-dimensional materials have emerged in the past decade. Apart from the general need for a sufficient thermoelectric characterisation for a majority of these materials, intriguing effects are expected when manipulating and combining these materials. Similar to graphene, nanostructuring in novel two-dimensional materials should lead to a change in the local thermoelectric properties and in addition heterostructures, junctions of different materials, as well as twisted devices offer a wealth of other possible pathways to change thermoelectric behaviour. Here a few avenues for exploration are highligthed.

Valleytronics. Similar to electron degeneracy investigated in chapter 7, other intrinsic properties of charge carriers have an influence on thermoelectric properties in devices. While spintronics and the spin Seebeck effect have been explored recently [265–267], another degree of freedom, the valley degeneracy, has been mostly neglected due to the difficulty of controlling this parameter. However, recent advances in manipulating valley parameters in graphene should allow for an in-depth examination of the connection between thermoelectrics and valley transport [268].

Graphene Nanoribbons. In this thesis, two-dimensional and zero-dimensional carbon structures were characterized. A one-dimensional system bridging the gap between these structures are graphene nanoribbons (GNRs). GNRs are thin stripes of graphene only a few nanometer wide that have been widely theoretically investigated and are believed to exhibit large ZT values [144, 269, 197]. However, these reports assumed a well-defined edge configuration, which has only recently been accomplished [270] and no representative thermoelectric studies have been

performed yet.
Using the device structure employed to measure C_{60} molecules in chapter 6 would enable the characterization of the global thermoelectric properties of GNRs. GNR structures, ideally comprising a graphene nanogap bridged by a GNR, thereby facilitating a good contact between the GNR and the leads, also represent an ideal system to employ STGM. Not only would STGM make it possible to visualize the local thermoelectric properties of GNRs but in addition the exact geometry of the junction can be inferred from the simultaneously acquired topography map. The main downside of using an STGM setup is the difficulty in reaching the low temperature necessary to observe quantization effects in the GNRs, though low temperature SThMs are under development and higher temperature thermoelectric properties of GNRs remain interesting.
Twisted Heterostructures. The combination of different two-dimensional materials makes it possible to individually address and manipulate thermoelectric, thermal and electronic properties of a device. Going one step further, twisted heterostructures can lead to a change in the band structure and behaviour of the material used and induce exotic effects such as the recently discovered superconductivity in twisted bilayer graphene [271]. These changes in the band structure, such as flat bands, which are already realized in twisted graphene [272], often lead to large local changes in the electron density of states, which can in turn result in a large Seebeck coefficient [273, 274].
In addition to the global thermoelectric properties arising from twisted devices, the local electronic phenomena in the resulting Moiré superlattices are of interest. These can be accessed with a thermoelectric scanning technique such as STGM. While some work in this direction has been done on twisted bilayer graphene using a scanning photocurrent setup [275], plenty of other twisted two-dimensional materials, antidot lattices and heterostructures with combinations of different materials have so far not been studied.
A Case for Additional STGM Measurements. In general, STGM represents a compelling alternative to global thermoelectric measurements in two-dimensional but also other low-dimensional structures. Even as temperatures below 150 K are not yet readily attainable, developments aimed at achieving low temperature SThM setups are under way. Lower temperatures would enable STGM to be used for the complete thermoelectric characterization of low-dimensional devices, which display a quantization of energy or Coulomb blockade only at sufficiently low temperatures (see chapter 2).

Close to room temperature, STGM already gives detailed information about the local thermoelectric effect and the influence from strain or contacts (studied in graphene devices here), which may differ from material to material and can display a significant Peltier or thermoelectric effect. At the same time, STGM can be used to reproduce results achieved by a global measurements. By placing the tip on and heating up one side of a device, such as a Au contact, a global thermovoltage measurement can be recreated, while an additional spatial distribution can be obtained by scanning the sample.

11.3 Hydrodynamics and Thermoelectrics

Another newly emerging research field that has seen little to no thermoelectric studies yet, are hydrodynamic phenomena, where strong electron-electron interaction leads to novel effects such as viscous flow and an enhancement of the thermal conductivity as a result of the decoupling of charge and heat currents [276, 277]. While overall results can be described well with the available theory, local patterns of hydrodynamic flow are still disputed (see, for example, the vortex or no vortex debate [278]). Hydrodynamic electron flow, and specifically electron vortices or whirlpools, should result in distinctive heating patterns compared to ohmic behaviour [279], making SThM measurements an attractive way to characterize hydrodynamic flow properties. However, apart from measuring the local temperature distribution or Peltier and Joule heating, an SThM system could also be used to locally manipulate the sample. Since the hydrodynamic effect is temperature dependent, an STGM setup can use its heated tip to locally change or switch off hydrodynamic flow. While temperatures significantly below room temperature are needed for hydrodynamic measurements these are already reachable in SThM setups [229].
Lastly, one of the most intriguing effects in hydrodynamic systems is the phenomenon of second sound. Second sound denotes the transmission of a heatwave with negligible damping in a hydrodynamic system (similar to the transmission of sound waves, hence the name), compared with conventional heat diffusion. This can result in almost lossless transmission of heat pulses in two-dimensional systems but as it requires an accurate and fast way to create and measure heat pulses there have been few investigations yet.

References

[1] Jian He and Terry M Tritt. Advances in thermoelectric materials research: Looking back and moving forward. *Science*, 357(6358):eaak9997, sep 2017.

[2] R. Amatya and R. J. Ram. Trend for thermoelectric materials and their earth abundance. *Journal of Electronic Materials*, 41(6):1011–1019, jun 2012.

[3] Xiao Zhang and Li Dong Zhao. Thermoelectric materials: Energy conversion between heat and electricity. *Journal of Materiomics*, 1(2):92–105, jun 2015.

[4] Anja Slikkerveer and Frederik A. de Wolff. Pharmacokinetics and Toxicity of Bismuth Compounds. *Medical Toxicology and Adverse Drug Experience*, 4(5):303–323, oct 1989.

[5] A. F. Ioffe, L. S. Stil'bans, E. K. Iordanishvili, T. S. Stavitskaya, A. Gelbtuch, and George Vineyard. Semiconductor Thermoelements and Thermoelectric Cooling. *Physics Today*, 12(5):42–42, 2009.

[6] Zhi Gang Chen, Guang Hana, Lei Yanga, Lina Cheng, and Jin Zou. Nanostructured thermoelectric materials: Current research and future challenge. *Progress in Natural Science: Materials International*, 22(6):535–549, dec 2012.

[7] Maria Telkes. The efficiency of thermoelectric generators. I. *Journal of Applied Physics*, 18(12):1116–1127, dec 1947.

[8] H J Goldsmid and R W Douglas. The use of semiconductors in thermoelectric refrigeration. *British Journal of Applied Physics*, 5(11):386–390, dec 1954.

[9] M.V. Vedernikov and E.K. Iordanishvili. A.F. Ioffe and origin of modern semiconductor thermoelectric energy conversion. In *Seventeenth International Conference on Thermoelectrics. Proceedings ICT98 (Cat. No.98TH8365)*, pages 37–42. IEEE, 2002.

[10] L. D. Hicks and M. S. Dresselhaus. Thermoelectric figure of merit of a one-dimensional conductor. *Physical Review B*, 47(24):16631–16634, jun 1993.

[11] L D Hicks and M S Dresselhaus. Effect of quantum-well structures on the thermoelectric figure of merit. *Physical Review B*, 47(19):12727–12731, 1993.

[12] Maria Ibáñez, Zhishan Luo, Aziz Genç, Laura Piveteau, Silvia Ortega, Doris Cadavid, Oleksandr Dobrozhan, Yu Liu, Maarten Nachtegaal, Mona Zebarjadi, Jordi Arbiol, Maksym V. Kovalenko, and Andreu Cabot. High-performance thermoelectric nanocomposites from nanocrystal building blocks. *Nature Communications*, 7:10766, 2016.

[13] T. C. Harman, P. J. Taylor, M. P. Walsh, and B. E. LaForge. Quantum Dot Superlattice Thermoelectric Materials and Devices. *Science*, 297(5590), 2002.

[14] Myoung-Jae Lee, Ji-Hoon Ahn, Ji Ho Sung, Hoseok Heo, Seong Gi Jeon, Woo Lee, Jae Yong Song, Ki-Ha Hong, Byeongdae Choi, Sung-Hoon Lee, and Moon-Ho Jo. Thermoelectric materials by using two-dimensional materials with negative correlation between electrical and thermal conductivity. *Nature Communications*, 7:12011, 2016.

[15] Devender, Pascal Gehring, Andrew Gaul, Alexander Hoyer, Kristina Vaklinova, Rutvik J. Mehta, Marko Burghard, Theodorian Borca-Tasciuc, David J. Singh, Klaus Kern, and Ganpati Ramanath. Harnessing Topological Band Effects in Bismuth Telluride Selenide for Large Enhancements in Thermoelectric Properties through Isovalent Doping. *Advanced Materials*, 28(30):6436–6441, 2016.

[16] L.-D. Zhao, S.-H. Lo, Y. Zhang, H. Sun, G. Tan, C. Uher, C. Wolverton, V. P. Dravid, and M. G. Kanatzidis. Ultralow thermal conductivity and high thermoelectric figure of merit in SnSe crystals. *Nature*, 508(7496), 2014.

[17] Yucheng Lan, Austin Jerome Minnich, Gang Chen, and Zhifeng Ren. Enhancement of thermoelectric figure-of-merit by a bulk nanostructuring approach. *Advanced Functional Materials*, 20(3):357–376, feb 2010.

[18] Thomas Ihn. *Semiconductor Nanostructures: Quantum States and Electronic Transport*, volume 9780199534. Oxford University Press, nov 2010.

[19] Yuli V. Nazarov and Yaroslav M. Blanter. *Quantum transport: Introduction to nanoscience*, volume 9780521832. Cambridge University Press, Cambridge, 2009.

[20] C M Finch, V M García-Suárez, and C J Lambert. Giant thermopower and figure of merit in single-molecule devices. *Physical Review B - Condensed Matter and Materials Physics*, 79(3), 2009.

[21] P N Butcher. Thermal and electrical transport formalism for electronic microstructures with many terminals. *Journal of Physics: Condensed Matter*, 2(22):4869–4878, jun 1990.

[22] U Sivan and Y Imry. Multichannel Landauer formula for thermoelectric transport with application to thermopower near the mobility edge. *Physical Review B*, 33(1):551–558, 1986.

[23] Yaakov Kleeorin, Holger Thierschmann, Hartmut Buhmann, Antoine Georges, Laurens W. Molenkamp, and Yigal Meir. How to measure the entropy of a mesoscopic system via thermoelectric transport. *Nature Communications*, 10(1):1–8, dec 2019.

[24] D. Gammon, E. S. Snow, B. V. Shanabrook, D. S. Katzer, and D. Park. Fine Structure Splitting in the Optical Spectra of Single GaAs Quantum Dots. 76(16), 1996.

[25] L. A. Ponomarenko, F. Schedin, M. I. Katsnelson, R. Yang, E. W. Hill, K. S. Novoselov, and A. K. Geim. Chaotic Dirac Billiard in Graphene Quantum Dots. *Science*, 320(5874), 2008.

[26] D. Kufer, I. Nikitskiy, T. Lasanta, G. Navickaite, F. H. L. Koppens, and G. Konstantatos. Hybrid 2D-0D MoS_2-PbS Quantum Dot Photodetectors. *Advanced Materials*, 27(1), 2015.

[27] W. Lu, J. Xiang, B. P. Timko, Y. Wu, and C. M Lieber. One-dimensional hole gas in germanium/silicon nanowire heterostructures. *Proceedings of the National Academy of Sciences of the United States of America*, 102(29), 2005.

[28] A. M. Rao, E. Richter, Shunji Bandow, Bruce Chase, P. C. Eklund, K. A. Williams, S. Fang, K. R. Subbaswamy, M. Menon, A. Thess, R. E. Smalley, G. Dresselhaus, and M. S. Dresselhaus. Diameter-Selective Raman Scattering from Vibrational Modes in Carbon Nanotubes. *Science*, 275(5297), 1997.

[29] R. Hanson, L. P. Kouwenhoven, J. R. Petta, S. Tarucha, and L. M. K. Vandersypen. Spins in few-electron quantum dots. *Rev. Mod. Phys.*, 79(4), 2007.

[30] J. M. Thijssen and H. S.J. Van Der Zant. Charge transport and single-electron effects in nanoscale systems. *Physica Status Solidi (B) Basic Research*, 245(8):1455–1470, aug 2008.

[31] B. R. Snell, P.H. Beton, P. C. Main, A. Neves, J. R. Owers-Bradley, L. Eaves, M. Henini, O. H. Hughes, S. P. Beaumont, and C. D. W. Wilkinson. Quantised Hall effect and magnetoresistance through a quantum point contact. *J. Phys.: Condens. Matter J. Phys.: Condens. Matter l*, 1(40), 1989.

[32] R. H. Blick, R. J. Haug, J. Weis, D. Pfannkuche, K. V. Klitzing, and K. Eberl. Single-electron tunneling through a double quantum dot: The artificial molecule. *Physical Review B*, 53(12), 1996.

[33] H. W. Ch. Postma, T. Teepen, Z. Yao, M. Grifoni, and C. Dekker. Carbon Nanotube Single-Electron Transistors at Room Temperature. *Science*, 293(5527), 2001.

[34] E. A. Osorio, T. Bjørnholm, J.-M. Lehn, M. Ruben, and H. S. J. van der Zant. Single-molecule transport in three-terminal devices. *Journal of physics. Condensed matter : an Institute of Physics journal*, 20(37), 2008.

[35] K. A. Matveev. Coulomb blockade at almost perfect transmission. 51(3), 1995.

[36] M. L. Perrin, E. Burzurí, and H. S. J. van der Zant. Single-molecule transistors. *Chem. Soc. Rev.*, 44(4), 2015.

[37] C. S. Lau, H. Sadeghi, G. Rogers, S. Sangtarash, P. Dallas, K. Porfyrakis, J. H. Warner, C. J. Lambert, G. A. D. Briggs, and J. A. Mol. Redox-Dependent Franck-Condon Blockade and Avalanche Transport in a Graphene-Fullerene Single-Molecule Transistor. *Nano Letters*, 16(1), 2016.

[38] B. C. Stipe, M. A. Rezaei, and W. Ho. Single-molecule vibrational spectroscopy and microscopy. *Science*, 280(5370), 1998.

[39] H. Grabert and M. H. Devoret. *Single charge tunneling : Coulomb blockade phenomena in nanostructures*. Springer US, New York, 2004.

[40] T. Böhler, A. Edtbauer, and E. Scheer. Conductance of individual C 60 molecules measured with controllable gold electrodes. *Physical Review B*, 76(12), 2007.

[41] M. Galperin, M. A. Ratner, A. Nitzan, and A. Troisi. Nuclear Coupling and Polarization in Molecular Transport Junctions: Beyond Tunneling to Function. *Science*, 319(5866), 2008.

[42] P. Liljeroth, J. Repp, and G. Meyer. Current-Induced Hydrogen Tautomerization and Conductance Switching of Naphthalocyanine Molecules. *Science*, 317(5842), 2007.

[43] L. H. Yu, Z. K. Keane, J. W. Ciszek, L. Cheng, M. P. Stewart, J. M. Tour, and D. Natelson. Inelastic Electron Tunneling via Molecular Vibrations in Single-Molecule Transistors. *Physical Review Letters*, 93, 2005.

[44] P. L. McEuen, H. Park, J. Park, A. K. L. Lim, E. H. Anderson, and A. P. Alivisatos. Nanomechanical oscillations in a single-C60 transistor. *Nature*, 407(6800), 2000.

[45] X. H. Qiu, G. V. Nazin, and W. Ho. Vibronic States in Single Molecule Electron Transport. *Physical Review Letters*, 92(20), 2004.

[46] K. Behnia. *Fundamentals of Thermoelectricity*. Oxford University Press, Oxford, 2015.

[47] C. Jeong, S. Datta, and M. S. Lundstrom. Full dispersion versus Debye model evaluation of lattice thermal conductivity with a Landauer approach. *J. Appl. Phys.*, 109(106), 2011.

[48] C. Jeong, R. Kim, M. Luisier, S. Datta, and M. Lundstrom. On Landauer versus Boltzmann and full band versus effective mass evaluation of thermoelectric transport coefficients. *Journal of Applied Physics*, 107(2), 2010.

[49] M Buttiker. Four-Terminal Phase-Coherent Conductance. *Physical Review Letters*, 57(14), 1986.

[50] M. Büttiker. Capacitance, admittance, and rectification properties of small conductors. *J. Phys.: Condens. Matter J. Phys.: Candens. Matter*, 5(50), 1993.

[51] S. Kurth, G. Stefanucci, C.-O. Almbladh, A. Rubio, and E. K. U. Gross. Time-dependent quantum transport: A practical scheme using density functional theory. *Physical Review B*, 72(3), 2005.

[52] J. M. Ziman and John M. *Principles of the theory of solids*. Cambridge University Press, Cambridge, 1972.

[53] N. W. Ashcroft and N. D.. Mermin. *Solid state physics*. Holt, Rinehart and Winston, New York, 1976.

[54] R. Landauer. Spatial Variation of Currents and Fields Due to Localized Scatterers in Metallic Conduction. *IBM Journal of Research and Development*, 1(3), 1957.

[55] M. Büttiker. Role of quantum coherence in series resistors. *Physical Review B*, 33(5), 1986.

[56] P. Streda. Quantised thermopower of a channel in the ballistic regime. *Journal of Physics: Condensed Matter*, 1(5), 1989.

[57] H. Van Houten, L. W. Molenkamp, J. Beenakker, and C. T. Foxons. Thermoelectric properties of quantum point contacts. *Semicond. Sci. Technol. B215 Semicond. Sci. Technol*, 7(38), 1992.

[58] K. Balzer and M. Bonitz. *Nonequilibrium Green's Functions Approach to Inhomogeneous Systems*, volume 867 of *Lecture Notes in Physics*. Springer Berlin Heidelberg, Berlin, 2013.

[59] Juan Carlos. Cuevas and Elke. Scheer. *Molecular electronics : an introduction to theory and experiment*. World Scientific, Munich, 2010.

[60] M. Paulsson and S. Datta. Thermoelectric effect in molecular electronics. *Physical Review B*, 67(24), 2003.

[61] G. D. Mahan, T. And, and J. 0. Sofo. The best thermoelectric. *Proceedings of the National Academy of Sciences of the United States of America*, 93(15), 1996.

[62] T. J. Scheidemantel, C. Ambrosch-Draxl, T. Thonhauser, J. V. Badding, and J. O. Sofo. Transport coefficients from first-principles calculations. *Physical Review B*, 68(12), 2003.

[63] R. Franz and G. Wiedemann. Ueber die Wärme-Leitungsfähigkeit der Metalle. *Annalen der Physik und Chemie*, 165(8), 1853.

[64] T. J. Seebeck. Ueber die magnetische Polarisation der Metalle und Erze durch Temperaturdifferenz. *Annalen der Physik*, 82(3), 1826.

[65] J. P. Small, K. M. Perez, and P. Kim. Modulation of Thermoelectric Power of Individual Carbon Nanotubes. *Physical Review Letters*, 95(25), 2003.

[66] M. Jonson and G. D. Mahan. Mott's formula for the thermopower and the Wiedemann-Franz law. *Physical Review B*, 21(10), 1980.

[67] A. M. Lunde and K. Flensberg. On the Mott formula for the thermopower of non-interacting electrons in quantum point contacts. *J. Phys.: Condens. Matter*, 17(25), 2005.

[68] Laura Rincon-Garcia, Charalambos Evangeli, Gabino Rubio-Bollinger, and Nicolas Agrait. Thermopower measurements in molecular junctions. *Chem. Soc. Rev.*, 45:4285–4306, 2016.

[69] Y. Dubi and M. D. Ventra. Colloquium: Heat flow and thermoelectricity in atomic and molecular junctions. *Reviews of Modern Physics*, 83(1), 2011.

[70] F. Ghahari, H.-Y. Xie, T. Taniguchi, K. Watanabe, M. S. Foster, and P. Kim. Enhanced Thermoelectric Power in Graphene: Violation of the Mott Relation by Inelastic Scattering. *Physical Review Letters*, 116(13), 2016.

[71] C. W. J. Beenakker and A. A. M. Staring. Theory of the thermopower of a quantum dot. *Physical Review B*, 46(15), 1992.

[72] Y.-M. Choi, R. Lee, D.-S .and Czerw, P.-W. Chiu, N. Grobert, M. Terrones, M. Reyes-Reyes, H. Terrones, J.-C. Charlier, P. M. Ajayan, S. Roth, D. L. Carroll, and Y.-W. Park. Nonlinear Behavior in the Thermopower of Doped Carbon Nanotubes Due to Strong, Localized States. *Nano Letters*, 3(6), 2003.

[73] A. S. Dzurakt, C. G. Smithl, L. Martin-Morenois, M. Peppert$, D. A. Ritchiet, G. A. C. Jonest, and D. G. Haskot. Thermopower of a one-dimensional ballistic constriction in the non-linear regime. *J. Phys.: Condens. Matter*, 5(43), 1993.

[74] R. Venkatasubramanian, E. Siivola, T. Colpitts, and B. O'Quinn. Thin-film thermoelectric devices with high room-temperature figures of merit. *Nature*, 413(6856), 2001.

[75] C. Fu, S. Bai, Y. Liu, Y. Tang, L. Chen, X. Zhao, and T. Zhu. Realizing high figure of merit in heavy-band p-type half-Heusler thermoelectric materials. *Nature Communications*, 6(8144), 2015.

[76] H. J. Wu, F S .an.d Wu D an.d Pei Y L .an.d Tong X an.d Kanatzidis M G. Zhao, L.-D an.d Zheng, and J. Q. He. *Nature Communications*, 5(4515), 2014.

[77] Jakub K. Sowa. *Vibrational effects in quantum transport through single-molecule junctions*. PhD thesis, 2019.

[78] Jakub K. Sowa, Jan A. Mol, G. Andrew D. Briggs, and Erik M. Gauger. Beyond Marcus theory and the Landauer-Büttiker approach in molecular junctions: A unified framework. *Journal of Chemical Physics*, 149(15):154112, oct 2018.

[79] Lars Onsager. Reciprocal relations in irreversible processes. I. *Physical Review*, 37(4):405–426, feb 1931.

[80] H. W. Kroto, J. R. Heath, S. C. O'Brien, R. F. Curl, and R. E. Smalley. C60: Buckminsterfullerene. *Nature*, 318:162–163, 1985.

[81] Sumio Iijima. Helical microtubules of graphitic carbon. *Nature*, 354(6348):56–58, 1991.

[82] Rania Bakry, Rainer M Vallant, Muhammad Najam-ul Haq, Matthias Rainer, Zoltan Szabo, Christian W Huck, and Günther K Bonn. Medicinal applications of fullerenes. *International journal of nanomedicine*, 2(4):639–49, 2007.

[83] Ray H Baughman, Anvar A Zakhidov, and Walt A de Heer. Carbon nanotubes–the route toward applications. *Science*, 297(5582):787–92, 2002.

[84] Markita Patricia Landry, Hiroki Ando, Allen Y. Chen, Jicong Cao, Vishal Isaac Kottadiel, Linda Chio, Darwin Yang, Juyao Dong, Timothy K. Lu, and Michael S. Strano. Single-molecule detection of protein efflux from microorganisms using fluorescent single-walled carbon nanotube sensor arrays. *Nature Nanotechnology*, 12(4):368–377, 2017.

[85] McClure J. W. Band structure of graphite and de haas-van alphen effect. *Physical Review Letters*, 108(1):612, 1957.

[86] Novosolev et al. Electric field effect in atomically thin carbon films. *Science*, 306(5696):666–669, 2004.

[87] Yuanbo Zhang, Yan Wen Tan, Horst L. Stormer, and Philip Kim. Experimental observation of the quantum Hall effect and Berry's phase in graphene. *Nature*, 438(7065):201–204, nov 2005.

[88] A. K. Geim. Graphene: Status and Prospects. *Science*, 324(5934), 2009.

[89] Novosolev et al. Room-temperature quantum hall effect in graphene. *Science*, 315(1379):5817, 2007.

[90] Luca Banszerus, Michael Schmitz, Stephan Engels, Matthias Goldsche, Kenji Watanabe, Takashi Taniguchi, Bernd Beschoten, and Christoph Stampfer. Ballistic transport exceeding 28 micrometers in cvd grown graphene. *Nano Lett.*, 16(2):1387–1391, 2016.

[91] K. S. Novoselov, V. I. Falko, L. Colombo, P. R. Gellert, M. G. Schwab, and K. Kim. A roadmap for graphene. *Nature*, 490(7419):192–200, 2012.

[92] Alexander A. Balandin. Thermal properties of graphene and nanostructured carbon materials. *Nature Materials*, 10(8):569–581, 2011.

[93] A. K. Geim and K. S. Novoselov. The rise of graphene. *Nature Materials*, 6(3):183–191, mar 2007.

[94] Alberto Bianco, Hui Ming Cheng, Toshiaki Enoki, Yury Gogotsi, Robert H. Hurt, Nikhil Koratkar, Takashi Kyotani, Marc Monthioux, Chong Rae Park, Juan M.D. Tascon, and Jin Zhang. All in the graphene family - A recommended nomenclature for two-dimensional carbon materials. *Carbon*, 65:1–6, dec 2013.

[95] Yuri M. Zuev, Willy Chang, and Philip Kim. Thermoelectric and magnetothermoelectric transport measurements of graphene. *Physical Review Letters*, 102(9), mar 2009.

[96] Peng Wei, Wenzhong Bao, Yong Pu, Chun Ning Lau, and Jing Shi. Anomalous thermoelectric transport of dirac particles in graphene. *Physical Review Letters*, 102(16), 2009.

[97] I. J. Vera-Marun, J. J. Van Den Berg, F. K. Dejene, and B. J. Van Wees. Direct electronic measurement of Peltier cooling and heating in graphene. *Nature Communications*, 12, 2015.

[98] Eduardo J.H. Lee, Kannan Balasubramanian, Ralf Thomas Weitz, Marko Burghard, and Klaus Kern. Contact and edge effects in graphene devices. *Nature Nanotechnology*, 3(8):486–490, 2008.

[99] Y. Xu, X. Chen, J.-S. Wang, B.-L. Gu, and W. Duan. Thermal transport in graphene junctions and quantum dots. *Physical Review B*, 81(19), 2010.

[100] K. S. Novoselov, D. Jiang, F. Schedin, T. J. Booth, V. V. Khotkevich, S. V. Morozov, and A. K. Geim. Two-dimensional atomic crystals. *Proceedings of the National Academy of Sciences of the United States of America*, 102(30):10451–10453, jul 2005.

[101] Sukang Bae, Hyeongkeun Kim, Youngbin Lee, Xiangfan Xu, Jae Sung Park, Yi Zheng, Jayakumar Balakrishnan, Tian Lei, Hye Ri Kim, Young Il Song, Young Jin Kim, Kwang S. Kim, Barbaros Özyilmaz, Jong Hyun Ahn, Byung Hee Hong, and Sumio Iijima. Roll-to-roll production of 30-inch graphene films for transparent electrodes. *Nature Nanotechnology*, 5(8):574–578, aug 2010.

[102] Xuesong Li, Weiwei Cai, Jinho An, Seyoung Kim, Junghyo Nah, Dongxing Yang, Richard Piner, Aruna Velamakanni, Inhwa Jung, Emanuel Tutuc, Sanjay K. Banerjee, Luigi Colombo, and Rodney S. Ruoff. Large-area synthesis of high-quality and uniform graphene films on copper foils. *Science*, 324(5932):1312–1314, jun 2009.

[103] Cecilia Mattevi, Hokwon Kim, and Manish Chhowalla. A review of chemical vapour deposition of graphene on copper. *Journal of Materials Chemistry*, 21(10):3324–3334, mar 2011.

[104] Thomas D. Anthopoulos, Birendra Singh, Nenad Marjanovic, Niyazi S. Sariciftci, Alberto Montaigne Ramil, Helmut Sitter, Michael Cölle, and Dago M. De Leeuw. High performance n -channel organic field-effect transistors and ring oscillators based on C 60 fullerene films. *Applied Physics Letters*, 89(21):213504, nov 2006.

[105] Daniel Ugarte. Morphology and structure of graphitic soot particles generated in arc-discharge C60 production. *Chemical Physics Letters*, 198(6):596–602, oct 1992.

[106] Steve F. A. Acquah, Anastasia V. Penkova, Denis A. Markelov, Anna S. Semisalova, Branden E. Leonhardt, and James M. Magi. Review—The Beautiful Molecule: 30 Years of C 60 and Its Derivatives. *ECS Journal of Solid State Science and Technology*, 6(6):M3155–M3162, mar 2017.

[107] Jerzy Cioslowski and Eugene D. Fleischmann. Endohedral complexes: Atoms and ions inside the C60 cage. *The Journal of Chemical Physics*, 94(5):3730–3734, mar 1991.

[108] C. Evangeli, K. Gillemot, E. Leary, M. T. González, G. Rubio-Bollinger, C. J. Lambert, and N. Agraït. Engineering the Thermopower of C_60 Molecular Junctions. *Nano Letters*, 13(5), 2013.

[109] S. K. Lee, T. Ohto, R. Yamada, and H. Tada. Thermopower of Benzenedithiol and C_60 Molecular Junctions with Ni and Au Electrodes. *Nano Letters*, 14(9), 2014.

[110] Yuchun Liu, Ling Xu, Chen Zhao, Ming Shao, and Bin Hu. Tuning the Seebeck effect in C 60 -based hybrid thermoelectric devices through temperature-dependent surface polarization and thermally-modulated interface dipoles. *Physical Chemistry Chemical Physics*, 19(22):14793–14800, 2017.

[111] Wolfgang Krätschmer. Formation of Fullerenes. In *Natural Fullerenes and Related Structures of Elemental Carbon*, pages 7–29. Springer Netherlands, feb 2007.

[112] Yahachi Saito, Tadanobu Yoshikawa, Motonori Inagaki, Masato Tomita, and Takayoshi Hayashi. Growth and structure of graphitic tubules and polyhedral particles in arc-discharge. *Chemical Physics Letters*, 204(3-4):277–282, mar 1993.

[113] Toshiki Sugai, Hideki Omote, Shunji Bandow, Nobuo Tanaka, and Hisanori Shinohara. Production of fullerenes and single-wall carbon nanotubes by high-temperature pulsed arc discharge. *Journal of Chemical Physics*, 112(13):6000–6005, 2000.

[114] Bart Limburg, James O. Thomas, Gregory Holloway, Hatef Sadeghi, Sara Sangtarash, Ian Cheng Yi Hou, Jonathan Cremers, Akimitsu Narita, Klaus Müllen, Colin J. Lambert, G. Andrew D. Briggs, Jan A. Mol, and Harry L. Anderson. Anchor Groups for Graphene-Porphyrin Single-Molecule Transistors. *Advanced Functional Materials*, 28(45):1803629, nov 2018.

[115] A. A. M. Staring, L. W. Molenkamp, and B. W. Alphenaar. Sawtooth-like thermopower oscillations of a quantum dot in the Coulomb blockade regime Coulomb-Blockade Oscillations in the Thermopower of a Quantum Dot. *Semiconductor Science and Technology*, 9(5), 1994.

[116] R. Scheibner, E. G. Novik, T. Borzenko, M. König, D. Reuter, A. D. Wieck, H. Buhmann, and L. W. Molenkamp. Sequential and cotunneling behavior in the temperature-dependent thermopower of few-electron quantum dots. *Physical Review B*, 75(4), 2007.

[117] Joshua P Small, Kerstin M Perez, and Philip Kim. Modulation of Thermoelectric Power of Individual Carbon Nanotubes. *Phys. Rev. Lett.*, 91:256801, 2003.

[118] R. Scheibner, M. König, D. Reuter, A. D. Wieck, C. Gould, H. Buhmann, and L. W. Molenkamp. Quantum dot as thermal rectifier. *New Journal of Physics*, 10(10), 2008.

[119] R. Scheibner, H. Buhmann, D. Reuter, M. N. Kiselev, and L. W. Molenkamp. Thermopower of a Kondo Spin-Correlated Quantum Dot. *Physical Review Letters*, 95(17), 2005.

[120] Artis Svilans, Martin Josefsson, Adam M Burke, Sofia Fahlvik, Claes Thelander, Heiner Linke, and Martin Leijnse. Thermoelectric Characterization of the Kondo Resonance in Nanowire Quantum Dots. *Physical Review Letters*, 121(20):206801, 2018.

[121] A. M. Staring, L. W. Molenkamp, B. W. Alphenaar, H. Van Houten, J. A. Buyk, M. A. A. Mabesoone, C. W. J. Beenakker, and C. T. Foxon. Coulomb-Blockade Oscillations in the Thermopower of a Quantum Dot. *Europhysics Letters*, 22(1), 1993.

[122] Artis Svilans, Adam M. Burke, Sofia Fahlvik Svensson, Martin Leijnse, and Heiner Linke. Nonlinear thermoelectric response due to energy-dependent transport properties of a quantum dot. *Physica E: Low-Dimensional Systems and Nanostructures*, 82:34–38, 2016.

[123] S Fahlvik Svensson, E A Hoffmann, N Nakpathomkun, P M Wu, H Q Xu, H A Nilsson, D. Sánchez, V Kashcheyevs, and H Linke. Nonlinear thermovoltage and thermocurrent in quantum dots. *New Journal of Physics*, 15(15):105011–105011, 2013.

[124] R. Scheibner, E. G. Novik, T. Borzenko, M. König, D. Reuter, A. D. Wieck, H. Buhmann, and L. W. Molenkamp. Sequential and cotunneling behavior in the temperature-dependent thermopower of few-electron quantum dots. *Physical Review B*, 75(4), 2007.

[125] S Fahlvik Svensson, A I Persson, E A Hoffmann, N Nakpathomkun, H A Nilsson, H Q Xu, L Samuelson, and H Linke. Lineshape of the thermopower of quantum dots. *New Journal of Physics*, 14(3):033041, mar 2012.

[126] H. Thierschmann, R. Sánchez, B. Sothmann, F. Arnold, C. Heyn, W. Hansen, H. Buhmann, and L. W. Molenkamp. Three-terminal energy harvester with coupled quantum dots. *Nature Nanotechnology*, 10(176), 2015.

[127] R. Sánchez and M. Büttiker. Optimal energy quanta to current conversion. *Physical Review B*, 83(8), 2011.

[128] Martin Josefsson, Artis Svilans, Adam M Burke, Eric A Hoffmann, Sofia Fahlvik, Claes Thelander, Martin Leijnse, and Heiner Linke. A quantum-dot heat engine operating close to the thermodynamic efficiency limits. *Nature Nanotechnology*, 13(10):920–924, 2018.

[129] P. Reddy, S.-Y. Jang, R. A. Segalman, and A. Majumdar. Thermoelectricity in Molecular Junctions. *Science*, 315(5818), 2007.

[130] Y. Kim, W. Jeong, K. Kim, W. Lee, and P. Reddy. Electrostatic control of thermoelectricity in molecular junctions. *Nature Nanotechnology*, 9(11), 2014.

[131] Jonathan R Widawsky, Pierre Darancet, Jeffrey B Neaton, and Latha Venkataraman. Simultaneous determination of conductance and thermopower of single molecule junctions. *Nano Letters*, 12(1):354–358, 2012.

[132] A. Tan, S. Sadat, and P. Reddy. Measurement of thermopower and current-voltage characteristics of molecular junctions to identify orbital alignment. *Applied Physics Letters*, 96(1), 2010.

[133] J. A. Malen, P. Doak, K. Baheti, T. D. Tilley, R. A. Segalman, and A. Majumdar. Identifying the Length Dependence of Orbital Alignment and Contact Coupling in Molecular Heterojunctions. *Nano Letters*, 9(3), 2009.

[134] K. Baheti, J. A. Malen, P. Doak, P. Reddy, S.-Y. Jang, T. Don Tilley, A. Majumdar, and R. A. Segalman. Probing the Chemistry of Molecular Heterojunctions Using Thermoelectricity. *Nano Letters*, 8(2), 2008.

[135] S. K. Yee, J. A. Malen, A. Majumdar, and R. A. Segalman. Thermoelectricity in Fullerene–Metal Heterojunctions. *Nano Letters*, 11(10), 2011.

[136] Hongkun Park, Jiwoong Park, Andrew K. L. Lim, Erik H. Anderson, A. Paul Alivisatos, and Paul L. McEuen. Nanomechanical oscillations in a single-c60 transistor. *Nature*, 407:57–60, 2000.

[137] Lam H. Yu and Douglas Natelson. The Kondo Effect in C60 Single-Molecule Transistors. *Nano Letters*, 4(1):79–83, jan 2004.

[138] Pascal Gehring, Achim Harzheim, Jean Spièce, Yuewen Sheng, Gregory Rogers, Charalambos Evangeli, Aadarsh Mishra, Benjamin J. Robinson, Kyriakos Porfyrakis, Jamie H. Warner, Oleg V. Kolosov, G. Andrew D. Briggs, and Jan A. Mol. Field-Effect Control of Graphene–Fullerene Thermoelectric Nanodevices. *Nano Letters*, 17(11):7055–7061, 2017.

[139] N Néel, J Kröger, L Limot, T Frederiksen, M Brandbyge, and R Berndt. Controlled contact to a C60 molecule. *Physical Review Letters*, 98(6), 2007.

[140] Laura Rincón-García, Ali K. Ismael, Charalambos Evangeli, Iain Grace, Gabino Rubio-Bollinger, Kyriakos Porfyrakis, Nicolás Agraït, and Colin J. Lambert. Molecular design and control of fullerene-based bi-thermoelectric materials. *Nature Materials*, 15(3):289–293, mar 2016.

[141] Manabu Kiguchi and Kei Murakoshi. Conductance of single C60 molecule bridging metal electrodes. *Journal of Physical Chemistry C*, 112(22):8140–8143, jun 2008.

[142] Yuki Anno, Yuki Imakita, Kuniharu Takei, Seiji Akita, and Takayuki Arie. Enhancement of graphene thermoelectric performance through defect engineering. *2D Materials*, 4(2):025019, feb 2017.

[143] Deqi Wang and Jing Shi. Effect of charged impurities on the thermoelectric power of graphene near the dirac point. *Phys. Rev. B*, 83:113403, 2011.

[144] Yijian Ouyang and Jing Guo. A theoretical study on thermoelectric properties of graphene nanoribbons. *Applied Physics Letters*, 94(26):263107, jun 2009.

[145] Gang Zhang and Yong Wei Zhang. Thermoelectric properties of two-dimensional transition metal dichalcogenides, aug 2017.

[146] Xiaoming Wang, Mona Zebarjadi, and Keivan Esfarjani. High-Performance Solid-State Thermionic Energy Conversion Based on 2D van der Waals Heterostructures: A First-Principles Study. *Scientific Reports*, 8(1):1–9, dec 2018.

[147] Hatef Sadeghi, Sara Sangtarash, and Colin Lambert. Robust Molecular Anchoring to Graphene Electrodes. *Nano Letters*, 17(8):4611–4618, aug 2017.

[148] Yanliang Zhang, Claudiu L. Hapenciuc, Eduardo E. Castillo, Theodorian Borca-Tasciuc, Rutvik J. Mehta, Chinnathambi Karthik, and Ganpati Ramanath. A microprobe technique for simultaneously measuring thermal conductivity and Seebeck coefficient of thin films. *Applied Physics Letters*, 96(6):062107, feb 2010.

[149] Ho Ki Lyeo, A. A. Khajetoorians, Li Shi, Kevin P. Pipe, Rajeev J. Ram, Ali Shakouri, and C. K. Shih. Profiling the Thermoelectric Power of Semiconductor Junctions with Nanometer Resolution. *Science*, 303(5659):816–818, feb 2004.

[150] Dong Sun, Grant Aivazian, Aaron M. Jones, Jason S. Ross, Wang Yao, David Cobden, and Xiaodong Xu. Ultrafast hot-carrier-dominated photocurrent in graphene. *Nature Nanotechnology*, 7(2):114–118, jan 2012.

[151] Nathaniel M. Gabor, Justin C.W. Song, Qiong Ma, Nityan L. Nair, Thiti Taychatanapat, Kenji Watanabe, Takashi Taniguchi, Leonid S. Levitov, and Pablo Jarillo-Herrero. Hot carrier-assisted intrinsic photoresponse in graphene. *Science*, 334(6056):648–652, nov 2011.

[152] Mark B. Lundeberg, Yuanda Gao, Achim Woessner, Cheng Tan, Pablo Alonso-González, Kenji Watanabe, Takashi Taniguchi, James Hone, Rainer Hillenbrand, and Frank H.L. Koppens. Thermoelectric detection and imaging of propagating graphene plasmons. *Nature Materials*, 16(2):204–207, feb 2017.

[153] Werner Kern. The Evolution of Silicon Wafer Cleaning Technology. *Journal of The Electrochemical Society*, 137(6):1887, jun 1990.

[154] Bryan Cord, Jodie Lutkenhaus, and Karl K. Berggren. Optimal temperature for development of poly(methylmethacrylate). *Journal of Vacuum Science and Technology B: Microelectronics and Nanometer Structures*, 25(6):2013–2016, dec 2007.

[155] D K Kaushik, S K Chattopadhyaya, and N Nath. Thin film thickness monitoring using a doubly oscillating quartz crystal and measurement of growth rate. *Journal of Physics E: Scientific Instruments*, 14(3):345–348, 1981.

[156] Matteo Todeschini, Alice Bastos Da Silva Fanta, Flemming Jensen, Jakob Birkedal Wagner, and Anpan Han. Influence of Ti and Cr Adhesion Layers on Ultrathin Au Films. *ACS Applied Materials and Interfaces*, 9(42):37374–37385, 2017.

[157] Yumeng Shi, Xiaochen Dong, Peng Chen, Junling Wang, and Lain Jong Li. Effective doping of single-layer graphene from underlying SiO2 substrates. *Physical Review B - Condensed Matter and Materials Physics*, 79(11), 2009.

[158] F. Prins, A. Barreiro, J. W. Ruitenberg, J. S. Seldenthuis, N. Uria Aliaga-Alcalde, L. M. K. Vandersypen, and H. S. J. Van Der Zant. Room-Temperature Gating of Molecular Junctions Using Few-Layer Graphene Nanogap Electrodes. *Nano Letters*, 11(11), 2011.

[159] A. Candini, N. Richter, D. Convertino, C. Coletti, F. Balestro, W. Wernsdorfer, M. Kläui, and M. Affronte. Electroburning of few-layer graphene flakes, epitaxial graphene, and turbostratic graphene discs in air and under vacuum. *Beilstein journal of nanotechnology*, 6, 2015.

[160] A. Barreiro, F. Bo, M. H. Ru, B. Bu, and K. L. M. Vandersypen. Graphene at High Bias: Cracking, Layer by Layer Sublimation, and Fusing. *Nano Letters*, 12(4), 2012.

[161] C. S. Lau, J. A. Mol, J. H. Warner, and G. A. D. Briggs. Nanoscale control of graphene electrodes. *Phys. Chem. Chem. Phys. Phys. Chem. Chem. Phys*, 16(16), 2039.

[162] J. G. Simmons. Generalized Formula for the Electric Tunnel Effect between Similar Electrodes Separated by a Thin Insulating Film. 341(35), 1963.

[163] Paweł Puczkarski, Pascal Gehring, Chit S. Lau, Junjie Liu, Arzhang Ardavan, Jamie H. Warner, G. Andrew D. Briggs, and Jan A. Mol. Three-terminal graphene single-electron transistor fabricated using feedback-controlled electroburning. *Applied Physics Letters*, 107(13):133105, sep 2015.

[164] S. Gomès, A. Assy, and P.-O. Chapuis. Scanning thermal microscopy: A review. *Physica Status Solidi (A)*, 212(3), 2015.

[165] Fabian Menges, Philipp Mensch, Heinz Schmid, Heike Riel, Andreas Stemmer, and Bernd Gotsmann. Temperature mapping of operating nanoscale devices by scanning probe thermometry. *Nature Communications*, 7:10874, mar 2016.

[166] K. Kim, W. Jeong, W. Lee, and P. Reddy. Ultra-High Vacuum Scanning Thermal Microscopy for Nanometer Resolution Quantitative Thermometry. *ACS Nano*, 6(5), 2012.

[167] P. Tovee, M. Pumarol, D. Zeze, Kevin Kjoller, and O. Kolosov. Nanoscale spatial resolution probes for scanning thermal microscopy of solid state materials. *Journal of Applied Physics*, 112(11):114317, dec 2012.

[168] Roger Taylor and David R.M. Walton. The chemistry of fullerenes. *Nature*, 363(6431):685–693, jun 1993.

[169] Muqing Chen, Runnan Guan, and Shangfeng Yang. Hybrids of Fullerenes and 2D Nanomaterials. *Advanced Science*, 6(1):1800941, jan 2019.

[170] Christian Larsen, Hamid Reza Barzegar, Florian Nitze, Thomas Wågberg, and Ludvig Edman. On the fabrication of crystalline C 60 nanorod transistors from solution. *Nanotechnology*, 23(34):344015, 2012.

[171] Zhang et al. Direct observation of a widely tunable bandgap in bilayer graphene. *Nature*, 459(1):820–823, 2009.

[172] Gonzalo Otero, Giulio Biddau, Carlos Sánchez-Sánchez, Renaud Caillard, María F. López, Celia Rogero, F. Javier Palomares, Noemí Cabello, Miguel A. Basanta, José Ortega, Javier Méndez, Antonio M. Echavarren, Rubén Pérez, Berta Gómez-Lor, and José A. Martín-Gago. Fullerenes from aromatic precursors by surface-catalysed cyclodehydrogenation. *Nature*, 454(7206):865–868, aug 2008.

[173] Joseph P. Heremans, Mildred S. Dresselhaus, Lon E. Bell, and Donald T. Morelli. When thermoelectrics reached the nanoscale. *Nat. Nanotechnol.*, 8(7):471–473, 2013.

[174] Rama Venkatasubramanian, Edward Siivola, Thomas Colpitts, and Brooks O'Quinn. Thin-film thermoelectric devices with high room-temperature figures of merit. *Nature*, 413(6856):597–602, 2001.

[175] Pramod Reddy, Sung-Yeon Jang, Rachel A. Segalman, and Arun Majumdar. Thermoelectricity in molecular junctions. *Science*, 315(5818):1568–1571, 2007.

[176] C. J. Lambert. Basic concepts of quantum interference and electron transport in single-molecule electronics. *Chemical Society Reviews*, 44(4):875–888, feb 2015.

[177] Emanuel Lortscher. Wiring molecules into circuits. *Nat. Nanotechnol.*, 8(6):381–384, 2013.

[178] Pascal Gehring, Hatef Sadeghi, Sara Sangtarash, Chit Siong Lau, Junjie Liu, Arzhang Ardavan, Jamie H Warner, Colin J Lambert, G Andrew D Briggs, and Jan A Mol. Quantum Interference in Graphene Nanoconstrictions. *Nano Lett.*, 16:4210–4216, 2016.

[179] Jan A. Mol, Chit Siong Lau, Wilfred J. M. Lewis, Hatef Sadeghi, Cecile Roche, Arjen Cnossen, Jamie H. Warner, Colin J. Lambert, Harry L. Anderson, and G. Andrew D. Briggs. Graphene-porphyrin single-molecule transistors. *Nanoscale*, 7:13181–13185, 2015.

[180] C. Schinabeck, A. Erpenbeck, R. Härtle, and M. Thoss. Hierarchical quantum master equation approach to electronic-vibrational coupling in nonequilibrium transport through nanosystems. *Phys. Rev. B*, 94:201407, 2016.

[181] Robert S Whitney, Rafael Sánchez, and Janine Splettstoesser. Quantum thermodynamics of nanoscale thermoelectrics and electronic devices. 2018.

[182] Pascal Gehring, Jakub Sowa, Jonathan Cremers, Qingqing Wu, Hatef Sadeghi, Jamie H. Warner, Colin J. Lambert, Harry L. Anderson, G. Andrew D. Briggs, and Jan A. Mol. Distinguishing lead and molecule states in graphene-based single-electron transistors. *ACS Nano*, 11(6):5325–5331, 2017.

[183] Leo P Kouwenhoven, Charles M Marcus, Paul L. McEuen, Seigo Tarucha, Robert M Westervelt, and Ned S Wingreen. Electron Transport in Quantum Dots. In *Mesoscopic Electron Transport*, pages 105–214. 1997.

[184] C.W.J. Beenakker. Theory of coulomb-blockade oscillations in the conductance of a quantum dot. *Phys. Rev. B*, 44(4):1646–1656, 1991.

[185] Justin C. W. Song, Mark S. Rudner, Charles M. Marcus, and Leonid S. Levitov. Hot carrier transport and photocurrent response in graphene. *Nano Lett.*, 11(11):4688–4692, 2011.

[186] Weishu Liu, Hee Seok Kim, Qing Jie, and Zhifeng Ren. Importance of high power factor in thermoelectric materials for power generation application: A perspective. *Scripta Materialia*, 111:3–9, jan 2016.

[187] Achim Harzheim, Jakub K. Sowa, Jacob L. Swett, G. Andrew D. Briggs, Jan A. Mol, and Pascal Gehring. The role of metallic leads and electronic degeneracies in thermoelectric power generation in quantum dots. *Physical Review Research*, 2(1):013140, feb 2020.

[188] Yuri M Zuev. Nanoscale Thermoelectric Energy Conversion. *PhD. Dissertation*, pages 1–33, 2011.

[189] W. J. De Haas and G. J. Van Den Berg. The electrical resistance of gold and silver at low temperatures. *Physica*, 3(6):440–449, 1936.

[190] Jakub K. Sowa, Jan A. Mol, and Erik M. Gauger. Marcus Theory of Thermoelectricity in Molecular Junctions. *Journal of Physical Chemistry C*, 123(7):4103–4108, feb 2019.

[191] L. P. Kouwenhoven, N. C. van der Vaart, A. T. Johnson, W. Kool, C. J.P.M. Harmans, J. G. Williamson, A. A.M. Staring, and C. T. Foxon. Single electron charging effects in semiconductor quantum dots. *Zeitschrift für Physik B Condensed Matter*, 85(3):367–373, oct 1991.

[192] Nikolaus Hartman, Christian Olsen, Silvia Lüscher, Mohammad Samani, Saeed Fallahi, Geoffrey C. Gardner, Michael Manfra, and Joshua Folk. Direct entropy measurement in a mesoscopic quantum system. *Nature Physics*, 14(11):1083–1086, nov 2018.

[193] L. Molenkamp, A A M Staring, B W Alphenaar, H. Van Houten, and C. W J Beenakker. Sawtooth-like thermopower oscillations of a quantum dot in the Coulomb blockade regime. *Semiconductor Science and Technology*, 9(5 S):903–906, 1994.

[194] P. A. Erdman, J. T. Peltonen, B. Bhandari, B. Dutta, H. Courtois, R. Fazio, F. Taddei, and J. P. Pekola. Nonlinear thermovoltage in a single-electron transistor. *Physical Review B*, 99(16):165405, apr 2019.

[195] Jae Hun Seol, Insun Jo, Arden L Moore, Lucas Lindsay, Zachary H Aitken, Michael T Pettes, Xuesong Li, Zhen Yao, Rui Huang, David Broido, Natalio Mingo, Rodney S Ruoff, and Li Shi. Two-dimensional phonon transport in supported graphene. *Science*, 328(5975):213–216, apr 2010.

[196] Xiangfan Xu, Luiz F.C. Pereira, Yu Wang, Jing Wu, Kaiwen Zhang, Xiangming Zhao, Sukang Bae, Cong Tinh Bui, Rongguo Xie, John T.L. Thong, Byung Hee Hong, Kian Ping Loh, Davide Donadio, Baowen Li, and Barbaros Özyilmaz. Length-dependent thermal conductivity in suspended single-layer graphene. *Nature Communications*, 5(1):3689, sep 2014.

[197] Jiuning Hu, Xiulin Ruan, and Yong P. Chen. Thermal conductivity and thermal rectification in graphene nanoribbons: A molecular dynamics study. *Nano Letters*, 9(7):2730–2735, jul 2009.

[198] D. L. Nika, E. P. Pokatilov, A. S. Askerov, and A. A. Balandin. Phonon thermal conduction in graphene: Role of Umklapp and edge roughness scattering. *Physical Review B - Condensed Matter and Materials Physics*, 79(15), apr 2009.

[199] William J. Evans, Lin Hu, and Pawel Keblinski. Thermal conductivity of graphene ribbons from equilibrium molecular dynamics: Effect of ribbon width, edge roughness, and hydrogen termination. *Applied Physics Letters*, 96(20), 2010.

[200] L Lindsay, D A Broido, and Natalio Mingo. Flexural phonons and thermal transport in graphene. *Physical Review B - Condensed Matter and Materials Physics*, 82(11), 2010.

[201] Enrique Muñoz, Jianxin Lu, and Boris I Yakobson. Ballistic thermal conductance of graphene ribbons. *Nano Letters*, 10(5):1652–1656, 2010.

[202] Alexander V. Savin, Yuri S. Kivshar, and Bambi Hu. Suppression of thermal conductivity in graphene nanoribbons with rough edges. *Physical Review B - Condensed Matter and Materials Physics*, 82(19), nov 2010.

[203] C. J. Glassbrenner and Glen A. Slack. Thermal conductivity of silicon and germanium from 3°K to the melting point. *Physical Review*, 134(4A), 1964.

[204] Xinxia Li, Yaping Yan, Lan Dong, Jie Guo, Adili Aiyiti, Xiangfan Xu, and Baowen Li. Thermal conduction across a boron nitride and SiO2 interface. *Journal of Physics D: Applied Physics*, 50(10), feb 2017.

[205] Achim Harzheim, Jean Spiece, Charalambos Evangeli, Edward McCann, Vladimir Falko, Yuewen Sheng, Jamie H. Warner, G. Andrew D. Briggs, Jan A. Mol, Pascal Gehring, and Oleg V. Kolosov. Geometrically Enhanced Thermoelectric Effects in Graphene Nanoconstrictions. *Nano Letters*, 18(12):7719–7725, dec 2018.

[206] Yuri M Zuev, Jin Seok Lee, Clément Galloy, Hongkun Park, and Philip Kim. Diameter dependence of the transport properties of antimony telluride nanowires. *Nano Letters*, 10(8):3037–3040, 2010.

[207] Pavlo Zolotavin, Charlotte I Evans, and Douglas Natelson. Substantial local variation of the Seebeck coefficient in gold nanowires. *Nanoscale*, 9(26):9160–9166, 2017.

[208] Y. S. Muzychka, M M Yovanovich, and J R Culham. Thermal spreading resistance in compound and orthotropic systems. *Journal of Thermophysics and Heat Transfer*, 18(1):45–51, jan 2004.

[209] Y. S. Muzychka. Spreading resistance in compound orthotropic flux tubes and channels with interfacial resistance. In *Journal of Thermophysics and Heat Transfer*, volume 28, pages 313–319. American Institute of Aeronautics and Astronautics, apr 2014.

[210] Byeonghee Lee, Kyeongtae Kim, Seungkoo Lee, Jong Hoon Kim, Dae Soon Lim, Ohmyoung Kwon, and Joon Sik Lee. Quantitative thermopower profiling across a silicon p-n junction with nanometer resolution. *Nano Letters*, 12(9):4472–4476, sep 2012.

[211] Fabian Könemann, Morten Vollmann, Tino Wagner, Norizzawati Mohd Ghazali, Tomohiro Yamaguchi, Andreas Stemmer, Koji Ishibashi, and Bernd Gotsmann. Thermal Conductivity of a Supported Multiwalled Carbon Nanotube. *Journal of Physical Chemistry C*, 123(19):12460–12465, may 2019.

[212] Wonho Jeong, Kyeongtae Kim, Youngsang Kim, Woochul Lee, and Pramod Reddy. Characterization of nanoscale temperature fields during electromigration of nanowires. *Scientific Reports*, 4(1):4975, may 2015.

[213] Kyle L. Grosse, Myung Ho Bae, Feifei Lian, Eric Pop, and William P. King. Nanoscale Joule heating, Peltier cooling and current crowding at graphene-metal contacts. *Nature Nanotechnology*, 6(5):287–290, may 2011.

[214] Jens Baringhaus, Mikkel Settnes, Johannes Aprojanz, Stephen R Power, Antti Pekka Jauho, and Christoph Tegenkamp. Electron Interference in Ballistic Graphene Nanoconstrictions. *Physical Review Letters*, 116(18), 2016.

[215] M. J.M. De Jong. Transition from Sharvin to Drude resistance in high-mobility wires. *Physical Review B*, 49(11):7778–7781, 1994.

[216] Qiuzi Li and S Das Sarma. Finite temperature inelastic mean free path and quasiparticle lifetime in graphene. *Physical Review B - Condensed Matter and Materials Physics*, 87(8), 2013.

[217] A. H. Castro Neto, F Guinea, N. M.R. Peres, K S Novoselov, and A K Geim. The electronic properties of graphene. *Reviews of Modern Physics*, 81(1):109–162, 2009.

[218] Achim Woessner, Pablo Alonso-González, Mark B. Lundeberg, Yuanda Gao, Jose E. Barrios-Vargas, Gabriele Navickaite, Qiong Ma, Davide Janner, Kenji Watanabe, Aron W. Cummings, Takashi Taniguchi, Valerio Pruneri, Stephan Roche, Pablo Jarillo-Herrero, James Hone, Rainer Hillenbrand, and Frank H.L. Koppens. Near-field photocurrent nanoscopy on bare and encapsulated graphene. *Nature Communications*, 7:10783, feb 2016.

[219] K. S. Novoselov, A. K. Geim, S. V. Morozov, D. Jiang, M. I. Katsnelson, I. V. Grigorieva, S. V. Dubonos, and A. A. Firsov. Two-dimensional gas of massless Dirac fermions in graphene. *Nature*, 438(7065):197–200, nov 2005.

[220] Myung-Ho Bae, Sharnali Islam, Vincent E. Dorgan, and Eric Pop. Scaling of High-Field Transport and Localized Heating in Graphene Transistors. *ACS Nano*, 5(10):7936–7944, oct 2011.

[221] Achim Harzheim, Charalambos Evangeli, Oleg V. Kolosov, and Pascal Gehring. Direct Mapping of Local Seebeck Coefficient in 2D Material Nanostructures via Scanning Thermal Gate Microscopy. *2D Materials*, 7(4):041004, aug 2020.

[222] Fengnian Xia, Thomas Mueller, Roksana Golizadeh-Mojarad, Marcus Freitage, Yu Ming Lin, James Tsang, Vasili Perebeinos, and Phaedon Avouris. Photocurrent imaging and efficient photon detection in a graphene transistor. *Nano Letters*, 9(3):1039–1044, mar 2009.

[223] Shuping Guo, Kaishuai Yang, Zhi Zeng, and Yongsheng Zhang. Influence of defect distribution on the thermoelectric properties of FeNbSb based materials. *Physical Chemistry Chemical Physics*, 20(21):14441–14449, may 2018.

[224] A. X. Levander, T. Tong, K. M. Yu, J. Suh, D. Fu, R. Zhang, H. Lu, W. J. Schaff, O. Dubon, W. Walukiewicz, D. G. Cahill, and J. Wu. Effects of point defects on thermal and thermoelectric properties of InN. *Applied Physics Letters*, 98(1):012108, jan 2011.

[225] D. Kraemer, L. Hu, A. Muto, X. Chen, G. Chen, and M. Chiesa. Photovoltaic-thermoelectric hybrid systems: A general optimization methodology. *Applied Physics Letters*, 92(24):243503, jun 2008.

[226] Kai Zhang, Fung Ling Yap, Kun Li, Chang Tai Ng, Lin Jun Li, and Kian Ping Loh. Large scale graphene/hexagonal boron nitride heterostructure for tunable plasmonics. *Advanced Functional Materials*, 24(6):731–738, feb 2014.

[227] Ahmet Avsar, Tsung Yeh Yang, Sukang Bae, Jayakumar Balakrishnan, Frank Volmer, Manu Jaiswal, Zheng Yi, Syed Rizwan Ali, Gernot Guöntherodt, Byung Hee Hong, Bernd Beschoten, and Barbaros Özyilmaz. Toward wafer scale fabrication of graphene based spin valve devices. *Nano Letters*, 11(6):2363–2368, jun 2011.

[228] Li Lynn Shiau, Simon Chun Kiat Goh, Xingli Wang, Minmin Zhu, Chuan Seng Tan, Zheng Liu, and Beng Kang Tay. Graphene-Metal Nanoparticles for Enhancing Thermoelectric Power Factor. *IEEE Transactions on Nanotechnology*, 18:1114–1118, 2019.

[229] Charalambos Evangeli, Jean Spiece, Sara Sangtarash, Aday J. Molina-Mendoza, Marta Mucientes, Thomas Mueller, Colin Lambert, Hatef Sadeghi, and Oleg Kolosov. Nanoscale Thermal Transport in 2D Nanostructures from Cryogenic to Room Temperature. *Advanced Electronic Materials*, 5(10):1900331, oct 2019.

[230] Alain Haché, Phuong Anh Do, and Stefano Bonora. Surface Heating by optical beams and application to mid-infrared imaging. *Applied Optics*, 51(27):6578–6585, 2012.

[231] Qing Hua Wang, Zhong Jin, Ki Kang Kim, Andrew J. Hilmer, Geraldine L.C. Paulus, Chih Jen Shih, Moon Ho Ham, Javier D. Sanchez-Yamagishi, Kenji Watanabe, Takashi Taniguchi, Jing Kong, Pablo Jarillo-Herrero, and Michael S. Strano. Understanding and controlling the substrate effect on graphene electron-transfer chemistry via reactivity imprint lithography. *Nature Chemistry*, 4(9):724–732, sep 2012.

[232] Jiamin Xue, Javier Sanchez-Yamagishi, Danny Bulmash, Philippe Jacquod, Aparna Deshpande, K. Watanabe, T. Taniguchi, Pablo Jarillo-Herrero, and Brian J. Leroy. Scanning tunnelling microscopy and spectroscopy of ultra-flat graphene on hexagonal boron nitride. *Nature Materials*, 10(4):282–285, 2011.

[233] Dong Sun, Charles Divin, Claire Berger, Walt A De Heer, Phillip N First, and Theodore B Norris. Spectroscopic measurement of interlayer screening in multilayer epitaxial graphene. *Physical Review Letters*, 104(13), 2010.

[234] Taisuke Ohta, Aaron Bostwick, J. L. McChesney, Thomas Seyller, Karsten Horn, and Eli Rotenberg. Interlayer interaction and electronic screening in multilayer graphene investigated with angle-resolved photoemission spectroscopy. *Physical Review Letters*, 98(20), 2007.

[235] Miguel Munoz Rojo, Zuanyi Li, Charles Sievers, Alex C. Bornstein, Eilam Yalon, Sanchit Deshmukh, Sam Vaziri, Myung Ho Bae, Feng Xiong, Davide Donadio, and Eric Pop. Thermal transport across graphene step junctions. *2D Materials*, 6(1):011005, jan 2019.

[236] Duhee Yoon, Young Woo Son, and Hyeonsik Cheong. Strain-dependent splitting of the double-resonance raman scattering band in graphene. *Physical Review Letters*, 106(15), 2011.

[237] Huihui Lu, Paul K. Chu, and Zhenghua An. Enhanced Peltier Effect in Wrinkled Graphene Constriction by Nano-bubble. *Small*, page 1907170, feb 2020.

[238] T. Mueller, F. Xia, M. Freitag, J. Tsang, and Ph Avouris. Role of contacts in graphene transistors: A scanning photocurrent study. *Physical Review B - Condensed Matter and Materials Physics*, 79(24), jun 2009.

[239] McCann E. and Koshino M. The electronic properties of bilayer graphene. *Reports on Progress of Physics*, 76(5):056503, 2013.

[240] M. Chung Nguyen, V. Hung Nguyen, Huy Viet Nguyen, J. Saint-Martin, and P. Dollfus. Enhanced Seebeck effect in graphene devices by strain and doping engineerings. *Physica E: Low-Dimensional Systems and Nanostructures*, 73:207–212, jul 2015.

[241] Peter D. Tovee, Manuel E. Pumarol, Mark C. Rosamond, Robert Jones, Michael C. Petty, Dagou A. Zeze, and Oleg V. Kolosov. Nanoscale resolution scanning thermal microscopy using carbon nanotube tipped thermal probes. *Physical Chemistry Chemical Physics*, 16(3):1174–1181, jan 2014.

[242] Achim Harzheim, Fabian Könemann, Bernd Gotsmann, Herre van der Zant, and Pascal Gehring. Single-Material Graphene Thermocouples. *Advanced Functional Materials*, page 2000574, apr 2020.

[243] P. A. Kinzie and Lawrence G. Rubin. Thermocouple Temperature Measurement. *Physics Today*, 26(11):52–55, nov 1973.

[244] Kevin Skadron, Mircea R. Stan, Wei Huang, Sivakumar Velusamy, Karthik Sankaranarayanan, and David Tarjan. Temperature-aware computer systems: Opportunities and challenges. *IEEE Micro*, 23(6):52–61, nov 2003.

[245] Stephen H. Gunther. Architectural approaches to reducing power related system costs. In *IEEE Topical Meeting on Electrical Performance of Electronic Packaging*, pages 7–8. IEEE, 2001.

[246] Oleg Semenov, Arman Vassighi, and Manoj Sachdev. Impact of self-heating effect on long-term reliability and performance degradation in CMOS circuits. *IEEE Transactions on Device and Materials Reliability*, 6(1):17–27, mar 2006.

[247] Rajarshi Mukherjee and Seda Ogrenci Memik. Systematic temperature sensor allocation and placement for microprocessors. In *Proceedings - Design Automation Conference*, pages 542–547, New York, New York, USA, 2006. ACM Press.

[248] Jonathan Machin, Declan Tucker, and Jonathan V Pearce. A comprehensive survey of thermoelectric homogeneity of commonly used thermocouple types. *Measurement Science and Technology*, 29(6):067002, jun 2018.

[249] Weiqiang Sun, Haixiao Liu, Weiwei Gong, Lian-Mao Peng, and Sheng-Yong Xu. Unexpected size effect in the thermopower of thin-film stripes. *Journal of Applied Physics*, 110(8):083709, oct 2011.

[250] Haixiao Liu, Weiqiang Sun, and Shengyong Xu. An Extremely Simple Thermocouple Made of a Single Layer of Metal. *Advanced Materials*, 24(24):3275–3279, jun 2012.

[251] Gergo P. Szakmany, Alexei O. Orlov, Gary H. Bernstein, and Wolfgang Porod. Single-metal nanoscale thermocouples. *IEEE Transactions on Nanotechnology*, 13(6):1234–1239, nov 2014.

[252] Xiaoye Huo, Haixiao Liu, Yiran Liang, Mengqi Fu, Weiqiang Sun, Qing Chen, and Shengyong Xu. A Nano-Stripe Based Sensor for Temperature Measurement at the Submicrometer and Nano Scales. *Small*, 10(19):3869–3875, oct 2014.

[253] Q. Zhang, Y. Sun, W. Xu, and D. Zhu. Organic Thermoelectric Materials: Emerging Green Energy Materials Converting Heat to Electricity Directly and Efficiently. *Advanced Materials*, 26(40), 2014.

[254] S Das Sarma, Shaffique Adam, E H Hwang, and Enrico Rossi. Electronic transport in two-dimensional graphene. *Reviews of Modern Physics*, 83(2):407–470, 2011.

[255] Shaffique Adam, E. H. Hwang, V. M. Galitski, and S. Das Sarma. A self-consistent theory for graphene transport. *Proceedings of the National Academy of Sciences of the United States of America*, 104(47):18392–18397, nov 2007.

[256] Ni Xiao, Xiaochen Dong, Li Song, Dayong Liu, Yeeyan Tay, Shixin Wu, Lain Jong Li, Yang Zhao, Ting Yu, Hua Zhang, Wei Huang, Huey Hoon Hng, Pulickel M. Ajayan, and Qingyu Yan. Enhanced thermopower of graphene films with oxygen plasma treatment. *ACS Nano*, 5(4):2749–2755, apr 2011.

[257] Fereshte Ghahari, Hong-Yi Xie, Takashi Taniguchi, Kenji Watanabe, Matthew S. Foster, and Philip Kim. Enhanced thermoelectric power in graphene: Violation of the mott relation by inelastic scattering. *Phys. Rev. Lett.*, 116:136802, 2016.

[258] Junxi Duan, Xiaoming Wang, Xinyuan Lai, Guohong Li, Kenji Watanabe, Takashi Taniguchi, Mona Zebarjadi, and Eva Y. Andrei. High thermoelectricpower factor in graphene/hBN devices. *Proceedings of the National Academy of Sciences of the United States of America*, 113(50):14272–14276, dec 2016.

[259] Kuang He, Gun Do Lee, Alex W. Robertson, Euijoon Yoon, and Jamie H. Warner. Hydrogen-free graphene edges. *Nature Communications*, 5, jan 2014.

[260] Zhang et al. Valley chern numbers and boundary modes in gapped bilayer graphene. *Proceedings of the National Academy of Sciences of the United States of America*, 110(26):10546–10551, 2013.

[261] G. Kucsko, P. C. Maurer, N. Y. Yao, M. Kubo, H. J. Noh, P. K. Lo, H. Park, and M. D. Lukin. Nanometre-scale thermometry in a living cell. *Nature*, 500(7460):54–58, 2013.

[262] Tingting Bai and Ning Gu. Micro/Nanoscale Thermometry for Cellular Thermal Sensing. *Small*, 12(34):4590–4610, sep 2016.

[263] Yuyan Shao, Jun Wang, Hong Wu, Jun Liu, Ilhan A. Aksay, and Yuehe Lin. Graphene based electrochemical sensors and biosensors: A review. *Electroanalysis*, 22(10):1027–1036, may 2010.

[264] B. Dutta, D. Majidi, N. W. Talarico, N. Lo Gullo, C. B. Winkelmann, and H. Courtois. A Single-Quantum-Dot Heat Valve. jan 2020.

[265] W. Lin, M. Hehn, L. Chaput, B. Negulescu, S. Andrieu, F. Montaigne, and S. Mangin. Giant spin-dependent thermoelectric effect in magnetic tunnel junctions. *Nature Communications*, 3, 2012.

[266] C. M. Jaworski, J. Yang, S. MacK, D. D. Awschalom, J. P. Heremans, and R. C. Myers. Observation of the spin-Seebeck effect in a ferromagnetic semiconductor. *Nature Materials*, 9(11):898–903, sep 2010.

[267] K. Uchida, S. Takahashi, K. Harii, J. Ieda, W. Koshibae, K. Ando, S. Maekawa, and E. Saitoh. Observation of the spin Seebeck effect. *Nature*, 455(7214):778–781, oct 2008.

[268] Jing Li, Rui Xing Zhang, Zhenxi Yin, Jianxiao Zhang, Kenji Watanabe, Takashi Taniguchi, Chaoxing Liu, and Jun Zhu. A valley valve and electron beam splitter. *Science*, 362(6419):1149–1152, dec 2018.

[269] Hâldun Sevinçli, Cem Sevik, Tahir Çain, and Gianaurelio Cuniberti. A bottom-up route to enhance thermoelectric figures of merit in graphene nanoribbons. *Scientific Reports*, 3(1):1228, dec 2013.

[270] Pascal Ruffieux, Shiyong Wang, Bo Yang, Carlos Sanchez-Sanchez, Jia Liu, Thomas Dienel, Leopold Talirz, Prashant Shinde, Carlo A. Pignedoli, Daniele Passerone, Tim Dumslaff, Xinliang Feng, Klaus Müllen, and Roman Fasel. On-surface synthesis of graphene nanoribbons with zigzag edge topology. *Nature*, 531(7595):489–492, mar 2016.

[271] Yuan Cao, Valla Fatemi, Shiang Fang, Kenji Watanabe, Takashi Taniguchi, Efthimios Kaxiras, and Pablo Jarillo-Herrero. Unconventional superconductivity in magic-angle graphene superlattices. *Nature*, 556(7699):43–50, apr 2018.

[272] Xing Ju Zhao, Yang Yang, Dong Bo Zhang, and Su Huai Wei. Formation of Bloch Flat Bands in Polar Twisted Bilayers without Magic Angles. *Physical Review Letters*, 124(8), 2020.

[273] Joseph P. Heremans, Vladimir Jovovic, Eric S. Toberer, Ali Saramat, Ken Kurosaki, Anek Charoenphakdee, Shinsuke Yamanaka, and G. Jeffrey Snyder. Enhancement of thermoelectric efficiency in PbTe by distortion of the electronic density of states. *Science*, 321(5888):554–557, jul 2008.

[274] Youngju Park, Bheema Lingam Chittari, and Jeil Jung. Gate tunable topological flat bands in twisted monolayer-bilayer graphene. Technical report.

[275] Sai S. Sunku, Alexander S. Mcleod, Tobias Stauber, Hyobin Yoo, Dorri Halbertal, Guangxin Ni, Aaron Sternbach, Bor Yuan Jiang, Takashi Taniguchi, Kenji Watanabe, Philip Kim, Michael M. Fogler, and D. N. Basov. Nano-photocurrent Mapping of Local Electronic Structure in Twisted Bilayer Graphene. *Nano Letters*, 2020.

[276] J. Crossno, J. K. Shi, K. Wang, X. Liu, A. Harzheim, A. Lucas, S. Sachdev, P. Kim, T. Taniguchi, K. Watanabe, T. A. Ohki, and K. C. Fong. Observation of the Dirac fluid and the breakdown of the Wiedemann-Franz law in graphene. *Science*, 351(6277), 2016.

[277] D. A. Bandurin, I. Torre, R. K. Kumar, M. Ben Shalom, A. Tomadin, A. Principi, G. H. Auton, E. Khestanova, K. S. Novoselov, I. V. Grigorieva, L. A. Ponomarenko, A. K. Geim, and M. Polini. Negative local resistance caused by viscous electron backflow in graphene. *Science*, 351(6277):1055–1058, 2016.

[278] Francesco M.D. Pellegrino, Iacopo Torre, Andre K. Geim, and Marco Polini. Electron hydrodynamics dilemma: Whirlpools or no whirlpools. *Physical Review B*, 94(15):155414, oct 2016.

[279] Leonid Levitov and Gregory Falkovich. Electron viscosity, current vortices and negative nonlocal resistance in graphene. *Nature Physics*, 12(7):672–676, jun 2016.

[280] Klaus D. Sattler. *21st Century Nanoscience – A Handbook*. CRC Press, volume 9 edition, 2020.

[281] Das Sarma et al. Electronic transport in two-dimensional graphene. *Reviews of Modern Physics*, 83(2):407–470, 2011.

[282] McClure J. W. Energy band structure of graphite. *IBM Journal of Research and Development*, 8(3):255–261, 1964.

[283] Slonczewski J. C. and Weiss P. R. Band structure of graphite. *Physical Review Letters*, 9(1):272–280, 1958.

[284] Reich et al. Tight-binding description of graphene. *Physical Review B*, 66(3):035412, 2002.

[285] Wallace P. R. The band theory of graphite. *Physical Review Letters*, 71(1):622, 1947.

[286] Semenoff G. W. Condensed-matter simulation of a three-dimensional anomaly. *Physical Review Letters*, 53(1):2449, 1984.

[287] McCann E. and Fal'ko V. I. Landau-level degeneracy and quantum hall effect in a graphite bilayer. *Physical Review Letters*, 96(1):086805, 2006.

[288] Dresselhaus M. S. and Dresselhaus G. Intercalation compounds of graphite. *Advances in Physics*, 51(1):1–186, 2002.

[289] Oostinga et al. Gate-induced insulating state in bilayer graphene devices. *Nature Materials*, 7(1):151 – 157, 2007.

[290] Ohta et al. Controlling the electronic structure of bilayer graphene. *Science*, 313(5789):951–954, 2006.

[291] Castro et al. Biased bilayer graphene: Semiconductor with a gap tunable by the electric field effect. *Physical Review Letters*, 99(1):216802, 2007.

[292] Nilsson et al. Electronic properties of bilayer and multilayer graphene. *Physical Review B*, 78(1):045405, 2008.

[293] M. Asheghi, K. Kurabayashi, R. Kasnavi, and K. E. Goodson. Thermal conduction in doped single-crystal silicon films. *J. Appl. Phys*, 91:079–5088, 2002.

[294] C S Lau, J A Mol, J H Warner, and G. A.D. Briggs. Nanoscale control of graphene electrodes. *Physical Chemistry Chemical Physics*, 16(38):20398–20401, oct 2014.

A

Band Structure of Graphene

In this Appendix the band structure of single-layer and bilayer graphene is derived and the respective implications are explained. This appendix is closely based on chapter 11 (Graphene Single Electron Transistors) in "21st Century Nanoscience – A Handbook, Industrial Applications (Volume 9)" published by CRC press [280].

A.1 Single-layer Graphene

As discussed in chapter 2, the π-band, and the corresponding single valence electron per atom, is what dominates the electronic properties of graphene at low energy levels.

Since the flat, two-dimensional hexagonal honeycomb structure formed by the carbon atoms is not a Bravais lattice (a distinct lattice type that through simple translation operations can represent the entire crystal structure of a material), we need to introduce two basis vectors $\vec{a_1}$ and $\vec{a_2}$ that span a unit cell with two atoms (Figure A.1a). The basis vectors are given by

$$\vec{a_1} = \frac{3}{2}a\hat{x} + \frac{\sqrt{3}}{2}a\hat{y} \tag{A.1}$$

and

$$\vec{a_2} = \frac{3}{2}a\hat{x} - \frac{\sqrt{3}}{2}a\hat{y}\,, \tag{A.2}$$

where a is the distance between two nearest neighbour atoms in the lattice and is given by $a \approx 0.142\,\text{nm}$. Both $\vec{a_1}$ and $\vec{a_2}$ have the same length, namely $|\vec{a_1}| = |\vec{a_2}| = \sqrt{3}a \equiv a_0$.

The unit cell spanned by $\vec{a_1}$ and $\vec{a_2}$ contains two atoms, A and B, which make up the basis. Note that both atoms are equivalent carbon atoms and possess a rotational symmetry for rotations of 180 degrees if we assume an infinite extension of the graphene sheet, which is usually a good approximation.

Switching to the reciprocal lattice, the lattice vectors spanning the reciprocal space are given by $\vec{b_1} = \frac{2\pi}{3a}\hat{x} + \frac{2\pi}{\sqrt{3}a}\hat{y}$ and $\vec{b_2} = \frac{\pi}{3a}\hat{x} - \frac{2\pi}{\sqrt{3}a}\hat{y}$. This defines the 1st Brillouin Zone (BZ) as shown in Figure A.1b where M is the bisector of a hypothetical line connecting two neighbouring lattice points. The corners of the BZ are defined by the two distinct corners $\vec{K} = \frac{2\pi}{3a}(\hat{x} + \frac{\hat{y}}{\sqrt{3}})$ and $\vec{K'} = \frac{2\pi}{3a}(\hat{x} - \frac{\hat{y}}{\sqrt{3}})$. Since the 1st BZ is naturally rotational invariant, we have three K and three K' points, marking the corners of our 1st BZ. Therefore, the six corners of the 1st BZ can be divided into two groups or two valley states, which are constructed by two equilateral triangles starting at K and K' respectively and connecting the corner points of the 1st BZ. These corners, specified by $\vec{K}$ and $\vec{K'}$, are called Dirac points and will be the focus of this section.

The band structure of graphene was first calculated in the early 1950's using a tight-binding approximation with the two-dimensional wave vector q

$$E_{\pm}(q) \approx 3t' \pm \hbar v_F |q| - \left(\frac{9t'a^2}{4} \pm \frac{3ta^2}{8}\sin(3\theta_q)\right)|q|^2 , \tag{A.3}$$

where t and t' are the nearest-neighbour (i.e. inter-sublattice $A - B$) or next-nearest-neighbour (i.e. intra-sublattice $A - A$ or $B - B$) hopping amplitudes ($t \approx 2.5\,\text{eV}$ which is $\gg t' \approx 0.1\,\text{eV}$), respectively, $v_F = 3ta/2$ is the Fermi velocity and $\theta_q = \arctan(q_x/q_y)$ [281, 85, 282–285].
For long wavelengths $t' = 0$, which gives us the linear dispersion relation widely used for small q values:

$$E_{\pm}(q) = \pm\hbar v_F q + O(q/k)^2 . \tag{A.4}$$

This linear dispersion relation is a good approximation and usually sufficient when considering transport properties in graphene at low energies and long wavelengths [281]. The linear dispersion leads to the formation of a Dirac cone at K and K' where the conduction and the valence band touch, making graphene a zero band-gap semiconductor (see Figure A.1c inset). Both holes in the valence band and electrons in the conduction band obey this relation. Since there are two distinct points at which Dirac cones are formed, namely K and K', this introduces a valley degeneracy

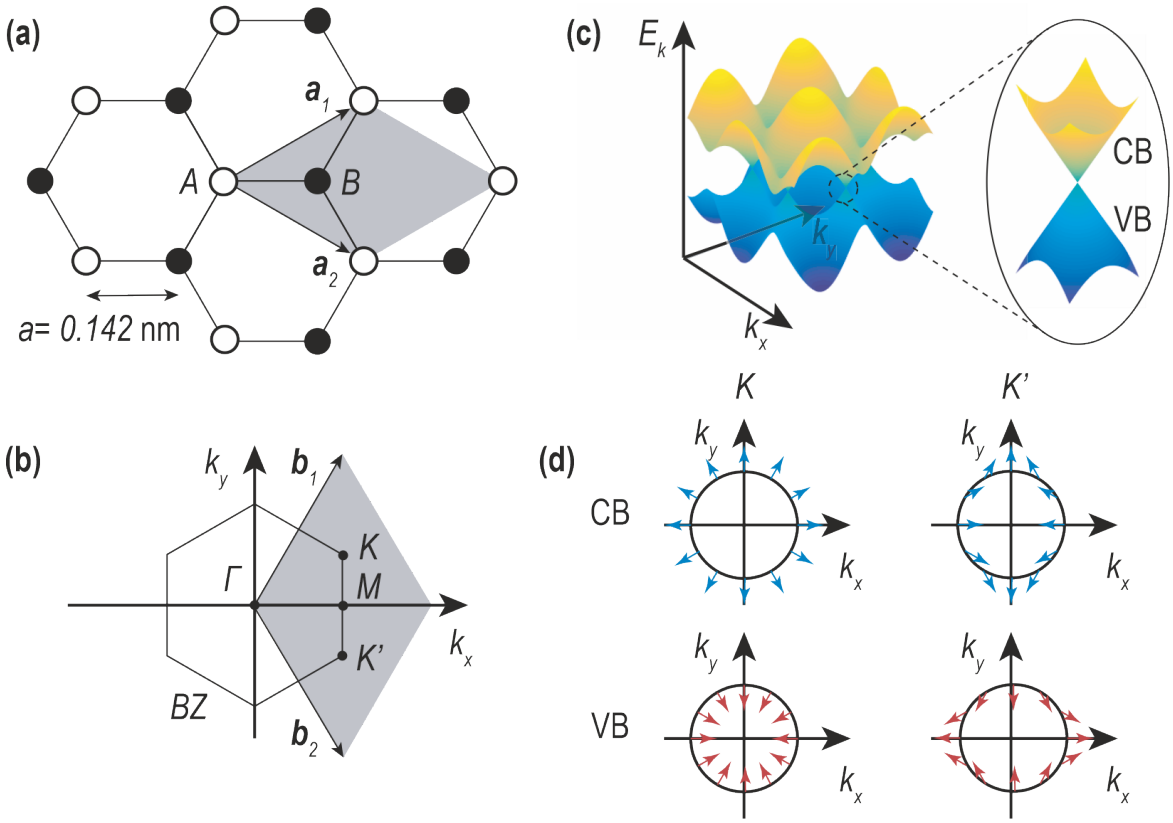


Figure A.1 The band and lattice structure of graphene. a) Graphene structure. The graphene lattice can be thought of as a combination of two triangular lattices (black and white dots) showing the two lattice unit vectors $\vec{a_1}$ and $\vec{a_2}$. b) Reciprocal space of graphene, showing the 1st Brillouin Zone and the reciprocal lattice vectors. The corners of the BZ, $\vec{K}$ and $\vec{K'}$, are called Dirac points, M is the bisector between adjacent lattice points and Γ marks the center of the B.Z. . c) Energy spectrum of graphene. The electronic dispersion for a graphene B.Z. showing the valence band (blue) and conduction band (yellow). The close up shows one of the six Dirac points where a Dirac cone is formed. d) Pseudospin orientation in k-space. The pseudo-spin orientation in k-space is indicated for the conduction band (blue arrows) and the valence band (red arrows) as well as the two different valleys K and K′.

($g_v = 2$) in graphene. The valley degeneracy is broken when inter-valley scattering occurs, typically caused by defects or contamination of the graphene. The Fermi velocity in graphene in the absence of any charge carriers in the conduction band can be calculated using contemporary estimates, which gives $v_F = 3ta/2\hbar \approx 10^6\,\mathrm{m\,s^{-1}}$ [281]. This value can potentially change when introducing carriers, especially in bilayer graphene.

Resulting from the two atoms per unit cell, graphene has two sublattices A and B. This leads to a chirality in graphene originating from the two branches of the Dirac cone being independent of each other and giving rise to a pseudo-spin quantum number. Carriers in graphene therefore possess three different quantum numbers, the usual carrier spin (up or down), the orbital index and the pseudo-spin index determined by the valleys.
Ignoring the real spin for now, the 2D continuum Schrödinger equation for long-wavelength and low energy graphene carriers can be written as

$$-i\hbar v_F q\sigma \cdot \nabla\psi(r) = E\psi(r)\,, \tag{A.5}$$

where σ is the vector of Pauli matrices in 2D and $\psi(r)$ is a 2D spinor wave function. $\psi(r)$ corresponds to the Hamiltonian given by:

$$\Xi = \hbar v_F q \begin{pmatrix} 0 & q_x - iq_y \\ q_x + iq_y & 0 \end{pmatrix} = \hbar v_F q\sigma \cdot q\,. \tag{A.6}$$

Here, equation (A.5) is simply the equation for massless chiral Dirac Fermions in 2D, with the spinor referring to the pseudo-spin, which allows the modelling of charge carriers in graphene as massless chiral Dirac Fermions [286].
The momentum space pseudo-spinor eigenfunctions can be expressed as

$$\psi(q,K) = \frac{1}{\sqrt{2}} \begin{pmatrix} e^{-i\theta_q/2} \\ \pm e^{i\theta_q/2} \end{pmatrix}$$

and

$$\psi(q,K') = \frac{1}{\sqrt{2}} \begin{pmatrix} e^{i\theta_q/2} \\ \pm e^{-i\theta_q/2} \end{pmatrix}\,.$$

In this equation, the $\pm$ refers to the conduction/valence band which is analogous to the respective energy being $E_\pm(q) = \pm\hbar v_F q$. It can be shown that the conduction band comes with positive chirality while the valence band exhibits a negative one

with both chiralities conserved. This is illustrated in Figure A.1d where the pseudo-spin orientation is reversed between the valence and the conductance band
Adding the real spin in the above equations would add an extra spinor structure but keep the overall results unchanged.

A.2 Bilayer Graphene

We will now give a quick overview of bilayer graphene and its difference to monolayer graphene. Bilayer graphene consists of two monolayers of graphene stacked on top of each other. This stacking leads to interlayer hopping, which may result in inter-lattice coupling, where the strength of this coupling depends on the way graphene is stacked. Here, we discuss the most common stacking configuration, that is $A - B$ stacking, as depicted in Figure A.2a.

The energy dispersion, neglecting small hopping terms and keeping only leading orders in momentum [287, 288] can be written as

$$E_{\pm}(q) = \pm \left[V - \frac{\hbar^2 v_F^2 q^2 V^2}{t_\perp^2} + \frac{\hbar^4 v_F^4 q^4}{t_\perp^2 V} \right] , \tag{A.7}$$

where $t_\perp$ is the interlayer hopping parameter, with $t_\perp \approx 0.4\,\mathrm{eV} < t \approx 2.5\,\mathrm{eV}$ [281] and V is the interlayer energy difference. V has the dimensions of energy, thereby accounting for a real shift in the electrochemical potential between the two layers [289–291, 171]. Such a shift can for example be induced by application of an external electric field through gating, thereby opening a band gap near the Dirac point.

From this equation we can see that bilayer graphene for $V \neq 0$ has a minimum band gap of $\Delta = 2V - 4V^3/t_\perp^2$ at $q = \sqrt{2}V/\hbar v_F$. Interestingly, for $V = 0$ and small q bilayer graphene exhibits a parabolic dispersion relation while for larger q a linear dispersion relation is recovered (see Figure A.2b). This can best be seen after rewriting Equation (A.7) in a hyperbolic form:

$$E_{\mathrm{BLG}} = \mp m v_F^2 \pm m v_F^2 \sqrt{1 + (k/k_0)^2} \tag{A.8}$$

where $k_0 = t_\perp/(2\hbar v_F)$ is the characteristic wave vector. Clearly, for $k \to 0$ $E_{\mathrm{BLG}} \to k^2$ and similarly for $k \to \infty$ $E_{\mathrm{BLG}} \to k$. For the parabolic regime, electrons in bilayer

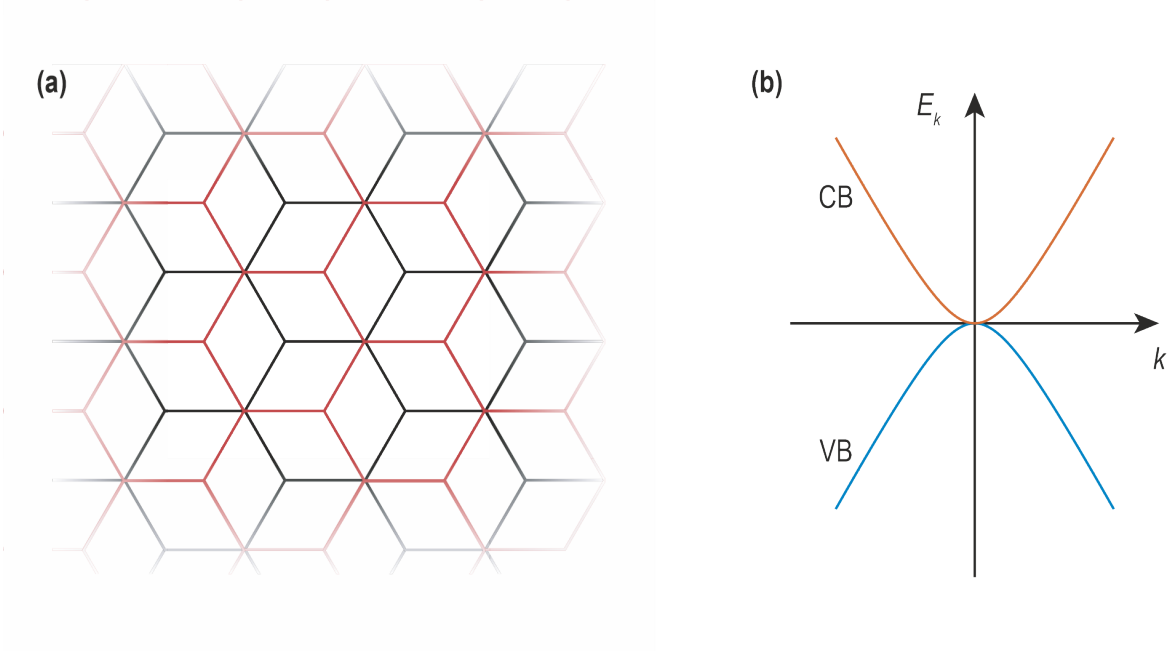


Figure A.2 Bilayer graphene AB stacking and band structure. (a) Schematic of A-B stacked bilayer graphene. The red and black lines depict the two respective lattices. (b) Band structure of bilayer graphene. The band does not exhibit a linear dispersion relation for small energies as is the case for single layer graphene case but is now parabolic. At higher energies, the linearity is recovered.

graphene have an effective mass $m \approx 0.03 m_e$ with $k_0 \approx 0.3\,\mathrm{nm}^{-1}$. From this, it can be concluded that the parabolic regime of the dispersion relation dominates for carrier densities smaller than $5 \times 10^{12}\,\mathrm{cm}^{-2}$ and the linear regime does for carrier densities above that (see Figure A.2b) [281].
Chirality of bilayer graphene is conserved since both layers still possess the $A - B$ sublattice symmetry independently from the non-linear dispersion relation. The new wave function now has a four-component chiral part to account for lattice and sublattice degrees of freedom [287, 292].

B

Standard Fabrication Details

In this Appendix, the standard fabrication procedure described in chapter 4 will be presented in further detail.

B.1 Chip Preparation

The substrate used for all devices is Si/SiO_2, with a 300 nm thick oxide layer where the silicon can be separately contacted and used as a global back gate. The substrate is purchased as a 3 inch wafer and subsequently divided in ≈1x1 cm pieces, either by hand with a diamond scribe or a dicing saw. When dicing the wafer, tape is often applied in order to hold the wafer together and a layer of photoresist is applied on the oxide layer to protect the substrate from dirt and contamination. The small chip size is necessary since multiple machines needed in the fabrication process, f.e. the electron beam lithography machine and the oxygen plasma are not designed for 3 inch wafers. Furthermore, the measuring setups are devised to take 1x1 cm chips and in addition the smaller size simplifies handling the sample.

Chip Cleaning. For fabrication on the scale of a few nanometres to succeed it is essential to both work in a clean environment (ensured by the cleanroom facilities) as well as to properly prepare and clean the samples one works with. Dust or dirt grains are often on the order or bigger than the structures written and therefore can substantially disturb the fabrication process. In addition, the light in a cleanroom is filtered, appearing yellow as high energy, short wavelength components of light could expose the photoresist.

After having diced the Si/SiO_2 wafer in 1x1 cm big pieces, the chips are sonicated in a beaker filled with Acetone and subsequently transferred to a beaker with Isopropanol (IPA) and again sonicated, with each sonication step being 5′ long.

This ensures that resist or tape residues applied to the wafer before dicing are removed. Depending on the perceived contamination of the wafer and on the eventual measurement planned (such as molecular measurements) the chips are afterwards immersed in a piranha solution. The piranha solution consists of sulphuric acid (H_2SO_4) and hydrogen peroxide (H_2O_2) in a 3:1 ratio and the chips are left for 10' to remove any organic residues [153]. Now that the chips are thoroughly cleaned, they can be prepared for the next step in the fabrication, Electron Beam Lithographic (EBL) patterning, which requires a photosensitive resist.

B.2 Photoresist Application (Figure B.1a-b).

The resist needs to coat the entire chip and have a constant height as well as be free of foreign particles or air bubbles to guarantee the best results. The established method to achieve this is spin coating where the chip is mounted on a spinning disk via a vacuum chuck. The thickness of the film is determined by the resist composition and evaporation rate as well as the spinning speed chosen for the spin coater. Typically, the thickness is proportional to the inverse square root of the spin speed.
The standard spin procedure is as follows. After the chip is mounted on the spincoater and the appropriate recipe is chosen, 15 µl of polymethyl methacrylate (PMMA) are pipetted out of the resist bottle to dispense on the chip. Here it is crucial to not contaminate the resist bottle by reusing a pipette tip or causing air bubbles and to not leave the resist bottle open for longer than necessary as the Anisole used to thin a resist to the right solid content concentration evaporates. Before applying the resist to the chip, two drops are deposited next to the chip preventing the formation of air bubbles and ensuring a clean flow and then three drops are deposited on the chip. Here it is useful to leave a bit of resist behind in the pipette as the last drop tends to be a mixture of resist and air.
Subsequently, the spin process is started. The chip is first spun slowly (at 1000 RPM) for ten seconds during the ramping stage to flow the resist all over the chip and get rid of excess solvent and afterwards it is spun at 3000 RPM for a minute to achieve the desired uniform thickness of the resist.
The last step to prepare the chips for lithography is to bake the resist after spinning it. This is done at a temperature above the glass transition point of the resist. Here we use 180 °C so that the resist starts to flow again, ensuring a uniform thickness covering the whole chip. In addition, this baking step will evaporate any remaining

solvent in the resist.
Now the chip can be further processed using EBL or if another layer of resist is required, the process of photoresist application is repeated.
Choice of Photoresist. Depending on the application, different photoresists are chosen. Two main groups of resist are available for EBL, depending on what the desired patterning procedure is. As mentioned, when aiming to deposit a metal layer we use PMMA, which is a positive resist. In a positive resist, the area exposed by the E-beam will get washed away in development and therefore this is where a subsequent etching process/metal deposition will be happening, see Figure B.1. The other sort of resist used is negative resist, where the exposed area remains and can function as for example an etch mask (see Figure B.2, we will use this resist later on to define the graphene pattern).
Positive resists are characterized by a molecular weight and solid concentration number. Resists with a higher molecular weight ensure a higher contrast between exposed and unexposed regions because they dissolve slower in a solvent developer. The two most common used resists are PMMA 495000 (495K) and PMMA 950000 (950K) where the number indicates the molecular weight (see Figure B.1). The thickness in the spin process is determined by both the spin speed and the percentage of solids in the resist. For example, PMMA 495K A6 indicates a resist with molecular weight 495K and a 6 % solid concentration in Anisol. When patterning the contacts and leads of our device, that is to prepare for a metal deposition, a two-layer resist strategy is used in order to create an undercut and facilitate the lift-off. For this, first a layer of PMMA 495K A6 is spun on the chip as the base layer creating the undercut and then PMMA 950K A3 is spun on top of the first layer, serving as the template layer. The reason to use two different layers with their respective molecular weights will become clear in the next section.

B.3 Electron Beam Lithography (Figure B.1c).

In a simplified way, the EBL machine works by shooting a beam of electrons in a user-predefined pattern on the photoresist, thereby exposing certain parts and performing molecular chain scission (positive resist) or cross-linking (negative resist). The crucial metric here is the exposure dose, which is measured in $\mu C\,cm^{-2}$ and which needs to be carefully adjusted in order to write small features with the required sharpness. If the dose is too low, the resist won't be completely exposed, meaning the feature will look spotty with holes in it and any metal deposition will be evaporated on resist

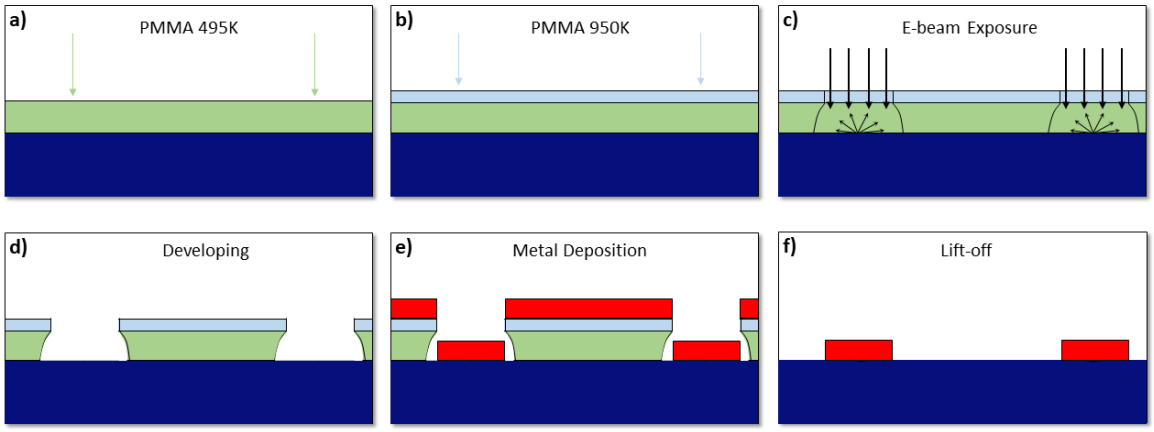


Figure B.1 Metal Deposition Schematic. a) Application of the first photoresist. b) Addition of the second layer of photoresist. c) E-beam exposure, with secondary electron scattering from the substrate. d) Developing of the resist, leaving an undercut. e) Deposition of metal using a thermal or e-beam evaporator. f) Lift-off aided by the undercut leaving the final metal structure.

residues, resulting in a rough rather than smooth surface. If the dose is too high on the other hand sharp features such as a corner will be bloated and closely spaced features will melt into each other, possibly short-cutting different leads. The right dose can be found by performing a dose test, where the desired feature is written in different doses ranging from clearly underexposing to clearly overexposing doses and subsequently inspected by for example an SEM.
For the fabrication in this work, a JEOL EBX 5500F S EBL system is used. In order to expose an area with a certain dose, the machine fills the pattern to be written with dots of the size of the electron beam width, about 0.5 nm. Then depending on the dose, the ebeam exposes every other dot or greater intervals, calculated from the beam current and the minimum beam speed to achieve the desired area dose. For our PMMA resists, we use an area dose of $600\,\mu C\,cm^{-2}$.
As can be seen in Figure B.1c, the effect of the electron beam hitting the first layer of PMMA 950K A3 exposes the resist only in the area of direct impact, defining the pattern to be written. The second layer on the other hand is also affected by the proximity effect and secondary scattered electrons backscattered from the SiO_2 substrate. These second hand back scattered electrons, which are still energetic enough to break the resist polymer chains, are creating an undercut (Figure B.1d). The undercut is desirable for metal depositions since it greatly facilitates a clean lift-off process as discussed later.

In a negative resist on the other hand, the E-beam exposure crosslinks rather than breaks the polymer resist, meaning the exposed area remains after development (see Figure B.2).

B.4 Development (Figure B.1d)

After the resist has been exposed, the chip needs to be developed in order to wash away the remaining resist that is not contributing to the pattern. Either the area where the polymer chains have been cut (positive resist) or where the resist is not cross-linked (negative resist) is washed away by the developer. For PMMA, we typically use an IPA:MIBK (3:1) mixture, developing the chip in the mixture for about 60 s and afterwards immersing it into IPA to stop the developing process. Brownian motion is usually sufficient to ensure a full development process and wash away the remaining resist but swirling the sample carefully in the developer at the beginning and end of the development can be performed to support the process. It is important to have the correct time for the developing process, as over or under developing has similar effects to over- or underexposing the sample. In order to improve the resolution of the writing or to prevent cracking of the resist due to strain (such as on top of a hexagonal Boron-Nitride flake) cold development can be used, which slows down the development process. Here, the resist is developed at or below 0 degree Celsius, increasing the required developing times by about two [154].

B.5 Deposition and Lift-off (Figure B.1e-f)

After the pattern has been developed and inspected under an optical microscope, the desired metal layer can be deposited. This is in our case done by a thermal evaporator, where the metal is placed in a metal boat, that is heated through Joule heating, causing the metal to evaporate. The sample is mounted upside down above the evaporation source and the thickness of the metal evaporated is measured via a quartz crystal sensor [155]. For the Au contacts, a few nanometres of chrome are deposited first to act as an adhesion layer for the gold [156]. Subsequently a layer of Au about 100 nm thick is deposited. It is important to deposit a sufficient layer of Au so that the wire bonding performed later to contact the sample does not punch through the Au and oxide and thereby shorts the back gate. However, when transferring graphene on the device after the contacts are written, a higher Au

layer means that the graphene has to bridge a bigger horizontal distance, making it more prone to breaking at this point. In order to satisfy both requirements, one can perform two evaporations, one for the contacts up to about 45 nm in height and a second one on the contact pads which can be up to 150 nm.
The limiting factor for deposition thickness is the thickness of the resist. In order to facilitate the lift-off, the process where the remaining photoresist is dissolved by Acetone, the metal deposition thickness should be smaller than one third of the undercut photoresist thickness. This ensures that the solvent can flow under the deposited metal deposition layer via the undercut defined earlier and dissolve the resist from multiple sides (see Figure B.1e). Issues with the lift-off, where parts of the metal are sticking to the substrate or hanging of the written patterns can often be solved by agitation of the sample. For a sample that is rather fragile gentle shaking in the solvent or agitation with a pipette, blowing solvent over the sample, can dislodge metal flakes that have not been deposited straight on the substrate. In order to have an ideal lift-off result it is advisable to agitate the sample about 15' after it has been placed in the solvent so that the metal layer will not lay down on the substrate and stick to it. If the substrate is not fragile, for example does not have graphene transferred to it, a short burst of sonication (about 3 to 10 s) can be used in most cases to ensure a clean lift-off.

B.6 Graphene Transfer

After the Au contacts and heater have been patterned by the procedure above, we are now ready to transfer graphene on top of the chip. We use mostly Chemical Vapour Deposited (CVD) graphene due to the ease of use and the ability to cover big areas. For further information on CVD graphene production see chapter 3. CVD graphene is grown on a copper substrate and will usually have PMMA spun on top of it to ease the transferring. The copper foil tends to be much bigger than the 1x1 cm chips and will have to be cut into the right shape, which is found to be easiest by utilizing a tool similar to a Pizza cutter. Here it is important not to cut the graphene too small, such that it does not cover the whole chip or too big such that it hangs over the edge of the chip (hanging over the edge of the chip will introduce creases and tears in the graphene and can shortcut the back gate).
The first preparation step is to remove the backside graphene. Since the copper foil is the growth nucleus for the graphene, not only the frontside of the copper has graphene on it but the backside does as well. This backside graphene tends to roll

up and stick to the front layer after the copper is etched away. In order to avoid this, the backside is etched in a Reactive Ion Etcher (RIE) to selectively remove only the backside graphene (an RIE is preferred to an oxygen plasma etcher since it offers greater directionality). Subsequently, the graphene on the copper foil is placed in an Ammonium Persulfate (APS) solution to etch away the copper. For this 3.6 g of APS dissolved in 80 mL of de-ionized water is usually sufficient to etch three 1x1 cm pieces of graphene on copper, with the etching being completed within 2 to 4 hours. In order to speed up the etching process, the APS solution can be placed on a hotplate and heated up to 60 °C. To ensure a complete removal of the copper (not only the optically visible part) it is advisable to leave the graphene on copper in the APS solution overnight.
After the copper is etched away, the graphene with the PMMA layer on top is floating in the APS solution. The PMMA is here important to support the graphene, preventing it from rolling up, tearing or developing creases. In order to wash away the APS residues from the graphene, the graphene sheet is subsequently transferred to a new beaker with fresh de-ionized water at least four times. This is done by picking the graphene up with a big piece of Si/SiO_2 wafer. After the APS residue has been washed away, we can now pick up the graphene with the pre-patterned Si/SiO_2 chip. Ideally we want the graphene to cover the whole chip but not hang over the edge as mentioned before. This process of "fishing" the graphene out of the de-ionized water can be tedious but spending additional time is important to guarantee a successful transfer. After the graphene is picked up, the water between the graphene and the chip, which is a residue of the transfer needs to be removed. There are three ways of doing this: Dipping the chip into IPA to force our the water (carefully as to not lose the graphene), blow drying the graphene on top of the chip and thereby pressing the water out or just leaving the chip to dry in air. In each case, the water (or the solvent replacing it) needs to be completely removed before the next step. In order to release tension in the graphene and make sure it conforms to the underlying profile, the chip is placed on a hot plate at 180 °C for at least two hours. This temperature is above the glass transition temperature of most commercially available PMMA. If there is still water or solvent underneath the graphene at this point, it will evaporate and rip holes in the graphene.
After this step, the chip is immersed in Acetone for a few hours to remove the PMMA resist on top of it and subsequently we have a patterned chip with graphene on top.

B.7 Graphene Patterning (Figure B.2)

In order to pattern the graphene structures, such as a graphene bow tie, a negative resist is used (typically MAN 2403 here). Similar to the previous procedure we start by applying the resist via a spin coater on a chip with a layer of graphene transferred to it, spinning for 60 s at 3000 rpm. Then the resist is baked at 90 °C for 60 s and subsequently loaded into the E-beam. Here as discussed previously, the area exposed represents the desired structure as exposure cross-links the resist. The dose used is 120 $\mu C\,cm^{-2}$. Afterwards the chip is developed in MAD525 for 60 s and then washed in deionized water. At this point, the graphene on the chip is covered with a pattern of cross-linked resist that is now used as an etching mask (Figure B.2c, d). The chip is then loaded into an oxygen plasma etcher and etched for about 60 s. The exact etching rate depends on the instrument used and the thickness of the graphene (single or multilayer). The cross linked resist can then be removed with REM660, leaving only the graphene pattern on the chip.

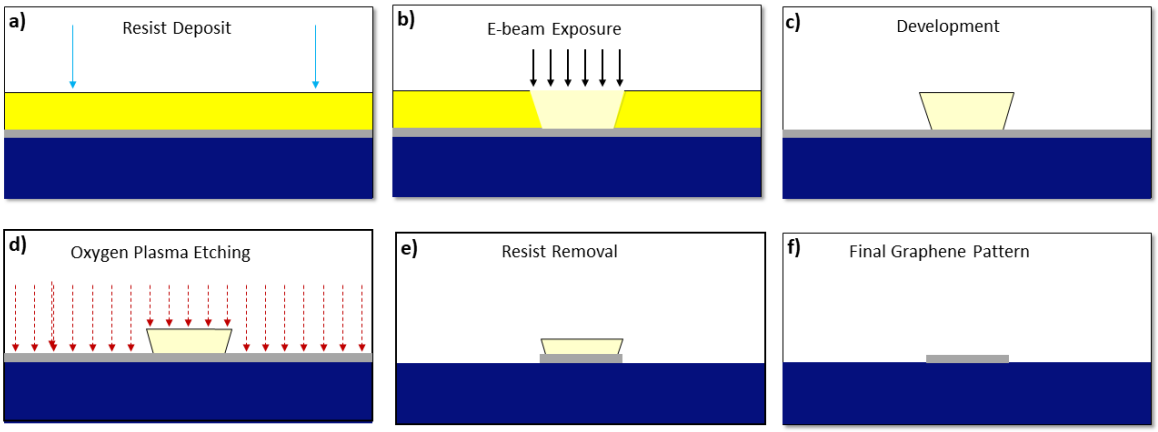


Figure B.2 Graphene Patterning Schematic. a) Deposit of negative resist on top of the graphene. b) Exposure with the e-beam, crosslinking the resist. c) Development, leaving the patterned resist structure on top of the graphene. d) Oxygen plasma etching, the resist serves as an etching mask. e) Removal of the resist layer on top of the graphene structure. f) Final graphene structure at the end of the fabrication run.

The graphene patterned in this way is highly p-doped due to both, exposure to the negative resist as well as interaction with SiO_2 surface charges [157]. This intrinsic doping can be reduced greatly through annealing of the sample, which can lower the Dirac voltage down to 40 to 80 V from over 100 V.

C

Further Experimental Details

In this Appendix, additional information on the experimental measurements described in part 3 of the thesis is given.

C.1 Thermoelectric Measurements of C_{60} Molecule Devices

This section presents further details on the additional heater calibration methods (SThM and COMSOL simulation) and supplementary transport and thermoelectric C_{60} molecule data. The section is closely based on the supplementary information available from Gehring *et al.* [182].

C.1.1 Calibration of the Heater: Vacuum and Variable Temperature Scanning Thermal Microscopy

The in-vacuum SThM measurements were performed in a NT-MDT high vacuum Solver system that operates at pressures of 10^{-6} to 10^{-7} torr, which is similar to the thermoelectric measurement conditions, and avoids heat convection through air between the sample and the probe,. The system has a custom made LN2 cold finger that allowed base temperatures down to $-120\,°C$. For precise temperature control the sample was attached to a Peltier heater/cooler stage via a heat conductive varnish. In addition, the plate temperature was monitored with a calibrated Pt resistive thermometer and the stage temperature $T_{st} = T_0$ was then controlled via a PID closed-loop control with an accuracy of 50 mK in the range from 300 K to 200 K. The thermal response of the SThM was measured as described elsewhere [167] through

the change in the resistance of the thermal probe via an AC Wheatstone bridge operating at 91 kHz frequency, with a low-noise instrumental amplifier followed by a lock-in amplifier.

C.1.2 "Additive" Method for Absolute Heater Temperature Calibration.

The method uses the fact that the total temperature of the sample is the sum of the temperature of the sample stage T_{st} and the heater defined on the probe $T_s = T_{st} + \Delta T_s$. Linearity of the SThM response then allows us to quantify a temperature increase generated by the micro-heater. Again, this "subtraction" method is implemented in the same high vacuum conditions (10^{-6} to 10^{-7} torr) as for the thermoelectric measurement to eliminate artefacts caused by heat convection. The wide temperature range and high precision provided by the Pt thermometer for T_{st} gives results with a total relative error for the temperature increase of 10 %. It should be noted that both the "null" and "addition" methods for determining absolute temperature increase do not depend on the sample-tip thermal resistance due to their differential nature and therefore provide reliable absolute measurements within the error specified.
In this measurement, a rectangular heating voltage on the heater was switched between 0 and 3 V with a period of 1 Hz resulting in a corresponding rectangular change in the SThM signal ΔV_h as shown in the experimental trace in Fig. C.1 b). The stage temperature was then increased by $\Delta T_0 = 5\,\mathrm{K}$, which lead to a corresponding shift of the SThM response by ΔV_{st} (see schematic in Fig. C.1 c). Due to the linearity of the SThM response, the rise of the chip surface temperature is then found directly as $\Delta T_h = \Delta T_{st}\,(\Delta V_h / V_{st}) = 5\,\mathrm{K}\,(\Delta V_h / V_{st})$.
This approach was extended to measurements of the spatial distribution of the heater temperature. For this measurement, the micro-heater was operated at about 70 Hz (a frequency confirmed to be well below the heater time constant) with a second lock-in amplifier measuring the local heating at this frequency. While this required large time constants of the second lock-in amplifier and long acquisition times of the heating image, the differential approach allowed practically complete elimination of spurious signals as well as thermal drift. The images in Fig C.2 a) show the temperature distribution image of the two heater lines (Fig. C.2 b)). We note that due to its differential nature this approach allows to directly map the additional surface temperature increase ΔT_h. The map shows that the temperature of the SiO_2

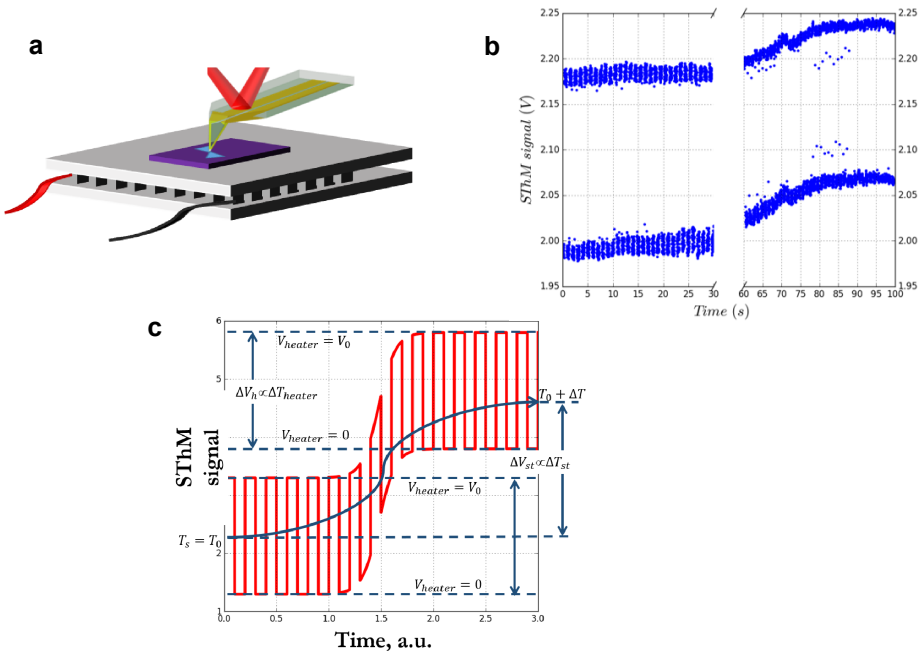


Figure C.1 Additive SThM method. a), Experimental setup with T controlled Peltier stage. b), Experimental measurement and c) explanation of the principle of "additive" approach to the calibration of the absolute rise of the sample temperature due to the heater. A rectangular heating voltage on the heater results in a change of the SThM signal ΔV_{h}, the stage temperature was then increased by $\Delta T_0 = 5\,\mathrm{K}$ leading to a shift of the SThM response by ΔV_{st}.

area close to the Au heater is about a factor 0.75 ± 0.05 smaller than the Au heater temperature, which is attributed to the thermal interface resistance between the Au heater and the substrate. At the same time, for the "passive" Au line (i.e. the source contact, Fig C.2 a,b), this thermal resistance does not affect the local temperature of the sample with the "passive" line showing the same temperature as the surrounding SiO_2 surface. The temperature profiles were compared to finite element modelling, which shows a good agreement between experimentally measured and modelled temperature distributions. The measurements using this method show that at 300 K the 3 V applied to the heater produced a temperature increase of $\Delta T_{\mathrm{h}} = 7.1 \pm 0.4\,\mathrm{K}$ for the Au heater, while at 200 K the temperature increase was $\Delta T_{\mathrm{h}} = 10.3 \pm 0.7\,\mathrm{K}$. Assuming a linear dependence of the properties in the system over the temperature range down to the temperature of thermoelectric measurements (77 K), we can reasonably estimate that the Au heating would be $13.5 \pm 1\,\mathrm{K}$, or approximately twice the room temperature value. However, to calculate the temperature increase

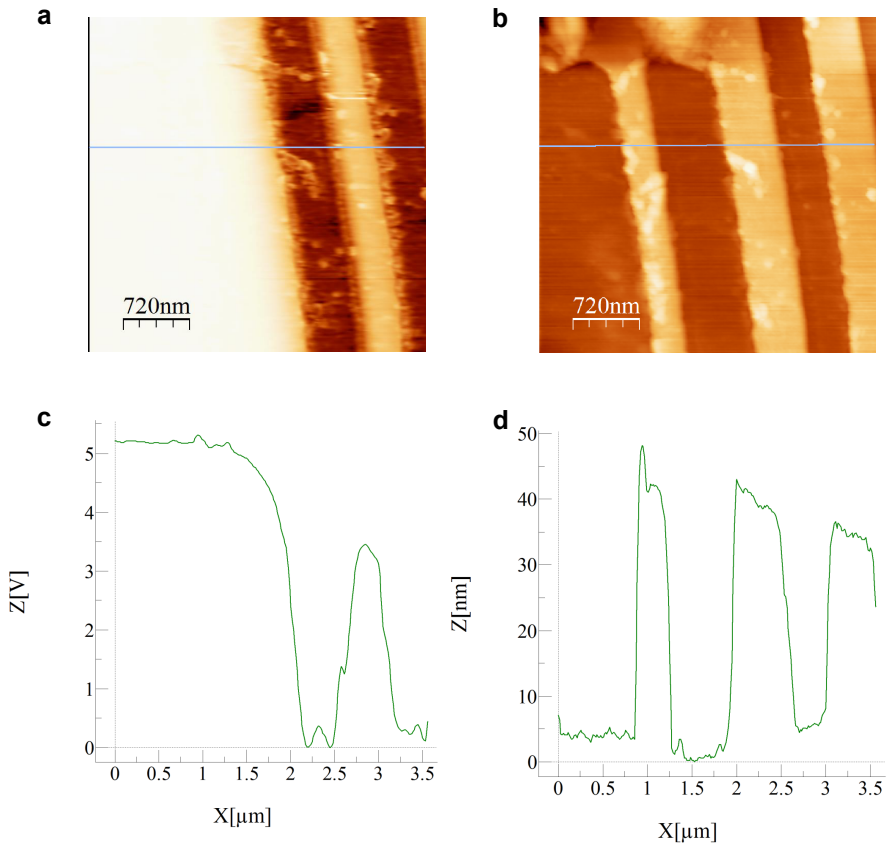


Figure C.2 Thermal a) and topographical b) images of the active heater with the corresponding linear profiles c), d) along the lines shown in the thermal and topography images.

as a function of heater power we need to include the temperature dependence of the resistance of the micro-heater. We find that the resistance of the heater drops linearly and decreases to about 60 % of its value when cooling the sample from room temperature to 77 K. With this value, we can estimate the temperature increase per heater-power at 77 K to be $63\,\mathrm{K\,W^{-1}} \times 1.9 \times 60\,\% = 71\,\mathrm{K\,W^{-1}}$.

C.1.3 Calibration of the Heater: COMSOL Simulations

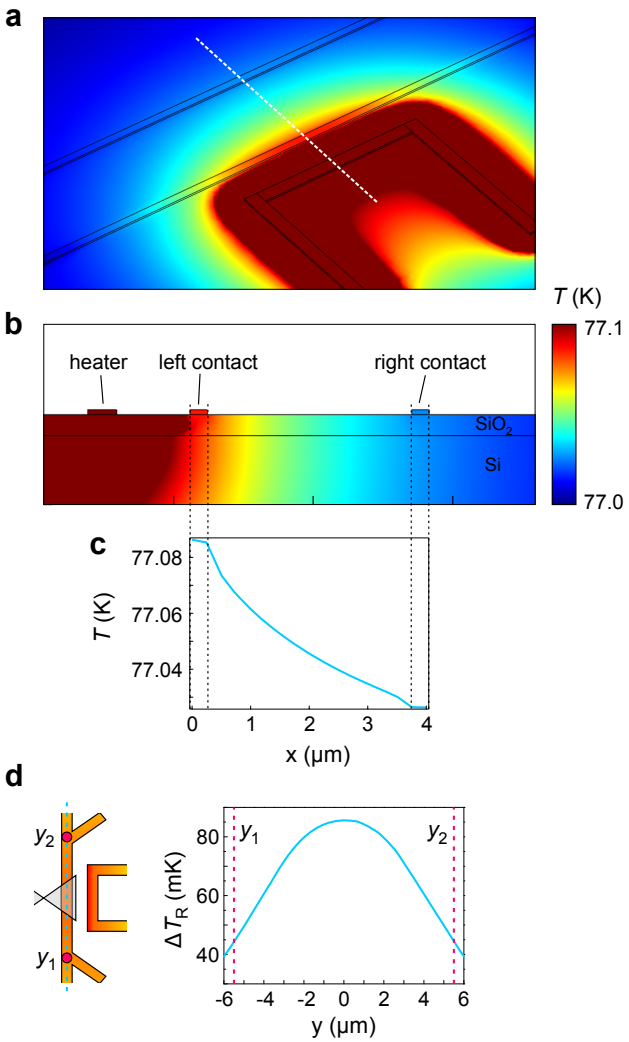


Figure C.3 Simulating Joule Heating with COMSOL software. a) Temperature map calculated at $T = 77\,\mathrm{K}$, with a heating power of $1.2\,\mathrm{mW}$ and using a thermal conductance of $\kappa_{\mathrm{Si}} = 450\,\mathrm{K\,W^{-1}\,m^{-1}}$ for the highly doped Si substrate [293]. b) Plane cut along the dotted white line in **a**. c) Temperature profile below the surface. We can extract a power dependent temperature drop on the device of $50\,\mathrm{K\,W^{-1}}$. d) Temperature increase along the contact, where $y = 0$ is the middle of the contact and y_1, y_2 are the connection points of the voltage probes used for four-terminal measurements.

C.1.4 Supporting Thermoelectric Data: C_{60} Junctions

For the study of C_{60} molecules, we fabricated 10 chips with 108 devices on each chip. After feedback controlled electroburning of all devices (yield about 70 %, defined as in Lau *et al.* [294] and Gehring *et al.* [178]) we wire bonded 10 devices per chip (the number of devices is limited by the amount of DC lines in our measurement setup, see chapter 5). The devices that were bonded were chosen according to their Simmons-like tunneling $I - V$ characteristic at room temperature and subsequently they were cooled down and their transport behaviour characterised at $T_0 = 77\,\mathrm{K}$. After the initial characterisation, C_{60} molecules are deposited from solution and a further low temperature characterisation is performed. We found that in 16 (out of 10 x 10 = 100) devices the transport changed from an "empty gap" nature to Coulomb blockade. After the thermoelectric measurements in a LN_2 dewar ($T_0 = 77\,\mathrm{K}$) were completed, we transferred the devices (inside a dip stick without warming up to more than 90 K or breaking the vacuum) to a LHe dewar ($T_0 = 4\,\mathrm{K}$) for the low temperature characterisation. Unfortunately, some devices got destroyed during this transfer. Table C.1 summarises the data collected for each device. The measurement results are summarised in table C.2.

To identify C_{60} molecules we investigated the sequential tunneling regime of each device at low temepratures in order to identify vibrational finger prints of the molecule. For each junction showing pronounced excited states (see table C.1) we show line cuts (conductance as a function of energy) and indicate the energetic position of all vibrational modes of the C_{60} bisadduct [37].

Table C.1 Summary of the data collected for each C_{60} device. (**X** = measured)

Device name	**Before/after at 77 K**	**Transport at** 77 K	**Transport at** 4 K	**Evidence for vibrational modes**	**Thermovoltage measurement**
B (Device 3)	**X**	**X**			**X**
C (Device 4)	**X**	**X**			**X**
D (Device 1)	**X**		**X**	**X**	**X**
E (Device 5)	**X**		**X**		**X**
F (Device 6)	**X**	**X**			**X**
G (Device 2)	**X**	**X**			**X**
H	**X**		**X**	**X**	
I	**X**		**X**	**X**	
J	**X**		**X**	**X**	
K	**X**		**X**	**X**	
L	**X**		**X**	**X**	**X**
M	**X**		**X**		
N	**X**		**X**	**X**	**X**
O	**X**	**X**	**X**		**X**
P	**X**	**X**	**X**		**X**
Q (Device 7)	**X**	**X**	**X**		**X**

Table C.2 Measurement results for each C_{60} device.

Device name	Γ **(μeV)**	χ	α **(meV/V)**	E_0 **(meV)**	$S_{\max}$ **(μV/K)**	$G_{\max}$ **(e^2/h)**	$(S^2G)_{\max}$ **(k_B^2/h)**	T_0 (K)
B	44	–	9	221	220	0.003	0.01	77
C	6.5×10^2	–	10	188	140	0.08	0.08	77
D	1.35×10^3	15	13	335	27	0.2	0.14	3.2
E	8	–	6	53	238	0.006	0.02	11
F	85	–	11	84	460	0.01	0.11	77
G	1	–	9	12	30	10^{-4}	0.04	77
L	42	–	18	-310	338	10		4.2
N	1.5×10^4	1.5×10^5	12	-105	0.4	3×10^{-5}	10^{-9}	4.2
O	2.2×10^3	2.2×10^3	13	113	2300	1.2		4.2
P	2.65×10^3	5.3×10^3	45	747	125	4×10^{-4}		4.2
Q	1.2×10^4	1.2×10^4	62	564	1.5	2×10^{-4}	7×10^{-4}	77

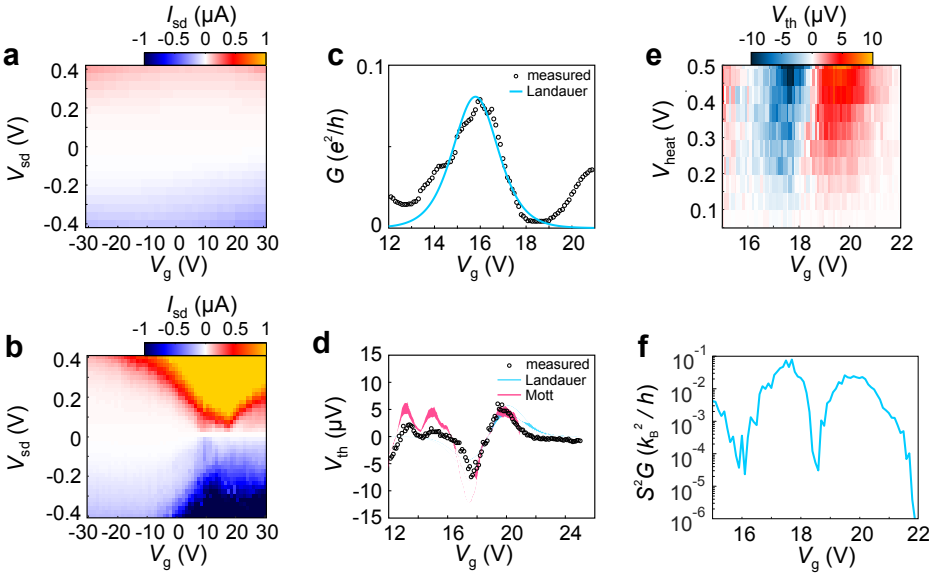


Figure C.4 Thermoelectric characterisation of a C_{60} junction (Device C). a) Current map as a function of back gate and bias voltage before and b) after molecule deposition recorded at $T_0 = 77\,\mathrm{K}$. c), AC Zero-bias conductance and d) Thermovoltage (measured with a temperature bias of $\Delta T = 53 \pm 11\,\mathrm{mK}$) as a function of back gate voltage measured at $T_0 = 77\,\mathrm{K}$. The blue and pink curves show theoretical calculations using a Landauer-type approach and the Mott formula, respectively. e) Thermovoltage as a function of back gate and heater voltage measured at $T_0 = 77\,\mathrm{K}$. **f**, Power factor as a function of back gate voltage measured at $T_0 = 77\,\mathrm{K}$ with $\Delta T = 53 \pm 11\,\mathrm{mK}$.

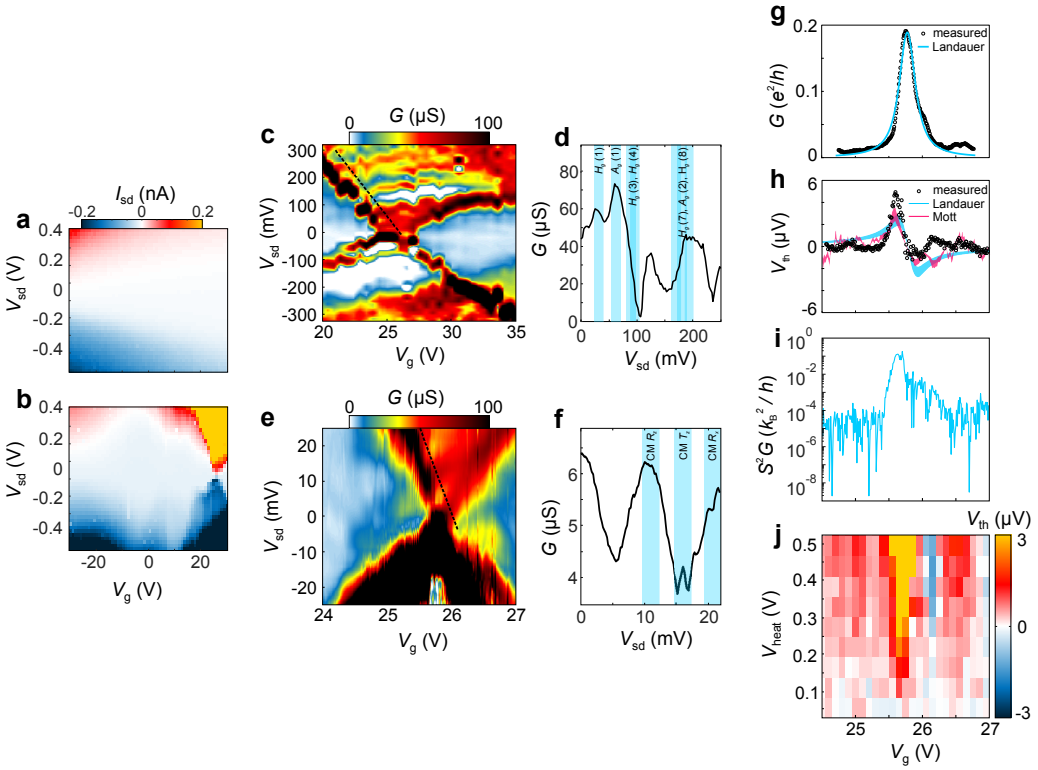


Figure C.5 Thermoelectric characterisation of a C_{60} junction (Device D). a) Current map as a function of back gate and bias voltage before and b) after molecule deposition recorded at $T_0 = 77\,\mathrm{K}$. c) Overview and **e** detailed differential conductance maps of the sequential tunnelling region in **b** measured at $T_0 = 3.2\,\mathrm{K}$. Line cuts along the dotted black lines are shown in d) and e) respectively. The blue shaded areas in (d) and (e) indicate the energies of different vibrational modes of the C_{60} bis-adduct. g) AC Zero-bias conductance and h) Thermovoltage (measured with a temperature bias of $\Delta T = 45 \pm 9\,\mathrm{mK}$) as a function of back gate voltage measured at $T_0 = 3.2\,\mathrm{K}$. The blue and pink curves show theoretical calculations using a Landauer-type approach and the Mott formula, respectively. i) Power factor as a function of back gate voltage. j) Thermovoltage as a function of back gate and heater voltage measured at $T_0 = 3.2\,\mathrm{K}$.

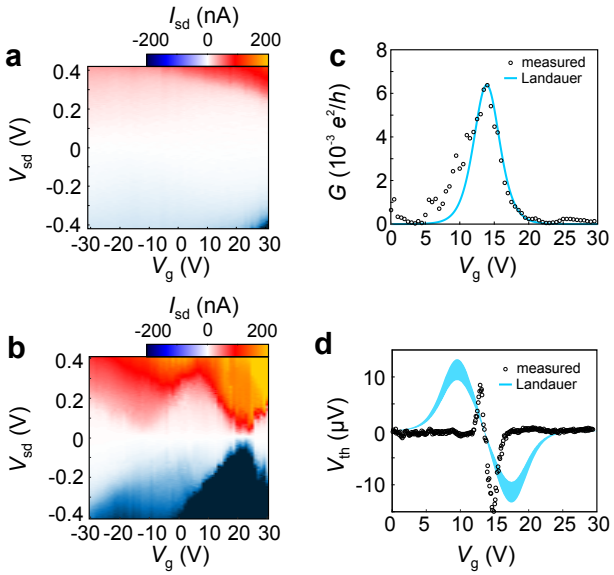


Figure C.6 Thermoelectric characterisation of a C_{60} junction (Device E). a) Current map as a function of back gate and bias voltage before and b) after molecule deposition recorded at $T_0 = 77\,\mathrm{K}$. c) AC Zero-bias conductance and d) Thermovoltage (measured with a temperature bias of $\Delta T = 63 \pm 13\,\mathrm{mK}$) as a function of back gate voltage measured at $T_0 = 11\,\mathrm{K}$. The blue curves show theoretical calculations using a Landauer-type approach. Although the Landauer approach fails to predict the exact line shape of the thermovoltage signal, it can be used to estimate its amplitude within the error bars of the measurement.

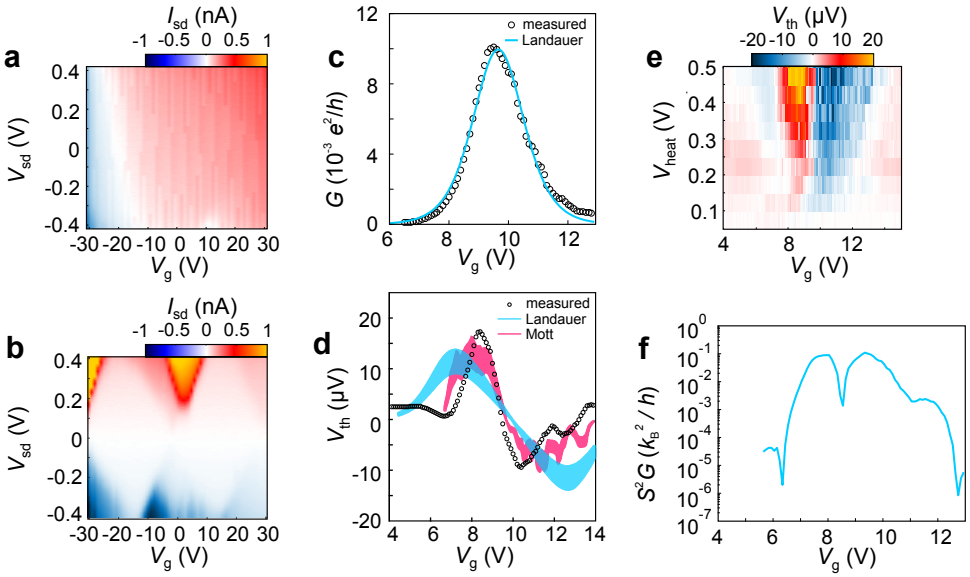


Figure C.7 Thermoelectric characterisation of a C_{60} junction (Device F). a) Current map as a function of back gate and bias voltage before and b) after molecule deposition recorded at $T_0 = 77\,\mathrm{K}$. c) AC Zero-bias conductance and d) Thermovoltage (measured with a temperature bias of $\Delta T = 40 \pm 8\,\mathrm{mK}$) as a function of back gate voltage measured at $T_0 = 77\,\mathrm{K}$. The blue and pink curves show theoretical calculations using a Landauer-type approach and the Mott formula, respectively. e) Thermovoltage as a function of back gate and heater voltage measured at $T_0 = 77\,\mathrm{K}$. f) Power factor as a function of back gate voltage measured at $T_0 = 77\,\mathrm{K}$ with $\Delta T = 40 \pm 8\,\mathrm{mK}$.

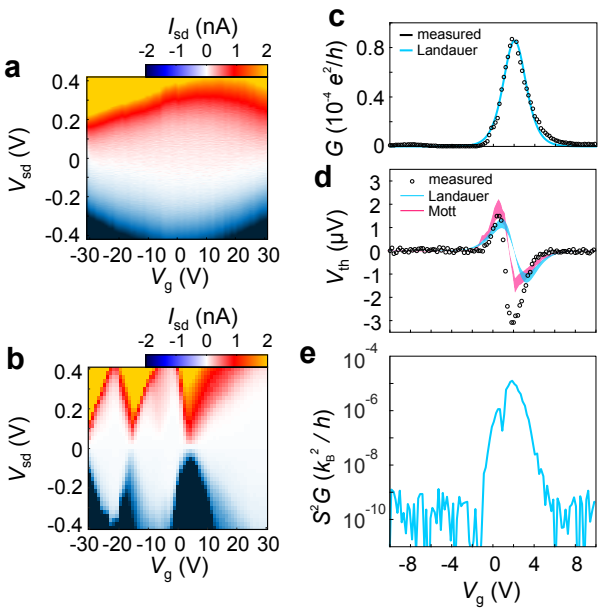


Figure C.8 Thermoelectric characterisation of a C_{60} junction (Device G). a) Current map as a function of back gate and bias voltage before and b) after molecule deposition recorded at $T_0 = 77\,\mathrm{K}$. c) AC Zero-bias conductance and d) Thermovoltage (measured with a temperature bias of $\Delta T = 100 \pm 20\,\mathrm{mK}$) as a function of back gate voltage measured at $T_0 = 77\,\mathrm{K}$. The blue and pink curves show theoretical calculations using a Landauer-type approach and the Mott formula, respectively. e) Power factor as a function of back gate voltage measured at $T_0 = 77\,\mathrm{K}$ with $\Delta T = 100 \pm 20\,\mathrm{mK}$.

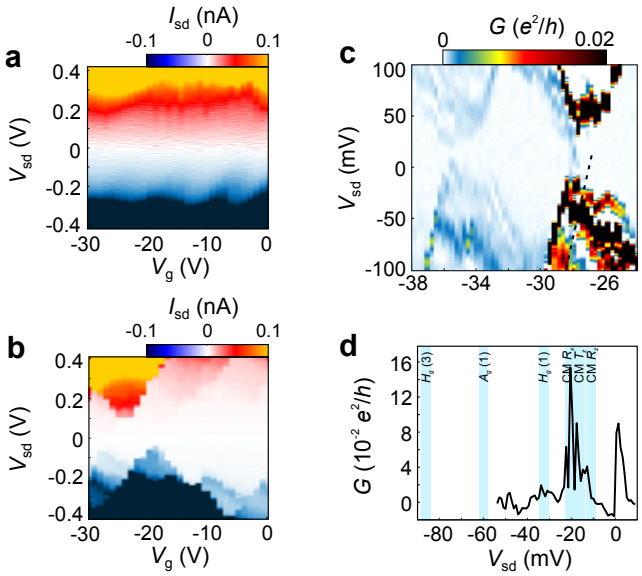


Figure C.9 Electric characterisation of a C_{60} junction (Device H). a) Current map as a function of back gate and bias voltage before and b) after molecule deposition recorded at $T_0 = 77\,\mathrm{K}$ c) Differential conductance maps of the sequential tunnelling region in (b) measured at $T_0 = 4.2\,\mathrm{K}$. Line cut along the dotted black line is shown in d) The blue shaded areas in (d) indicate the energies of different vibrational modes of the C_{60} bis-adduct.

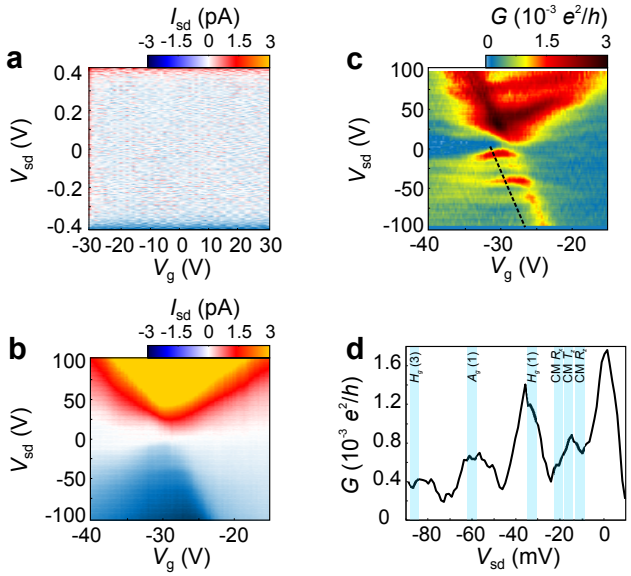


Figure C.10 Electric characterisation of a C_{60} junction (Device I). a) Current map as a function of back gate and bias voltage before and b) after molecule deposition recorded at $T_0 = 4.2\,\mathrm{K}$. c) Differential conductance maps of the sequential tunnelling region in (b) measured at $T_0 = 4.2\,\mathrm{K}$. Line cut along the dotted black line is shown in d) The blue shaded areas in (d) indicate the energies of different vibrational modes of the C_{60} bis-adduct.

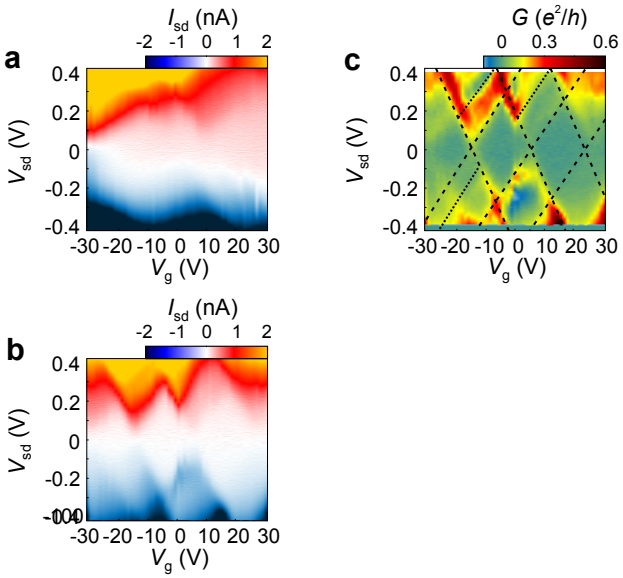


Figure C.11 Electric characterisation of a C_{60} junction (Device J). a) Current map as a function of back gate and bias voltage before and b) after molecule deposition recorded at $T_0 = 4.2\,\mathrm{K}$. c), Differential conductance maps of the sequential tunnelling region in (b) measured at $T_0 = 4.2\,\mathrm{K}$. Black dotted lines indicate the positions of the edges of the Coulomb diamonds and excited states. The energy of the excited states is 94 meV and 170 meV and could be attributed to the $H_g(4)$ and $H_g(7)$ Raman mode of the C_{60} bis adduct, respectively.

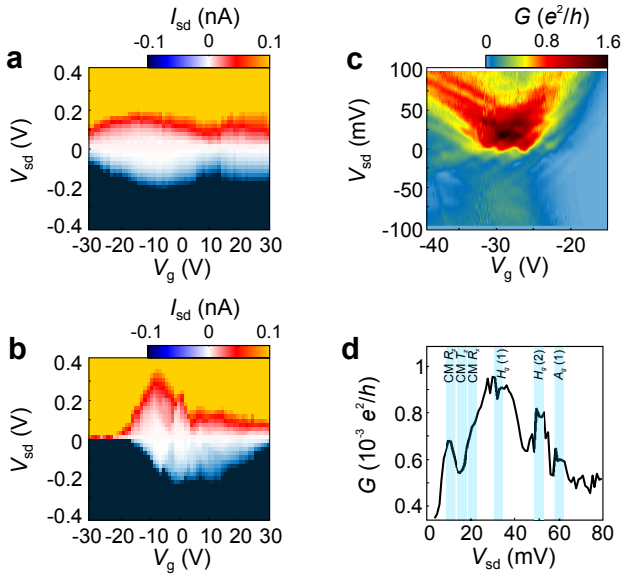


Figure C.12 Electric characterisation of a C_{60} junction (Device K). a) Current map as a function of back gate and bias voltage before and b) after molecule deposition recorded at $T_0 = 4.2\,\mathrm{K}$. c) Differential conductance maps of the sequential tunnelling region in (b) measured at $T_0 = 4.2\,\mathrm{K}$. Line cut along the dotted black line is shown in d). The blue shaded areas in (d) indicate the energies of different vibrational modes of the C_{60} bis-adduct.

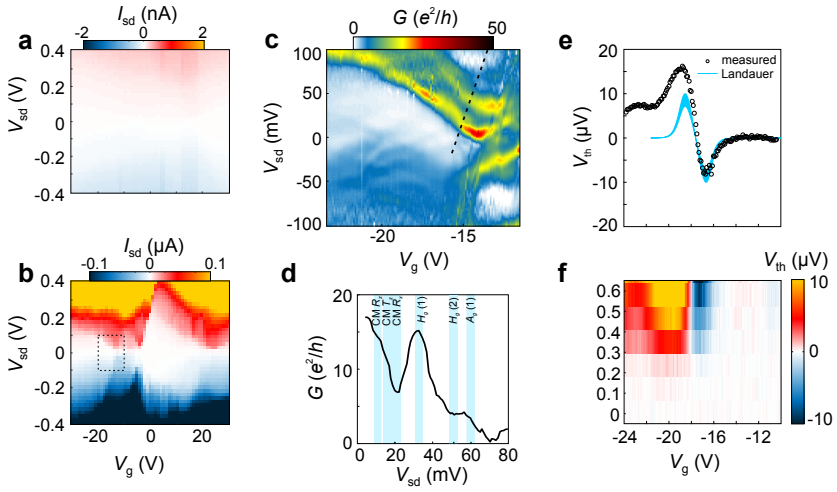


Figure C.13 Electric characterisation of a C_{60} junction (Device L). a) Current map as a function of back gate and bias voltage before and b) after molecule deposition recorded at $T_0 = 4.2\,\mathrm{K}$. c) Differential conductance maps of the sequential tunnelling region in (b) measured at $T_0 = 4.2\,\mathrm{K}$. Line cut along the dotted black line is shown in d). The blue shaded areas in (d) indicate the energies of different vibrational modes of the C_{60} bis-adduct. **e**, Thermovoltage (measured with a temperature bias of $\Delta T = 48 \pm 10\,\mathrm{mK}$) as a function of back gate voltage measured at $T_0 = 4.2\,\mathrm{K}$. Since we were not able to record a conductance trace for this device we extracted $\alpha = 17.6\,\mathrm{meV}$ and $\Gamma = \Gamma_\mathrm{L} + \Gamma_\mathrm{R} = 0.084\,\mathrm{meV}$ from the data in **b** which we used to estimate the thermovoltage in e) using the Landauer approach (blue curve). f) Thermovoltage as a function of back gate and heater voltage measured at $T_0 = 4.2\,\mathrm{K}$.

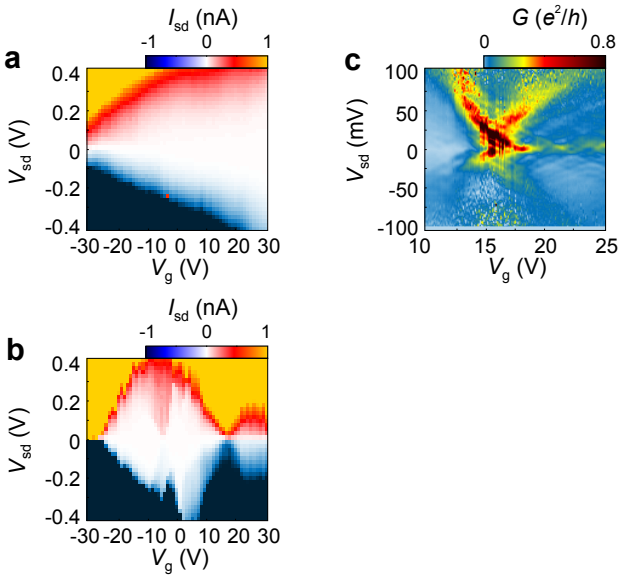


Figure C.14 Electric characterisation of a C_{60} junction (Device M). a) Current map as a function of back gate and bias voltage before and b) after molecule deposition recorded at $T_0 = 3.2\,\mathrm{K}$. c) Differential conductance maps of the sequential tunnelling region in (b) measured at $T_0 = 3.2\,\mathrm{K}$.

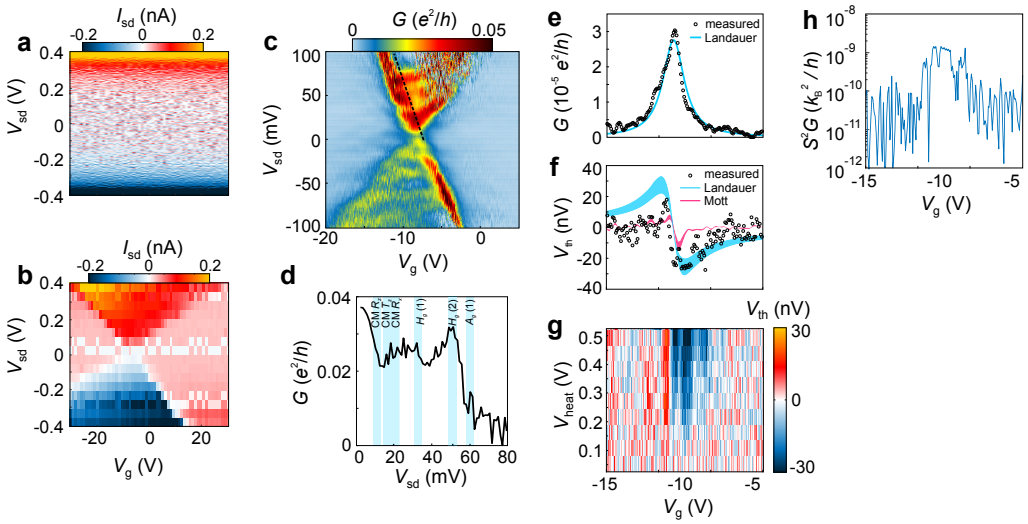


Figure C.15 Thermoelectric characterisation of a C_{60} junction (Device N). a) Current map as a function of back gate and bias voltage before ($T_0 = 77\,\mathrm{K}$) and b) after molecule deposition ($T_0 = 4.2\,\mathrm{K}$). c) Differential conductance map of the sequential tunnelling region in (b) measured at $T_0 = 4.2\,\mathrm{K}$. Line cut along the dotted black line is shown in d). The blue shaded areas in (d) indicate the energies of different vibrational modes of the C_{60} bis-adduct. e) AC Zero-bias conductance and f) Thermovoltage (measured with a temperature bias of $\Delta T = 73 \pm 15\,\mathrm{mK}$) as a function of back gate voltage measured at $T_0 = 4.2\,\mathrm{K}$. The blue and pink curves show theoretical calculations using a Landauer-type approach and the Mott formula, respectively. g) Thermovoltage as a function of back gate and heater voltage measured at $T_0 = 4.2\,\mathrm{K}$. h) Power factor as a function of back gate voltage.

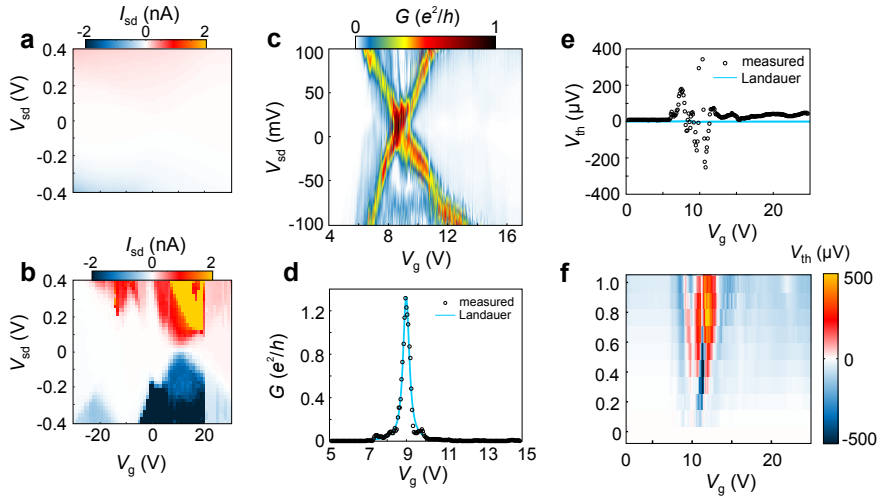


Figure C.16 Thermoelectric characterisation of a C_{60} junction (Device O). a) Current map as a function of back gate and bias voltage before and b) after molecule deposition recorded at $T_0 = 77\,\mathrm{K}$. c) Differential conductance map of the sequential tunnelling region in (b) measured at $T_0 = 4.2\,\mathrm{K}$. d) AC Zero-bias conductance and e) Thermovoltage (measured with a temperature bias of $\Delta T = 86 \pm 17\,\mathrm{mK}$) as a function of back gate voltage measured at $T_0 = 4.2\,\mathrm{K}$. The blue curves show theoretical calculations using a Landauer-type approach. The thermovoltage signal for this device is about one order of magnitude bigger than the value estimated using the Landauer approach. The reason for this discrepancy is unclear. f) Thermovoltage as a function of back gate and heater voltage measured at $T_0 = 4.2\,\mathrm{K}$.

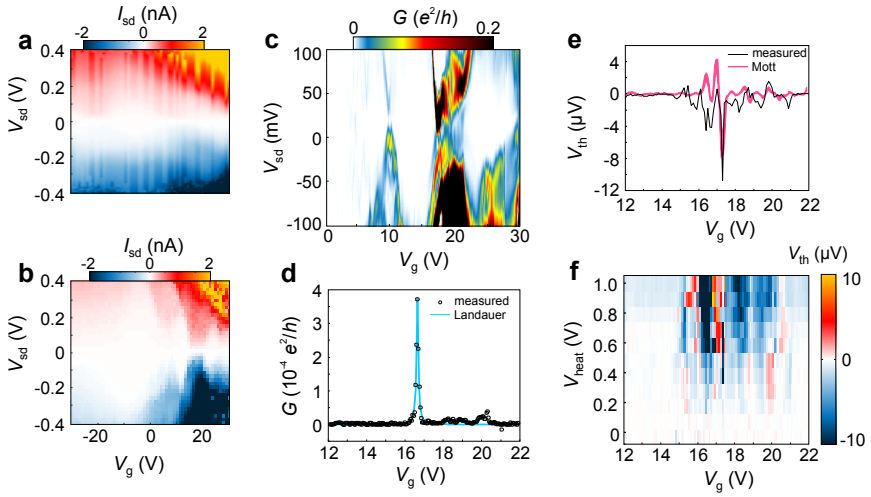


Figure C.17 Thermoelectric characterisation of a C_{60} junction (Device P). a) Current map as a function of back gate and bias voltage before and b) after molecule deposition recorded at $T_0 = 77\,\mathrm{K}$. c) Differential conductance map of the sequential tunnelling region in (b) measured at $T_0 = 4.2\,\mathrm{K}$. d) AC Zero-bias conductance and e) Thermovoltage (measured with a temperature bias of $\Delta T = 80 \pm 16\,\mathrm{mK}$) as a function of back gate voltage measured at $T_0 = 4.2\,\mathrm{K}$. The blue and pink curves show theoretical calculations using a Landauer-type approach and the Mott approximation, respectively. The complex conductance data (see (c)) can not be fully described by a single peak. Thus the Mott approximation is used to compare the measured and theoretical thermovoltage. f) Thermovoltage as a function of back gate and heater voltage measured at $T_0 = 4.2\,\mathrm{K}$.

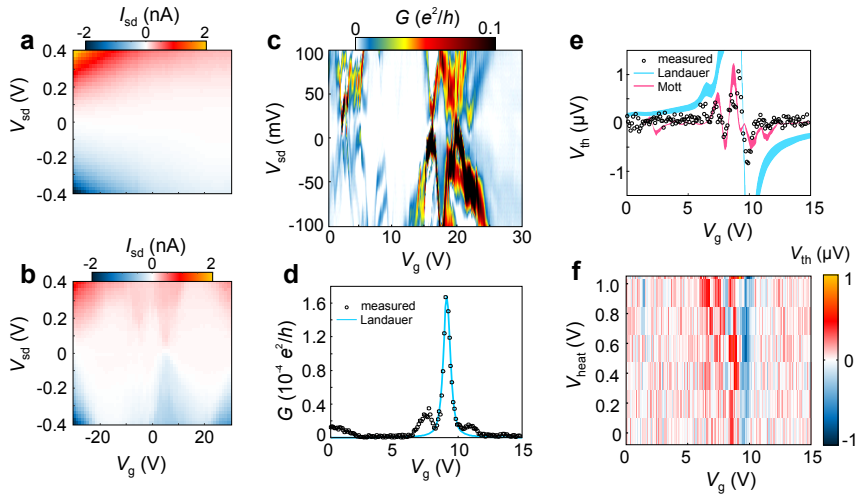


Figure C.18 Thermoelectric characterisation of a C_{60} junction (Device Q). a) Current map as a function of back gate and bias voltage before and b) after molecule deposition recorded at $T_0 = 77\,\mathrm{K}$. c) Differential conductance map of the sequential tunnelling region in (b) measured at $T_0 = 77\,\mathrm{K}$. d) AC Zero-bias conductance and e) Thermovoltage (measured with a temperature bias of $\Delta T = 660 \pm 130\,\mathrm{mK}$) as a function of back gate voltage measured at $T_0 = 77\,\mathrm{K}$. The blue and pink curves show theoretical calculations using a Landauer-type approach and the Mott approximation, respectively. f) Thermovoltage as a function of back gate and heater voltage measured at $T_0 = 77\,\mathrm{K}$.

C.2 Local Mapping of Thermoelectric Properties of Two-dimensional Structures via Scanning Thermal Gate Microscopy

Here, further details on the tip calibration, Gaussian fitting and Deconvolution operation used in chapter 9 are provided. The section is closely based on the supplementary information in Harzheim *et al.* [221].

C.2.1 Temperature Tip Calibration

The temperature of the tip apex is a fraction of the tip-resistor temperature when a heating current is applied to the tip. The difference between the two temperatures is a function of the conical shape of the tip as well as the tip material and the substrate material the tip is in contact with. For a low thermal conductivity substrate material with poor heat dissipation the temperature at the tip-sample contact will be higher than for a material with a higher thermal conductivity. The tip apex temperature when in contact with different materials can be obtained by experiments and COMSOL simulations [167, 229]. For example, the temperature increase at the apex of the tip when in contact with gold (thermal conductivity of $310\,\mathrm{W\,m^{-1}\,K^{-1}}$) is ≈ 3 to $5\,\%$ of the heater temperature and for 300 nm of SiO_2 (thermal conductivity of about $1\,\mathrm{W\,m^{-1}\,K^{-1}}$) it is ≈ 80 to $85\,\%$ of the heater temperature.

C.2.2 Pseudo 2D Deconvolution

In order to deconvolute the thermovoltage maps and extract the Seebeck coefficient, a pseudo 2D deconvolution is used. In a first step, a 2D map of the assumed temperature distribution on the sample based on a Gaussian function is calculated (see Figure C.19a).
In a second step, this temperature distribution is differentiated along the x-axis as shown in Figure C.19b. The differentiation is along the x-axis since we later align all thermovoltage maps such that the two contacts used for measurement are aligned along the x-axis. We then assume any thermovoltage that builds up as a result of a temperature gradient in the y-direction does not contribute to the measured thermovoltage and can be neglected in the following.
In order to calculate the 2D Seebeck coefficient, the temperature gradient is then transposed on top of part of the thermovoltage image, that is with each line corre-

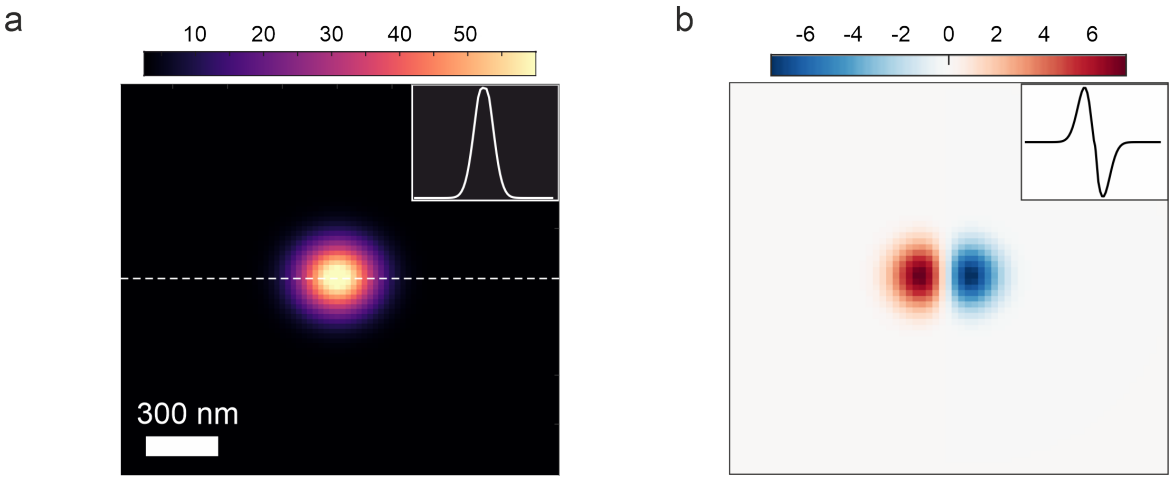


Figure C.19 (a) Temperature distribution based on a Gaussian function, insets shows the linecut through the white dashed line. (b) Temperature distribution in a) differentiated with respect to the x-axis, insets shows the linecut through the black dashed line.

sponding to one line in the thermovoltage image (see Figure C.20). Then each line of the temperature gradient image is deconvoluted with each line of the thermovoltage image in a 1D line deconvolution and the result added up. Since here the middle of the temperature gradient image represents the position of the heated SThM tip, this gradient image is then scanned over the thermovoltage image, with each pixel in the resulting Seebeck picture corresponding to the deconvolution of the temperature gradient with the surrounding area around the respective pixel in the thermovoltage map. The algorithm used here is deconvreg which is part of the Matlab image

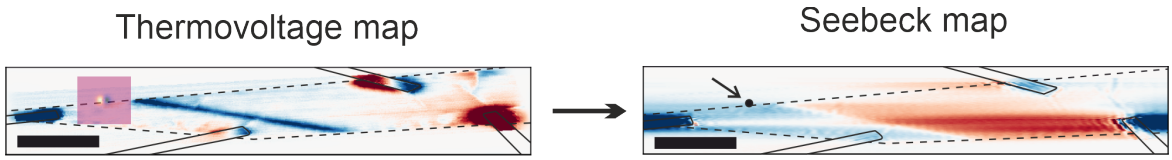


Figure C.20 (a) Schematic showing the deconvolution of the temperature gradient (semi-transparent overlaid on the thermovoltage map) with the thermovoltage map (left) and the resulting pixel in the Seebeck map (marked by the black arrow in the Seebeck map).

processing toolbox and uses a regularized filter algorithm. It assumes that the image to be deconvoluted (the thermovoltage map) was created by convolving the original image (the Seebeck coefficient map) with a point spread function (the temperature profile of the SThM tip) and the addition of noise. Crucially, since this algorithm is developed for images, it does not take into account the dimension of the original

image or the deconvolved image. We will examine below how to correct for this.

For two recorded images (f and g) that are physical fields (that is moving along the pixels in the x and y direction of the image is associated with a change in a physical quantity such as position), their deconvolution h is again a physical field. The units of the deconvolution are then given by $dim(h) = dim(f)dim(g)dim(A)$ where $dim(A)$ is the dimension of the image area, usually square meters. The convolution $h = f * g$ can then be written as a discrete Riemann sum

$$h_n \approx \Delta A \sum_k f_{n-k} g_k \,, \tag{C.1}$$

where the dimensionality of the image is taken into account by ΔA, the area of one pixel. In digital image processing, the units of the image are often ignored (as is the case in our deconvolution algorithm), meaning the convolution in this case is just given by

$$h_n \approx \sum_k f_{n-k} g_k \,. \tag{C.2}$$

In order to arrive at the right expression for the deconvolution we then have to take into account the dimensionality of the original image by correcting the final deconvolved image h_n by ΔA.
In our case, the algorithm used is essentially employing Fourier transforms to perform the deconvolution, that is the deconvolution is given by:

$$f = \text{ifft}(F) = \text{ifft}(H/G) \,, \tag{C.3}$$

where F, G and H are the Fourier transforms of f, g and h respectively and ifft() denotes the inverse Fourier transform. Since Fourier transforms and therefore its inverse obey linearity the deconvolution, taking into account the dimensionality via ΔA, is given by

$$f = \text{ifft}(H/G)\Delta A \,. \tag{C.4}$$

Therefore, we need to multiply the resulting deconvolved Seebeck map by ΔA, which is equal to $0.0022\,\mu m^2$ for the rectangular device shown in Figure 9.2 and $0.0047\,\mu m^2$ for the SLG/BLG junction device shown in Figure 9.3.

C.2.3 Approximation of the Width of the Temperature Distribution

In order to estimate the temperature distribution created by the tip, the derivative of the sigmoidal Boltzmann curve in Figure 9.6e is fitted with a Gaussian curve. The Gaussian curve has the form

$$f(x) = \frac{1}{\sigma\sqrt{2\pi}} e^{\frac{-(x-\mu)^2}{2\sigma^2}}, \tag{C.5}$$

where μ is the position of the peak of the gaussian distribution and σ is the standard deviation. The fit (see Figure C.21) gives $\sigma = 100\,\text{nm}$ which is then used to inform the deconvolution of the thermovoltage maps and calculate the Seebeck maps. In addition, a width of the temperature distribution of $l_{\text{dT}} \approx 1\,\mu\text{m}$ can be extracted.

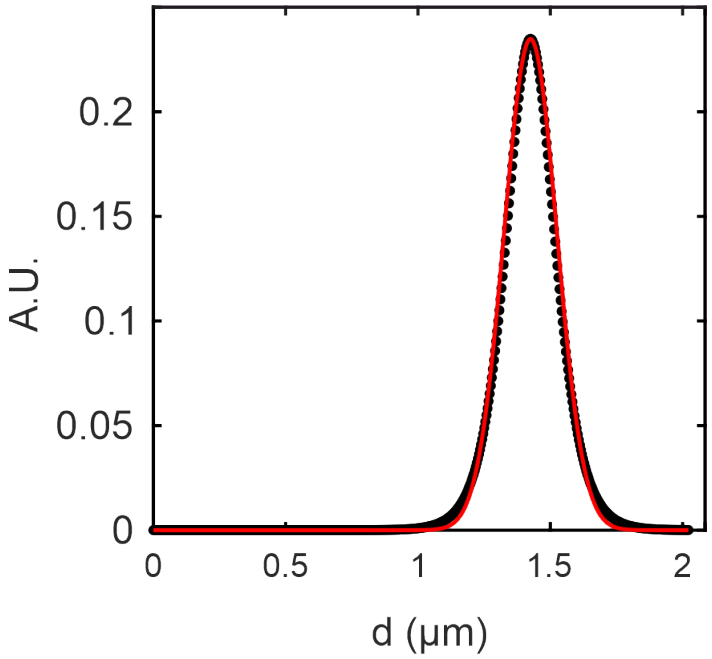


Figure C.21 Fit of the derivative of the sigmoidal Boltzmann curve in Figure 9.6e (black dots) with a Gaussian (red line).

C.2.4 Extraction of Average Thermovoltage and Seebeck Coefficient from 2D Maps via Gaussian Fitting

In order to extract the Seebeck coefficient of the graphene channel from the deconvoluted Seebeck maps in Figure 9.6a, the values in the channel are plotted in

a bar graph, where the y-axis represents the amount of pixels occupied by each Seebeck value on the x-axis (see Figure C.22). We fit the distribution of values using a four-peaked Gaussian to account for the multiple clusters clearly visible (see Figure C.22). The clusters around a Seebeck coefficient of $0\,\mu V K^{-1}$ are attributed to charge puddles in the graphene that are still noticeable at high carrier concentrations. Similarly, small clusters at exceedingly high or negative S are most likely due to effects near the contact and not chosen either. The peaks used are marked by a black arrow with the error then being determined by the width of the respective peak. The same procedure was repeated for the thermovoltage signal on the contacts extracted from the thermovoltage maps in Figure 9.2. Here, clear outliers in the thermovoltage values around $0\,\mu V K^{-1}$ were excluded.

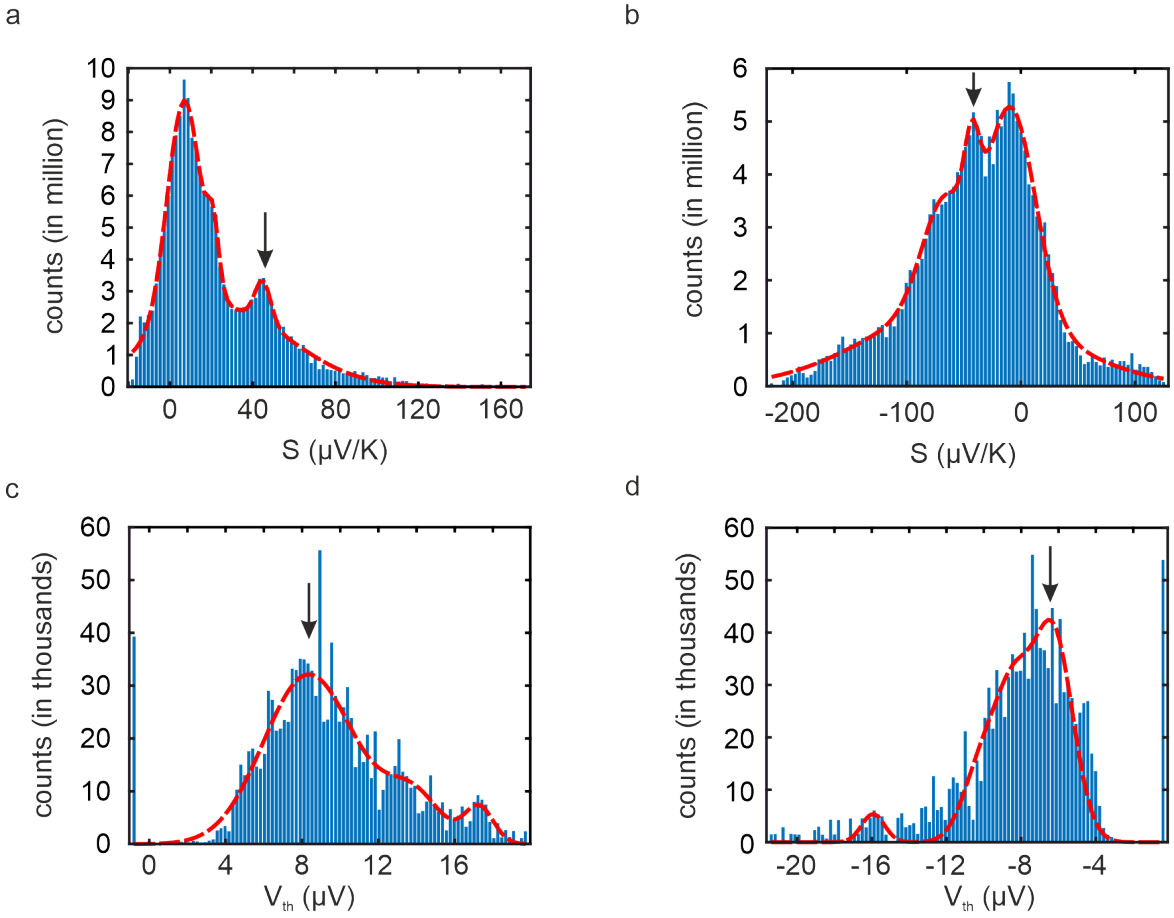


Figure C.22 a-b) Bar graph showing the distribution of deconvoluted Seebeck values along the graphene channel in Figure 9.6a for a p-doped (a) and n-doped (b) sample. c-d) Bar graph showing the distribution of thermovoltage values in Figure 9.2a on the contacts for a p-doped (c) and n-doped (d) sample.